

# Microwave Methods for Additive Layer Manufacturing

by

Nicholas CLARK



A thesis submitted to Cardiff University  
for the degree of Doctor of Philosophy

2nd July 2017



# *Abstract*

This thesis presents the novel application of microwave technology to the process of additive layer manufacturing (ALM).

A particle size sensor, based on microwave cavity perturbation, is described and subsequently demonstrated by the measurement of the complex permeability of a series of Titanium powders. The results are compared with existing theory and finite element simulations of metallic powders. The ability to discern changing particle size distributions is important in ensuring the reliable operation of selective laser melting machines but, to remain industrially relevant, it is vital that the proposed system can be produced at low cost. By way of demonstration, the design and construction of an inexpensive scalar network analyser was completed.

A systematic study of surface resistance of a number of metal surfaces, produced by Selective Laser Melting, was undertaken. Using a dielectric resonator with a “lift-off” calibration procedure, the losses of surfaces manufactured in orthogonal orientations and different surface finishes were compared. Surface roughness measurements showed that microwave losses were not monotonically dependent on root-mean-square surface roughness; this was attributed to differing roughness feature size distributions.

For microwave characterization of materials over a wide temperature range, it is often desirable to perform cavity perturbation measurements at elevated temperatures. However, it is shown here that heat treatment can permanently modify the surface resistance of a metal surface and potentially lead to inaccurate perturbation results. X-Ray diffraction measurements confirm the source of modification is due to changes in surface stress and the appearance of solution precipitates. The sensitivity of microwave measurements to surface stress also demonstrates the potential for microwave assessment of surfaces produced by ALM.

Finally, to stimulate further work in this area, the design of a single mode microwave heating system was discussed and a prototype developed.

# *Acknowledgements*

My supervisor Prof Adrian Porch who has made this thesis possible receives my utmost respect and thanks.

All those in the Centre for High Frequency Engineering especially Heungae Choi, Jerome Cuenca, Jon Hartley and Sam Hefford.

My various collaborators at Cardiff University; Dr Emmanuel Brousseau, Dr Greg Shaw, Dr Mark Eaton and Dr Alastair Clarke.

My industrial supervisors at Renishaw plc; Prof Geoff McFarland and Nick Jones.

Funding provided by EPSRC in collaboration with Renishaw via their Industrial CASE studentship programme. (Award 13440025)

Finally, my love and thanks go to my family, parents and especially my wife Naomi.

## *Publications*

N. Clark, N. Jones and A. Porch, “Measurement of Average Particle Size in Metal Powders by Microwave Cavity Perturbation in the Magnetic Field”, *Sensors and Actuators A: Physical*. DOI: *10.1016/j.sna.2017.03.037*

N. Clark, S. Hefford and A. Porch, “Effect of Build Orientation and Surface Finish on Surface Resistance in Microwave Components Produced by Selective Laser Melting”, *European Microwave Week 2017, Nuremberg - To be presented*

N. Clark, N. Jones, R. Setchi and A. Porch, “Particle Size Characterisation of Metals Powders for Additive Manufacturing Using a Microwave Sensor”, *Powder Technology - Under Review*

N. Clark, G. Shaw and A. Porch, “Effect of Surface Stresses on Microwave Surface Resistance and its Impact for Cavity Perturbation Measurements”, *IEEE Microwave and Wireless Components Letters - Accepted, awaiting publication*

UK Patent GB1609856.8, “A Particle Size Sensor for Metallic Powders” - *Filed 20/07/2016*

### CO-AUTHOR

A.A. Abduljabar, N. Clark, J. Lees and A. Porch, “Dual Mode Microwave Microfluidic Sensor for Temperature Variant Liquid Characterization”, *IEEE Transactions on Microwave Theory and Techniques*. DOI: *10.1109/TMTT.2016.2647249*



# Contents

<b>Abstract</b>	<b>i</b>
<b>Acknowledgements</b>	<b>ii</b>
<b>Publications</b>	<b>iii</b>
<b>Contents</b>	<b>iv</b>
<b>List of Figures</b>	<b>viii</b>
<b>List of Tables</b>	<b>xv</b>
<b>Abbreviations</b>	<b>xvi</b>
<b>1 Introduction and Motivation</b>	<b>1</b>
1.1 Introduction to Additive Layer Manufacturing . . . . .	1
1.2 Metallic Powders and Microwave Spectroscopy . . . . .	3
1.3 Electrical Properties and SLM . . . . .	6
1.4 Microwave Heating . . . . .	7
1.5 Project Aims . . . . .	7
1.6 Novel Contribution . . . . .	7
<b>2 Microwave Cavity Perturbation</b>	<b>9</b>
2.1 Complex Permittivity and Permeability . . . . .	9
2.2 Perturbation Theory . . . . .	11
2.3 Cavity Resonator Design . . . . .	13
2.3.1 Finite Element Modeling . . . . .	15
2.3.2 Coupling . . . . .	16
2.4 Complex Resonant Frequency . . . . .	17
2.5 Mode Scaling Constant . . . . .	18
2.6 Cavity Resonator Analysis . . . . .	19
2.6.1 Lorentzian Fit and 3dB points . . . . .	20
2.6.2 Circle Fit . . . . .	21
2.6.3 Measurement Error . . . . .	22
2.6.4 Degeneracy . . . . .	24
2.6.5 Low Q Considerations . . . . .	29
2.7 Sample Orientation and Depolarisation . . . . .	30
2.8 Common Measurement Modes . . . . .	31
2.9 Software . . . . .	32

2.10	Temperature Correction . . . . .	33
2.10.1	Analytical Analysis . . . . .	35
2.10.2	Reference Mode . . . . .	40
2.11	Measurement Uncertainty . . . . .	43
2.12	Summary . . . . .	45
<b>3</b>	<b>Microwave Electromagnetic Properties of Conducting Powder</b>	<b>47</b>
3.1	Introduction . . . . .	47
3.2	Powder Samples . . . . .	48
3.2.1	Sample Preparation . . . . .	49
3.2.2	Oxide Layer . . . . .	49
3.2.3	Particle Size . . . . .	50
3.2.4	Sample Density . . . . .	53
3.3	Magnetic Field and Permeability . . . . .	54
3.3.1	Theory and Background . . . . .	54
3.3.2	Simulation of Metallic Particles in a Magnetic Field . . . . .	58
3.3.3	Experimentation . . . . .	65
3.3.4	Discussion . . . . .	68
3.4	Electric Field and Permittivity . . . . .	72
3.4.1	Theory and Background . . . . .	72
3.4.2	Initial Experimentation . . . . .	73
3.4.3	Temperature Measurements . . . . .	75
3.4.4	Discussion . . . . .	79
3.5	Conclusions . . . . .	79
<b>4</b>	<b>Measurement of Surface Resistance Using Microwave Methods</b>	<b>81</b>
4.1	Introduction . . . . .	81
4.2	Dielectric Resonator Test Fixture . . . . .	83
4.2.1	Measurement Principle . . . . .	83
4.2.2	Measurement Procedure . . . . .	84
4.2.3	Resonator Design . . . . .	87
4.2.4	Errors and Accuracy . . . . .	89
4.3	Loss and Roughness . . . . .	92
4.3.1	Simulation . . . . .	92
4.3.2	Roughness Measurement . . . . .	93
4.3.3	Spectral Analysis of Roughness Profile . . . . .	96
4.4	SLM Plate Samples . . . . .	97
4.5	Results . . . . .	98
4.6	Discussion . . . . .	98
4.6.1	Ti6Al4V - Titanium . . . . .	99
4.6.2	Al10SiMg - Aluminium . . . . .	103
4.6.3	CoCr - Cobalt-Chrome . . . . .	104
4.7	Conclusions . . . . .	105
<b>5</b>	<b>Effect of Heat Treatment on the Conductivity of Aluminium</b>	<b>109</b>
5.1	Introduction . . . . .	109
5.2	Samples and Procedure . . . . .	110

---

5.3	Results and Discussion . . . . .	112
5.3.1	Surface Resistance . . . . .	112
5.3.2	XRD . . . . .	113
5.4	Conclusion . . . . .	114
<b>6</b>	<b>Basic Scalar Network Analyser</b>	<b>117</b>
6.1	BSA Prototypes . . . . .	118
6.1.1	Software . . . . .	119
6.1.2	Basic Specifications . . . . .	120
6.2	Design Considerations . . . . .	120
6.2.1	Frequency Resolution . . . . .	120
6.2.2	Frequency Pulling . . . . .	122
6.2.3	Noise and Dynamic Range . . . . .	124
6.2.4	Temperature . . . . .	125
6.2.5	Tune Ramp . . . . .	125
6.2.6	Speed . . . . .	125
6.2.7	Reflection Measurement . . . . .	126
6.2.8	Filtering and Averaging . . . . .	126
6.3	Calibration . . . . .	127
6.3.1	Frequency Calibration . . . . .	127
6.3.2	Power Meter Calibration . . . . .	128
6.4	Sample Measurements and Sensitivity . . . . .	130
6.5	Discussion and Conclusions . . . . .	132
<b>7</b>	<b>Heating in a Single-Mode Cavity Resonator</b>	<b>135</b>
7.1	Introduction . . . . .	135
7.2	Theory of Operation . . . . .	136
7.3	System Description . . . . .	141
7.4	Conclusion . . . . .	143
<b>8</b>	<b>Final Summary and Further Work</b>	<b>145</b>
8.1	Microwave Cavity Perturbation . . . . .	145
8.2	Perturbation and Metal Powders . . . . .	145
8.3	SLM and Surface Resistance . . . . .	146
8.4	Cavity Q and Annealing . . . . .	146
8.5	Scalar Network Analyser . . . . .	146
8.6	Single-mode Microwave Heating . . . . .	147
8.7	Closing Remarks . . . . .	147
	<b>Bibliography</b>	<b>149</b>
	<b>Appendix</b>	<b>165</b>



# List of Figures

1.1	Single piece, SLM produced cylindrical microwave resonant cavity. . . . .	1
1.2	(a) Renishaw AM-250. (b) Operation overview. . . . .	2
1.3	Microwave cavity perturbation system showing cavity with simulated magnetic field operating in the $TE_{011}$ mode. . . . .	4
2.1	Cylindrical cavity geometry. . . . .	13
2.2	E-field simulation of open circuit, electric field coupling. . . . .	16
2.3	H-field simulation of short circuit, magnetic field coupling. . . . .	16
2.4	Basic LCR resonator model. . . . .	20
2.5	Measured and rotated complex $S_{21}$ data, $TM_{010}$ . . . . .	22
2.6	Measured $ S_{21} $ $TE_{022}$ trace and attempted lorentzian fit. . . . .	23
2.7	Cylindrical cavity with $TM_{111}$ mode-trap caused by hole placed on cavity axis. . . . .	25
2.8	Simulated effect of axial hole mode-trap on $TM_{111}$ and $TE_{011}$ modes. . . . .	25
2.9	$TM_{110}$ potential coupling positions. . . . .	26
2.10	Degenerate system circuit model. . . . .	26
2.11	Calculated distortion caused by a single degeneracy. . . . .	28
2.12	Calculated perturbation of a singly rotationally degenerate mode. . . . .	29
2.13	Calculated perturbation error for a single mismatched degeneracy. . . . .	29
2.14	Potential measurement error for low Q resonators using a lorentzian fit when the frequency dependence of the Q and coupling co-efficient is ignored. . . . .	30
2.15	Sample dipole orientation in the presence of an electric field. . . . .	31
2.16	Mode catalog. Frequencies show for cavity with $a = 4.6cm$ and $d = 4cm$ . . . . .	32
2.17	Cardiff Cavity Perturbation (CCP) software - data viewer. . . . .	33
2.18	Cardiff Cavity Perturbation (CCP) software - main acquisition window. . . . .	33
2.19	Cardiff Cavity Perturbation (CCP) software - acquisition configuration window. . . . .	34
2.20	Cardiff Cavity Perturbation (CCP) software - raw trace and data fit. . . . .	34
2.21	Microwave cavity, network analyser and oven used in temperature correction experiments. . . . .	35
2.22	$TM_{010}$ frequency modification by thermal expansion. . . . .	36
2.23	(a) $TM_{010}$ current distribution. (b) Length split configuration. (c) Diameter split configuration. . . . .	37
2.24	Typical $TM_{010}$ Q-factor for diameter split configuration during cavity heating showing strongly non-linear and chaotic response. . . . .	38
2.25	$TM_{010}$ Q during heat treatment in the favourable, diameter split, configuration. Theory curve given by Equation 2.56. . . . .	38
2.26	$TM_{010}$ Q during repeated heat treatment. . . . .	39

2.27	TM <sub>010</sub> Q repeated heat treatment after re-assembly. . . . .	39
2.28	Measured Q of TM <sub>210</sub> and TM <sub>010</sub> during heat treatment. . . . .	42
2.29	Error distribution and raw error when deriving TM <sub>010</sub> Q from measured TM <sub>210</sub> Q in range 30-200°C. . . . .	42
2.30	Simulated TM <sub>210</sub> surface current distribution. . . . .	43
2.31	Q-factor instability of TM <sub>210</sub> during third heat treatment cycle and sta- bility after subsequent re-assembly. . . . .	43
2.32	Relative frequency shift of acetone, normalised to the average shift. Ef- fective sample volume error distribution. . . . .	44
3.1	As sold base Ti6Al4V powder particle size distribution. . . . .	51
3.2	Fractionated Ti6Al4V powder particle size distributions. Separate fractions obtained by sieving base powder purchased from manufacturer. . . . .	51
3.3	Optical microscope images of fractionated Ti6Al4V powder. . . . .	52
3.4	Theoretical metallic powder complex permeability. . . . .	55
3.5	Normalised metallic powder magnetic absorption for a fixed frequency. The 3 curves represent 3 separate conductivities. . . . .	56
3.6	Changing absorption characteristic for metallic powder as conductivity is reduced. . . . .	56
3.7	Comparison of predicted permeability for single particle (solid lines) and when considering a particle size distribution (dashed lines). (A) Raw permeability. (B) Percentage difference of two curves. . . . .	57
3.8	Single particle magnetic simulation. Dimensions in $\mu\text{m}$ (a) Magnetic field distribution, field applied in Y direction. (b) Induced current, field applied out of the page. . . . .	58
3.9	Simulated and theoretical single particle magnetic absorption. . . . .	59
3.10	Relative magnetic absorption as two spheres are brought close together, $a/\delta = 5$ at 2.45 GHz, $a = 20\mu\text{m}$ . . . . .	59
3.11	Relative magnetic absorption of two adjacent spheres as a function of the particle size. . . . .	60
3.12	Packing Schemes . . . . .	60
3.13	HCP particle array generated for COMSOL simulation. . . . .	61
3.14	Simulation results based on the 216 sphere HCP array. The subscript denotes the direction of the applied magnetic field. Cases where the particles touch and are separated by $0.1\mu\text{m}$ show distinct results. . . . .	61
3.15	Magnetic field strength cross-section in xy plane taken through the third HCP layer. $a/\delta = 6$ . Field applied in Z direction (out of the page). (a) Separated spheres. (b) Touching spheres. . . . .	62
3.16	Simulated magnetic absorptions based on the 216 particle HCP array compared to the predicted absorption for a single particle. Stacked layers have been separated but particles touch within each layer. Magnetic field is applied perpendicular to the layers and it is therefore shown that only particle contacts perpendicular to the applied magnetic field are significant. . . . .	63
3.17	Comparison of single particle absorption and simulated magnetic absorp- tion based on a tightly packed $3\times 3\times 3$ HCP particle matrix. . . . .	63
3.18	Cubic close pack 3D simulation model with periodic boundaries across x and z showing the maximum 4 layers. . . . .	64
3.19	Multi-layer cubic close pack periodic simulation of magnetic absorption. . . . .	65

3.20	Cylindrical cavity used for measurement. (a) Photograph. (b) Schematic cut-away showing sample in situ and simulated $TE_{011}$ magnetic field distribution. . . . .	65
3.21	Fractioned Ti6Al4V $TE_{011}$ measurement traces. . . . .	67
3.22	Measured magnetic absorption of fractioned Ti6Al4V powder samples. . . . .	68
3.23	Real permeability of fraction Ti6Al4V powder samples. (a) $TE_{011}$ . (b) $TE_{012}$ . (c) $TE_{022}$ . . . . .	69
3.24	Measured changing magnetic absorption of powder samples as temperature is changed in-situ. Measured using the cavity's $TE_{011}$ mode at 5.35GHz . . . . .	69
3.25	Ti6Al4V colour change after heat treatment under a small butane torch. . . . .	70
3.26	Raw measurement, using $TE_{011}$ , of the various powders created by mixing the base powder with fraction 1 showing the sensitivity of the measurement to small changes in average particle size. A linear fit is made through the points in order to extract the sensitivity gradient. . . . .	70
3.27	Relative absorption of powder samples compared to the theoretical single particle case. Simulation data taken from periodic cubic close pack COMSOL simulation. . . . .	71
3.28	Theoretical rate of change of real and imaginary permeability with changing particle size. The peak value, along with its corresponding particle size, is labelled. . . . .	72
3.29	Relative theoretical electric field absorption with increasing particle size, plotted independent of frequency. . . . .	73
3.30	Aluminium $TM_{010}$ measurement cavity used for electric field measurements. . . . .	73
3.31	Simulated $TM_{010}$ frequency and Q of cavity perturbed by a 2mm rod perturbation. . . . .	74
3.32	$TM_{010}$ E-field as the result of a on axis perturbation of a 2mm rod. The rod conductivity was set at $10^5$ S/m. . . . .	75
3.33	$TM_{010}$ resonator parameters as 2mm rod is lowered into the cavity. Experimental results obtained with Ti6Al4V filled quartz tube. Simulated rod conductivity is set to $10^3$ S/m. . . . .	75
3.34	Experimental setup used to measure DC conductivity as powder sample is heated. $x = 10$ mm and tube diameter = 2mm. . . . .	76
3.35	Measured DC current in column of Ti6Al4V powder as the result of raised temperature. . . . .	77
3.36	Measured $TM_{010}$ frequency shift for powder sample as temperature is raised. Measurements conducted in-situ within an oven. . . . .	77
3.37	$TM_{010}$ frequency shift for powder sample during 10 annealing cycles undertaken in an oven. Effect of sample sintering labelled (1) and an increasing oxide layer labelled (2). . . . .	78
3.38	$TM_{010}$ resonator parameters of two powder samples as they cool after rapid heating. The results have been normalised to the measured values of the sample before heat treatment. Permanent changes have been highlighted with labels (a) and (b). (1) highlights the initial cooling phase. . . . .	78
4.1	High Q cylindrical cavity despite rough surface. . . . .	82
4.2	Simulated dielectric resonator $TE_{018}$ EM-Fields. . . . .	84

4.3	Dielectric resonator design schematic. . . . .	85
4.4	Changing frequency of the various cavity and dielectric modes as the dielectric position, $x$ , is changed. The measurement mode, $TE_{01\delta}$ , is highlighted and is seen to not be intersected by another mode across the full range of $x$ . . . . .	88
4.5	Completed dielectric resonator alongside sample pieces. . . . .	88
4.6	Loss contributions of the various components in the dielectric resonator . Calculated assuming an aluminium sample base plate using Equation 4.6. . . . .	89
4.7	DR test fixture measured Q-Factor with changing temperature. Measured in-situ in an oven with an aluminium sample piece. . . . .	90
4.8	Dielectric resonator Q as measured and subsequently derived from the resonator model. (A) Q as a function of the dielectric position $x$ . (B) Error between the measured Q and the Q subsequently derived from the model. . . . .	91
4.9	2D simulated roughness profile. . . . .	92
4.10	Simulated normalised microwave surfaces losses relative to the perfectly flat case plotted against feature size for a variety of peak heights, $h$ , and resultant surface roughness values $r_q$ . . . . .	93
4.11	Simulated current density at the two extremes of feature size. Dimensions in $\mu m$ . $\delta = 2\mu m$ . (A) Small features. (B) Large features. . . . .	94
4.12	Simulated losses for different roughness profiles. Normalised surfaces losses are shown to increase with increasing surface roughness, $r_q$ . Different feature widths, $b$ , exhibit a different gradients and the Hammerstad model is shown to match the characteristic when the feature width is 3 times as large as the skin depth.. . . .	95
4.13	3-Dimensional roughness simulation geometry. . . . .	95
4.15	Section of typical roughness profile from drag profilometer. . . . .	95
4.14	2D and 3D roughness simulation loss comparison. . . . .	96
4.16	Build plate and sample orientation. . . . .	97
4.17	SLM plate sample dimensions. The directions X and Y are defined for surface profile measurements. . . . .	98
4.18	Normalised loss of SLM plate samples measured at 5.7GHz using dielectric resonator. . . . .	99
4.19	SLM plate samples RMS surface roughness. (A) Measured in X direction. (B) Measured in Y direction. (C) Difference between directions. . . . .	100
4.20	SLM plate sample density, relative to accepted bulk values, and microwave loss normalised relative to a perfectly flat sample. . . . .	101
4.21	Surface roughness and microwave loss normalised relative to a perfectly flat sample. . . . .	101
4.22	Microscope image of loose powder on vertical orientation, as-built, aluminium sample. . . . .	102
4.23	Feature spectrum of horizontally built Ti6Al4V surfaces. A significantly greater proportion of features smaller than 200 $\mu m$ are seen in the EDM surface. (A) As-Built surface. (B) Wire eroded EDM surface. . . . .	102
4.24	Changing titanium surfaces as measured by WLI. 12 $\times$ 16 mm measurement area. (A) Horizontally produced surface. (B) Vertically produced surface. (C) Wire eroded surface. . . . .	102
4.25	Additively manufactured titanium surface cumulative feature spectrum. . . . .	103

4.26	Horizontal, grit-blasted aluminium surface showing surface pores. . . . .	104
4.27	Vertical, aluminium and cobalt chrome roughness trace comparison. . . . .	104
4.28	Aluminium samples cumulative feature distribution. (X) and (Y) refer to drag profile directions. Subscript G refers to a grit blasted surface and W is a wire eroded surface. A and B are the specific sample sides for the vertically built sample. . . . .	105
4.29	Changing aluminium surfaces as measured by WLI shown as a relief map. 1.4×1.4 mm measurement area. (a) Vertically produced surface. (b) Horizontally produced surface. . . . .	105
4.30	Horizontally built, grit blasted Cobalt Chrome roughness feature spectrum. Highlighted features as the result of patterning from laser scan. . . . .	106
4.31	Horizontally built, grit blasted Cobalt Chrome WLI relief map (1.4 × 1.4mm). . . . .	106
4.32	CoCr cumulative feature distribution. (X) and (Y) refer to drag profile directions. Subscript G refers to a grit blasted surface and W is a wire eroded surface. A is the specific sample side for vertically built sample. . . . .	107
5.1	Relative microwave loss of treated 6082-T6 Aluminium samples. Tested at 5.7 GHz using the dielectric resonator test method described in Chapter 4. . . . .	113
5.2	6082 XRD Spectrum . . . . .	114
5.3	6082 XRD - Al . . . . .	114
5.4	6082 XRD - Mg <sub>2</sub> Si . . . . .	115
6.1	BSA top-level system schematic. . . . .	118
6.2	Photograph of BSA prototype circuits. From the top referred to as A, B and C. Prototype A pictured with connectorised circulator attached. . . . .	119
6.3	Prototype C closeup. (A) Voltage doubler circuit. (B) V-tune signal conditioning. (C) Power meter. (D) Oscillator and output amplifier. . . . .	120
6.4	Tune voltage signal conditioning scaling 0-10V input to 3-7V output with offset voltage noise rejection. . . . .	121
6.5	Measured response, using prototype A, of empty cavity without isolation between oscillator and cavity. . . . .	122
6.6	S <sub>11</sub> of empty cavity and cable. Measured using an Agilent ENA. . . . .	123
6.7	Measured response, using prototype B, of empty cavity with a circulator providing isolation between the oscillator and cavity. The strong non-linear frequency response has been successfully suppressed. . . . .	123
6.8	Comparison of output frequency of prototype B measured either by direct termination into the spectrum analyser or via a 20dB directional coupler with the output left open-circuit. . . . .	124
6.9	Mixing products generated by amplifier. Prototype C output measured directly with Agilent N9010A spectrum analyser. . . . .	125
6.10	Modified frequency tune voltage ramp to minimise post tuning drift. . . . .	126
6.11	BSA system diagram extended to include switchable measurement of reflected power through the circulator. . . . .	127

6.12	A comparison between averaging types showing the acquired data and subsequent lorentzian fit. Obtained from prototype B with a point rate of 2kHz. Plots A and B contain 21 points and C and D contain 101 points. Plots A and C have no point averaging whereas in B and D each point is the average of 10 ADC samples. Additionally, the standard deviation over 100 sweeps for the resonant frequency and Q factor is shown in each case. $Q = 8590$ .	127
6.13	BSA calibration setup.	128
6.14	Output frequency characteristic for prototype BSAs B and C.	128
6.15	Calibration setup. Left of dashed line is BSA.	129
6.16	Measured power meter output voltage characteristic for prototype B.	130
6.17	BSA output response to a variable attenuator showing the effectiveness of the calibration. Open response is also shown were the BSA input is left unconnected. Measured with prototype B with additional external circulator.	131
6.18	Raw measurement traces of cavity perturbation of a 3mm PTFE rod. Taken using Prototype B.	131
7.1	Single port resonator equivalent circuit.	136
7.2	Single-mode microwave heating cavity cut-away diagram. The sample is positioned in order to maximise exposure to electric or magnetic field as required. In the typical $TM_{010}$ setup and for electric field heating, the sample is placed axially and coupling is provided by a short circuit loop. The loop is held by a screw but can be rotated in order to modify the coupling co-efficient and achieve critical coupling.	137
7.3	Effect of rotating coupling loop to the reflected power. At a specific position, $ S_{11} $ is minimised and the cavity is critically coupled. Either side of this position the cavity is under or over coupled. The resonant frequency is also modified during rotation due to the perturbation by the coupling loop.	138
7.4	Reflected power as water is heated via electric field in the $TM_{010}$ mode. Reflected power is seen to increase as the cavity becomes increasingly de-tuned due to the changing dielectric properties of water.	139
7.5	$ S_{11} $ transformed to lorentzian line-shape in order to extract Q using curve fitting procedure.	140
7.6	Heating system schematic.	142
7.7	Heating system with 30W RFPA.	142
7.8	VNA isolator switch configuration.	142
7.9	Dielectric response measured during simultaneous dielectric heating of epoxy resin. Maximum temperature of approximately 60°C reached.	143

# List of Tables

2.1	Comparison of fitting and data collection methods for resonance parameters. . . . .	24
2.2	Cylindrical cavity (radius = 4.6cm, height = 4cm) mode sample energy density. Cylindrical sample placed axially along full cavity height with 5mm diameter. Calculated using Equation 2.57. . . . .	41
3.1	Ti-6Al-4V chemical composition. . . . .	49
3.2	Fractioned Ti6Al4V powder particle size statistics. For example, 10% of the particles, by volume, have radii smaller than $D_{x10}$ . . . . .	52
3.3	Modified base powder average particle sizes. Achieved by mixing of base powder by increasing quantities of fraction 1. . . . .	53
3.4	Ti6Al4V sample filled quartz tube density. Calculated as density relative to bulk Ti6Al4V. $\varnothing$ is inner quartz tube diameter. . . . .	53
3.5	Magnetic measurement mode summary . . . . .	66
3.6	Standard and heat treated Ti64 fractioned samples. . . . .	67
4.1	Dielectric resonator dimensions, labeled in Figure 4.3. . . . .	88
4.2	Measured dielectric resonator loss terms. $\epsilon_1$ of the sapphire was found to be 9.45. . . . .	91
4.3	SLM Plate processing details. <sup>1</sup> Vacuum furnace. <sup>2</sup> Argon quench. [1] . . . . .	97
5.1	6082 Chemical Composition . . . . .	111
5.2	6082-T6 Aluminium sample treatment regimes. . . . .	111
6.1	BSA prototype specifications. . . . .	120
6.2	PTFE rod cavity perturbation comparison between BSA (Prototype B) and Agilent-ENA. . . . .	132

## *Abbreviations*

AC	<b>A</b> lternating <b>C</b> urrent
ADC	<b>A</b> nalog to <b>D</b> igital <b>C</b> onverter
ALM	<b>A</b> dditive <b>L</b> ayer <b>M</b> anufacturing
BSA	<b>B</b> asic <b>S</b> calar <b>A</b> nalyser
DAC	<b>D</b> igital to <b>A</b> nalog <b>C</b> onverter
DC	<b>D</b> irect <b>C</b> urrent
DMLS	<b>D</b> irect <b>M</b> etal <b>L</b> aser <b>S</b> intering
EBM	<b>E</b> lectron <b>B</b> eam <b>M</b> elting
EM	<b>E</b> lectro- <b>M</b> agnetic
ESR	<b>E</b> quivalent <b>S</b> eries <b>R</b> esistance
FEM	<b>F</b> inite <b>E</b> lement <b>M</b> odel
HCP	<b>H</b> exagonal <b>C</b> lose <b>P</b> ack
MCP	<b>M</b> icrowave <b>C</b> avity <b>P</b> erturbation
MCR	<b>M</b> icrowave <b>C</b> avity <b>R</b> esonator
PCB	<b>P</b> rinted <b>C</b> ircuit <b>B</b> oard
PSD	<b>P</b> article <b>S</b> ize <b>D</b> istribution
RF	<b>R</b> adio <b>F</b> requency
SLM	<b>S</b> elective <b>L</b> aser <b>M</b> elting
VNA	<b>V</b> ector <b>N</b> etwork <b>A</b> nalyser
WLI	<b>W</b> hite <b>L</b> ight <b>I</b> nterferometry
XRD	<b>X</b> - <b>R</b> ay <b>D</b> iffraction

# Chapter 1

## Introduction and Motivation

### 1.1 Introduction to Additive Layer Manufacturing

Additive layer manufacturing (ALM) is an exciting and vibrant technology which has promised to revolutionise much of the manufacturing industry. ALM can take many forms and produce parts in many materials but a number of techniques can be grouped together under the heading ‘Powder-Bed Fusion’. This basis of the operation is an iterative process which involves repeatedly laying down a layers of fine powder and using directed energy to melt or sinter the shape of the object into the powder. In this way, complex 3D objects can be created, including designs which are impossible to make using traditional subtractive methods. For instance Figure 1.1 shows a hollow single-piece cylindrical resonant microwave cavity.

The direct production of metal parts by powder-bed fusion comes in two forms: Electron-beam Melting (EBM) and, the main focus of this thesis, selective laser melting (SLM). SLM, since first demonstrated in 1996 [2], has become a high-value commercially available process capable of creating fully-dense metallic parts. As the name suggests, it utilises a high-power laser to directly melt a bed of fine metallic powder.

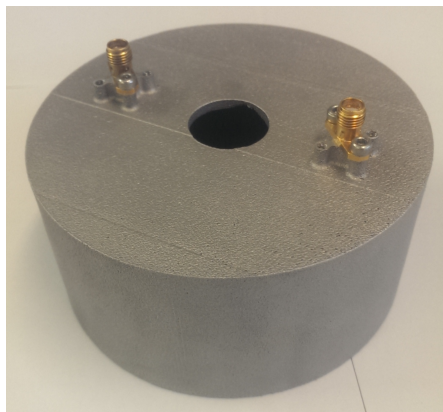


FIGURE 1.1: Single piece, SLM produced cylindrical microwave resonant cavity.

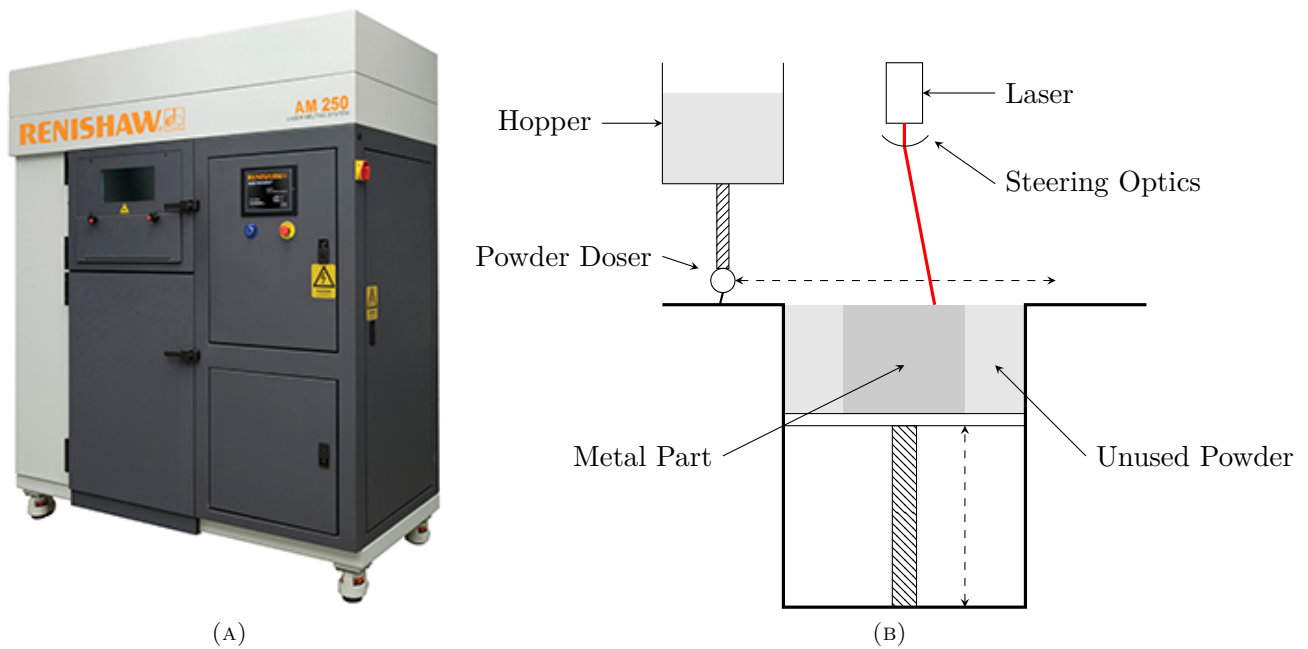


FIGURE 1.2: (a) Renishaw AM-250. (b) Operation overview.

Renishaw plc currently produce ALM machines. Their current state-of-the-art machine, the AM250, produces parts within a  $25 \times 25 \times 30\text{cm}$  volume with the smallest features  $70\mu\text{m}$  in size. The basic principle of its operation can be seen in Figure 1.2. Unlike other techniques, parts can be produced in many metals including alloys of Steel, Aluminum, Nickel, Titanium and Cobalt-Chrome. Typically powders in the range  $10\text{-}50\mu\text{m}$  are used [3].

Many advantages are touted for SLM; this includes a reduction in cost due to a reduction in tooling and need for expert operators, the ability to create complex geometries with hidden features and potentially much quicker manufacture times.

In a number of potential application areas, for example aerospace and healthcare, quality is of paramount importance and the technique will only see widespread use once quality assurance is absolute [4]. In addition, the complex thermal history and processing conditions lead to significant complexity in the part microstructure [5]. As a result, a significant effort has focused on processes and techniques which can aid in SLM quality control [6, 7]. A plethora of machine parameters can be adjusted to account for process change [8, 9] and routes for process control can take the form of in-situ process monitoring and feedback [10], feedstock measurement and control [11], post-processing and post-production verification [12]. A comprehensive review of the techniques used in metal additive manufacturing is provided in [13].

More generally, the advantages of ALM, namely the potential for reduced cost and novel designs, has attracted significant interest in the microwave industry [14]. A exhaustive list of example applications is unfeasible in the scope of this introductory chapter but recent research includes techniques which post-coat 3D-printed plastics in metal [15],

produce waveguide structures using a process which binds copper to a 3D printed steel frame [16] and various techniques to produce planar circuits [17, 18, 19, 20].

Whilst SLM is known to be actively used industrially for production of waveguide components, relatively few published studies have demonstrated the use of SLM or systematically investigated the direct production of metallic microwave parts by SLM. Since the surfaces of the SLM parts have a rough appearance, suggesting high surface resistance, it is assumed extensive mechanical or chemical polishing and surface finishing is required. This is the case in various published examples. For example, the construction of a superconducting aluminium cavity [21] or the construction of copper antennas [22, 23]. An aluminium antenna array using direct metal laser sintering (DMLS) was produced in [24] without the requirement for extensive surface finishing. Whilst the terms sintering and melting in DMLS and SLM respectively suggest different underlying physical mechanisms for particle fusion, in this context, they are essentially the same technology which involves the melting of metallic powder. The term DMLS remains due to its value as a recognisable trademark. Furthermore, an interesting comparison is made in [25] between those directly printed SLM surfaces, those chemically polished and those electro-plated in silver. They observe an increase in electrical losses of 40-50% for the directly printed surfaces in comparison to machined surfaces.

## 1.2 Metallic Powders and Microwave Spectroscopy

As can be expected, the quality of powder feedstock plays a vital role in ensuring quality in the finished part. A number of studies have sought to quantify the effect powder variation can have on the metallic powder bed fusion processes [26, 27, 28].

It has been shown that different powder suppliers require different processing parameters in order to achieve optimum density [29]. More specifically, changes in the particle size distribution can modify surface finish and mechanical properties such as hardness and porosity [30, 31].

One impact of this is that new ALM machines typically have to go through an extensive commissioning procedure whereby various machine parameters, sensitive to particle size, are optimised for part performance.

A variety of techniques exist to measure the powder properties including: particle size distribution of a sample by laser diffraction or X-ray computed tomography, chemical composition by X-Ray photo-electron spectroscopy and inert gas fusion, crystal structure determination by X-Ray diffraction and general structural analysis by studying the surface morphology using scanning electron microscopy [32, 33].

All of these techniques listed require large, complex and expensive scientific equipment. It is not deemed practical, in the context of industrial manufacture, to routinely undertake these measurements in-processes and by the machine operators themselves.

In addition, since the raw powder is relatively expensive, it is vital for economic operation that any unused powder from a particular build is collected and re-used in subsequent builds. A number of studies have investigated the potential impact this recycling process can have on powder characteristics and subsequent part properties.

It has been noted that, with continued powder recycling, particle size distributions change [34], modifying the flowability and density of the powder bed [32, 35]. This can then have significant effect on built part porosity [36, 37]. In addition, oxygen content can be seen to progressively increase [35] which can have significant consequence if parts need to conform to strict composition standards.

The systems used to measure these parameters require significant ongoing maintenance and replenishment of consumables which makes them unattractive for many applications. Since speed and cost are very important aspects in production, the chemical composition, the PSD or indeed any size characteristics of the powder, are not routinely measured due to the need for expensive measurement equipment.

Since no active monitoring is undertaken, operators have to follow a recycling procedure to ensure powder quality is maintained and to guarantee quality in the finished parts. However, as revealed by [34, 32, 35, 36, 37] the powder does inevitably degrade over time and has to be discarded.

To summarise, the ability to conveniently gain a measure of particle size and/or powder oxygen content could prove a valuable measurement for machine operators and designers as they look to maximise part performance. It is hoped microwave spectroscopy may be able to fill this need.

In the past, the majority of work concerning the interaction of conducting powders with a microwave electromagnetic field has been with the aim of understanding powder heating by microwave excitation. As a result, a number of models describing the absorption of microwave energy in conducting powders have been developed [38]. Using this as a starting point, it is hoped sensors can be developed in order to assess a powder's condition with the main measurement outputs being particle size and extent of oxidation. A study looking specifically at Titanium powder is presented in Chapter 3.

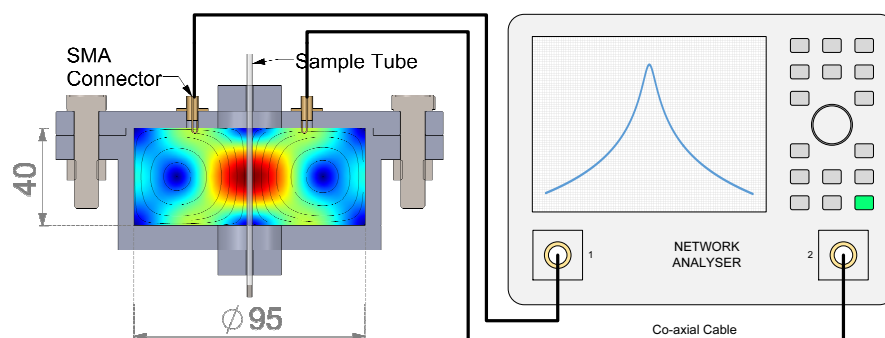


FIGURE 1.3: Microwave cavity perturbation system showing cavity with simulated magnetic field operating in the  $TE_{011}$  mode.

Measurement of material properties using microwave techniques has many potential advantages. The measurements typically require little sample preparation and are non-destructive. Furthermore, modern advances in electronics has increased the potential for cheap measurement electronics and embedded applications.

Whilst the measured properties typically relate indirectly to the desired material parameters, they can reveal valuable information and are usually very sensitive to small changes in the material. One potential challenge is separating out different effects when multiple factors act to change the microwave response simultaneously. For instance, temperature, crystal structure and water content.

There are many different approaches to measurement of microwave properties each having their own set of features and disadvantages, such as field penetration and sample form. The methods can be broadly split into non-resonant and resonant methods [39].

Non-resonant methods can include the measurement of microwave reflection and transmission through a waveguide or other transmission line either completely or partially blocked with a sample. A different approach involves the measurement of the change in reflection co-efficient caused by the loading of the evanescent field of an open-circuit co-axial probe by a sample. These methods have the advantage of being broadband but typically depend on very accurate calibration and, as a result, accuracy and uncertainty is usually better in a resonant technique [40].

Most resonant methods involve the perturbation of a resonant system by the sample although, in the case of some dielectric samples and geometries, the sample may form part of the resonator itself. Resonator based measurements are typically narrow band but a sparse frequency spectrum can be obtained in many cases by utilising a spectrum of different resonant modes. The resonators themselves come in many different forms, each suited to different sample sizes and geometries.. Perhaps the simplest form of resonator is the resonant transmission line created by short or open circuit and perturbed along its length or in the evanescent field at the end of the line. A popular configuration is the resonant co-axial probe [41] which is convenient for liquid measurements since there is no air gap at the open end and the probe can simply dip into the fluid. Solid surface measurements are possible but require that the probe makes a flat and intimate contact with the probe. Microstrip ring resonators are also popular for small sample measurements such as microfluidics [42]. Another popular dielectric test method is the Split Post Dielectric Resonator [43] allowing for the measurement of very low loss dielectrics. The final method is the basic cavity resonator and is the extensively discussed in this thesis in Chapter 2. Careful selection of the mode and sample position allows for isolation of the magnetic and electric field response.

### 1.3 Electrical Properties and SLM

As well as to the testing of powder, there is also a motivation to explore the use of microwave methods to test completed SLM produced parts.

Whilst in the machine commissioning process, parts are created in order to test their structural properties, tests are rarely carried out in process. The tests, examining strength, ductility and porosity are usually destructive and require the production of specific test pieces and complex specialist equipment [44, 45, 46, 47, 48].

Furthermore, during the laser melting process, variation build-to-build, such as inconsistencies in the powder bed or laser application, can cause micro structural deficiencies in the final product which lead to compromised mechanical performance [49, 47, 46]. It would be advantageous to be able to monitor for these deficiencies during or after manufacture [50, 13]. An example would be the in-situ monitoring of the porosity of completed parts using ultra-sonic techniques [10].

The monitoring of electrical properties might also provide insight into the micro-structure as any structural abnormalities would usually result in an increased resistivity. Practically, DC techniques are not desirable due to the necessity of a physical connection. In order to undertake DC resistivity measurements, samples have to be specifically designed with specific features, such as probe connections. However, by subjecting a sample to an oscillating magnetic field, a measure of the resistivity can be obtained from the eddy currents induced in the metal. Non-destructive testing of metal parts based on eddy currents is a very well established technique. Most commonly, coil structures are used to generate the magnetic fields and measurements are undertaken at relative low frequencies (<10MHz) [51].

In addition, as previously discussed, the production of microwave parts by SLM is not yet very widespread. As a result, many questions regarding its potential and best practice remain. In order to maintain the advantages offered by SLM, components should ideally be directly produced by SLM without the need for extensive surface finishing or re-coating. Since there has been little previous exploration of the possibility of using SLM techniques to directly produce microwave parts, little is known regarding the effect the various build parameters have on microwave performance.

The opportunity is taken here, in Chapter 4, to undertake a study where a variety of different SLM produced surfaces are measured at microwave frequencies. Samples in Aluminium, Titanium and Cobalt Chrome, in two build orientations, both grit-blasted and as-built are tested. The technique is again resonant and based upon a dielectric resonator fixture.

## 1.4 Microwave Heating

An additional obvious application area for microwave technology, especially in the light of metallic powders absorptive properties, is the bulk heating of powders. Direct sintering of metallic powders by microwave radiation has previously been demonstrated [52, 53], however, it is not typically seen as having great potential for the production of high-tolerance, small feature components due to simple wavelength limitations. However, microwave heating can still have applications within SLM.

SLM machines routinely raise the temperature of the build chamber for two purposes: to reduce the required laser power and to slow the part cooling in order to reduce residual stresses. In order to successfully implement a microwave heating system, alongside the EM absorption characteristics of the powder, detailed heating characteristics are needed.

If an accurate measure of the heating characteristics of a sample is required, it is imperative that the applied power is known accurately and can be finely controlled. Multi-mode cavity systems, typically driven by a high power magnetron, can not achieve this due to the broad source spectrum and chaotic nature of the various overlapping modes. A single mode system, much like the cavities used for the sensing applications, can meet these requirements as has been previously demonstrated [54, 55].

The final part of this thesis, as a preface to potential further work in the area, presents some of the work undertaken to develop a microwave heating system using a single-mode microwave cavity resonator describing the many engineering challenges encountered when designing such a system.

## 1.5 Project Aims

To summarise, a list of aims are presented as follows:

1. Ascertain whether there is potential to develop a in-process powder quality microwave sensor.
2. Investigate the ability for a microwave system to detect defects in a solid metal part.
3. Investigate the suitability of SLM produced parts for microwave engineering.
4. Develop a system for efficient continual heating in a cavity resonator.

## 1.6 Novel Contribution

1. Demonstration of the importance of annealing for Aluminium alloy cavities to be used for perturbation measurements.

2. The first direct measurement of magnetic absorption in metallic powders by cavity perturbation revealing potential for particle size sensor.
3. Surface resistance comparison of SLM surfaces produced in different orientations and in as-built and grit blasted condition.

## Chapter 2

# Microwave Cavity Perturbation

The application of perturbation theory for a microwave cavity resonator enables the non-destructive measurement of complex permittivity and permeability of small samples through the use of relatively simple resonator designs. As a background to subsequent measurement chapters, this chapter details the application of microwave cavity perturbation (MCP) starting from the design of cavities used through to the data collection procedure itself. Furthermore, work is presented which enables for temperature fluctuations of the cavity system to be corrected for.

### 2.1 Complex Permittivity and Permeability

As a starting point, it is pertinent to present the concept of a complex material permittivity and permeability.

Starting first with the electric field case, when considering a time varying electric field, the material permittivity can be expressed as a complex number.

$$\varepsilon = \varepsilon_1 - j\varepsilon_2 \quad (2.1)$$

The real part signifies relates to the energy storage due to polarisation in the presence of an applied electric field and the imaginary part energy loss due to the oscillating dipoles in an applied varying field.

Furthermore, given a linear and isotropic material where

$$\bar{J} = \sigma \bar{E} \quad (2.2a)$$

$$\bar{D} = \varepsilon \bar{E} \quad (2.2b)$$

and assuming that E is a vector in the form

$$\bar{E} = \bar{E} e^{j\omega t} \quad (2.3)$$

then from Maxwell's equations we can write

$$\nabla \times \bar{H} = j\omega\bar{D} + \bar{J} \quad (2.4a)$$

$$= j\omega \left( \varepsilon_1 - j\varepsilon_2 - j\frac{\sigma}{\omega} \right) \bar{E} \quad (2.4b)$$

This equation illustrates that there are in fact two loss mechanisms in a material. Firstly there is loss given by the imaginary permittivity, the dielectric losses, and secondly there is loss due to the material's conductivity. The conductivity loss is due to the movement of free charges (electrons or ions in solution) in the material caused by the varying electric field. Since conductivity loss and dielectric losses are usually indistinguishable, the loss term, often defined as a loss tangent, is

$$\tan\delta = \frac{\omega\varepsilon_2 + \sigma}{\omega\varepsilon_1} \quad (2.5)$$

There are 3 main mechanisms which can give rise to dielectric loss: orientational polarisation of individual molecules, polarisation of ionic compounds and finally atomic polarisation caused by the distortion of individual atom's electron cloud. Each of these mechanisms has a material dependent associated relaxation time which causes a frequency dependent permittivity.

Similarly, magnetic permeability can be defined as a complex number as a measure of magnetic polarisability of a material in response to an applied magnetic field. Since there is no isolated magnetic charge, no magnetic current exists.

$$\mu = \mu_1 - j\mu_2 \quad (2.6)$$

However, the internal polarisation is defined such that a material which produces a field which opposes the applied magnetic field produces real permeability of  $< 1$  (diamagnetic) and materials which produce a magnetisation which act to increase the internal field have permeabilities  $> 1$  (paramagnetic and ferromagnetic).

With the magnetic field it is important to emphasise the condition of the linearity of the material which is the case when

$$\bar{B} = \mu\bar{H} \quad (2.7)$$

that is  $\mu$  itself is not a function of  $H$ . This would not be the case for ferromagnetic materials.

## 2.2 Perturbation Theory

Perturbation theory describes the technique by which the dielectric or magnetic properties of a material can be calculated by measurement of the change caused to a resonator by the introduction of the sample to the resonator.

Many papers have been published proposing different resonator designs and analysis aiming to improve the accuracy and practicality of the technique. A comprehensive guide to perturbation is given by Klein et al. in a three part series, “Microwave Cavity Perturbation Technique I-III” [56, 57, 58].

Many demonstrations of the technique have been completed in different contexts [59, 60, 61, 62] with some suggesting improvements on the basic method and analysing its accuracy [63, 64]. A few notable examples include the use of higher order resonant modes [65] and corrections for sample insertion holes [64, 66].

The standard first-order perturbation equation as given by Waldron is [67],

$$\frac{\Delta\omega}{\omega} \simeq \frac{\iiint_{V_S} [(E_1 \cdot D_0 - E_0 \cdot D_1) - (H_1 \cdot B_0 - H_0 \cdot B_1)] dV}{\iiint_{V_C} (E_0 \cdot D_0 + H_0 \cdot B_0) dV} \quad (2.8)$$

where  $E_0$  and  $H_0$  are the unperturbed fields and  $E_1$  and  $H_1$  are the perturbed fields.  $V_S$  and  $V_C$  represents the volume of the sample and cavity respectively and  $\frac{\Delta\omega}{\omega}$  represents the change in complex resonant frequency of the cavity upon the introduction of a sample.

Equation 2.8 describes the change in resonant frequency of a resonator when its electromagnetic fields are perturbed by a small sample. In order for the theorem to hold, the primary assumption states that  $\Delta\omega \ll \omega$  and that the fields outside the sample are unchanged during perturbation [68].

If the sample is placed in a region of zero magnetic field, the second term in the numerator can be ignored. Also, it is observed that the denominator is proportional to the energy stored in the empty cavity and since, at resonance, the energy stored in the magnetic and electric fields is equal, it can be simplified with reference to only the electric or magnetic field. Taking in this instance the electric field case, as,

$$D_0 = \epsilon_0 E_0 \quad (2.9a)$$

$$D_1 = \epsilon_0 \epsilon_s E_1 \quad (2.9b)$$

equation 2.8 reduces to, [69]

$$-\frac{\Delta\omega}{\omega} \simeq \frac{(\epsilon_s - 1) \iiint_{V_S} E_1 \cdot E_0 dV}{2 \iiint_{V_C} |E_0|^2 dV} \quad (2.10)$$

Equating real and imaginary co-efficients leads to the following relationships

$$\varepsilon_{1s} \simeq 2G' \frac{f_0 - f_S}{f_0} + 1 \quad (2.11a)$$

$$\varepsilon_{2s} \simeq G' \left( \frac{1}{Q_S} - \frac{1}{Q_0} \right) \quad (2.11b)$$

where

$$G' = \frac{\iiint_{V_C} |E_0|^2 dV}{\iiint_{V_S} E_1 \cdot E_0 dV} \quad (2.12)$$

$G'$  can be described as a dimensionless mode scaling constant and is fixed for a specific mode, sample position and sample geometry. It can be obtained analytically, numerically or by experiment as discussed further in Section 2.7. For convenience and assuming a small sample,  $G'$  is further reduced to,

$$G' = G \frac{V_C}{V_S} \quad (2.13)$$

which allows for uncertainty in the sample and cavity volume to be accounted for [70]. Physically, this scaling constant can therefore be interpreted as the proportion of the field energy present in the sample volume compared to the whole cavity. Further detail on how to obtain the mode scaling constant is given in Section 2.5.

The final perturbation equations are then,

$$\varepsilon_1 \simeq -2G_{nmp} \frac{V_C}{V_S} \frac{\Delta f}{f_0} + 1 \quad (2.14a)$$

$$\varepsilon_2 \simeq G_{nmp} \frac{V_C}{V_S} \Delta \frac{1}{Q} \quad (2.14b)$$

and similarly for permeability

$$\mu_1 \simeq 2G_{nmp} \frac{V_C}{V_S} \frac{\Delta f}{f_0} + 1 \quad (2.15a)$$

$$\mu_2 \simeq G_{nmp} \frac{V_C}{V_S} \Delta \frac{1}{Q} \quad (2.15b)$$

where  $G_{nmp}$  is the mode scaling constant for the TM/TE<sub>nmp</sub> mode being used. It is important to note that, changes in resonator Q represent changes in loss and changes in frequency represent changes in polarisation (stored energy) in the sample [71]. A minus sign separates the electric and magnetic cases. This is expected given the opposite direction defined for the internal polarisation or magnetisation vector.

Commonly, the values obtained from perturbation are termed effective in the case of powders, where variable grain shapes and powder packing density render a full analytic treatment intractable[72].

Furthermore, a sparse but broadband measurement can be made by simultaneous measurement of different modes and normalising using the mode scaling constant.

## 2.3 Cavity Resonator Design

As has been described, geometric field separation at the sample insertion point is required for perturbation measurements. This is achieved by careful selection of resonator geometry and resonant mode. Cylindrical cavities are found to be a convenient geometry and have been used here as defined in Figure 2.1.

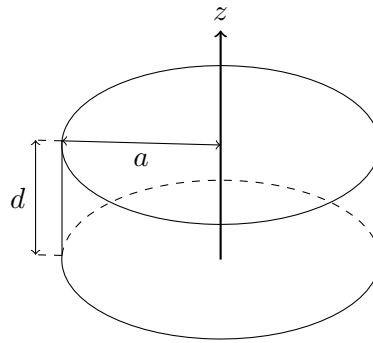


FIGURE 2.1: Cylindrical cavity geometry.

By solving Maxwell's equations with appropriate boundary conditions, expressions describing the resonant modes can be derived.

For a cylindrical cavity, the resonant frequencies of  $TE_{nml}$  modes are

$$f_{nml} = \frac{c}{2\pi\sqrt{\mu_1\epsilon_1}} \sqrt{\left(\frac{\alpha'_{nm}}{a}\right)^2 + \left(\frac{l\pi}{d}\right)^2} \quad (2.16)$$

and for  $TM_{nml}$  modes

$$f_{nml} = \frac{c}{2\pi\sqrt{\mu_1\epsilon_1}} \sqrt{\left(\frac{\alpha_{nm}}{a}\right)^2 + \left(\frac{l\pi}{d}\right)^2} \quad (2.17)$$

where  $\alpha_{nm}$  is the  $m^{\text{th}}$  root of the bessel function  $J_n(x)$ ,  $\alpha'_{nm}$  is the  $m^{\text{th}}$  root of the derivative of the  $n^{\text{th}}$  bessel function with respect to its argument,  $a$  is the radius and  $d$  is the depth of the cavity [73].

Setting cavity radius,  $a = 4.6\text{cm}$ , places  $TM_{010}$ , the dominant mode of a cylindrical cavity where  $\left(\frac{2a}{d}\right)^2 > 1$ , at 2.45 GHz. This frequency is in the centre of the 2.4-2.5 GHz

industrial, scientific and medical band commonly used in modern communications systems and, as a result, electronic components for use at this frequency are commonplace which potentially allows for measurement electronics to be produced at greatly reduced cost.

The perturbation equation reveals that, in order to maximise sensitivity, it is advantageous to maximise the Q-factor. This is because, for a given, sample the perturbation is increased by increasing the empty resonator Q.

The resonator Q-factor describes the ability of a resonator to maintain an oscillation and is defined as  $Q = \omega_0 \frac{\langle U \rangle}{\langle P \rangle}$  where  $\langle U \rangle$  is the time averaged stored energy in the resonator and  $\langle P \rangle$  is the sum of power lost in the system. In a real-world system, the Q-factor is composed of contributions from a variety of factors including the cavity surface current losses, coupling structures and cavity filling. High conductivity metals are therefore desirable for cavity construction. As a compromise between cost and performance, aluminium and copper are popular choices. It is also noted that due to the skin depth, which at microwave frequencies is typically  $<10 \mu\text{m}$ , only a thin surface of high conductivity metal is required.

For an ideal empty cavity, the losses can be entirely attributed to surface currents given by

$$\langle P \rangle = \frac{R_s}{2} \int_S |H_S|^2 dS \quad (2.18)$$

where  $S$  is the cavity surface,  $R_s = \sqrt{\frac{\rho\omega\mu}{2}}$  is the metallic surface resistance for a metal with resistivity  $\rho$ , and  $H_S$  is the tangential magnetic field at the cavity wall.

by evaluating the field integrals, the Q can be shown to be, for TM and TE modes, [74]

$$Q_{TM_{nml}} = \begin{cases} \sqrt{\frac{\mu_0\pi f_0}{\rho}} \left(\frac{ad}{a+d}\right) & l = 0 \\ \sqrt{\frac{\mu_0\pi f_0}{\rho}} \left(\frac{ad}{2a+d}\right) & l \geq 1 \end{cases} \quad (2.19)$$

$$Q_{TE_{nml}} = \frac{\sqrt{\frac{\pi\mu_0 f_0}{\rho}} \left(\frac{2f_0}{lc}\right)^2}{\frac{2}{d^3} + \frac{1}{a} \left( \left[\frac{n}{d}\right]^2 + \left[\frac{\alpha'_{mn}}{l\pi a}\right]^2 \right) (\alpha'_{mn}{}^2 - n^2)^{-1}} \quad (2.20)$$

For a  $TM_{0m0}$  cylindrical cavity resonator, the equation can be elegantly simplified so that,

$$Q = \frac{\frac{a}{\delta}}{1 + \frac{a}{d}} \quad (2.21)$$

where the skin depth  $\delta$  is

$$\delta = \sqrt{\frac{\rho}{\pi f \mu_0}} \quad (2.22)$$

It can be seen that  $Q$  is maximized to a value of  $\frac{a}{\delta}$  by increasing the cavity height  $d$ . It is also noted that this is achieved without affecting the resonator frequency. As discussed later, it is important samples under test pass completely through the cavity. Therefore, often the dimensions are traded off with the available sample size. It is also important to ensure that  $TM_{010}$  is not affected by the  $TE_{111}$  or  $TE_{112}$  modes which approach the same frequency as the height is increased. For the 2.45 GHz cavity, a height of 4cm was chosen in later experiments since it ensures adequate mode separation, allows for realistically sized samples and still supports a  $Q$  of half the maximum theoretical value - approximately 10 000 for aluminium.

### 2.3.1 Finite Element Modeling

Throughout this thesis, Finite Element Modeling (FEM) is extensively used to aid design and trivialise potentially complex numerical and analytical analysis. The premise of FEM is to discretise the simulation area into a number of elements and calculate the fields by solving a base equation and applying a number of boundary conditions. Many texts are available which explore the method in depth and validate the FEM approach with Electromagnetics [75, 76].

The FEM package COMSOL is utilised in this work. Within the RF module, COMSOL solves for the wave equation given as

$$\nabla \times \mu_r^{-1}(\nabla \times \bar{E}) - \omega^2 \varepsilon_0 \mu_0 \left( \varepsilon_r - \frac{j\sigma}{\omega \varepsilon_0} \right) = 0 \quad (2.23)$$

Commonly, the simulation area is enclosed by metal walls and imposes the boundary condition of a perfect conductor where the electric field component parallel to the wall is zero ( $n \times \bar{E} = 0$ ) or an impedance boundary with associated loss.

Simulations can be calculated in a 2D or 3D geometry and symmetries can be exploited to reduce computational load and increase simulation accuracy. For example, the axial symmetry of a cylindrical cavity operating in a mode with no azimuthal field dependence.

Two distinct strategies are employed in order to provide solutions for microwave electromagnetic resonator problems. Firstly, a frequency domain approach where the entire system, including TEM excited co-axial ports leading to coupling structures, is simulated. The simulation frequency is typically swept around the expected resonant frequency. S-parameter data can then also be extracted from the excitation ports.

The second and potentially simpler approach is to use the software to solve the wave equation for a number of computed complex eigen-frequencies negating the need for separate excitation.

### 2.3.2 Coupling

Careful selection of coupling method, orientation and position will allow for certain modes to be excited and interfering modes avoided.

#### Capacitive Coupling Probe

This method allows coupling into a particular cavity mode's electric field. The central conductor forms a co-axial feed and is extended slightly into the cavity itself (Figure 2.2) appearing electrically similar to an open circuit. There is an assumption that the length of the probe is much shorter than the wavelength. The current is small but the voltage forms an electric field radiating into the walls of the cavity. As a result, modes with electric fields perpendicular to the wall where the coupling structures are located are coupled into.

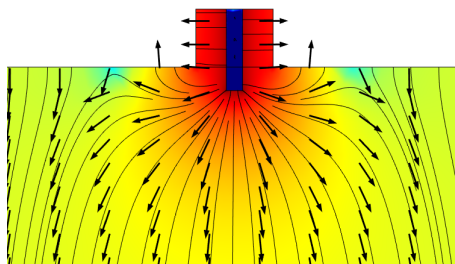


FIGURE 2.2: E-field simulation of open circuit, electric field coupling.

#### Inductive Coupling Loop

In contrast to the probe, the coupling loop couples into a cavity mode's magnetic field. Similarly to the probe, the coaxial feed's centre conductor is extended into the cavity but in this case is looped to connect with the cavity wall (Figure 2.3) and thus appearing electrically as a short circuit. There is also an assumption that the length of the loop is much shorter than the wavelength. The generated fields allow magnetic fields tangential to the wall but perpendicular to the plane of the loop to be coupled into.

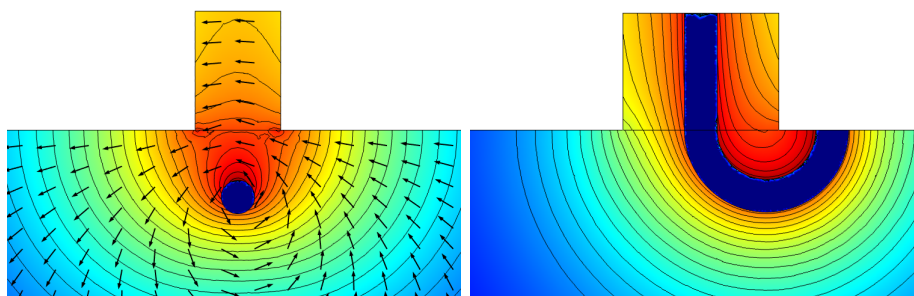


FIGURE 2.3: H-field simulation of short circuit, magnetic field coupling.

### Aperture Coupling

For completeness, it should be mentioned that it is possible to couple into a cavity through an aperture connected via a waveguide. Practically, this method is not usually employed due to the flexibility of easily attachable co-axial cables but may be essential when attempting to deliver elevated power to a cavity.

## 2.4 Complex Resonant Frequency

In the application of perturbation theory, it is important that the resonant frequency of a resonator can be expressed as a complex quantity which includes a relationship to the resonator  $Q$  such that,

$$\omega_0 \leftarrow \omega_0 \left( 1 + \frac{j}{2Q} \right) \quad (2.24)$$

Pozar [73] presents a simple proof of this using a simple series RLC circuit to model the microwave resonator. This proof is outlined here.

To begin, an expression for the resonant frequency,  $\omega_0$ , can be obtained by simply equating the energy stored in the inductor and capacitor to give  $\omega_0 = \frac{1}{\sqrt{LC}}$ . This also leads to an expression for the resonator  $Q$ ,  $Q = \frac{\omega_0 L}{R}$ .

Next, let us consider the input impedance of the circuit at a frequency close to its resonant frequency such that  $\omega = \omega_0 + \Delta\omega$ . This can be written as,

$$\begin{aligned} Z_{in} &= R + j\omega L - \frac{j}{\omega C} \\ &= R + j\omega L \left( \frac{\omega^2 - \omega_0^2}{\omega^2} \right) \end{aligned} \quad (2.25)$$

The fraction can be simplified by taking  $\omega^2 - \omega_0^2 = (\omega + \omega_0)(\omega - \omega_0) \approx 2\omega\Delta\omega$  for small  $\Delta\omega$ . This leads to,

$$\begin{aligned} Z_{in} &\approx R + 2jL\Delta\omega \\ &\approx R \left( 1 + 2jQ \frac{\Delta\omega}{\omega_0} \right) \end{aligned} \quad (2.26)$$

If now the resonator is considered loss-less ( $R = 0$ ) but with complex resonant frequency,

$$\begin{aligned} Z_{in} &= 2jL \left( \omega - \omega_0 - j \frac{\omega_0}{2Q} \right) \\ &= 2jL\Delta\omega - j^2 \frac{2\omega_0 L}{2Q} \\ &= R + 2jL\Delta\omega \end{aligned} \quad (2.27)$$

It can be seen that the result for the lossy resonator is the same as a loss-less one but with a complex resonant frequency. This result shows us that a real-world lossy resonator can be modeled simply as a loss-less one with a complex resonant frequency. Furthermore,

$$\begin{aligned}\frac{\Delta\omega}{\omega_0} &= \frac{\omega}{\omega_0} \left(1 + \frac{j}{2Q}\right) - \frac{\omega_0}{\omega_0} \left(1 + \frac{j}{2Q}\right) \\ &= \frac{\Delta f}{f_0} + \frac{j}{2} \left(\frac{\omega}{\omega_0} \frac{1}{Q} - \frac{1}{Q_0}\right)\end{aligned}\quad (2.28)$$

and assuming that the change in resonator  $Q$  is much greater than  $\Delta\omega$  this further reduces to,

$$\frac{\Delta\omega}{\omega_0} = \frac{\Delta f}{f_0} + \frac{j}{2} \left(\frac{1}{Q} - \frac{1}{Q_0}\right)\quad (2.29)$$

## 2.5 Mode Scaling Constant

As was previously described, the mode scaling constant can be calculated analytically for a particular mode and sample geometry assuming field solutions exist for that mode. In the typical cylindrical cavity design and for samples of basic geometric shape, this is usually the case, however, the value will assume a perfectly constructed cavity. In addition to any manufacturing tolerance, any practical design has a number of modifications, for instance, sample holes and the coupling structures which modify the field distributions. However, two alternative approaches can be pursued: simulation and calibration by experiment.

This simplest experimental calibration will utilise a precision calibration sample of known permittivity or permeability (mode dependent) in order to conduct a perturbation experiment to obtain the scaling constant. In the electric field case, this is certainly possible but care must be taken to carefully consider the measurement frequency and temperature. The magnetic field case is not trivial however due to the difficulty in obtaining a sample with a fixed known permeability at the typical measurement frequencies. Due to these practical difficulties, this approach is not usually favoured.

For the magnetic case, Cuenca et al. [77], demonstrates the use of a metal rod to calculate the constant by a cavity shape perturbation. Mathematically, this can be expressed in two ways. The simplest route to form a relationship with Equation 2.15a is to interpret the metal rod as having a permeability of zero. This is a valid interpretation of a metal at microwave frequencies, since the electric field, except in small skin depth region, is effectively zero. Alternatively, consider the energy interpretation of the perturbation equation where

$$\frac{\Delta f}{f_0} = \frac{\Delta W_m}{2W_m}\quad (2.30)$$

Since a metal rod will screen the field, the energy change will be the integral of the unperturbed field in the region of the metal rod. Therefore,

$$\frac{\Delta f}{f_0} = \frac{\Delta W_m}{2W_m} \quad (2.31a)$$

$$\frac{\Delta f}{f_0} = \frac{\frac{\epsilon_0}{2} \iiint_{V_S} |E_0|^2 dV}{2 \cdot \frac{\epsilon_0}{2} \iiint_{V_C} |E_0|^2 dV} \quad (2.31b)$$

and

$$G_{nmp} = \frac{1}{2} \cdot \frac{f_0}{\Delta f} \cdot \frac{V_S}{V_C} \quad (2.32)$$

Therefore, by perturbation using a metal rod of known radius and measuring the frequency shift, the scaling constant can be obtained.

It is implicitly assumed, in the application of the mode scaling constant, that the field in the sample region before and after perturbation is the same. For non-depolarising or demagnetising geometries, this can be safely assumed but this is a fundamental limitation in the application of the theory. In a similar idea, in the magnetic field case, using a metal rod will satisfy the conditions of perturbation since parallel magnetic fields can exist along the length of the rod and the perturbed fields approximate to the unperturbed ones. This is not the case in the electric field for  $TM_{0n0}$  modes since a finite electric field cannot be maintained in a direction parallel to a metal rod and its introduction into the cavity effectively destroys the mode. However, for those modes where the field does not vary along the height of the resonator, it is possible to utilise a sample with a known dipole moment (known energy change), such as a metal sphere, to calculate the scaling constant. Unfortunately, this method cannot completely account for field deformation at the sample holes.

In the previously cited paper [77] they show very good agreement between the experimental values using a metal rod and values obtained through COMSOL simulation. The small discrepancies, typically less than 1%, can be attributed to the uncertainty in the metal rod and the simulated sample. To conclude, their results demonstrate the robustness of the simulated approach which is the favoured method of determining the scaling constant in all cases. Further discussion of the accuracy of the technique can be found in Section 2.11.

## 2.6 Cavity Resonator Analysis

As has been discussed, changes in resonant frequency and resonator Q need to be measured in order to give indication of a sample's electric or magnetic properties. Here, the relevant theory is presented in order to gain an understanding of how these values can be measured. Again, it is useful to model the resonator as a simple series LCR circuit with the addition of input and output coupling represented by a pair of mutual inductances  $m_1$  and  $m_2$  (Figure 2.4).

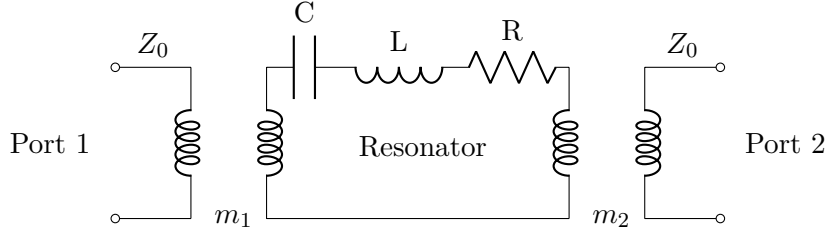


FIGURE 2.4: Basic LCR resonator model.

Analysis of this circuit leads to an expression for the complex transmission co-efficient,  $S_{21}$ ,

$$S_{21}(f) = \frac{2\sqrt{g_1 g_2}}{1 + g_1 + g_2 + jQ_0 \left( \frac{f}{f_0} - \frac{f_0}{f} \right)} \quad (2.33)$$

where

$$g_n = \frac{\omega_0 m_n^2}{Z_0 R} \quad (2.34)$$

and

$$Q_0 = \omega_0 \frac{L}{R} \quad (2.35)$$

is the coupling co-efficient. Near near resonance [78], it can be assumed

$$\left( \frac{f}{f_0} - \frac{f_0}{f} \right) \approx 2 \left( \frac{f}{f_0} - 1 \right) \quad (2.36)$$

and ,furthermore, to simplify the analysis further assume symmetric coupling,  $g_1 = g_2$  and Equation 2.33 is simplified to,

$$S_{21}(f) = \frac{\frac{2g}{1+2g}}{1 + 2jQ_L \left( \frac{f}{f_0} - 1 \right)} \quad (2.37)$$

which introduces the concept of the loaded Q-factor,  $Q_L = \frac{Q_0}{1+2g}$ , which is somewhat smaller than  $Q_0$  due to the effects of coupling. It is also noted that the numerator is equal to the maximum value of  $S_{21}$  taken at resonance. A number of methods can be used to extract the Q-factor and resonant frequency as detailed by Petersan and Anlage's 1998 paper [79] who conclude that a phase versus frequency fit is the superior for clean data and a Lorentzian curve fit is best for noisy data. In the subsequent sections, two methods which have been used during the course of this project are presented: Circle fit and Lorentzian Fit.

### 2.6.1 Lorentzian Fit and 3dB points

Taking the power spectrum

$$P(f) = |S_{21}|^2 = \frac{P_0}{1 + 4Q_L^2 \left(\frac{f-f_0}{f_0}\right)^2} \quad (2.38)$$

where,

$$P_0 = \left(\frac{2g}{1+2g}\right)^2 \quad (2.39)$$

and,

$$Q_L = Q_0(1 - \sqrt{P_0}) \quad (2.40)$$

Inspection of Equation 2.38 reveals  $P(f)$  to be in the form of a Lorentzian function. This allows us to measure  $S_{21}$  in a small span around the resonant frequency and fit a Lorentzian curve to the collected data and extract the resonator parameters from the fit co-efficients.

In most circumstances, the Lorentzian fit provides an accurate and precise measure of the resonator characteristics. Furthermore, it does not rely on complex data allowing simplification of the measurement electronics and is also relatively insensitive to precise calibration. However, occasionally, a different approach is needed when the line shape is distorted by nearby resonances.

Furthermore, inspection of Equation 2.38 reveals a simple marker method of quickly obtaining the Q-factor using the 3dB bandwidth. If Q is defined as  $Q = \frac{f_0}{f_{BW}} = \frac{f_0}{2(f_B - f_0)}$ , at  $f = f_B$ ,  $|S_{21}|^2$  becomes half its peak value. Therefore, by measuring the frequency at 3dB less than the peak, a loaded bandwidth can be calculated and thus a loaded Q.

### 2.6.2 Circle Fit

Plotting Equation 2.37 in the complex plane reveals a circle with real and imaginary parts expressed as follows:

$$\Re(S_{21}) = \frac{\sqrt{P_0}}{1 + 4Q_L^2 \left(\frac{f-f_0}{f_0}\right)^2} \quad (2.41a)$$

$$\Im(S_{21}) = \frac{2Q_L \left(\frac{f-f_0}{f_0}\right) \sqrt{P_0}}{1 + 4Q_L^2 \left(\frac{f-f_0}{f_0}\right)^2} \quad (2.41b)$$

Observation of the above equations shows that the resonant frequency,  $f = f_0$ , occurs as the circle crosses the real axis with the real component equal to  $\sqrt{P_0} = \frac{2g}{1+2g}$ . Furthermore, plotting frequency against the ratio between imaginary and real parts allows the extraction of  $Q_L$  and  $f_0$  from a simple linear fit: [80]

$$\frac{\Im(S_{21})}{\Re(S_{21})} = 2Q_L - 2\frac{Q_L}{f_0}f \quad (2.42)$$

In order to maximise the accuracy, the fit is heavily weighted in a small span around the resonant frequency.

Inevitably, the measured circles will be rotated around the origin through some angle  $\phi$  due to the measurement plane typically being at the end of the cables and does not include the coupling ports and resonator directly. However, by fitting a circle to the data and finding the centre, the data can be rotated into its canonical position.

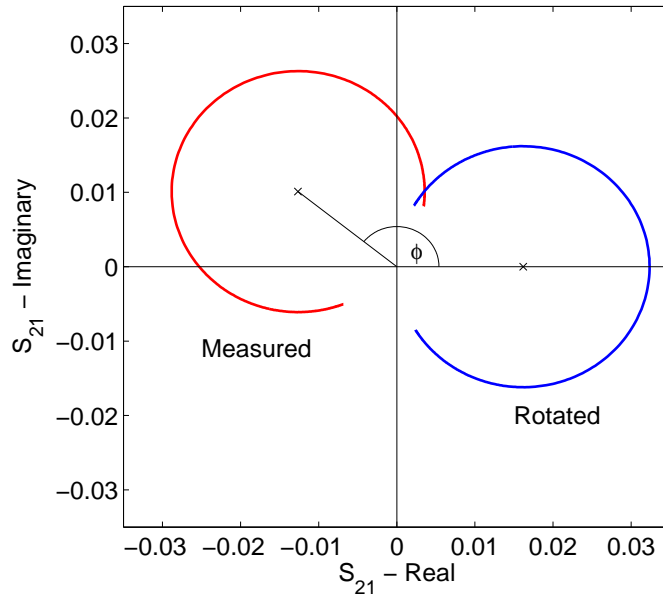


FIGURE 2.5: Measured and rotated complex  $S_{21}$  data,  $TM_{010}$ .

Furthermore, the method is potentially able to recover data more accurately in the presence of distortions caused by crosstalk or other nearby resonances. The Lorentzian fit method is easily distorted and, in order to obtain accurate data, can require the measurement span to be minimised to values much smaller than the bandwidth. However, if the resonant frequency is changing rapidly it can be difficult to track the resonant frequency as it moves out of the measurement span. In this case, the circle fit maybe more appropriate. Figure 2.6 shows the typical distortion seen for the  $TE_{022}$  mode where a circle fit is more appropriate.

### 2.6.3 Measurement Error

Following the discussion of different techniques for the measurement of resonant parameters, it is pertinent to discuss their relative performance in terms of random error.

As has been discussed, the simplest approach to measurement of frequency and Q-factor in a resonator, is to use the inbuilt marker functions of the network analyser to measure

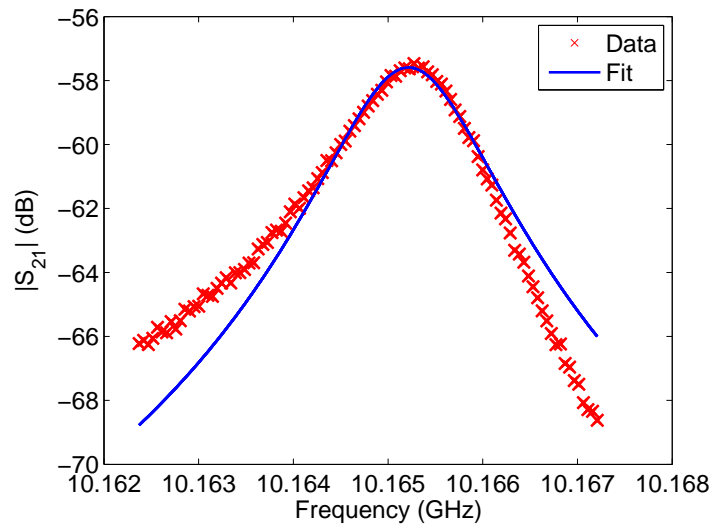


FIGURE 2.6: Measured  $|S_{21}|$  TE<sub>022</sub> trace and attempted lorentzian fit.

the peak frequency and 3dB bandwidth of the resonant peak present in  $|S_{21}|$ . By its nature, the accuracy of this measurement is very dependent on the frequency resolution being used. Therefore, it is desirable to use a high number of points in the frequency sweep. This reveals a trade-off because it is advantageous to keep sweep times as short as possible to eliminate ambient temperature variations during the measurement. This problem is exacerbated by the desire to use a low IF bandwidth to minimise the measurement noise.

In order to reduce uncertainty and maintain accuracy while using a small number of measurement points, a computer is used to produce a fit to the lorentzian and circle line shapes. From the fitting parameters the resonant parameters can be extracted.

In order to do this, a LabVIEW program was developed. In the Lorentzian case, an in-built curve fitting function which uses the Levenberg-Marquardt algorithm was utilised and, in the circle case, a standard least squared approach was taken. Furthermore, the program dynamically tracks the resonant peak in order to minimise the measurement span and maximise the available points.

A comparison between the three measurement methods can be seen in Table 2.1. The figure shows the frequency and Q with standard error of TM<sub>010</sub> averaged over 20 samples in 4.5 seconds with an IF bandwidth of 1kHz. The insertion loss was measured at -47.9dB. In this case, the network analyser (Agilent PNA N5232A) is using interpolation to give greater marker precision.

Both fitting strategies report a significantly lower random error than the basic marker approach. It is worth noting that the errors here are very small which indicate that even small changes in frequency and Q can be measured accurately. Further discussion of the measurement error can be found in Section 2.11.

Method	Centre Frequency (Hz)	Q-Factor
Lorentzian Fit	$2519451557 \pm 7$	$12028 \pm 1.4$
Circle Fit	$2519451560 \pm 5$	$12030 \pm 2$
Markers	$2519451550 \pm 30$	$12021 \pm 4$

TABLE 2.1: Comparison of fitting and data collection methods for resonance parameters.

#### 2.6.4 Degeneracy

By inspecting the equations in Section 2.3, it is clear that it is possible for a TE and TM mode to appear at the same frequency for a fixed geometry. In this case, the modes are said to be degenerate [81].

This phenomena may be of use when designing filters using cavity resonators allowing for significant reduction in the overall filter size [82]. However, in the context of perturbation, if this occurs at a mode of interest, strategies need to be utilised to break the degeneracy.

Later on, due to its non-demagnetising configuration (see Section 2.7) and lack of rotational degeneracy, it is desirable to take magnetic measurements using the cylindrical  $TE_{011}$  mode. However, this mode is degenerate with  $TM_{111}$ . The field configuration of  $TE_{011}$  necessitates inductive coupling using a short circuit loop antenna placed on the top surface of the cavity. This is true of all TE modes which by their nature have no electric field component in the z direction. However, this arrangement will also couple to the interfering  $TM_{111}$  mode.

Examination of the surface currents of the two modes reveals a solution. In the top plate,  $TE_{011}$  will have azimuthal currents circulating around whose density reduces towards the edges and the centre. In contrast, in  $TM_{111}$  a large current is formed directly across the centre of the top plate. Therefore, by drilling a hole in the centre of the cavity,  $TM_{111}$  can be significantly perturbed whilst leaving  $TE_{011}$  relatively unaffected [77]. Figure 2.8 shows the effect, as simulated in COMSOL, of placing a 10mm and 20mm on axis hole (as seen in Figure 2.7) in a cavity with radius 4.6cm and height 4cm. In real-world designs, an RF choke must be included to stop loss caused by the evanescent fields emanating from the holes.

In the unperturbed, no hole, state, it can be seen how  $TM_{111}$  strongly interferes with  $TE_{011}$ . The small separation is only caused by a small perturbation of the coupling structures themselves. At 10mm, the  $TM_{111}$  peaks have shifted significantly and by 20mm they do not appear within the simulation bandwidth. It is noted that  $TM_{111}$  is itself rotationally degenerate and in this simulation appears as a set of twin peaks due to the perturbation caused by the coupling structures.

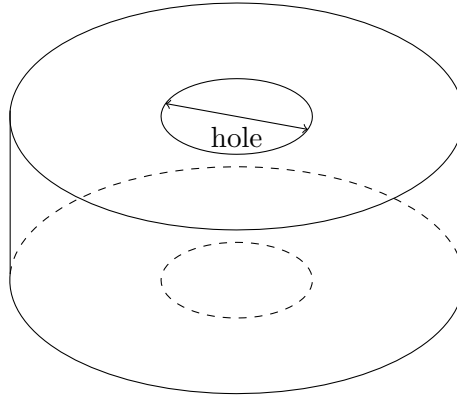


FIGURE 2.7: Cylindrical cavity with  $TM_{111}$  mode-trap caused by hole placed on cavity axis.

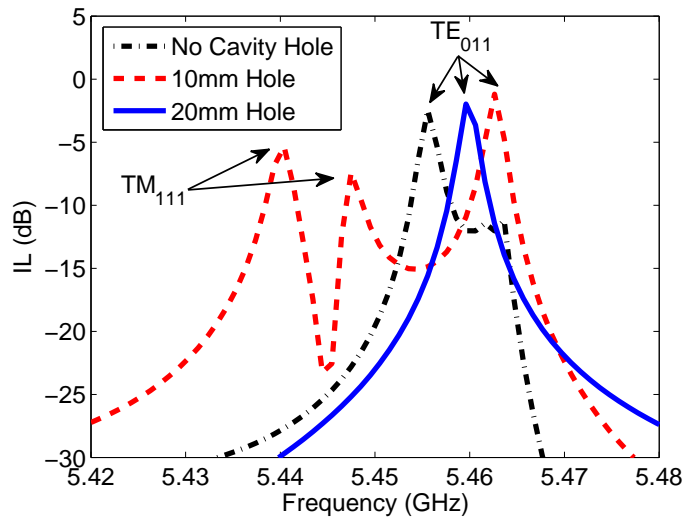


FIGURE 2.8: Simulated effect of axial hole mode-trap on  $TM_{111}$  and  $TE_{011}$  modes.

As well as the effect described above, certain modes can exhibit rotational degeneracy where the same mode appears simultaneously in two or more orientations. It is possible to exploit rotationally degenerate modes to measure permittivity or permeability tensors of anisotropic materials [83, 84, 85] but may cause measurement inaccuracy in other cases.

An example mode which displays rotational degeneracy in a cylindrical cavity is  $TM_{110}$ . Inspection of Figure 2.9 reveals a single degeneracy where the mode is rotated  $90^\circ$  relative to the one shown. Mathematically, this is the result of the azimuthal field component having a valid solution in both the sine and cosine case. Therefore, as expected, the two solutions are identical with a  $90^\circ$  azimuthal difference.

Taking the case of short circuit coupling on the top surface of the cavity, a common arrangement for the excitation of  $TM$  modes, initial inspection might reveal that rotational degeneracy will not be observed. With the field aligning with the coupling structures denoted by the label '1' in Figure 2.9, the orthogonal mode should not couple strongly.

However, experimental observation, by sample perturbation at various locations, reveals that both modes are approximately equally coupled with the arrangement labeled ‘2’. This is the natural state of the oscillator where the preference of the system is to excite all available states equally.

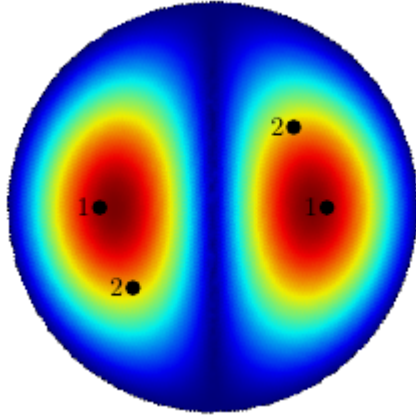


FIGURE 2.9:  $TM_{110}$  potential coupling positions.

The effect of the combination of the two resonant systems can be examined by first considering the circuit model for a degenerate system as seen in Figure 2.10.

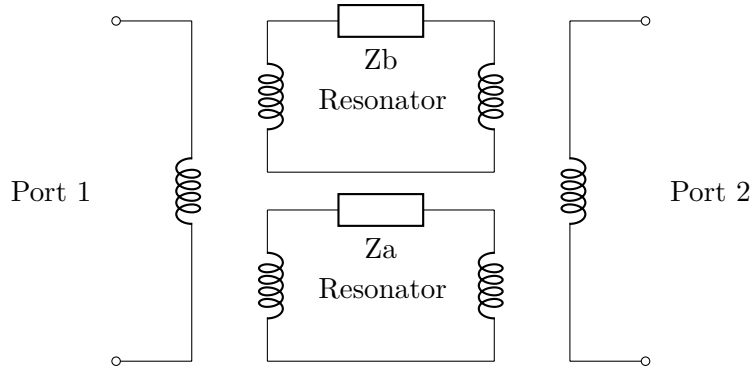


FIGURE 2.10: Degenerate system circuit model.

In order to calculate  $S_{21}$ , first consider the Z-parameters of the network.

$$\begin{pmatrix} V_1 \\ V_2 \end{pmatrix} = \begin{pmatrix} Z_{11} & Z_{12} \\ Z_{21} & Z_{22} \end{pmatrix} \begin{pmatrix} I_1 \\ I_2 \end{pmatrix} \quad (2.43)$$

Using Kirchoff's Voltage law, we get

$$\begin{aligned} V_1 &= j\omega m_a I_a + j\omega m_b I_b \\ 0 &= j\omega m_a (I_1 + I_2) + I_a Z_a \\ 0 &= j\omega m_b (I_1 + I_2) + I_b Z_b \end{aligned} \quad (2.44)$$

Substituting for  $I_a$  and  $I_b$  leads to

$$V_1 = \left[ \frac{\omega^2 m_a^2}{Z_a} + \frac{\omega^2 m_b^2}{Z_b} \right] I_1 + \left[ \frac{\omega^2 m_a^2}{Z_a} + \frac{\omega^2 m_b^2}{Z_b} \right] I_2 \quad (2.45)$$

revealing that  $Z_{11} = Z_{22} = Z_{21} = Z_{12}$ . The resonator series impedance  $Z_n$  can be modeled as a series LRC circuit such that

$$\begin{aligned} Z &= R + j\omega L + \frac{1}{j\omega C} \\ &= R + j\omega_0 L \left( \frac{\omega}{\omega_0} - \frac{\omega_0}{\omega} \right) \\ &= R \left( 1 + 2jQ \left( \frac{\omega}{\omega_0} - \frac{\omega_0}{\omega} \right) \right) \\ &= R \cdot \Psi(\omega) \end{aligned} \quad (2.46)$$

where the resonant frequency is  $\omega_0 = \frac{1}{\sqrt{LC}}$  and  $Q = \omega_0 \frac{L}{R}$ . Furthermore, a coupling co-efficient is defined

$$g_n = \frac{\omega^2 m_n^2}{Z_0 R_n} = \frac{\omega m_n^2 Q}{Z_0 L} \quad (2.47)$$

and, given that

$$S_{21} = \frac{2Z_0 Z_{12}}{(Z_{11} + Z_0)(Z_{22} + Z_0) - Z_{12} Z_{21}} \quad (2.48)$$

where  $Z_0$  is the characteristic impedance at each port,  $S_{21}$  becomes

$$S_{21} = \frac{2}{2 + \frac{\Psi_a \Psi_b}{g_a \Psi_b + g_b \Psi_a}} = \frac{2}{2 + \frac{1}{\frac{g_a}{\Psi_a} + \frac{g_b}{\Psi_b}}} \quad (2.49)$$

It is observed that when the second coupling co-efficient,  $g_b$ , becomes very small the equation reduces for the familiar result for a single resonator (Equation 2.37). When the two degenerate resonators are identical,  $g_a = g_b$  and  $\Psi_a = \Psi_b$ , there is a modification to the insertion loss and resultant loaded Q, however, unloading using the same method previously described will yield the same unloaded Q. Therefore, in the ideal case, degenerate modes can be used without any modification to the measurement procedure. However, it is noted that this is not a simple addition of two Lorentzian functions. Furthermore, the equation describing a resonator with a single degeneracy can be easily expanded to contain any number of degeneracies, N, by including additional denominator terms as follows:

$$S_{21} = \frac{2}{2 + \frac{1}{\frac{g_1}{\Psi_1} + \frac{g_2}{\Psi_2} + \dots + \frac{g_N}{\Psi_N}}} \quad (2.50)$$

Considering a single degeneracy where both resonances are approximately equally coupled, as expected, differences in the  $Q$  and resonant frequency will distort the Lorentzian response and cause inaccuracies in a measurement. This situation is unfortunately inevitable due to subtle inaccuracies in resonator preparation. For instance, geometry distortion due to machining errors, inconsistent metal surfaces and perturbations caused by sample holes. In many cases this mismatch can be observed in the traces and simply avoided. Figure 2.11 shows an analytical simulation based on Equation 2.49 of a single degeneracy. In this example  $g \propto Q$  but the frequency dependence of  $g$  is ignored in this small region around  $f_0$ .

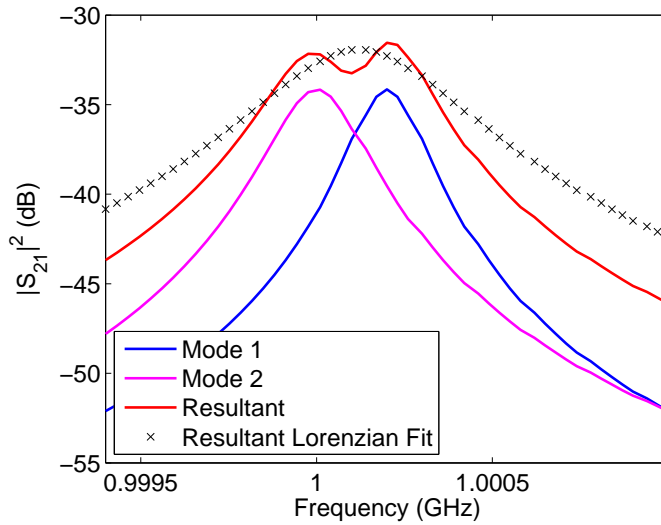


FIGURE 2.11: Calculated distortion caused by a single degeneracy.

However, in more subtle cases, the measurement can be distorted without obvious and clear evidence. For example, let us consider the perturbation of a single degeneracy with initially matching frequencies, again where  $g \propto Q$  and has no frequency dependence but the two resonances have different initial  $Q$  values. The two individual resonances as well as the resultant response with a fitted Lorentzian curve before and after the perturbation can be seen in Figure 2.12. It is assumed that the perturbation on the two constituent resonances is identical:  $\frac{f_1 - f_{01}}{f_{01}} = \frac{f_2 - f_{02}}{f_{02}}$  and  $\frac{1}{Q_{01}} - \frac{1}{Q_1} = \frac{1}{Q_{02}} - \frac{1}{Q_2}$ . In the case of an orthogonal degeneracy at frequencies distant from the dominant relaxation frequency this assumption remains valid, however, more complex phase relationships between the degenerate resonances could potentially cause the sample to exhibit an apparently different permittivity or permeability.

As can be seen, the resultant curves retain a Lorentzian shape. However, measuring the fractional  $Q$  change in the resultant curves results in a  $\sim 2\%$  error compared to the non-degenerate case. Therefore, care must be taken when performing perturbation experiments on rotationally degenerate cavity modes. If the modes show distortion similar to Figure 2.11, perturbing the cavity to re-align the modes will not necessarily produce accurate results due to the mismatch in  $Q$ .

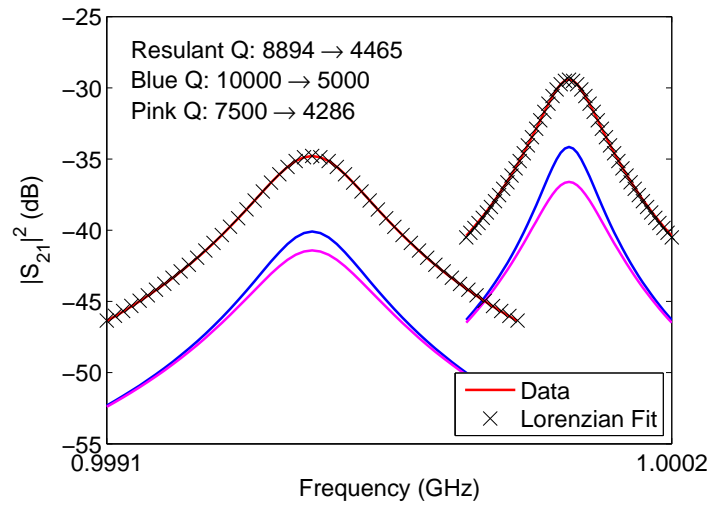


FIGURE 2.12: Calculated perturbation of a singly rotationally degenerate mode.

In cases where the  $Q$  is significantly different, some improvement can be made using the complex circle/linear fit strategy. A comparison of the two methods can be seen in Figure 2.13 where the mismatch in the two constitutive  $Q$ s is given by  $\frac{Q_1}{Q_2} - 1$ . The graph shows expected behaviour at the extremities: for matched  $Q$ s there is no error and when one  $Q$  becomes much smaller than the other, it is coupled increasingly weakly and so does not effect a measurement.

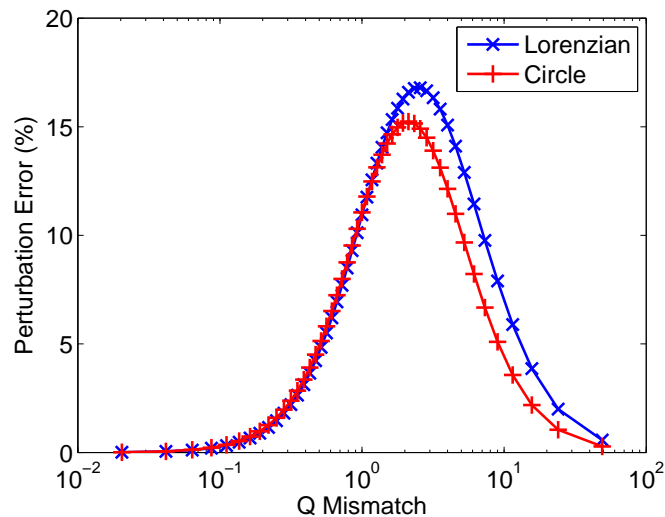


FIGURE 2.13: Calculated perturbation error for a single mismatched degeneracy.

### 2.6.5 Low $Q$ Considerations

An additional subtlety can be added by considering the frequency dependence of the  $Q$ -factor and coupling co-efficient,  $g$ . Given that  $Q = \omega_0 \frac{\langle U \rangle}{\langle P \rangle}$  and that  $\langle P \rangle \propto R_s \propto \sqrt{\omega}$ , it can be seen that the  $Q$ -factor is frequency dependent. Furthermore, this changing  $Q$

will also effect the coupling-coefficient  $g$ , which is also linearly dependent on frequency, adding more potential for systematic error when extracting  $Q$  using equation 2.38. For resonators with a high  $Q$ , these dependencies make little difference in the region around the 3dB Bandwidth. However, as the  $Q$  approaches zero, this has an increasing effect. This effect is explored by by letting  $Q = Q_0 \left(\frac{\omega}{\omega_0}\right)^{\frac{1}{2}}$  and  $g = g_0 \left(\frac{Q}{Q_0}\right) \left(\frac{f}{f_0}\right)$ . The error in measured  $Q$  with a resonant frequency of 1 GHz, using the standard fitting procedure without modification, is shown in Figure 2.14. It can be seen that the error only becomes appreciable at very low ( $<10$ )  $Q$  values and can therefore, in this work, be safely ignored.

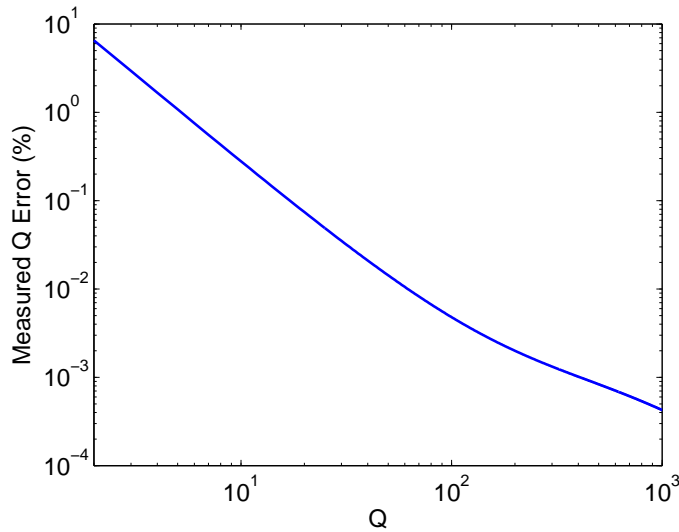


FIGURE 2.14: Potential measurement error for low  $Q$  resonators using a lorentzian fit when the frequency dependence of the  $Q$  and coupling co-efficient is ignored.

## 2.7 Sample Orientation and Depolarisation

When a sample is placed in an electric or magnetic field (diamagnetic material) the individual relevant dipoles within the sample with align such to reduce the field within the sample as illustrated in Figure 2.15 with a set of electric dipoles.

In the case of a long sample, the orientation of the applied field can dramatically affect the strength of the field internal to the sample. In the first diagram, where the field is applied perpendicularly, all dipole charges act to reduce the internal field. In the second diagram, the majority of the dipoles in the sample cancel each other out. Only charges at the ends of the sample act to reduce the internal field. The smaller the ratio of surface area perpendicular to the field to the area parallel to the field the smaller the depolarisation effect. In other words, the effect is reduced for samples which are tall and thin in the direction of the applied field.

The internal field can be related, in the electric field case and assuming the host medium is air, to the applied field by the following equation [86]

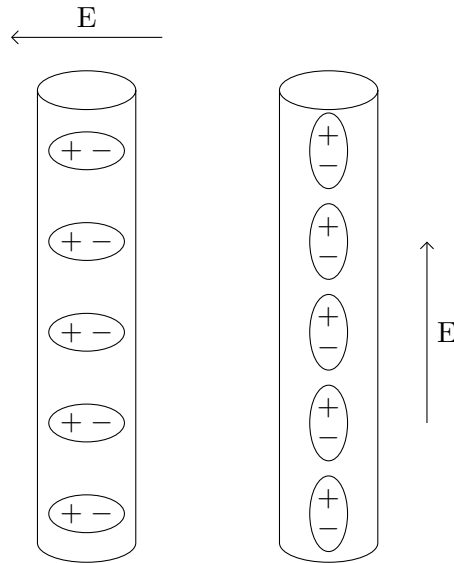


FIGURE 2.15: Sample dipole orientation in the presence of an electric field.

$$E_1 = \frac{E_0}{1 + N(\epsilon_r - 1)} \quad (2.51)$$

This introduces the depolarisation factor,  $N$ , which is based on the geometry of the sample in relation to the direction of the field. In the worse case, a thin flat plate normal to the field,  $N = 1$  and the internal field reduces to  $\frac{E_0}{\epsilon_r}$ . For a sphere  $N = 1/3$ , however, for a tall thin needle like structure it can be assumed that  $N = 0$  [87]. This is the case, for example, for a thin cylindrical sample placed axially along the entire length of the cavity operating in  $TM_{010}$ .

As seen in Section 2.2, this assumption is important when forming equations for effective permittivity and permeability from perturbation theory where the internal field is approximated as being equal to the applied field. It is possible to modify the perturbation equations for different sample geometries [88, 89, 90] but this requires knowledge of the depolarisation or demagnetising factor which may not always be trivial for complex shapes. Furthermore, different modes with different field configurations are likely to produce different depolarisation factors.

The analysis is equally valid for linear materials in the magnetic field case.

## 2.8 Common Measurement Modes

In order to measure both permeability and permittivity of a sample it is necessary to exploit modes which enable the sample to be placed independently in regions of magnetic and electric field. For convenience, Figure 2.16 displays a catalog of modes which have been used in this thesis.

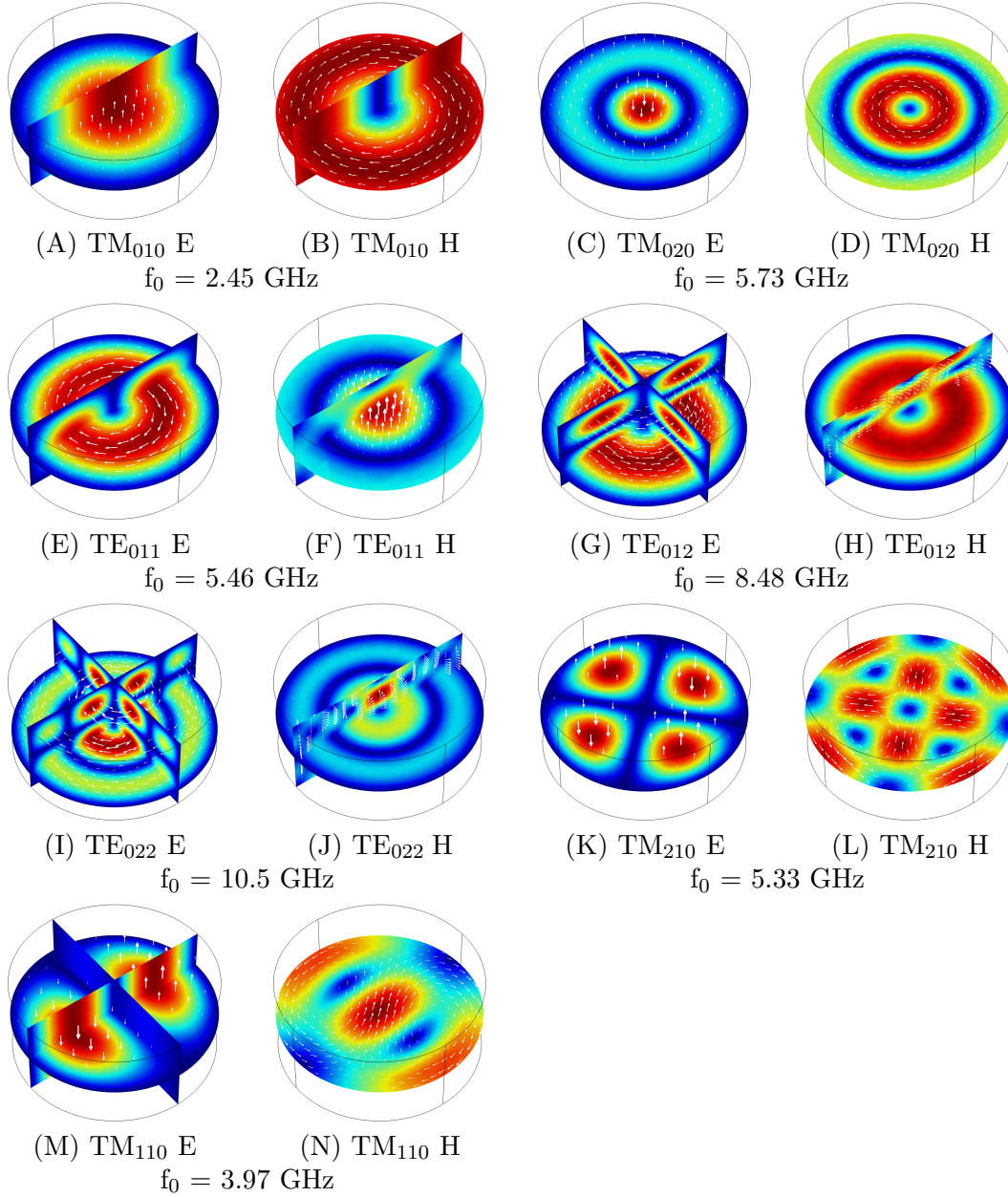


FIGURE 2.16: Mode catalog. Frequencies show for cavity with  $a = 4.6\text{cm}$  and  $d = 4\text{cm}$ .

## 2.9 Software

As was described in Section 2.6.3, software was developed in order to automatically capture  $S_{21}$  from the network analyser, perform the appropriate fitting and save the necessary data. Significant effort was made to create an integrated piece of software which manages the collected data and performs the necessary analysis. Utilising object-oriented principles, support for both ENA and PNA Keysight network analysers is included. Additionally, using the 4-port PNA, data can be simultaneously acquired in transmission from two separate resonators.

The software is split into two main sections. The first, seen in Figure 2.17, is the data viewer which allows for previously acquired data sets to be loaded and analysed.

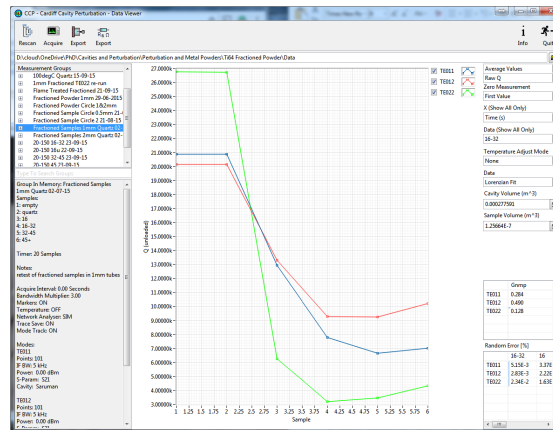


FIGURE 2.17: Cardiff Cavity Perturbation (CCP) software - data viewer.

Selecting 'Acquire' loads the window shown in Figure 2.18. Here the resonator parameters are shown in real-time from the network analyser and saved to disk.

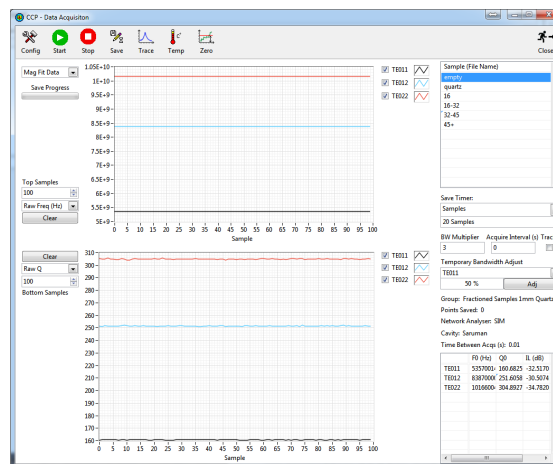


FIGURE 2.18: Cardiff Cavity Perturbation (CCP) software - main acquisition window.

The acquisition parameters, including mode selection, are accessed under config and seen in Figure 2.19.

Additionally the software includes the ability to view the raw traces and fit - shown in Figure 2.20.

## 2.10 Temperature Correction

Since changes in temperature, due to thermal expansion and resistivity changes, will modify the cavity frequency and Q, without correction, the measurement sensitivity is dependent on the ability to control ambient temperature. In order to maximise the

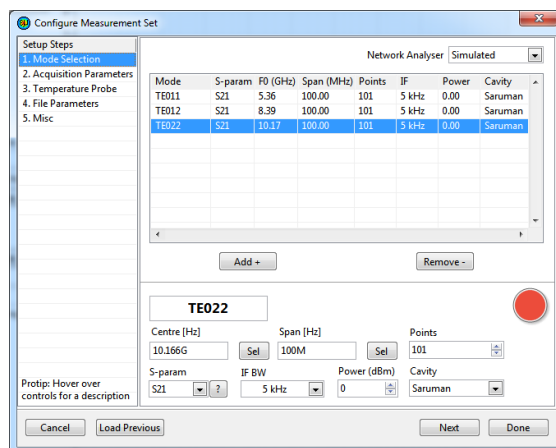


FIGURE 2.19: Cardiff Cavity Perturbation (CCP) software - acquisition configuration window.

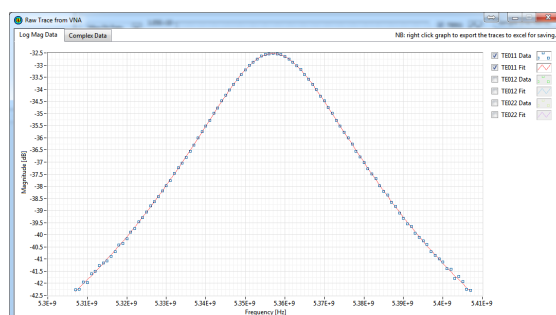


FIGURE 2.20: Cardiff Cavity Perturbation (CCP) software - raw trace and data fit.

measurement sensitivity, it is important that the ambient temperature is controlled and stabilised as finely as possible.

If sample measurements at varying temperature is desired, a challenge is therefore presented. Traditionally, in order to avoid changes in the cavity frequency and  $Q$ , the cavity temperature is isolated from the sample [91]. However, this will likely require complex heating apparatus. A simpler solution is to heat the entire measurement setup and correct for the independently changing  $Q$  and frequency. Using a readily available convection oven, measurements in the range of 0-300°C are easily achieved. A typical set-up is seen in Figure 2.21.

Whilst co-axial cables can be easily obtained which operate at elevated temperature, one potential limitation is the construction of coupling structures. Connectors with an extended centre conductor can be purchased which serve well as a capacitive probe. However, inductive loops are produced in-house and soldered together using temperatures ( $\sim 300^\circ\text{C}$ ) similar to those encountered here. Therefore, in order to extend this technique to modes which require loop coupling, different manufacturing techniques would have to be investigated; for instance welding.

An additional consideration when conducting experiments over a temperature range is to ensure the sample holder itself does not exhibit temperature dependent dielectric

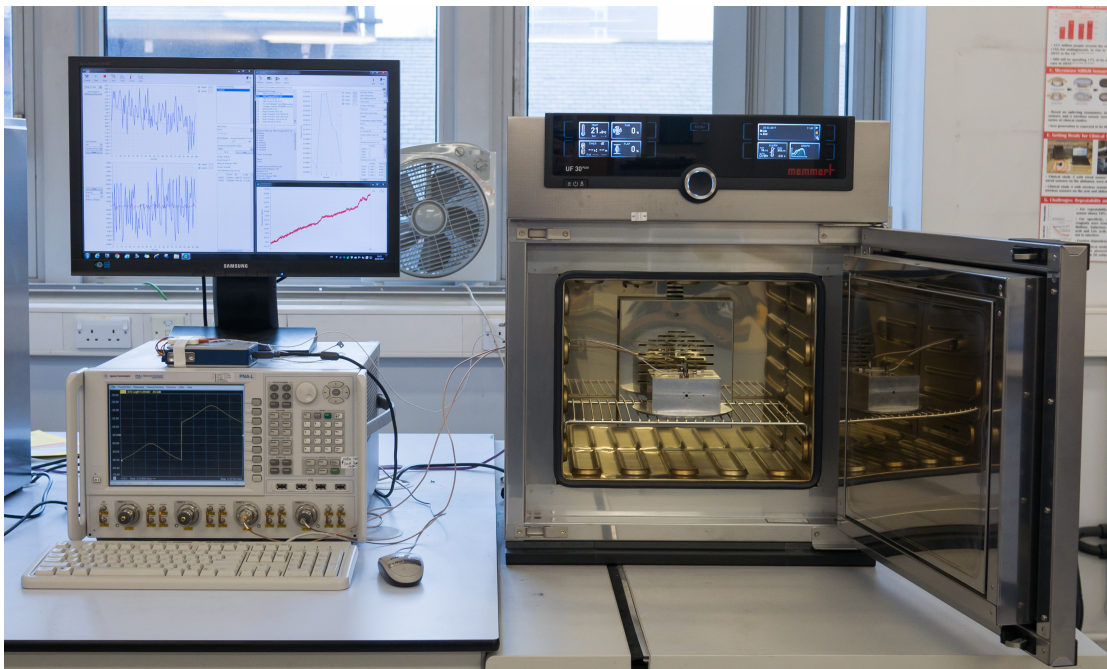


FIGURE 2.21: Microwave cavity, network analyser and oven used in temperature correction experiments.

or magnetic properties. Quartz shows very little response with regards to magnetic field, however, care must be taken in the electric field case at elevated temperatures. Below  $175^{\circ}\text{C}$ , no temperature dependence can be safely assumed allowing the use of the  $\text{TM}_{210}$  correction procedure, above this however, previous reports have shown significant variation which would require the use of a calibration ramp [92].

This section begins with an analytical analysis of cavity mode temperature dependence comparing the expected result and measured values. The dielectric measurement mode  $\text{TM}_{010}$  is used as a base although the analysis could easily be repeated for any measurement mode. The knowledge of the resonator response to temperature can then be used for correction when undertaking measurements. However, this approach requires accurate knowledge of the cavity temperature which may not always be possible to the required precision. The later part of this Section (2.10.2) details the use of a reference mode, typically  $\text{TM}_{210}$ , in order to more accurately and flexibly correct for cavity temperature.

### 2.10.1 Analytical Analysis

The frequency of  $\text{TM}_{010}$  in a cylindrical cavity is, from 2.17, is given by

$$f_{010} = \frac{K}{a} \quad (2.52)$$

where,

$$K = \frac{c \cdot \alpha_{nm}}{2\pi \sqrt{\mu_r \epsilon_r}} \quad (2.53)$$

and  $a$  is the cavity radius. Basic linear thermal expansion theory tells us that the radius at temperature  $T$ ,  $a_T$ , is related in the initial radius,  $a_0$ , by

$$a_T = a_0(1 + \alpha\Delta T) \quad (2.54)$$

So by substituting this into Equation 2.52 we get,

$$\frac{K}{f_0 a_0} = 1 + \alpha\Delta T \quad (2.55)$$

An empty aluminum cylindrical cavity of radius 4.6cm was heated from 20 - 180 °C and the resonant frequency and temperature simultaneously measured. Cavity temperature was measured in direct contact by a PT100 RTD. Figure 2.22 shows the results.

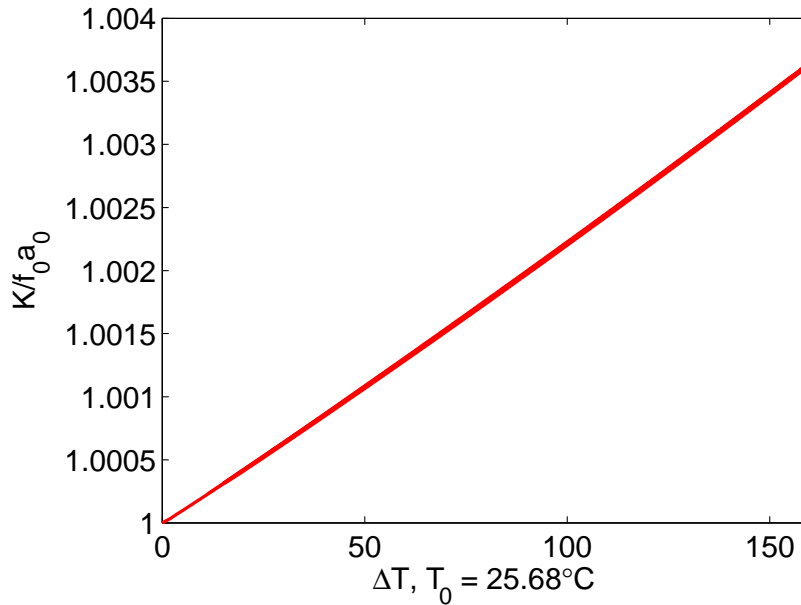


FIGURE 2.22:  $\text{TM}_{010}$  frequency modification by thermal expansion.

The extracted expansion co-efficient, using a simple linear fit, gives a value of  $22.8 \times 10^{-6} K^{-1}$  which compares favourably with the accepted value, for aluminium, of  $23.1 \times 10^{-6} K^{-1}$ . The inaccuracy is assumed to be due to the impurities in the aluminium since a machine grade (not pure) aluminium was used in construction.

It is of note here that typical measurements permit frequency changes to the order of 10 Hz to be measured. In this case, a change of 10 Hz would be caused by an expansion of  $1.85 \times 10^{-10} m$  which would be the result of a  $0.176 mK$  change in temperature. It is clear that changes in temperature through resonator frequency can be observed with much more precision than can easily be routinely measured. This illustrates one of the shortcomings of a temperature measurement approach to correction.

A similar analysis can be conducted for the resonator Q, which also considers the temperature co-efficient of resistivity. For a  $\text{TM}_{010}$  cylindrical cavity, the Q is given by

Equation 2.21. In reality the  $Q$  is somewhat smaller than given by Equation 2.21 due to additional contributions,  $Q_A$ . These additional contributions can be attributed to a rough inner cavity surface, sample and coupling holes and, commonly, a bolted joint necessitated by the cavity construction. Evaluating the temperature response of these elements is non-trivial.

The dimensions  $a$  and  $l$ , conductivity and frequency can all be modeled to exhibit a linear temperature dependence resulting in Equation 2.56.

$$\frac{1}{Q_{TOT}} = \frac{(a_0 + l_0) \left( \frac{\rho_0 a_0 (1 + \beta \Delta T)(1 + \alpha \Delta T)}{\pi \mu_0 k} \right)^{\frac{1}{2}}}{a_0^2 (1 + \alpha \Delta T)} + \frac{1}{Q_A} \quad (2.56)$$

For aluminium, the temperature of co-efficient of resistivity,  $\beta = 43 \times 10^{-4} K^{-1}$ , is much larger than expansion,  $\alpha = 23.1 \times 10^{-6} K^{-1}$ , and will therefore dominate.

Practically, it has been observed that the  $Q$  of a typical cavity is not a linear function temperature. An additional consideration is the location of any mechanical joint in the cavity. Traditional manufacturing techniques necessitate that cavity resonators are built in two or more pieces. If current flows across this joint, it forms an electrical contact and will contribute to (i.e. reduce) the resonator  $Q$ . When the cavity is heated and thermal expansion occurs, stresses can be put on the joint, thus modifying its electrical properties. Experience, detailed here, has shown that this effect can be very non-linear. Careful design can however practically eliminate this problem for certain resonator configurations.

For instance, for the cylindrical cavity resonator operating in the  $TM_{010}$  mode for dielectric measurement, surface currents flow radially. Therefore, a split placed along its diameter is preferable to one placed along its height because the split will not significantly perturb the surface currents. This is seen in Figure 2.23.

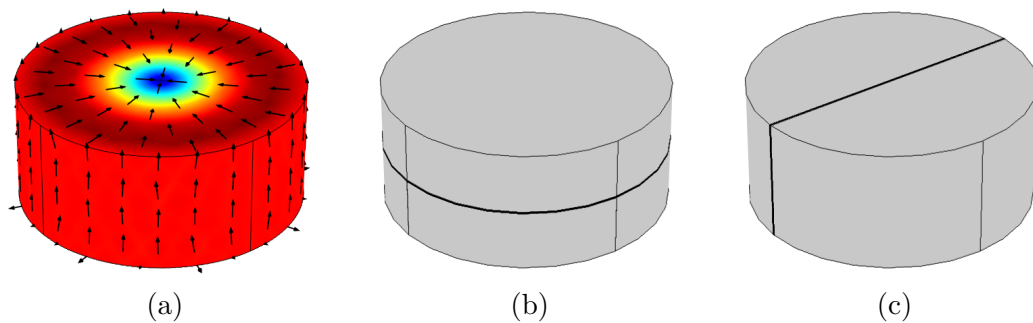


FIGURE 2.23: (a)  $TM_{010}$  current distribution. (b) Length split configuration. (c) Diameter split configuration.

Figure 2.24 shows a typical measurement of  $Q$  as temperature is varied for the diameter split configuration. Coupling is kept weak to ensure minimal  $Q$  loading and practically eliminate any potential non-linearity from changing coupling. In this case, the insertion loss was  $\sim 50$ dB, corresponding to a loaded and unloaded  $Q$  difference of 0.3%.

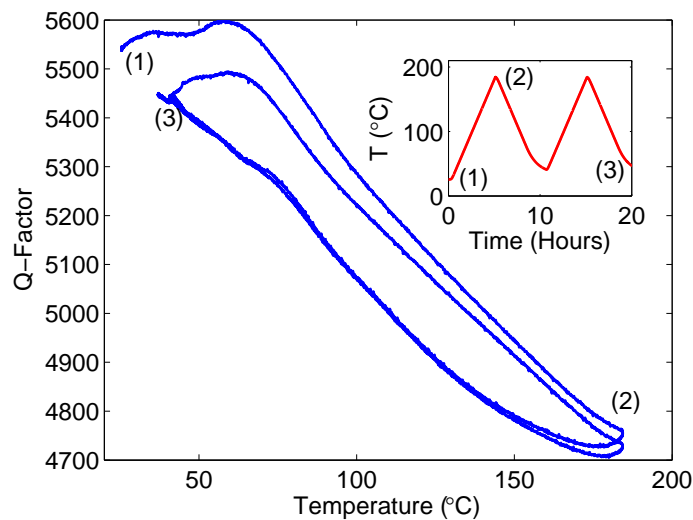


FIGURE 2.24: Typical  $TM_{010}$  Q-factor for diameter split configuration during cavity heating showing strongly non-linear and chaotic response.

Figure 2.25 shows the behaviour of a cavity in the length split configuration. As can be seen, the theory given by Equation 2.56, for the most part, accurately describes the Q behaviour. An offset,  $Q_A$ , is included and is constant across the whole temperature range. An additional observation, however, is that the Q is somewhat smaller on the initial temperature rise compared with subsequent cycles.

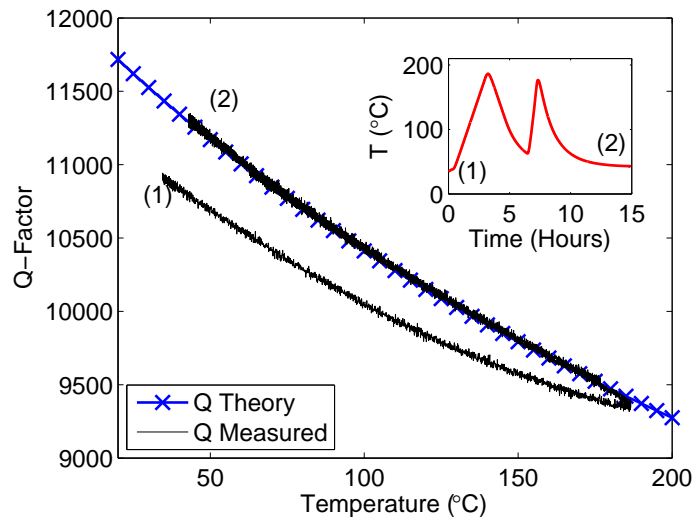


FIGURE 2.25:  $TM_{010}$  Q during heat treatment in the favourable, diameter split, configuration. Theory curve given by Equation 2.56.

The experiment was repeated a further two times with the same cavity resulting in Figure 2.26. During the second run, there is a similar, although smaller, increase in Q during the initial temperature rise. By the third run, no appreciable change is observed.

In order to discount the any possible effect caused by the mechanical join of the cavity, two further ramps were conducted after unbolting and subsequently rejoining the halves.

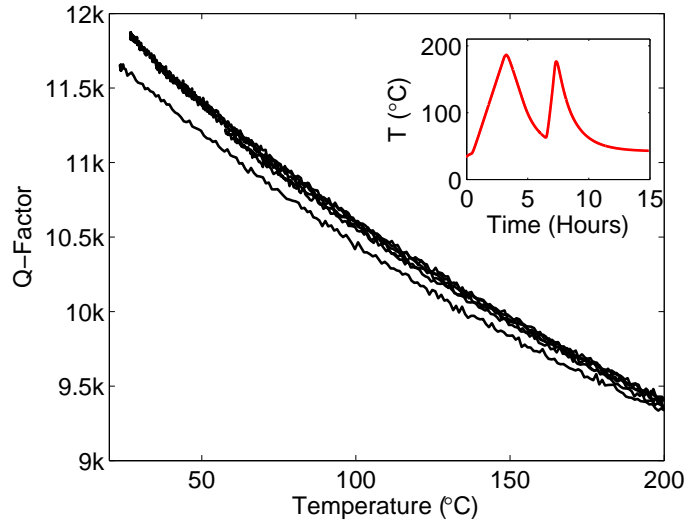
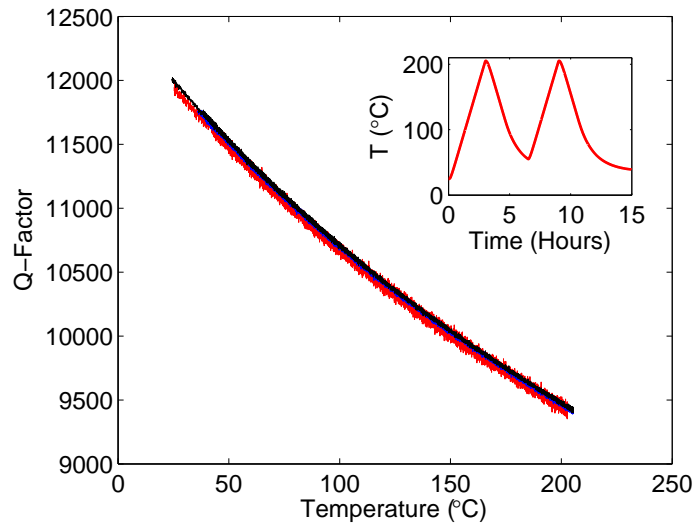
FIGURE 2.26:  $TM_{010}$  Q during repeated heat treatment.

Figure 2.27 shows three data sets: one before re-bolting and two after. As can be seen there is no significant measurable effect on Q.

FIGURE 2.27:  $TM_{010}$  Q repeated heat treatment after re-assembly.

Since the effect of coupling can be eliminated, the increasing Q during the initial treatment is interpreted as a decrease in the Aluminum's resistivity. There are two potential causes for this. The first is the role of impurities and alloying elements and the second is residual stresses causing dislocations and lattice defects. Both of these effects are widely studied in aluminium due to their significant role in determining material strength and hardness. For further discussion and additional investigation see Chapter 5.

From this initial data, it is clear that following the manufacture of a metal microwave cavity, if temperature stability is important, that it is important to pre-treat the cavity with heat in order to stabilise any impurities and remove any residual stresses caused

by the cold work during manufacture. This will ensure that the  $Q$  remains predictable and will minimise the resistive surface losses thus maximising resonant  $Q$ .

To summarise, the analytical analysis and subsequent experimental verification, it has been shown, that with careful design and pre-treatment, a cavity can be constructed which has a predictable response over a wide temperature range. The knowledge of this response can be used to conduct accurate perturbation measurements across this temperature range. However, it has been demonstrated that the smallest measurable change in resonator parameters is smaller than that caused by measurable temperature changes. Rather than correcting the resonator parameters in real-time with measured temperatures, one solution is to conduct experiments over a well defined temperature cycle and use a previously obtained set of calibration data for the unperturbed resonator data. However, the limitations here are clear.

### 2.10.2 Reference Mode

In order to address the shortcomings described previously, environmental changes can be tracked and corrected for using an additional reference resonant mode. Commonly a suitable mode will be one of the so called 'whispering gallery' modes. These modes are often used in the form of a dielectric resonators in order to very accurately measure the permittivity of a dielectric puck [93, 94, 95], however, these modes prove useful as they have a magnetic and electric field node at the centre position where the sample is usually placed. Therefore, any resonance changes can be attributed to the cavity and not the sample.

The work undertaken here uses  $TM_{210}$  as the reference mode because it is the lowest frequency suitable mode. Table 2.2 compares the relative total magnetic and electric energy for a 5mm diameter cylindrical sample placed axially in  $TM_{210}$  to other common measurement modes. It can be seen that the energy density,  $W_{SE}$ , is, in the worst case, three orders of magnitude lower than any measurement mode. The values were calculated in COMSOL by computing the following integral.

$$W_{SE} = \frac{\int_{V_S} \epsilon_0 |E|^2 + \mu_0 |H|^2 dV}{\int_{V_C} \epsilon_0 |E|^2 + \mu_0 |H|^2 dV}. \quad (2.57)$$

Due to linear thermal expansion, the frequency of the unperturbed measurement mode is related to the frequency of the reference mode by a simple ratio.

This allows us to say, for the unperturbed case and using  $TM_{010}$  as an example,

$$\frac{\Delta f_M}{f_{M_0}} = \frac{\Delta f_R}{f_{R_0}} = 1 - \frac{a_0}{a_T} \quad (2.58)$$

where  $f_M$  is the measurement mode,  $TM_{010}$ , frequency and  $f_R$  is the reference,  $TM_{210}$ , mode.  $a_0$  and  $a_T$  are the initial and temperature changed cavity radius respectively.

Mode	Function	Sample Energy Proportion (%), $W_{SE}$
TM <sub>010</sub>	Electric	0.546
TM <sub>020</sub>	Electric	0.0126
TM <sub>110</sub>	Magnetic	0.00454
TE <sub>011</sub>	Magnetic	0.00483
TE <sub>012</sub>	Magnetic	0.00207
TE <sub>022</sub>	Magnetic	0.00812
TM <sub>210</sub>	Reference	0.0000617

TABLE 2.2: Cylindrical cavity (radius = 4.6cm, height = 4cm) mode sample energy density. Cylindrical sample placed axially along full cavity height with 5mm diameter. Calculated using Equation 2.57.

Therefore, in the context of perturbation, the temperature dependent unperturbed measurement frequency,  $f_{M_0}(T)$ , can be inferred from the frequency of the reference mode.

$$f_{M_0}(T) = \left( \frac{\Delta f_R}{f_{R_0}} + 1 \right) f_{M_0} \quad (2.59)$$

Experimental evidence shows this method to be robust when determining the temperature dependent frequency of the measurement mode. Across the full range of 20 - 200 °C, the average inferred frequency error was 0.0012% which corresponds to a temperature change of 0.5°C. Reducing this range to within 10°C of the reference temperature reduces this error to 0.02°C.

Whilst in this example both measurement and reference modes share a simple frequency dependence on the cavity radius, the method is equally valid for modes which include a dependence on the cavity height. This is valid assuming that the material is consistent throughout the whole cavity and the height expands at the same rate as the radius.

As seen above, the temperature dependence of the Q-factor depends on many different aspects of the resonator geometry and, primarily, the square root of the metal wall's conductivity. It then follows that therefore, it should be possible to take a similar approach as taken with frequency.

However, as previous results indicate, the Q of a resonator is not as easily predicted as frequency and the measurement mode and reference mode may not have a simple linear dependence.

Figure 2.28 shows the Q of TM<sub>010</sub> and TM<sub>210</sub> as the temperature is changed.

Performing a linear and quadratic fit on this data and then using the reference mode to calculate the measurement mode Q results in Figure 2.29. The result shows that a linear approximation can adequately used to calculate the unperturbed measurement Q

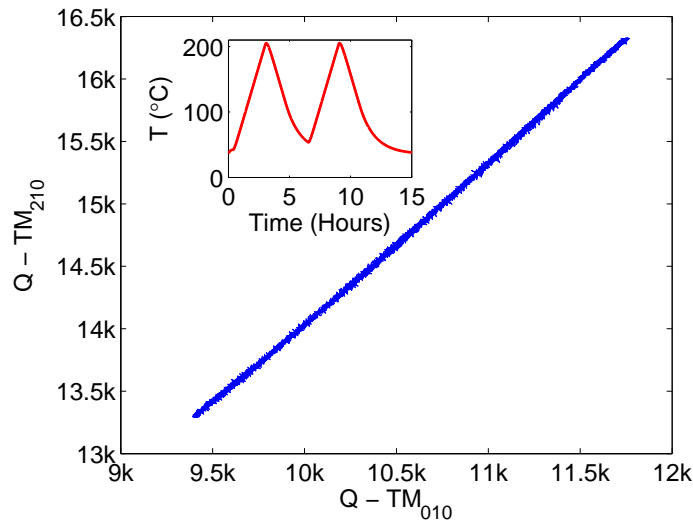


FIGURE 2.28: Measured  $Q$  of  $TM_{210}$  and  $TM_{010}$  during heat treatment.

although a higher order term is clearly present. Here the average error of the quadratic fit, 0.09%, would be the result of an approximately  $0.7^{\circ}\text{C}$  change.

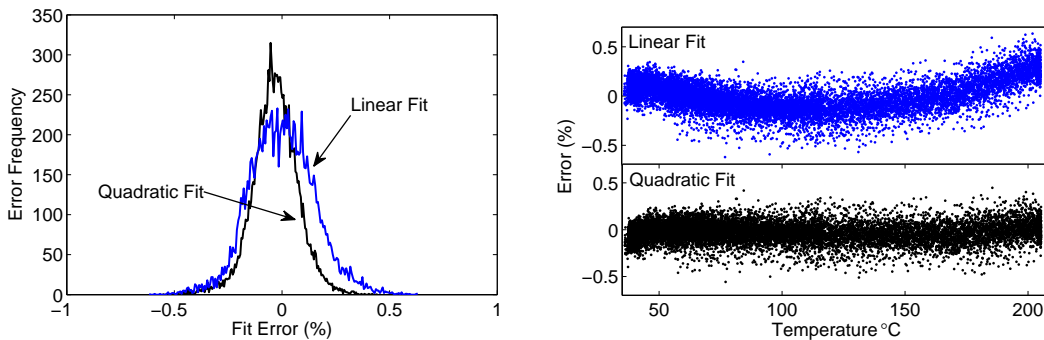
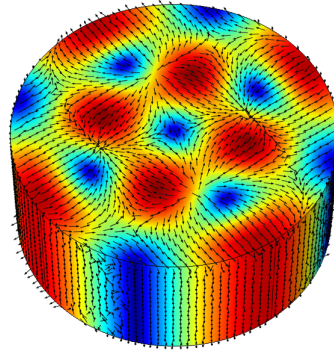
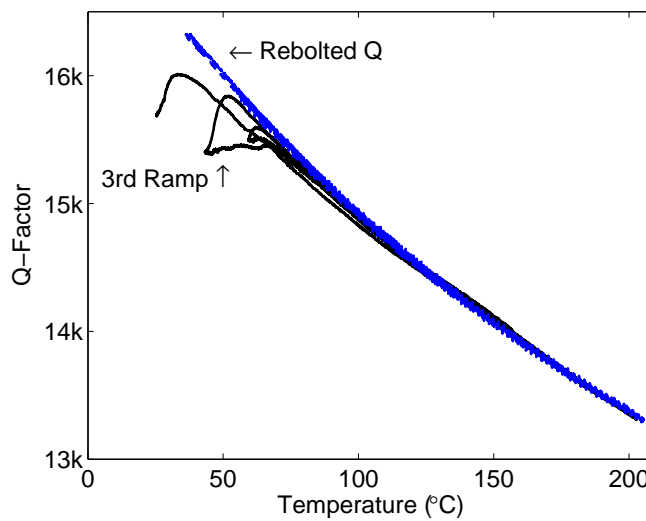


FIGURE 2.29: Error distribution and raw error when deriving  $TM_{010}$   $Q$  from measured  $TM_{210}$   $Q$  in range  $30\text{-}200^{\circ}\text{C}$ .

Similarly as seen with  $TM_{010}$ , careful cavity design can also impact the potential use of  $TM_{210}$ . Examination of the surface currents (Figure 2.30) show neither the length or diameter split configurations offer the perfect solution. During the re-assembly procedure described in the subsection above, it was observed that a strong non linearity was observed at the initial stages of the temperature ramp which was eliminated during re-assembly (Figure 2.31). This demonstrates that the stability of the bolted join is important and care must be taken during cavity design and assembly.

To conclude, the use of a reference mode is a useful technique which has the potential to flexibly resolve and correct for temperature changes with higher precision than can easily be achieved in the lab - without the need for additional measurement hardware. It follows that the main usefulness of this technique comes when it is desirable to monitor small changes in temperature across a small temperature range or when environmental conditions make temperature measurement difficult.

FIGURE 2.30: Simulated  $TM_{210}$  surface current distribution.FIGURE 2.31: Q-factor instability of  $TM_{210}$  during third heat treatment cycle and stability after subsequent re-assembly.

## 2.11 Measurement Uncertainty

As a final discussion point, the error in cavity perturbation measurements is considered.

As has been previously seen, the absolute measurement error in frequency and  $Q$  is small. As an example, consider the frequency perturbation of the typical quartz sample tube.

$$f_0 - f_s = 2516705695 - 2519458239 = 2752544 \pm 10 \text{ Hz} \quad (2.60)$$

Even for this relatively small perturbation, the error in frequency remains very small at 4ppm. The error in loss measurements are more modest but still very small, for instance a cylinder, filled with nylon powder of radius 2mm and length 40mm produces an error of 0.12% as follows:

$$\frac{1}{Q_s} - \frac{1}{Q_0} = \frac{1}{10310} - \frac{1}{12029} = 1.386 \pm 0.002 \times 10^{-5} \quad (2.61)$$

It is assumed that the measurement time is short enough so that temperature changes can be ignored this is confirmed by noting the normal distribution of the measured values.

Considering the terms of Equation 2.14a, the only other random source of error comes from the sample volume.

In order to characterise this for the typical measurements in this thesis, a set of 10 quartz tubes (1.5mm ID) were tested each filled with the same liquid dielectric. Since the permittivity in each case is held constant, by observing the spread in frequency shifts, a measure of the spread of sample volumes can be found.

In order to do this, each tube was filled with Acetone. Acetone was chosen over simply using water since it still has a relatively high dielectric constant (~20) to produce large frequency shifts but a relatively small loss factor so as not to excessively depress the Q.

The set of frequency shifts are shown below in Figure 2.32, normalised to the average value.

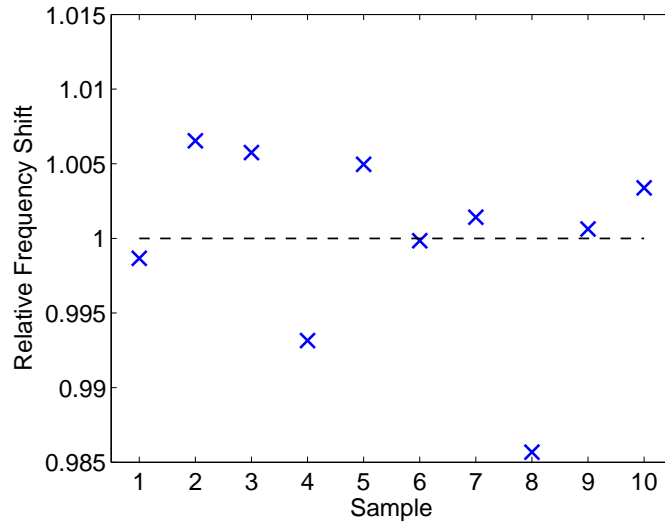


FIGURE 2.32: Relative frequency shift of acetone, normalised to the average shift. Effective sample volume error distribution.

The standard error in frequency shifts is found to be 0.2%.

In addition to the basic volume and for a powdered sample, the density of the sample may play a significant role in the measurement uncertainty. It will depend strongly on morphological powder characteristics such as grain shape and size but for samples of a known density, the weight of the sample will usually provide a sufficient measure of the density and resultant sample volume.

These results indicate that the random errors associated with a perturbation measurement are dominated by the container but are still small. As a result, samples can be compared with high accuracy with the results usually quoted as effective. However, in order to quote absolute values of permeability, additional sources of error must be considered.

Firstly, is the role of depolarisation. As has been previously discussed, unless it can be accurately determined for the sample shape and a correction made, it will significantly effect the perceived permittivity or permeability.

Attributing an uncertainty to the mode scaling constant can be difficult and will depend on the technique used to calculate it. Generally, it will include an error in the cavity volume, calibration sample volume and calibration piece permittivity. The calibration sample volume error will be similar to the value described before and the permittivity of a sample will typically have an error of less than 1%. A more broad indication can be obtained by comparing simulated and experiment values as discussed in Section 2.5. Using the difference between the experimental and simulated values as an upper and lower bound, a sensible uncertainty value of 1% can be assigned.

To summarise, assuming consistent sample preparation and conditions, microwave cavity perturbation measurements can very accurately compare samples. In a number of use-cases, simple quoting a relative  $Q$  or frequency shift or an effective permeability or permittivity will suffice. This can be quoted with a small error; typically better than 0.3%. However if the absolute error is considered, this will be in the region of 1%, the majority of which is attributed to the mode scaling constant.

## 2.12 Summary

To conclude, this chapter provides all the necessary background information needed in order to undertake cavity perturbation measurements. Starting with the theory which describes the relationship between changes in resonator frequency and  $Q$  and the complex permittivity or permeability of an inserted sample, the necessary steps to design a cavity of suitable dimensions operating in the desired mode and at a specific frequency and the procedure measure its frequency and  $Q$  are described. Furthermore, software used to conduct the measurements by control of a network analyser is shown.

A number of key design trade-offs and considerations must be taken. Significantly, this includes careful selection of the sample geometry to avoid depolarisation and careful correction for changing ambient temperature. Since the resonant frequency can be measured with very high precision, cavity perturbation systems can be very sensitive to small changes in temperature with measurements here capable of resolving changes in temperature of less than 1mK. This may be significant if the change in temperature across a measurement is large compared to the change caused by the sample or if the measurement of small changes in sample properties are desired.

The final analysis of the expected measurement uncertainty shows the technique excels when a comparison of different samples is required. If the sample preparation is consistent, uncertainties of less than 0.01% can easily be achieved. The absolute uncertainties in measured permittivity or permeability are much larger due to difficulties in precise cavity calibration. However, it is worth noting that any measurement is only valid at the measurement frequency which may not match the specific use-case for the measurement.

## Chapter 3

# Microwave Electromagnetic Properties of Conducting Powder

### 3.1 Introduction

Throughout the last 40 years, there has been a lot of research effort concerning the electromagnetic absorption of conducting powders for the application of sintering a powder in an RF field. The first successful demonstration of this was performed by Roy et al. [52] who comments that the “findings are surprising in view of the reflectivity of bulk metals at microwave frequencies”. It is commonly understood that the free electrons in a metal act to reduce any applied field to zero inside the metal and as a result their microwave properties are uninteresting. However, powdered metals have proven to display more interesting characteristics. A powder in this context refers to particulates whose diameter is much smaller than the applied wavelength such that scattering effects can be ignored.

The theoretical basis for electromagnetic absorption in conducting metal powders is well established. A variety of studies have taken a first principles approach to the absorption of an individual particle within both electric and magnetic fields [38, 96, 97]. It is accepted that, for any practical size of particles which are considered to be metallic on the basis of a high value of electrical conductivity, magnetic absorption via eddy current loss is much greater than loss in an equivalent electric field and this has been demonstrated experimentally [98, 99, 55].

Typically, studies are interested in energy absorption for the application of heating a powder. With this in mind, previous works have been undertaken to experimentally verify the absorption in metallic powders by applying high power microwave radiation and measuring the powder temperature. This has been done relatively successfully by measuring the temperature gradients and maximum temperature achieved [100, 55, 101]. The peak absorption rates, as predicted at specific particle sizes by theory, have also been observed experimentally [102, 103, 54]. However, using the temperature as

a measure of the absolute absorption has many difficulties. Firstly, the precise power delivered to the sample must be calculated and this may not be trivial due to the complex loading and changing condition of the applicator caused by the heated powder. Also, accurate determination of other powder characteristics will likely be difficult. For instance, the powder thermal conductivity and dissipation rates can be massively affected by the ambient conditions, such as initial temperature and airflow, and other powder characteristics such as packing density, sample size and chemical composition.

As previously discussed, motivation for this work comes from additive manufacturing. Since speed and cost are a very important aspect in production, the PSD or indeed any size characteristics of the powder, are not routinely measured due to the need for expensive measurement equipment.

Conversely, microwave cavity perturbation could provide a convenient method which relies on a simple metal structure for the cavity, and solid-state electronics to interrogate it. Information regarding the average particle size of a metallic powder can then be obtained non-destructively. The information it provides, although not a detailed particle size distribution (PSD), can be useful, for instance, in determining the evolution of powder properties over time.

Therefore, distinct from the majority of previous work in this area, in this study, interest does not lie in the heating effect of the microwaves. In contrast, interest lies in measuring absolute absorption with the aim of taking an unknown powder and using microwave measurements to determine particle size and chemical composition.

It is convenient to separate this chapter into two distinct parts dealing with the magnetic and electric fields respectively. Using the cavity perturbation technique as discussed in detail in earlier chapters, the electric and magnetic properties of the samples can be measured separately and compared with the relevant theory.

The majority of the theoretical background is taken from previous work by Porch, Slocombe and Edwards as detailed in their 2013 paper [38].

## 3.2 Powder Samples

In order to establish how well the theory withstands a practical treatment, powder of varying particle size needed to be obtained. The base powder is an alloy of titanium used by Renishaw in its ALM process, The powder is usually referred to as Ti-6Al-4V and conforms to the ASTM B348 Grade 23 specification [104]. The powder, produced by plasma atomisation, is supplied by LPW Ltd and its chemical composition can be seen in Table 3.1 as supplied by the manufacturer. The small percentages of non-metals can be attributed to the oxide layer on the powder, formed spontaneously as soon as it is exposed to air. Ti6Al4V is a common Titanium alloy frequently used in aerospace and medical applications due to its high strength and biocompatibility. As Ti6Al4V is not

usually used for its conductive properties, there is uncertainty regarding its conductivity. However, the bulk conductivity is assumed to be approximately  $6 \times 10^5 \text{ Sm}^{-1}$  [105].

Element	% weight
C	0.01
O	0.11
N	0.01
H	0.0077
Fe	0.21
Al	6.4
V	4.0
Ti	Balance

TABLE 3.1: Ti-6Al-4V chemical composition.

### 3.2.1 Sample Preparation

Unless otherwise stated, powder samples were placed into cylindrical quartz tubes for testing. Tubes were sealed at one end with molten wax or, in the case of high temperature experiments, with a silicone adhesive. The quartz tubes are 100 mm in length with varying inner diameter (0.5-2mm).

Once the tubes were filled, to ensure uniform density, the samples were vibrated on a small 1 kHz platform for 10 seconds.

The vibration time is kept short to avoid any significant granular convection even though this effect is expected to be negligible due to the long thin container geometry. It is observed that no discernible compaction occurs after 10 seconds.

### 3.2.2 Oxide Layer

The oxide layer is assumed to be amorphous because it is only formed spontaneously at room temperature. The powder is prepared and initially stored under Argon and not exposed to air until testing. The structure of the oxide layer, especially in alloyed Titanium, is relatively complex and numerous studies have been conducted to characterise the oxide layer due to its importance in bio-compatibility.

Typically the thickness of the oxide layer is regarded to be thin ( $\sim 4\text{-}6\text{nm}$ ) and relatively stable [106]. Thicker oxide layers are known to discolour the metal with the colour going from golden to light blue as the layer increases from 10nm to 80nm [107]. This can be easily observed by heating the powder for  $\sim 1$  minute with a small butane torch. The oxide layer is often reported to be composed of different layers corresponding to the

different oxide states of the metals [108]. However, the majority of the surface oxide in Ti-6Al-4V is known to be  $\text{TiO}_2$  with an enriched composition of  $\text{Al}_2\text{O}_3$  when compared to the bulk metal content, and little Vanadium Oxide [109, 110, 111].

The dielectric properties of these metal oxides, as expected, can vary significantly dependent on preparation and crystal structure but are typically generally regarded as low loss. For  $\text{TiO}_2$ , typically, dielectric constants around 75-100 are quoted alongside  $\tan\delta$  values around  $10^{-4}$  [112] at GHz frequencies. Conversely, aluminum oxide exhibits a much smaller dielectric constant at around 10 and single crystals of alumina are some of the lowest loss materials known with  $\tan\delta$  approaching  $10^{-5}$  [113]. However, in the case of both alumina and titanium oxides in the context of an oxide coating, the loss tangents will be significantly larger (1-2 orders of magnitude) due to complex grain boundaries and oxygen vacancies caused by impurities. Neither oxides exhibit a significant response in a magnetic field.

A 5nm thick oxide layer contributes  $\sim 0.06\%$  of the total volume for a powder with average particle size  $\sim 25\mu\text{m}$ . It might then be assumed that it is not therefore expected to make sizable impact on any measurements. However, a number of studies point to a different conclusion. Buchelnikov et al. suggests the oxide layer plays a key role in the ability for the electric and magnetic fields to penetrate a sample [114]. This effect is further explored by Gupta et al. in a unit cell simulation approach [115] who similarly conclude that the presence of a very thin oxide layer can significantly modify its heating behaviour by providing electrical isolation between particles.

Ignatenko and Tanaka have conducted a rigorous analysis of coating metal powders in both electric and magnetic field. Their analysis uses Mie theory to generate the scattered field from an individual particle and Bruggeman's effective medium approximation to generate an effective properties for a collection of particles. They propose that the shell thickness has a dramatic effect on effective permittivity but little effect on permeability. Furthermore, as described previously, both permittivity and permeability are expected to depend strongly on particle size [116].

Since it is expected that thickness is the key oxide parameter, an exhaustive analysis of the intricacies and subtle differences in oxide composition has not been conducted.

### 3.2.3 Particle Size

The powder is supplied as having particles with diameter in the range 16 - 45 $\mu\text{m}$ . The particle size distribution (PSD) was obtained for the powder using a Malvern Mastersizer 3000 which utilised laser diffraction in order to determine the distribution. This distribution can be seen in Figure 3.1.

In order to obtain samples of differing PSDs, the samples were sieved with increasingly bigger sieves in order to obtain 4 separate fractions: '<16 $\mu\text{m}$ ', '16-32 $\mu\text{m}$ ', '32-45 $\mu\text{m}$ ' and '>45 $\mu\text{m}$ ', labelled 1-4. The separate PSDs of these fractions can be seen in Figure 3.2.

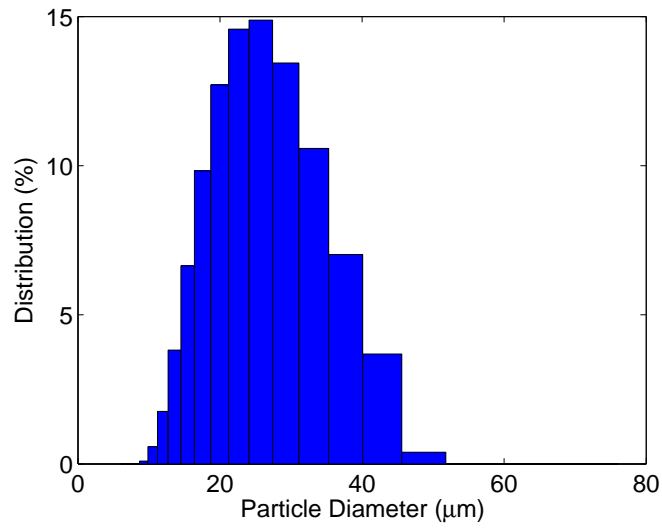


FIGURE 3.1: As sold base Ti6Al4V powder particle size distribution.

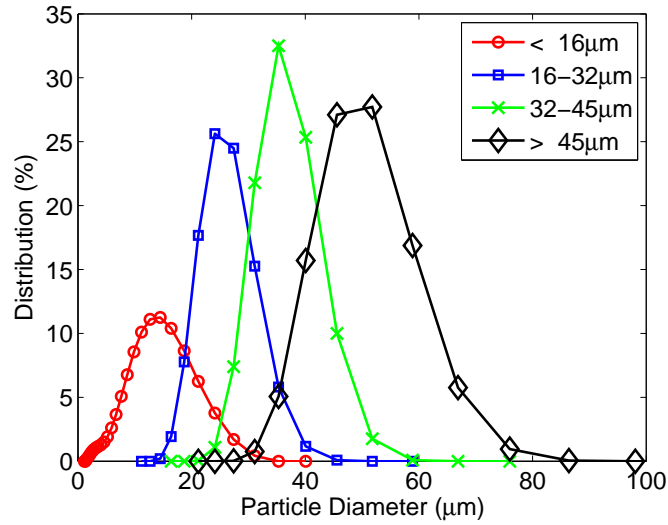


FIGURE 3.2: Fractionated Ti6Al4V powder particle size distributions. Separate fractions obtained by sieving base powder purchased from manufacturer.

The following integral can be evaluated to give a measure of the average particle size:

$$a_{int} = \int_0^{\infty} a \cdot f(a) da \approx \sum_{i=0}^{\infty} a_i \cdot f_i \quad (3.1)$$

where  $a$  is the particle radius and  $f(a)$  is the particle size distribution. The value is estimated from the discrete PSD by calculating the shown sum. A summary of the fraction statistics can be seen in Table 3.2.

The three larger fractions appear approximately symmetrical, however, the smallest is noticeably broader. This similarity is also shown in the physical look and feel of the powders. The three larger fractions appear identical: light grey in colour and smoothly

Fraction	Dx10 ( $\mu\text{m}$ )	Dx50 ( $\mu\text{m}$ )	Dx90 ( $\mu\text{m}$ )	$a_{int}$ ( $\mu\text{m}$ )
Base	9.55	15.45	24.4	11.7
1	3.14	6.80	11.4	6.60
2	10.7	13.5	17.3	12.9
3	15.7	19.1	13.3	18.1
4	20.0	25.2	31.9	24.0

TABLE 3.2: Fractioned Ti6Al4V powder particle size statistics. For example, 10% of the particles, by volume, have radii smaller than Dx10.

flowing. However, the smaller fraction is slightly darker in colour and tends to form powder clumps. Imaging the separate fractions with optical microscopy (utilising focus stacking) illustrates the cause of this difference. Figure 3.3 shows the four particle fractions at  $\times 20$  magnification. In each case, the radius of a single highlighted particle has been measured to illustrate the relative size of the particles in each fraction.

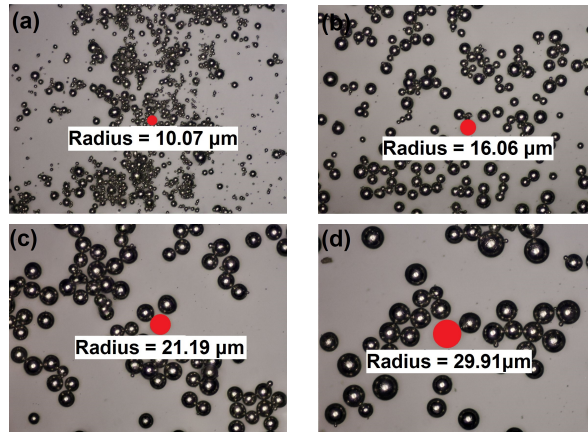


FIGURE 3.3: Optical microscope images of fractioned Ti6Al4V powder.

Firstly, the images reveal the powder particles are highly spherical. This a very useful quality since any theoretical considerations can confidently consider spherical particles. Secondly, whilst small satellite particles are visible in all fractions, the smallest fraction shows a large concentration of these small sub-micron size particles. In this fraction, very few particles appear isolated but each larger particle is surrounded by many very small particles. This tendency to clump together can be assumed to be the cause of its different flow characteristic.

In addition to the fractioned samples, 4 samples with much closer average sizes were created by combining base powder with fraction 1. The result can be seen in Table 3.3. The PSDs for these samples is calculated by combining the constituent PSDs linearly scaled by weight.

	Weight Proportion of Fraction 1	Estimated $a_{int}$ ( $\mu\text{m}$ )
Stage 1	16.5 %	10.8
Stage 2	32.8 %	10.0
Stage 3	49.9 %	9.10
Stage 4	68.7 %	8.11

TABLE 3.3: Modified base powder average particle sizes. Achieved by mixing of base powder by increasing quantities of fraction 1.

### 3.2.4 Sample Density

Since perturbation measurements are volumetric, for powder samples, the relative density or, in other words, the volume packing fraction of the different samples must be considered. This was calculated by weighing the prepared samples, with known tube volume, and calculating the packing fraction from the known density of Ti6Al4V of  $4.42 \text{ gcm}^{-3}$ [117]. The samples achieve densities near or above what can be expected from an ideal close pack arrangement (0.63). It is not surprising to see values greater since the powders contain a distribution of particle sizes. The smaller samples tubes exhibit a higher packing fraction, mostly likely due to the difficulty in filling - the samples had to be slightly compressed to encourage the powder to fall down the tube and fill it completely. Due to agglomeration restricting the free flow of particles, the smallest tube was not able to be filled with Sample 1. Errors from the sample volume and weighing process were considered.

Fractioned Base Powder Samples				
Sample	1	2	3	4
Packing Fraction ( $\varnothing=2\text{mm}$ )	$0.50 \pm 0.01$	$0.55 \pm 0.02$	$0.57 \pm 0.03$	$0.58 \pm 0.02$
Packing Fraction( $\varnothing=1\text{mm}$ )	$0.54 \pm 0.01$	$0.58 \pm 0.01$	$0.58 \pm 0.01$	$0.60 \pm 0.01$
Packing Fraction ( $\varnothing=0.5\text{mm}$ )	-	$0.63 \pm 0.01$	$0.62 \pm 0.02$	$0.62 \pm 0.02$
Base Powder Mixed with Fraction 1				
Stage	1	2	3	4
Packing Fraction ( $\varnothing=1.5\text{mm}$ )	$0.65 \pm 0.01$	$0.65 \pm 0.01$	$0.64 \pm 0.01$	$0.62 \pm 0.01$

TABLE 3.4: Ti6Al4V sample filled quartz tube density. Calculated as density relative to bulk Ti6Al4V.  $\varnothing$  is inner quartz tube diameter.

### 3.3 Magnetic Field and Permeability

#### 3.3.1 Theory and Background

The magnetic polarisation, or magnetisation  $\underline{M}$ , of a particle is related to the applied field by the dimensionless magnetic polarisability  $\alpha$ ,

$$\underline{M} = \alpha \underline{H}_0 \quad (3.2)$$

where the polarisability is a function of both the particle material and geometry. The magnetic dipole moment,  $m$ , from Equation 3.2 becomes

$$m = \alpha H_0 V_s \quad (3.3)$$

where  $V_s$  is the sphere volume. From perturbation theory, the change in resonant frequency due to a perturbation is related to the change in resonator energy by

$$\frac{\Delta\omega}{\omega_0} = \frac{\Delta W}{4W} = -\frac{m \cdot B}{4U} \quad (3.4)$$

Recalling the standard perturbation equations

$$\mu_2 \simeq \Delta \frac{1}{Q} \frac{V_C}{V_S} G_{nmp} \quad (3.5a)$$

$$\mu_1 \simeq 2G_{nmp} \frac{V_C}{V_S} \frac{\Delta f}{f_0} + 1 \quad (3.5b)$$

it can be seen that the summation of dipoles for a collection of particles constitutes the bulk material permeability:

$$\mu_1 = \Re(\alpha) + 1 \quad (3.6a)$$

$$\mu_2 = -\Im(\alpha) \quad (3.6b)$$

Porch et al. calculates the magnetic dipole moment of an isolated spherical particle placed in a uniform applied magnetic field  $H_0$  as

$$\underline{m} = 2\pi a^3 \underline{H}_0 \left( \frac{(\mu + 2)(1 - kacot(ka)) - \mu(ka)^2}{(\mu - 1)(1 - kacot(ka)) - \mu(ka)^2} \right) \quad (3.7)$$

where  $a$  is the particle radius and  $k = \frac{\omega\sqrt{\epsilon\mu}}{c}$ .

For a non-magnetic conducting particle, this reduces to Equation 3.8 describing how the time average power dissipation, per unit volume, changes with varying particle size and frequency

$$\langle P_M \rangle = \frac{3}{4} \omega \mu_0 H_0^2 \Im \left( 1 + \frac{3 \cot(ka)}{ka} - \frac{3}{(ka)^2} \right) \quad (3.8)$$

For highly-conducting non-magnetic particles,  $\mu \approx 1$  and  $\varepsilon \approx 1 - \frac{i\sigma}{\omega\varepsilon_0}$ . Even for traditionally high permeability metals these approximations hold since the permeability will tend to 1 at microwave frequencies.

In order to normalise the result for different frequencies, the particle skin depth ratio,  $\frac{a}{\delta}$  is used. It is then seen in the small particle limit,

$$\lim_{\frac{a}{\delta} \rightarrow 0} \langle P_M \rangle \propto \omega^2 a^2 \sigma \quad (3.9)$$

and the large particle limit,

$$\lim_{\frac{a}{\delta} \rightarrow \infty} \langle P_M \rangle \propto \frac{1}{a} \sqrt{\frac{\omega}{\sigma}} \quad (3.10)$$

where

$$\delta = \sqrt{\frac{2}{\omega \sigma \mu}} \quad (3.11)$$

At the size extremes the absorption becomes very small revealing a peak absorption behaviour. Plotting the complex permeability, as a function of the particle-size:skin-depth ratio, results in Figure 3.4. It can be seen that a peak absorption is found when  $a = 2.41\delta$ .

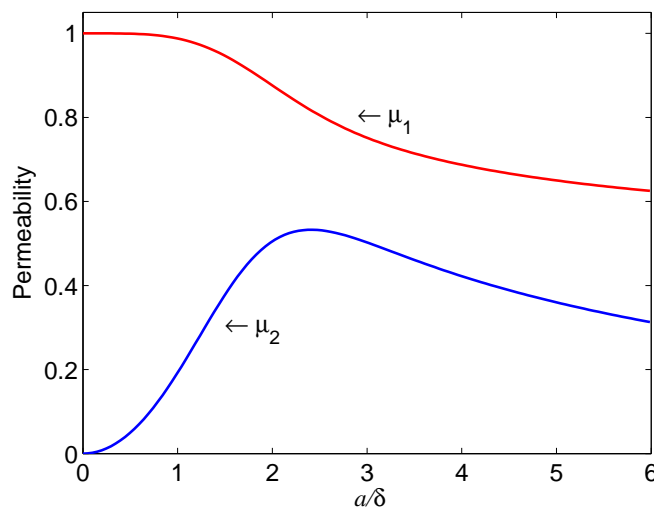


FIGURE 3.4: Theoretical metallic powder complex permeability.

Alternatively, when plotting against particle size for a fixed conductivity, as seen in Figure 3.5, the peak absorption is seen to migrate to bigger particles as the conductivity is reduced.

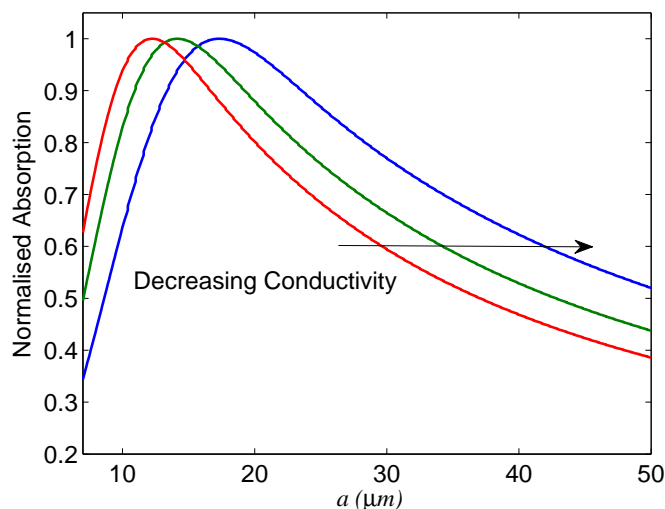


FIGURE 3.5: Normalised metallic powder magnetic absorption for a fixed frequency. The 3 curves represent 3 separate conductivities.

Figure 3.6 below considers the absorption characteristic of particles at some initial conductivity and then at a second, somewhat smaller, conductivity. For the illustration the effect has been exaggerated but it can be seen that, if one considers specific particle sizes, the loss can either increase or decrease as the skin-depth changes. For particles above a certain size, a reduction in conductivity would result in an increase in loss and, conversely, for smaller particles the reduction results in a reduction in loss.

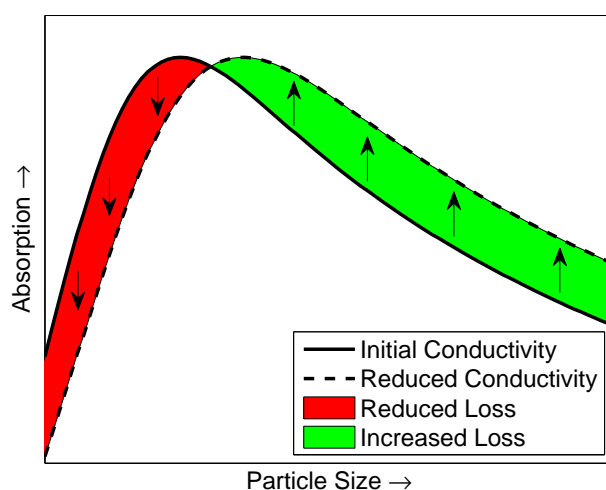


FIGURE 3.6: Changing absorption characteristic for metallic powder as conductivity is reduced.

The above results are calculated simply as a collection of isolated spheres. Therefore, a key assumption is that the particles are arranged suitably sparsely such that local magnetic field corrections caused by particle-particle interactions can be ignored. However, meeting this criterion in reality is difficult due to the nature of the powder itself. Attempts to suspend the powder in some type of setting liquid are unlikely to be successful due to the high density of the individual metal particles, thus leading to particle settling. The relevance of the theoretical predictions are therefore in question. In order to begin to answer this question, a number of COMSOL simulations were conducted as described below in Section 3.3.2.

The second assumption is that all particles are the same size. In reality, any real-world powder will contain a range of particle sizes as described by the particle size distribution. This has the potential to make a significant impact since the characteristic is not symmetric: larger particles may dominate since the loss per unit volume reduces proportional to  $\frac{1}{a}$  in the large case and  $a^2$  in the small case.

A set of predicted values can be obtained by performing a weighted sum of the permeability given by Equation 3.8 over the entire PSD ( $\mu = \sum_{i=0}^{\infty} \mu_i \times f_i$ ). In order to demonstrate the impact this may have on the measurements intended here, this is done for the fractioned Ti6Al4V samples, plotting against the average particle size, and a comparison is made against curves which assume a uniform particle size (Figure 3.7).

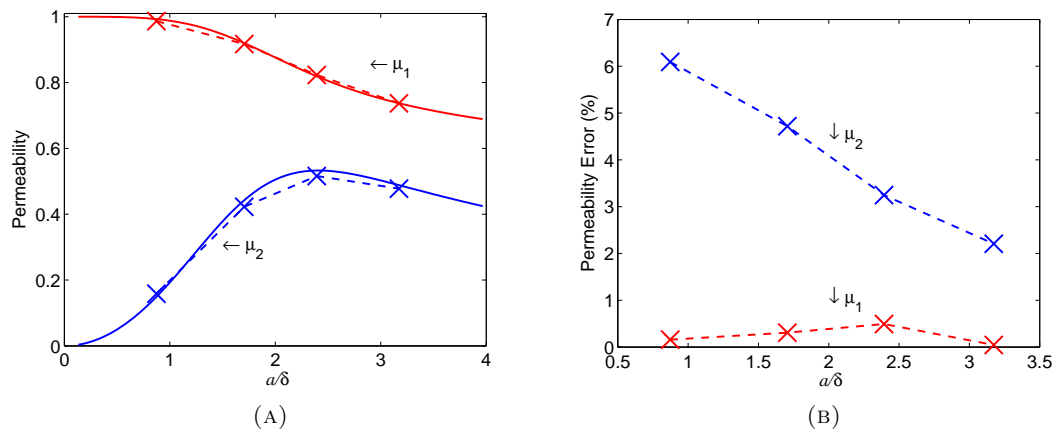


FIGURE 3.7: Comparison of predicted permeability for single particle (solid lines) and when considering a particle size distribution (dashed lines). (A) Raw permeability. (B) Percentage difference of two curves.

It is seen that, for the samples here, the average particle size should generally give a good representation of the response of the particle size distribution. The error, especially in the case of  $\mu_2$  is not insignificant however - becoming easily as large as the expected measurement error.

An additional consideration is that the theoretical analysis assumes perfect packing. Therefore, in order to undertake practical measurements, the sample volume must be modified by the density achieved.

### 3.3.2 Simulation of Metallic Particles in a Magnetic Field

Simulations were undertaken using COMSOL Multiphysics at 2.45 GHz using a quasi-static approximation. A uniform magnetic field of amplitude 1 A/m was applied in a region of space with boundaries kept suitably far away from the particles such that the magnetic field at the boundary is unaffected by local field corrections owing to the particles. This condition mirrors the assumption made when applying first order perturbation theory. All simulations were conducted at 2.45 GHz with particle radius of 20  $\mu\text{m}$  unless otherwise stated. The electrical size of the particles, denoted by the radius to skin depth ratio, is adjusted by changing the particle conductivity and not the particle size itself. This ensures the number of meshing elements within the volume is kept constant.

The first step involved simulating a single particle. Figure 3.8 shows the dipole field caused by an individual particle and the induced currents. Figure 3.9 shows the result for a single, 20  $\mu\text{m}$ , simulated particle showing good agreement between the theory and simulation.

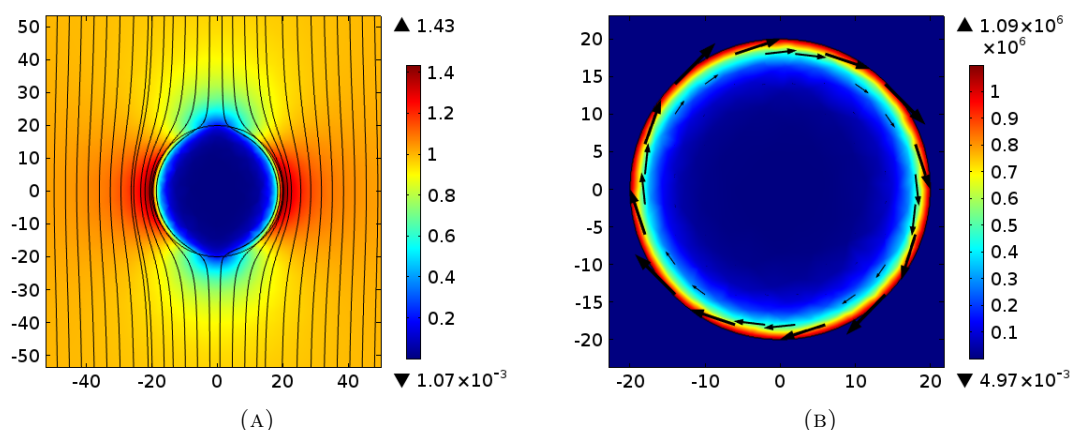


FIGURE 3.8: Single particle magnetic simulation. Dimensions in  $\mu\text{m}$  (a) Magnetic field distribution, field applied in Y direction. (b) Induced current, field applied out of the page.

Extracting the absorption from the model and comparing with theory results in Figure 3.9. As can be seen, very good agreement between absorption and theory is seen in this single particle case.

The simulations are not intended to completely characterize the absorption for multi-particle systems but simply give an indication of their behavior. In order to characterize the absorption empirically, many different packing schemes would need to be considered as well as various field orientations. However to begin, the interaction of two particles is considered.

The interaction between two particles can have one of two opposing effects. If the field is applied in a direction perpendicular to a line which passes through the centre of the

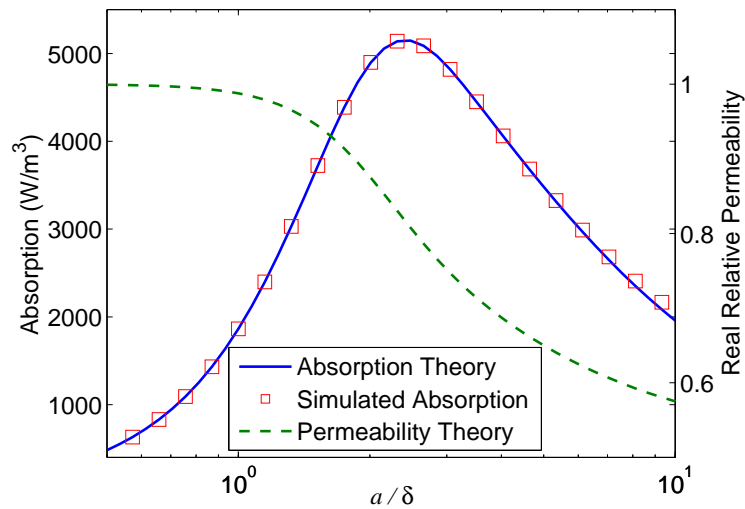


FIGURE 3.9: Simulated and theoretical single particle magnetic absorption.

particles, an increase in loss is observed. Conversely, applying field parallel to this line causes a reduction in loss. This is an intuitive result given the dipole field created by the individual particles. In the perpendicular orientation, the particles are placed within a region of increased field and, in the parallel orientation, a reduced field. In order to quantify this effect, the relative absorption was observed as two particles are moved closer together. The results, for particles 5 times bigger than the skin depth, can be seen in figure 3.10. The change in loss, with touching particles, as the particle size changes can be seen in Figure 3.11. As expected, the effect is reduced in smaller particles, with the relative loss approaching 1 as the particles become smaller than the skin depth. These results demonstrate the complex nature of particle-particle interactions.

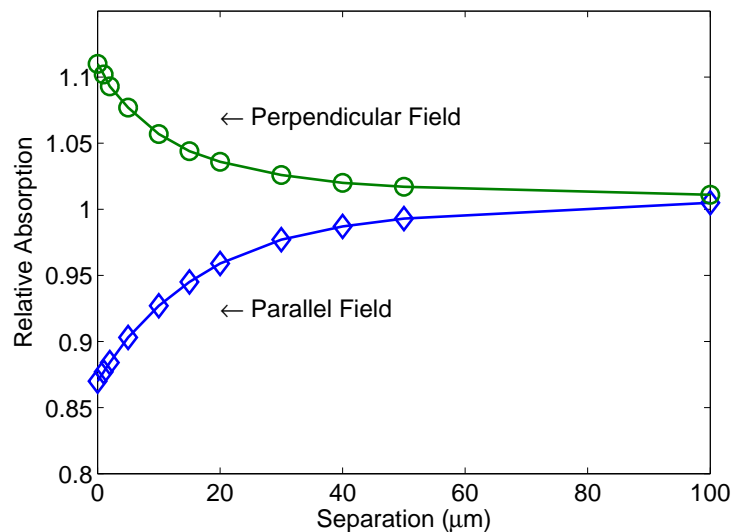


FIGURE 3.10: Relative magnetic absorption as two spheres are brought close together,  $a/\delta = 5$  at 2.45 GHz,  $a = 20\mu m$

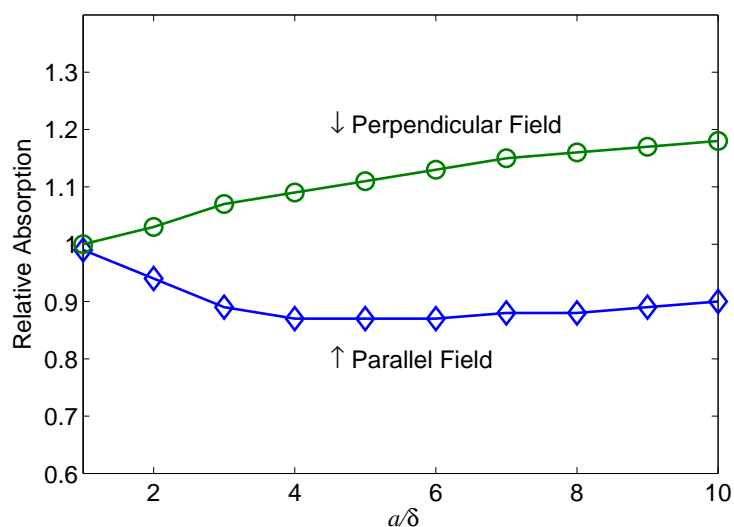


FIGURE 3.11: Relative magnetic absorption of two adjacent spheres as a function of the particle size.

Whilst, as previously mentioned, a complete analysis of packing schemes is not undertaken, in the first instance, a simple hexagonal close packed (HCP) system was used as it gives a relative packing density close to what was measured during future experimentation ( $\sim 0.6$ ).

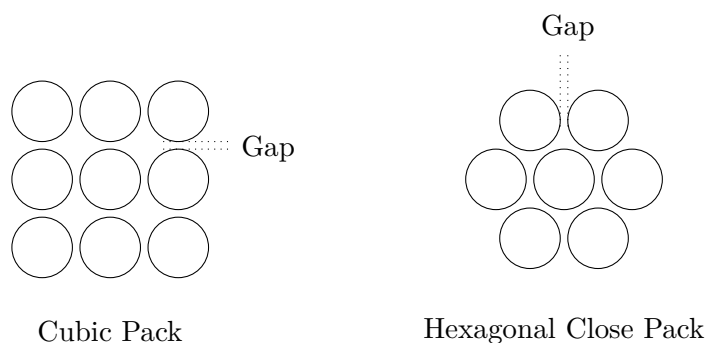


FIGURE 3.12: Packing Schemes

The simulation considers a hexagonally close packed matrix of 216 particles (i.e. a  $6 \times 6 \times 6$  array). This array is as large as practically possible given the computing limitations available. The generated particle agglomeration can be seen in Figure 3.13. Note the axis directions, which are referred to later. The HCP planes are stacked in the  $z$  direction.

Four distinct conditions are considered: the field applied in either  $x$  or  $z$  direction and with the particles either touching or with a  $0.1\mu\text{m}$  gap separating all particles. The  $z$  direction indicates field application perpendicular to the 6 HCP planes. Figure 3.14 shows the result of these simulations with the touching a separated cases showing distinct results. With small inter-particle separation, the measured absorption closely resembles the profile predicted by the earlier theory. This is enabled by total magnetic field penetration in the space between particles.

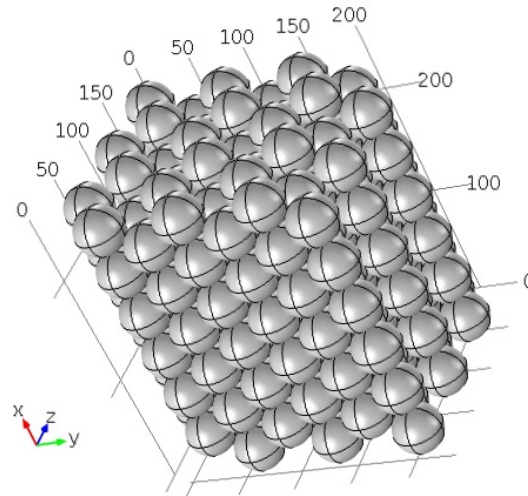


FIGURE 3.13: HCP particle array generated for COMSOL simulation.

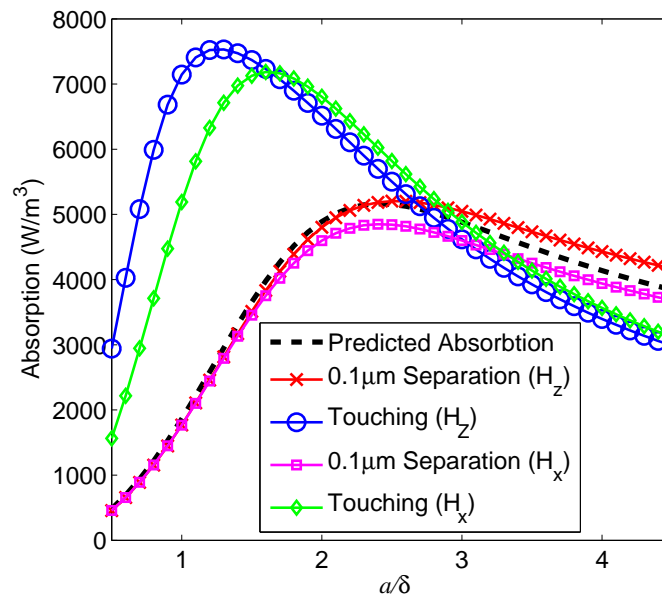
FIGURE 3.14: Simulation results based on the 216 sphere HCP array. The subscript denotes the direction of the applied magnetic field. Cases where the particles touch and are separated by  $0.1\mu\text{m}$  show distinct results.

Figure 3.15 shows the magnetic field distribution in the cross section drawn through the middle of the particles in both the separated and touching cases. The radius is 6 times the skin depth and the magnetic field is applied in the  $z$  direction, i.e. perpendicular to the plane of the image. The separated case can be seen to allow total field penetration. However, with no separation, electrical contacts between particles enable macro currents to flow in the agglomeration. These currents screen the inner particles and cause a different absorption characteristic. This can be interpreted as the small particles combining to effectively increase the particle size and, due to the voids effectively trapped by the touching particles, the peak absorption per unit volume is increased.

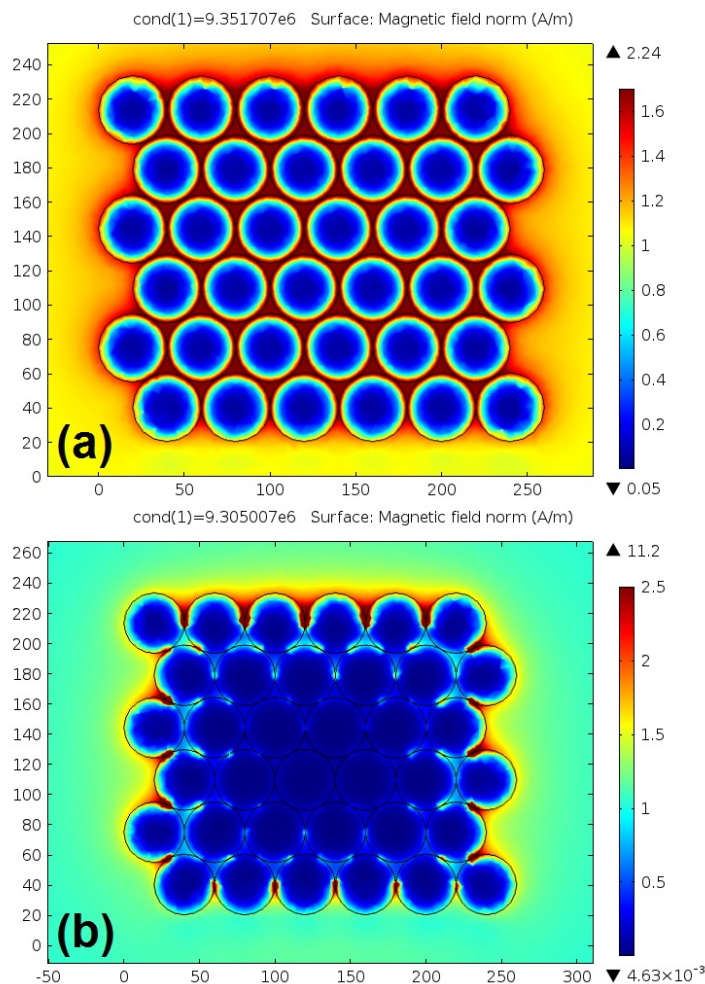


FIGURE 3.15: Magnetic field strength cross-section in  $xy$  plane taken through the third HCP layer.  $a/\delta = 6$ . Field applied in  $Z$  direction (out of the page). (a) Separated spheres. (b) Touching spheres.

It is important to note that these currents flow in a perpendicular direction to the applied magnetic field. Therefore, only contacts made in the direction perpendicular to the applied field contribute to the overall screening affect. This can be demonstrated by considering the same 216 particle matrix with the field applied in the  $x$  direction but with the HCP planes slightly separated, thus eliminating any electrical contacts in the  $z$  direction. Figure 3.16 shows the absorption characteristic which closely matches the theoretical prediction. The significance of the result is thus: Since the compressive weight of the powder will cause electrical contacts to form above and below the particles, as long as the magnetic field is applied along the same direction as gravity, these contacts will be relatively inconsequential.

A further interesting effect is also observed when considering small particle agglomerations. A touching  $3 \times 3 \times 3$  HCP was constructed and simulated with field applied in the  $z$  direction. Figure 3.17 shows the results and, in contrast to the larger case, the per unit volume absorption still exhibits a peak in a similar location but the absorption is significantly increased in magnitude.

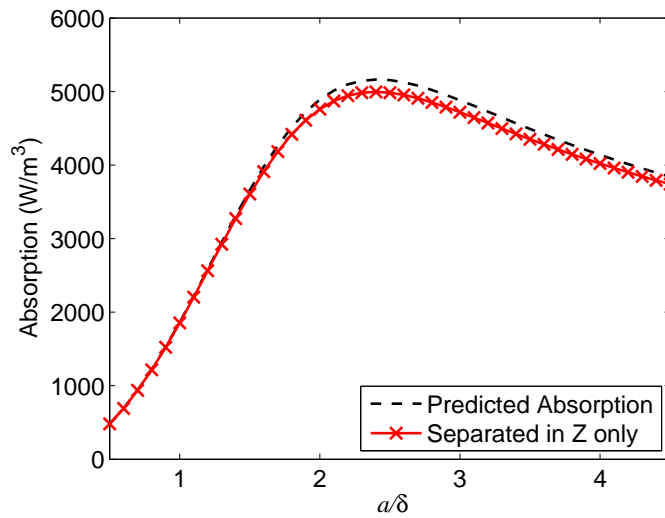


FIGURE 3.16: Simulated magnetic absorptions based on the 216 particle HCP array compared to the predicted absorption for a single particle. Stacked layers have been separated but particles touch within each layer. Magnetic field is applied perpendicular to the layers and it is therefore shown that only particle contacts perpendicular to the applied magnetic field are significant.

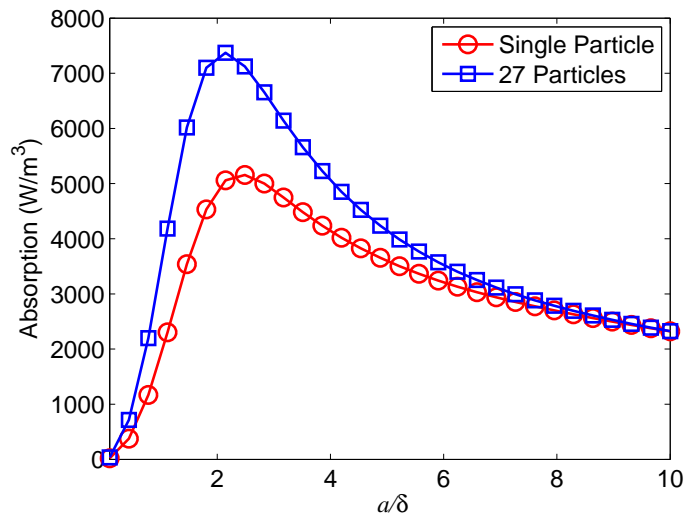


FIGURE 3.17: Comparison of single particle absorption and simulated magnetic absorption based on a tightly packed  $3 \times 3 \times 3$  HCP particle matrix.

To conclude the initial simulation study, it is hypothesized that, as long as electrical contact is not made between particles, a relatively large group of closely packed particles will share the absorption behaviour of a single particle up to (and close to) the absorption peak. The isolation between light particle contacts in the plane perpendicular to the magnetic field can be provided by the native oxide layer that will be present on the surfaces of many metal particles. It is not expected that this oxide layer itself will contribute significantly to the magnetic absorption, as reported previously [116]. In addition, if small conducting groups are formed, an increase in absorption is expected.

Similarly to previous studies [118, 96], an effort was made to simulate an infinitely large configuration by utilizing the simple symmetry of a cubic close packed system and a periodic boundary condition (density = 0.52). Figure 3.18 shows the 3D model created for simulation where the excitation ports are placed at the y limits and a periodic condition applied at the x and z limits. As defined by the periodic boundary conditions, the simulation is continuous across the x and z boundaries. In the y direction, the simulation is finite. Simulations of up to 4 layers in this direction are considered, where the number of layers is denoted by N. The boundaries at y are places sufficiently far away such that they do not influence local field distortions caused by the particles. Adjusting the distance between the particles and simulation boundary did not significantly affect simulation results.

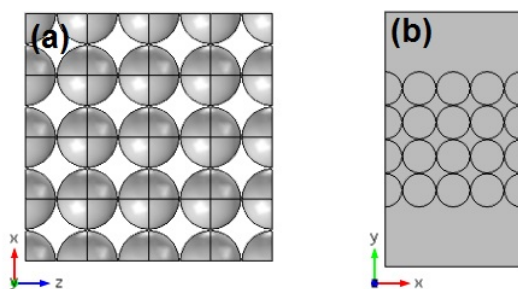


FIGURE 3.18: Cubic close pack 3D simulation model with periodic boundaries across x and z showing the maximum 4 layers.

The absorption, presented as the average absorption in the center  $9 \times N$  particles, is shown in Figure 3.19. It can be seen that, while the curves retain the approximate characteristic shape of absorption, significant reduction of loss is observed as the particles increase in size. This result is similar to the previously cited studies. Whilst a slight decrease in absorption can be seen for 1 layer, subsequent simulations show a very similar results, thus adding confidence that the result is scalable to larger geometries.

A slightly different approach can be taken by utilising the various effective medium theories such as Buchelnikov et al. 2008 theory and subsequent experimental paper [119] [114]. Using a core-shell model, they predict significant penetration into  $74\mu\text{m}$  iron powder with 0.375 relative density at 2.45GHz. The penetration is strongly dependent on the oxide shell thickness. This is perhaps expected due to its role in keeping conducting cores separated and allowing the magnetic field to penetrate the particle matrix. Although the field does penetrate to some extent throughout the sample in most cases, its magnitude is significantly reduced even 1mm into their 10mm thick sample. This is congruent with the periodic simulation where total absorption can be expected to be reduced compared to the isolated sphere case.

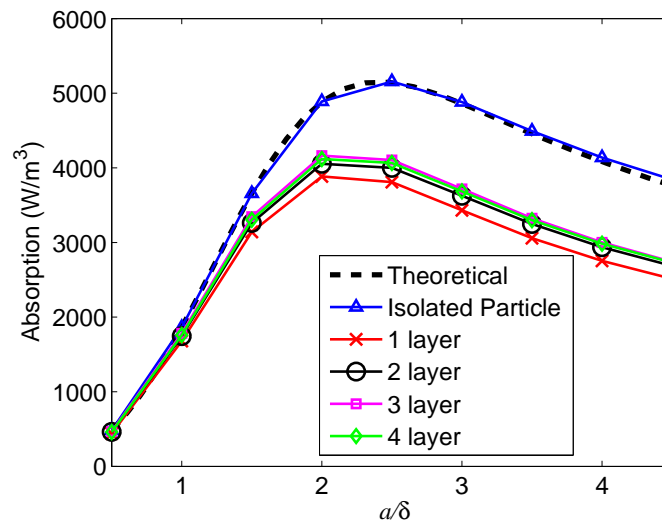


FIGURE 3.19: Multi-layer cubic close pack periodic simulation of magnetic absorption.

### 3.3.3 Experimentation

The cavity used was cylindrical in design with an internal radius 4.75cm and height 4cm, machined from aluminium. Shown in Figure 3.20.

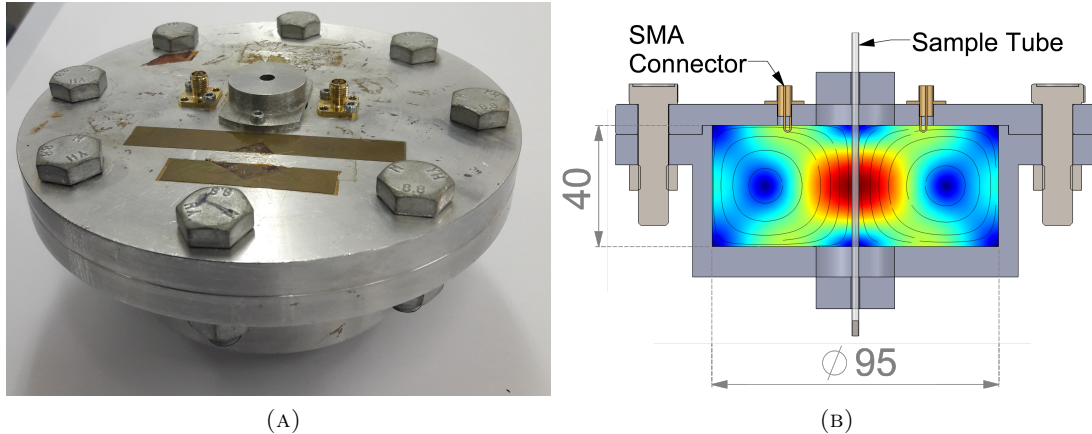


FIGURE 3.20: Cylindrical cavity used for measurement. (a) Photograph. (b) Schematic cut-away showing sample in situ and simulated  $TE_{011}$  magnetic field distribution.

A hole is placed on its axis, as discussed in Section 2.6.4, with suitable RF chokes at either end, to act as a mode trap for degenerate TM modes (explicitly  $TM_{111}$ ,  $TM_{112}$  and  $TM_{122}$  in this case). Cavity coupling was achieved using two near-identical, co-axial loops fed through the flat, top cavity surface. Resonator Q and resonant frequency were obtained, simultaneously, from all the modes, from measurements of the voltage transmission coefficient  $S_{21}$  in the frequency domain using an Agilent PNA-L (N5232A) utilizing a circle and linear fit strategy, as detailed previously.

Furthermore, in order to provide further verification, measurements were taken with varying metal conductivity by elevating the temperature. The sample and cavity were placed entirely in an oven (Mettler UF30Plus) and the temperature risen slowly to 150°C and back to room temperature over 5 hours ensuring uniform heating in the sample and cavity. Cavity temperature correction was done using a baseline measurement obtained by measuring the cavity response during the heat ramp without a sample. The temperature was measured using a PT-100 RTD platinum resistance thermometer, in contact with the metal cavity surface.

### Measurement Modes

In order to more thoroughly investigate the theory, it is advantageous to test over multiple frequencies. This can be achieved by utilising different resonant modes. A summary of these modes is listed in Table 3.5. The values for of the mode scaling co-efficient were calculated using COMSOL.

Mode	Frequency (GHz)	$Q_0$	$G_{\text{nmp}}$
TE <sub>011</sub>	5.36	20062	0.284 ± 0.006
TE <sub>012</sub>	8.39	17917	0.490 ± 0.01
TE <sub>022</sub>	10.2	26711	0.128 ± 0.003

TABLE 3.5: Magnetic measurement mode summary

### Results

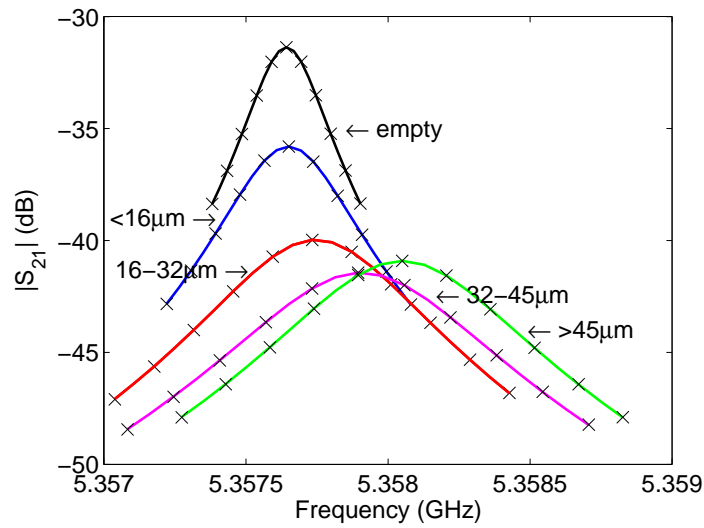
The samples with 1mm inner diameter were used as it was found that the  $Q$ , especially for the higher order modes, became too low such that measurement became difficult and the error large for the larger samples.

The measurement traces for the TE<sub>011</sub> mode can be seen in Figure 3.21.

After performing the perturbation analysis, the absorption results, plotted as both imaginary permeability and an absorption per unit volume and alongside curves generated by the previous theory, can be seen in Figure 3.22. In order to calculate the absolute absorption  $H_0$  was set at 0.002654 Am<sup>-1</sup> so as to be equivalent to a 1 Vm<sup>-1</sup> electric field as defined by  $H = E/\eta_0$  where  $\eta_0 = 376.7\Omega$  is the wave impedance of free space. The model appears to accurately predict the absorption profile of the powder. The absorption peak is observed and is seen to be at a fixed skin depth ratio.

Data for the real relative permeability, plotted alongside a set of theoretical curves, are shown in Figure 3.23.

Additionally, Figure 3.24 shows the changing relative absorption of the powder as it is heated and its conductivity reduced. Theoretical curves were constructed given the

FIGURE 3.21: Fractioned Ti6Al4V TE<sub>011</sub> measurement traces.

temperature co-efficient of conductivity for Ti6Al4V as  $0.0004 / ^\circ\text{C}$  and an initial, room temperature, conductivity of  $6 \times 10^5 \text{ S/m}$ . As predicted by the model, with decreasing conductivity and, as a result, an increasing skin depth, the smaller particles show reduced absorption and the larger particles increased absorption.

During heat treatment in the oven no visible change was seen in the powder.

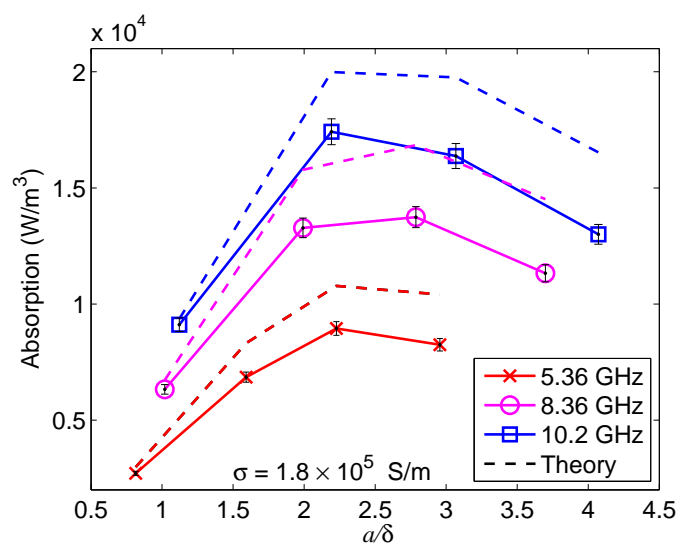
In order to experimentally verify the significance of the oxide layer, significant oxidation of the powder was required. To achieve this it was heated using a small butane torch for approximately 2 minutes in an open glass vial. The flame was moved across the entire surface in an attempt to uniformly heat the powder.

The effect of the heat treatment can be seen in a colour change of the powder from grey to brown.

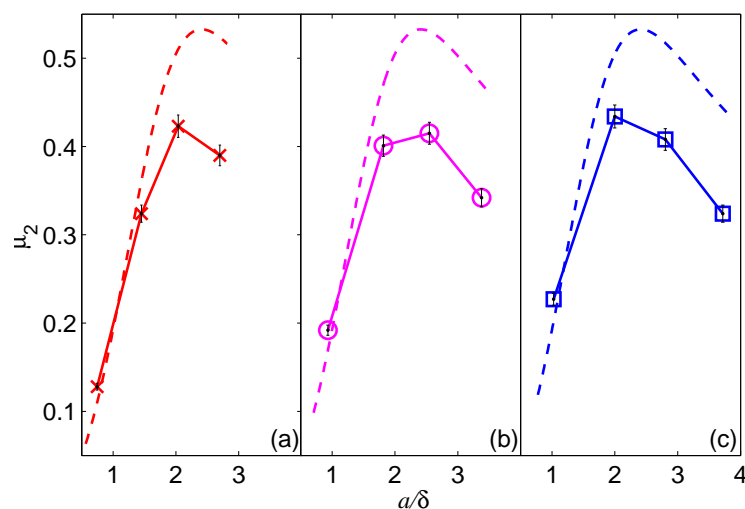
Sample	Before Treatment (Grey)		After Treatment (Brown)	
	$\mu_2$ (5.35 GHz)	$\mu_2$ (8.38 GHz)	$\mu_2$ (5.35 GHz)	$\mu_2$ (8.38 GHz)
1	$0.128 \pm 0.004$	$0.192 \pm 0.006$	$0.130 \pm 0.004$	$0.200 \pm 0.006$
2	$0.324 \pm 0.010$	$0.401 \pm 0.013$	$0.322 \pm 0.013$	$0.404 \pm 0.02$
3	$0.423 \pm 0.014$	$0.415 \pm 0.014$	$0.420 \pm 0.02$	$0.417 \pm 0.02$
4	$0.390 \pm 0.013$	$0.342 \pm 0.011$	$0.389 \pm 0.015$	$0.342 \pm 0.014$

TABLE 3.6: Standard and heat treated Ti64 fractioned samples.

Table 3.6 show the loss measured before and after treatment. No significant change in loss was observed. This is inline with the predictions made by Ignatenko and Tanaka [116]. The oxide layer itself has very low magnetic loss and is not thick enough to make any significant effect on eddy current losses in the metal itself.



(A) Absorption per unit volume assuming  $0.002654 \text{ Am}^{-1}$  applied field.



(B) Imaginary permeability. (a)  $\text{TE}_{011}$ . (b)  $\text{TE}_{012}$ . (c)  $\text{TE}_{022}$ .

FIGURE 3.22: Measured magnetic absorption of fractioned Ti6Al4V powder samples.

Finally, the raw measurement data can be seen plotted against the average particle size for the samples of base powder mixed with fraction 1 in Fig. 10. Since the conversion to permeability is not undertaken, the error in cavity calibration (mode scaling constant) can be ignored. Also, in this small particle size range, the relationships between particle size and measurement parameter can be assumed linear. This plot shows the potential for highly accurate measurements as is further discussed later.

### 3.3.4 Discussion

The frequency shift and resultant real permeability shows a strong negative trend with increasing particle size. Within this range, the values appear consistent with those

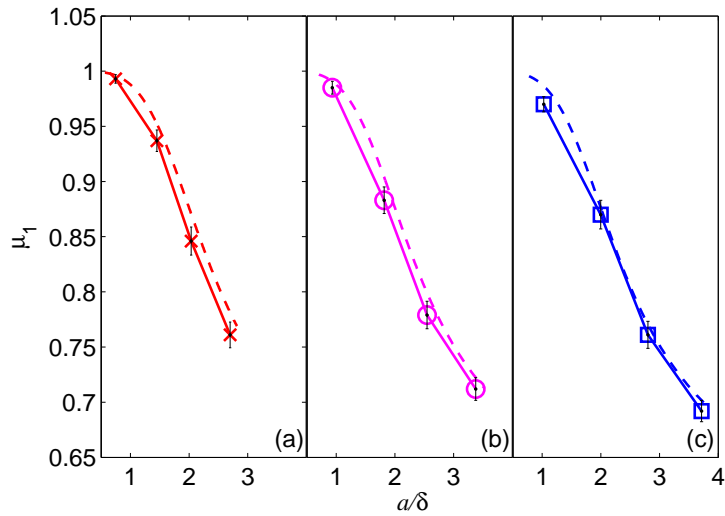


FIGURE 3.23: Real permeability of fraction Ti6Al4V powder samples. (a)  $TE_{011}$ . (b)  $TE_{012}$ . (c)  $TE_{022}$ .

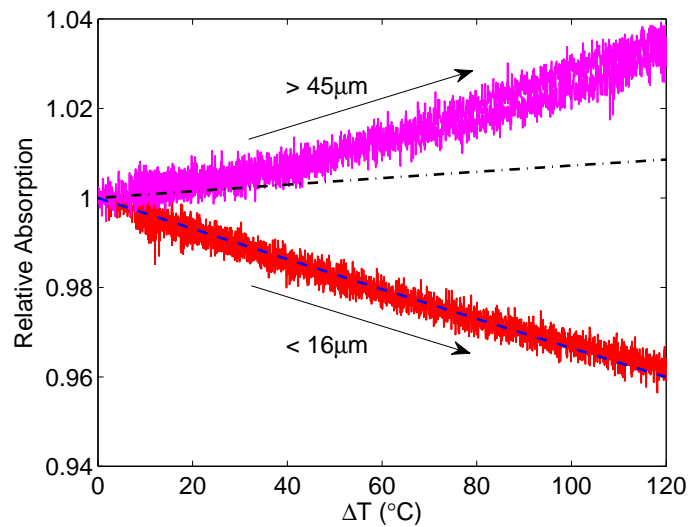


FIGURE 3.24: Measured changing magnetic absorption of powder samples as temperature is changed in-situ. Measured using the cavity's  $TE_{011}$  mode at 5.35GHz

predicted by the presented theory.

The measured loss values also show strong correlation with the theory. Figure 3.27 shows the measured relative absorption compared with the single theoretical isolated particle case. A curve is also given showing the result of the periodic simulation. Consistent with the simulation, the larger fractions show relatively reduced absorption with increased particle size. However, the smaller fraction, where the majority of particles are below the skin depth limit, do not follow the trend exhibiting enhanced absorption per unit volume.

This outlier can be explained by the previously mentioned differences of this powder fraction. Firstly, the particles have a tendency to cluster together. Assuming these



FIGURE 3.25: Ti6Al4V colour change after heat treatment under a small butane torch.

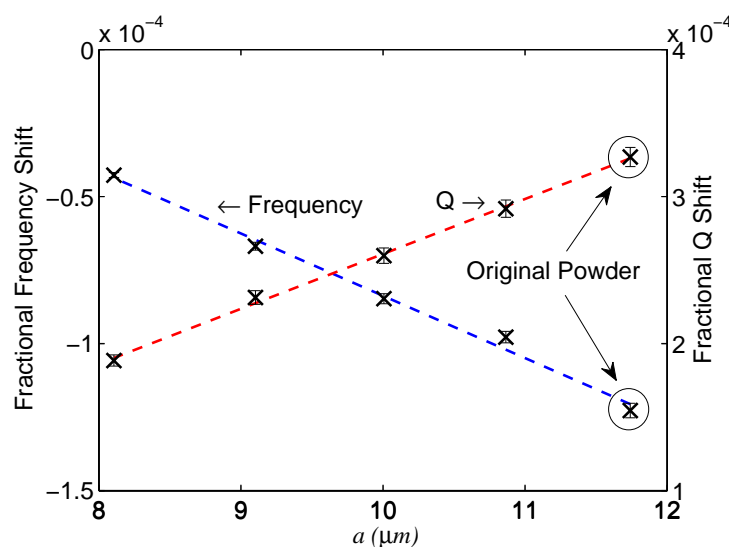


FIGURE 3.26: Raw measurement, using  $\text{TE}_{011}$ , of the various powders created by mixing the base powder with fraction 1 showing the sensitivity of the measurement to small changes in average particle size. A linear fit is made through the points in order to extract the sensitivity gradient.

clusters form electrically connecting networks, the result of this is an increased effective particle size without, however, a corresponding increase in weight. Therefore, the absorption per unit volume is seen to increase. This effect was demonstrated in the earlier simulation in the case of touching particles. Secondly, this fraction has a concentrated proportion of very small particles many of which are small pieces of debris formed during the gas atomization process. Particles forming this debris are less likely to be spherical in nature and therefore less likely to conform to theoretical predictions.

Comparing the two temperature dependency plots given in Figure 3.24, the small particle case can be seen to closely match the predicted trend. The larger particle case, although initially following the prediction, proceeds to exhibit enhanced absorption. This is a surprising result but one that can be explained by the earlier simulation. During heating, the particles will thermally expand. Although this expansion is relatively small, not causing significant change to the electrical size, it will cause an increased density of electrical contacts. The increased density of contacts is not sufficient to cause

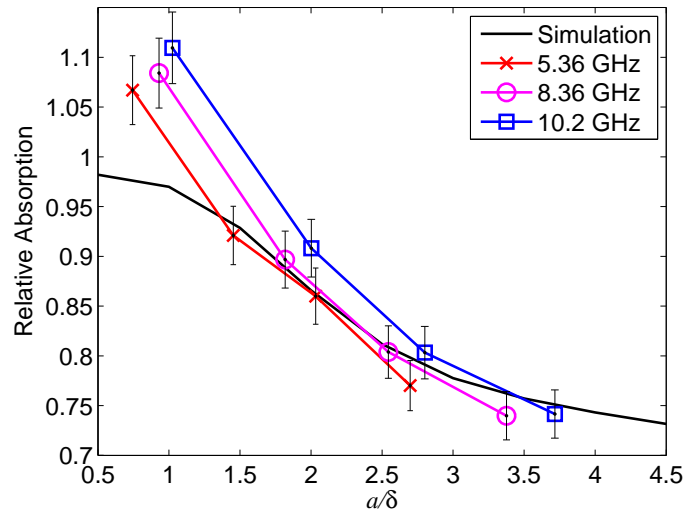


FIGURE 3.27: Relative absorption of powder samples compared to the theoretical single particle case. Simulation data taken from periodic cubic close pack COMSOL simulation.

a reduction of the absorption caused by screening but the contacts create small particle agglomerations which show increased absorption per unit volume, as demonstrated by the earlier simulation. It is expected that this behavior will be strongly dependent on the sample container geometry.

Next the measurement sensitivity is considered. It is not fixed across the range of particle sizes measured since the permeability gradient is a function of particle size itself. However, an approximate sensitivity limit for this measurement setup can be calculated by plotting the raw measurement parameter (relative frequency Q shift), simply corrected for density, against the particle size, taking the gradient and multiplying by the measurement error. The typical raw error is very small,  $\pm 5$  for the Q and  $\pm 10$  Hz for the frequency leading to errors, in the worst case for these measurements, of 0.1% and 0.01% respectively. However, this does not account for sample preparation errors, which form the majority of uncertainty here, such as inaccurate density and sample volume. Conservatively placing an error of 2% on the perturbation results, for TE<sub>011</sub>, the measured sensitivity is approximately  $\pm 0.14 \mu\text{m}$  and  $\pm 0.080 \mu\text{m}$  for the Q and frequency method respectively in the centre of the measured range.

As stated, these measurements give only an indication on the fundamental limits of sensitivity. Careful design of the measurement system can maximise the achieved sensitivity.

Examining Figure 3.28, which shows the rate of change of permeability plotted against the skin depth normalised particle size, reveals the points of maximum permeability gradient and therefore greatest sensitivity. Depending on the desired measurement, the resonator frequency would be chosen, considering the bulk metal conductivity and particle sizes, to ensure the measurements coincide with these points.

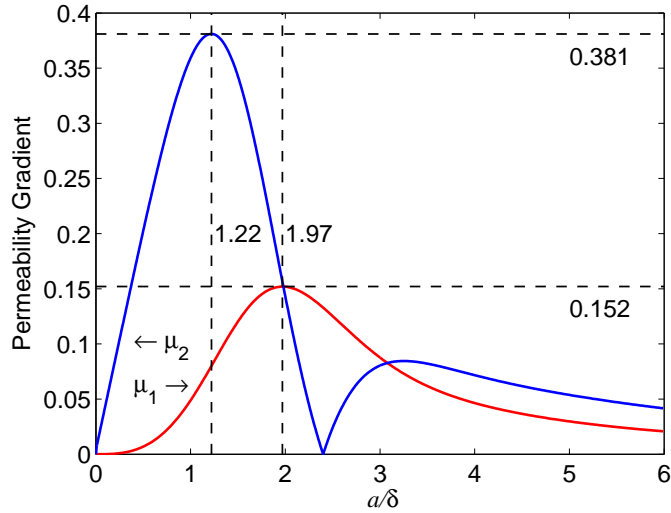


FIGURE 3.28: Theoretical rate of change of real and imaginary permeability with changing particle size. The peak value, along with its corresponding particle size, is labelled.

Using this information, the potential sensitivity for a system similar to the one implemented here is estimated but optimised to exploit the peak permeability gradient. Assuming ideal sample preparation the theoretical sensitivity limit for this titanium powder becomes  $0.007\mu\text{m}$  for the Q method (at 4.95 GHz,  $a = 11.7\mu\text{m}$ ,  $a/\delta = 1.22$ ) and  $0.003\mu\text{m}$  (at 12.0 GHz,  $a = 11.7\mu\text{m}$ ,  $a/\delta = 1.97$ ) for the frequency method.

Further increases could be sought by maximising the resonator disturbance by increasing initial resonator Q and sample size. However, care must be taken when increasing the sample size so that the Q does not drop near the noise floor of the measurement instrument and dramatically increase the measurement uncertainty.

## 3.4 Electric Field and Permittivity

### 3.4.1 Theory and Background

Similarly to that seen Section 3.3.1, by solving for the dipole field of a conducting sphere in an electric field equations can be formed which describe how the electric field losses vary with particle size and frequency. A key assumption of this analysis is that the particles are sufficiently sparse such that any local field corrections can be ignored.

$$\langle P_E \rangle = -\frac{3}{4}\omega\epsilon_0 E_0^2 \Im \left( \frac{(2\epsilon + 1)(1 - kacot(ka)) - (ka)^2}{(\epsilon - 1)(1 - kacot(ka)) + (ka)^2} \right) \quad (3.12)$$

Unlike the magnetic case, no particle size dependent absorption peak is seen. The absorption behaviour can be seen in Figure 3.29.

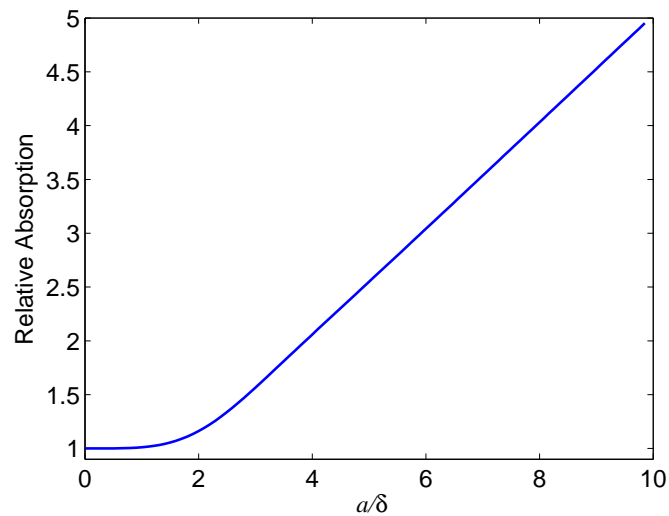


FIGURE 3.29: Relative theoretical electric field absorption with increasing particle size, plotted independent of frequency.

In the same range, the real component of the electric dipole moment is nearly static, changing by less than  $10^{-5}\%$ .

### 3.4.2 Initial Experimentation

Since interest now lies in the electric field response, experimentation was undertaken using the  $TM_{010}$  mode of a cylindrical cavity resonator. The cavity had a radius of 4.6cm and a height of 4cm. Coupling was achieved using identical straight antennas placed on the top surface and is shown in Figure 3.30.



FIGURE 3.30: Aluminium  $TM_{010}$  measurement cavity used for electric field measurements.

Numerous preliminary perturbation experiments were conducted using the powder described in Section 3.2. However, the behaviour of the metal powder was found to be

chaotic and measurements were not repeatable. For instance mechanical agitation of the powder causes the  $Q$  to vary significantly: from  $\sim 8000 \rightarrow 10$ .

In order to understand this behaviour, the problem can be considered in two different ways. Firstly, a model which simplifies the geometry and considers a cylindrical sample of varying conductivity. Secondly, a complex model which considers the interaction of the individual particles.

Let us first consider the simplified geometry case.

In some cases, introducing a metal rod along the axis of a cavity cannot be viewed as a traditional perturbation due to the boundary condition the metal enforces. Since the potential along a metal surface must be constant, that the tangential electric field at the metal boundary must be zero. In the case of  $TM_{010}$ , where the electric field only has components along the length of the cylinder, the addition of a metal rod along the axis will stop this mode from propagating.

This can be demonstrated in simulation. Figure 3.31 shows the frequency and  $Q$ -factor for  $TM_{010}$  for the 2.5GHz measurement cavity (4.6cm radius) perturbed by a 2mm rod of varying conductivity. Initially as the conductivity increases, the  $Q$  and frequency reduce as is expected. At conductivity of approximately 1000 S/m, the trend reverses and the frequency and  $Q$ -factor increase. The large frequency change and  $Q$  recovery can be attributed to the excitation of a separate co-axial  $TM$  mode. In this limit, perturbation theory can be regarded as no longer valid. The field distribution for this limit can be seen in Figure 3.32. It is noted that the  $Q$ -factor drops to unmeasurable values.

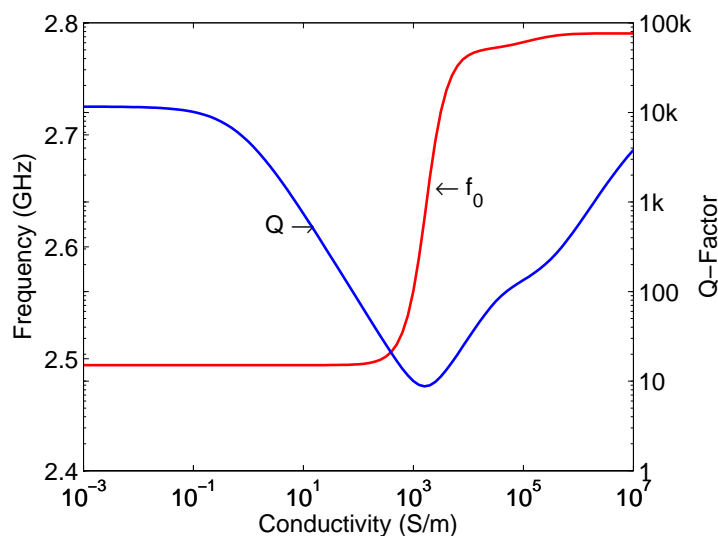


FIGURE 3.31: Simulated  $TM_{010}$  frequency and  $Q$  of cavity perturbed by a 2mm rod perturbation.

These observations lead to a hypothesis for the powdered samples. In some samples, percolating molecule chains form along the length of the tube which cause the effective conductivity to rise above the critical limit.

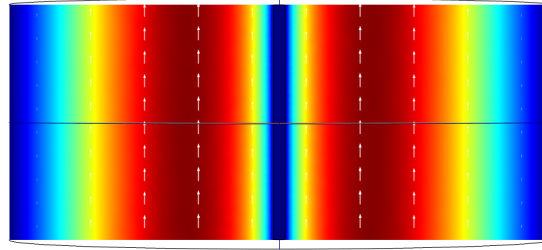


FIGURE 3.32:  $TM_{010}$  E-field as the result of a on axis perturbation of a 2mm rod. The rod conductivity was set at  $10^5$  S/m.

Since the coaxial TM mode is not seen above the unperturbed mode, it suggests the sample's effective conductivity resides near this critical value as described in Figure 3.31.

Figure 3.33 shows a simple comparison between experiment and simulation when lowering a 'lossy' (one where the Q drops very low) sample into a  $TM_{010}$  resonant cavity. For the simulation, the conductivity of the rod was set to  $10^3$  S/m. The experimental data shows similar results to the simulation but offset by 15mm. This is an interesting result as it shows that percolation is likely present in the lossy sample but not along its entire length.

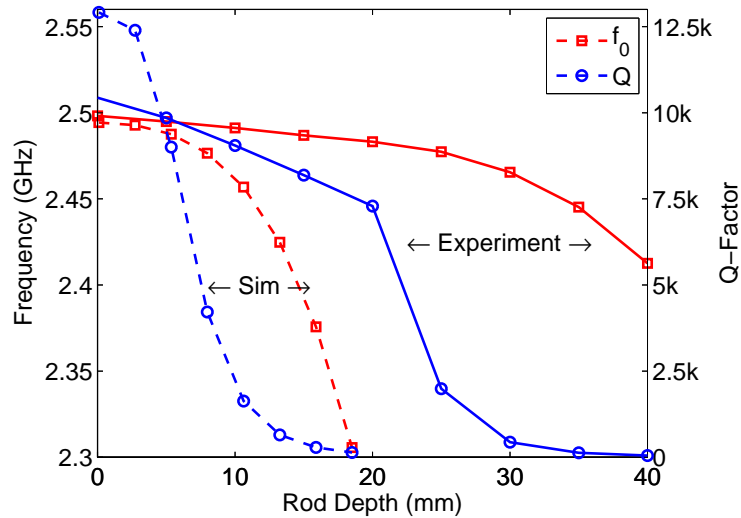


FIGURE 3.33:  $TM_{010}$  resonator parameters as 2mm rod is lowered into the cavity. Experimental results obtained with Ti6Al4V filled quartz tube. Simulated rod conductivity is set to  $10^3$  S/m.

### 3.4.3 Temperature Measurements

A logical step in the investigation of the percolation phenomena is to consider the behaviour of the powder when heated. The expansion in radius,  $a$ , is given by

$$\Delta L = a_0 \alpha \Delta T \quad (3.13)$$

The co-efficient of thermal expansion,  $\alpha$ , can vary dramatically with temperature depending of phase and structure changes, however, in the range 0-300°C it is assumed to be constant as this is well below the  $\beta$ -transus temperature [120]. For a 200°C rise, a particle of radius 11.7 $\mu\text{m}$  will expand by 21nm - a value approximately 4 times the expected oxide layer thickness.

A moderate, 200°C, temperature rise will not lead to dramatic changes in conductivity but could cause increased effective conductivity through percolation caused by thermal expansion. For Ti6Al4V, the temperature co-efficient of resistivity is established at 0.0004 K<sup>-1</sup>[117], therefore, conductivity will rise by  $\sim 400\,000\text{ Sm}^{-1}$  over this range. This change would only represent a  $\sim 7\%$  change in loss according to Equation 3.12.

The principle can be demonstrated by considering the behaviour of the bulk DC conductivity. Figure 3.34 shows the experimental setup used. Whilst it is not possible to obtain an accurate measurement of conductivity using this method due to the dominance of the contact resistance with the probes [59], Figure 3.35 shows a sample result demonstrating the sharp rise and abrupt cessation of sample current indicating electrical percolation. The probe distance,  $x$ , was set at 10mm, the excitation voltage was set to 10V and the sensing resistor used was 491.3 $\Omega$  (as measured using an Agilent DMM). The IR temperature probe was a Micro-Epsilon Thermo Meter CT. The sample internal diameter was 2mm.

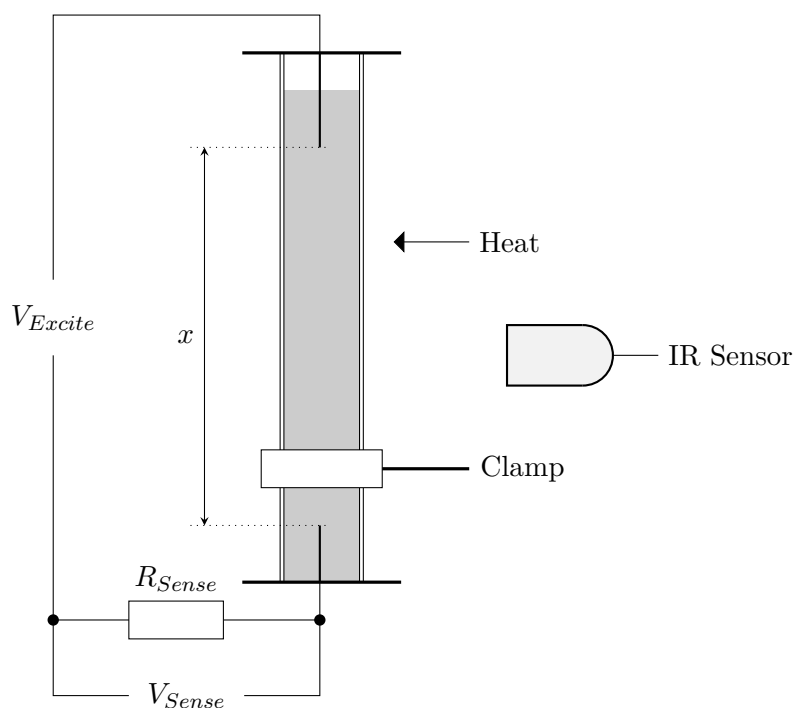


FIGURE 3.34: Experimental setup used to measure DC conductivity as powder sample is heated.  $x = 10\text{mm}$  and tube diameter = 2mm.

Subsequently, a more controlled experiment was conducted to accurately assess the percolation behaviour of the powder. The response of a standard sample of Ti6Al4V was

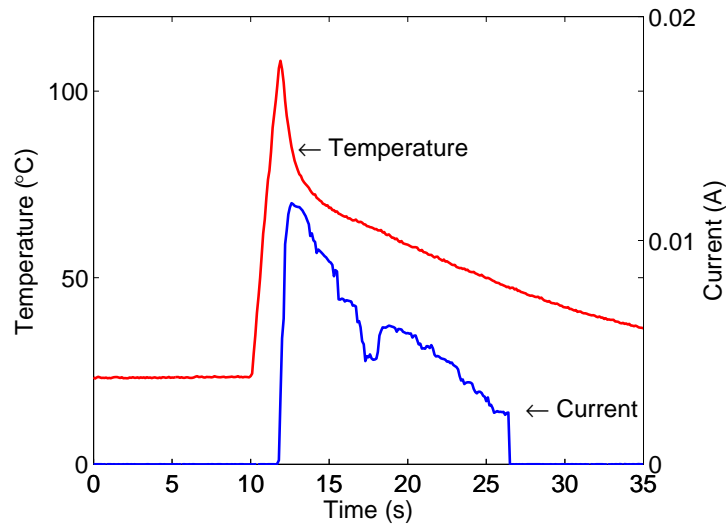


FIGURE 3.35: Measured DC current in column of Ti6Al4V powder as the result of raised temperature.

obtained between 20-200°C by measuring  $TM_{010}$  within an oven using the temperature correction techniques described in Section 2.10. Figure 3.36 shows the frequency shift across the range, taken from the initial temperature. There is a small change until a clear transition at approximately 120°C. It is assumed that it is at this point that some percolation initially occurs.

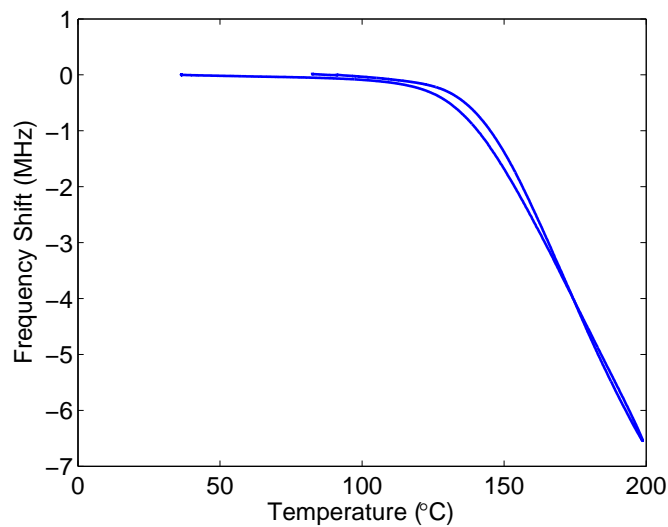


FIGURE 3.36: Measured  $TM_{010}$  frequency shift for powder sample as temperature is raised. Measurements conducted in-situ within an oven.

This experiment was repeated over a total of 10 annealing cycles and plotted in Figure 3.37. Two features have been highlighted with arrows and labeled (1) and (2). Firstly, after an initial drop during the first cycle, gradual increased shift at low temperature and, secondly, a gradually smaller maximum shift at elevated temperature. It is proposed that this first new behaviour is the result of increasing sample sintering and the second the

result of gradual oxidation of the particles preventing electrical contact in the expanded, hot, case.

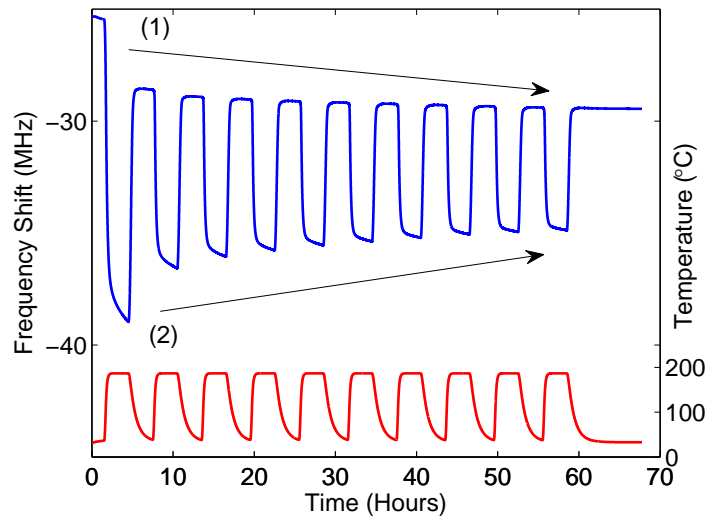


FIGURE 3.37:  $TM_{010}$  frequency shift for powder sample during 10 annealing cycles undertaken in an oven. Effect of sample sintering labelled (1) and an increasing oxide layer labelled (2).

Further understanding was gained by taking a standard sample of Ti6Al4V and rapidly heating it outside the cavity using a small butane torch before being placed immediately into the cavity. Immediately before measurement, a thermal camera (Micro-epsilon TIM 400) was used to measure the sample temperature. Figure 3.38 summarises the results of two separate experiments where two different temperatures were obtained as the result of different heating times. Time zero represents the moment the sample was placed into the cavity after heating and microwave measurements begin.

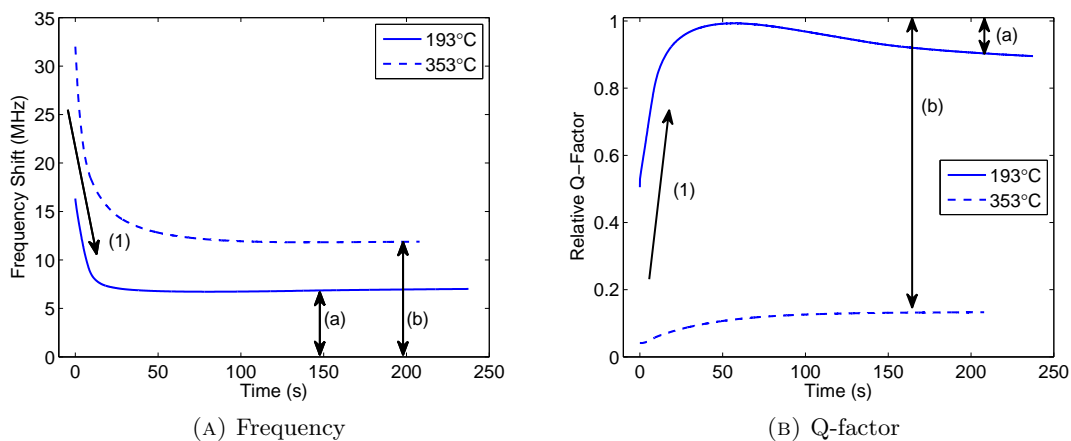


FIGURE 3.38:  $TM_{010}$  resonator parameters of two powder samples as they cool after rapid heating. The results have been normalised to the measured values of the sample before heat treatment. Permanent changes have been highlighted with labels (a) and (b). (1) highlights the initial cooling phase.

In both figures, the samples can be seen to begin returning to their original values as time progresses and they cool down (feature labeled with arrow (1)). However, all samples exhibit some permanent change (labeled (a) and (b)). The permanent change caused by heating to 353°C was greater in both changes. This is attributed to sintering in this case. Casual observation when emptying the quartz containers, consistent with the measurements, noted that, at the high temperatures (>300°C) the particles tended to agglomerate and form solid blocks of powder.

Furthermore, in both cases, if the sample was vibrated, so to disturb the particle matrix, both the Q and frequency would recover closer to the previous (unheated value).

#### 3.4.4 Discussion

The experimentation conducted here has shown that microwave cavity perturbation measurements conducted in the electric field are not suitable for determination of the particle size. Percolation effects cause the samples to behave like a bulk sample with significant conductivity. This effect is not compatible with perturbation measurements.

When cycling the sample temperature, a suggestion was made of a measurable effect caused by the oxidation of particles. This being that the oxide layer has an effect on the number of conductive paths formed when the material expands due to temperature. However, the data were not conclusive and would require further investigation for confirmation. This investigation would need to discount any other chemical effects causing material conductivity change. Furthermore, it seems unlikely that this style of measurement could provide useful information regarding the state of the oxide layer on the particles as it would be destructive.

### 3.5 Conclusions

The measurements undertaken here have proven the potential to design a microwave based sensor to determine the average particle size for a metallic powder. Whilst this method does not provide detailed PSD information, it is very sensitive to small changes in particle size.

A number of use cases can be imagined for the sensor. Two are briefly outlined here.

The simplest scenario involves a stand-alone sensor. When adding new powder to the ALM machine, it can easily be tested and compared with previously used powder. Any changes can be adjusted for by either adjusting the machine or mixing and sieving the powder until it meets requirements.

A more complex realisation involved placing the sensor within the machine itself performing in-line measurements of the powder. A mechanical system can easily be envisaged where powder is automatically taken from the main feed, dosed and settled into

a microwave cavity and measured. The information gained could be fed directly back into the control system or simply an alert displayed to the operator warning of changing powder characteristics.

Dependent on the favoured measurement (frequency or  $Q$ ), the cavity can be designed around the metal to be used.

The basic structure has a simple mechanical design which can be produced very easily. This coupled with easily produced electronics, as demonstrated in Chapter 6, means that sensors could be built at very low cost. Conservatively, the entire sensor could be produced for under 200 GBP. These factors make this technology an attractive opportunity for manufacturers of SLM machines.

## Chapter 4

# Measurement of Surface Resistance Using Microwave Methods

### 4.1 Introduction

When considering the application of microwave techniques to metallic components produced by additive techniques, as discussed in the introduction, two clear application areas present themselves:

1. The production of microwave components, mainly waveguides and cavities, by additive techniques.
2. The use of microwave techniques to measure the quality of produced parts.

This chapter undertakes a series of measurements on a variety of SLM produced surfaces in order to address these two points.

A limitation of any AC measurement of conductivity will be that only a surface layer of the metal will be probed as defined by the skin depth  $\delta$  where  $\delta = \sqrt{\frac{2\rho}{\omega\mu_0}}$  and  $\rho$  is the bulk resistivity. Furthermore, the loss in the conductor is directly proportional to the surface resistance,  $R_S = \frac{\rho}{\delta}$ , with the RMS power loss of an induced current given by

$$P = \frac{R_s}{2} \int_S |\overline{H_S}|^2 dS \quad (4.1)$$

where  $S$  is the surface through which the current flows and  $H_S$  is the tangential magnetic field at the metal surface. However, since the currents flow in the surface, any features of micro surface roughness will act to increase the loss in the metal. These additional loss caused by roughness features much smaller in scale than the surface itself are captured within the  $R_s$  term.

The relative effect of these features is dependent on the size relationship with skin depth and it can be difficult to predict the microwave loss of metals by superficial inspection alone. For example, Figure 4.1 shows the inside of a cavity constructed for measurements and used in previous chapters. On the inner surface, clear ridges can be seen as a result of the machining process which might suggest low performance. However, experiment proves otherwise as this particular cavity exhibits a  $Q$  much higher than other, apparently smoother, cavities.

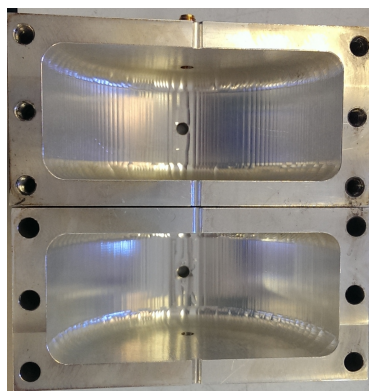


FIGURE 4.1: High  $Q$  cylindrical cavity despite rough surface.

Since skin depths at microwave frequencies are typically less than  $10\mu\text{m}$ , even microscopic roughness can play a significant role in the apparent resistive losses. Therefore, if any analysis of metals using microwave methods are to be considered, an understanding of the surface roughness of the samples and its effects on surface resistance must be known.

For clarity it is worth clarifying the terms which describe surface morphology. Typically, though not exclusively, when referring to surface roughness, the literature is referring to some measure of the vertical displacement within the rough surface. As can be expected this will not be the sole contributor to surface performance. Here, when referring to the surface performance more generally the term surface quality will be used. The term surface roughness is used when discussing a measure of the peak to peak roughness. Furthermore, to avoid confusion, surface roughness measures are denoted by a lower case  $r$  and surface resistance an upper case  $R$ .

The first widely cited examination of the effect of surface roughness was given by Morgan in 1949 [121]. The majority of the work considers a regularly grooved surface and demonstrates increasing loss with increasing roughness as characterised by the RMS roughness value,  $r_q$ . The approach is a numerical one and considers current flows parallel and transverse to square and triangular grooves considering across a range of RMS roughness values but with a fixed groove period. In order to provide guidance for design, Hammerstad and Bekkadal, utilising Morgan's results, provide a design equation relating surface loss to roughness [122]. Whilst their result proves useful and has been widely used for copper strip lines at relatively low frequencies ( $< 5$  GHz), it has been reported to underestimate losses at higher frequencies and, as a result, a number of approaches exist

to characterise surface roughness [123, 124, 125, 126]. Curran et al. presents a useful overview of roughness models and concludes that all models are limited to specific types of roughness (those caused by specific physical processes) across limited bandwidths [127].

This chapter is broadly split into three sections. Firstly (Section 4.2), a presentation of a dielectric resonator based surface resistance measurement fixture. Secondly (Section 4.3), further discussion of surface quality effects on loss including simulation and, finally (Section 4.5), an experimental study of metal plates produced by SLM. Plates were produced in three metals; Aluminium, Titanium and Cobalt Chrome and in two separate build orientations.

## 4.2 Dielectric Resonator Test Fixture

### 4.2.1 Measurement Principle

For any resonator, the Q can be defined as  $Q = \omega_0 \frac{\langle U \rangle}{\langle P \rangle}$  where  $\langle U \rangle$  is the time averaged stored energy and  $\langle P \rangle$  is the time averaged sum of all the losses in the system. For a cavity system, these losses can be attributed to the loss from dielectric filling and the surface resistance losses due to the metal cavity walls. Therefore, by replacing all or part of a cavity wall with a sample metal of unknown resistivity it is possible to calculate this resistivity by measuring the cavity Q and subtracting the contribution from the known walls and dielectric to leave the contribution from the unknown sample. Analytically this can be expressed as

$$\frac{1}{Q_{TOT}} = \frac{1}{Q_{Resistive-Sample}} + \frac{1}{Q_{Resistive-Walls}} + \frac{1}{Q_{Dielectric}} \quad (4.2)$$

When designing a measurement system a number of factors must be considered, primarily; measurement accuracy, sample size and measurement frequency.

From Equation 4.2, it can be seen that, for a fixed Q measurement accuracy, in order to maximise the sample measurement accuracy, it is advantageous to increase the contribution from the sample and to reduce the contributions from the other walls and dielectric as much as possible. Also, accurate knowledge of these extra contributions, or parasitic elements, is paramount. In the context of this thesis and the usefulness of this technology in additive layer manufacturing, it is sensible that samples are a few cm<sup>2</sup> in size and measurement frequency is low to avoid added complexity and cost. A lower frequency also increases the skin depth which enables the measurement to probe a larger proportion of the sample.

Numerous studies have demonstrated the use of this technique, often called ‘end wall replacement’, most commonly in the context of sensitive measurements of superconductors [128, 129, 130, 131, 132, 133]. In order to satisfy the conditions discussed above,

measurement systems usually consist of a sapphire dielectric resonator enclosed by two metal plates or a complete metal host cavity, a solution described by Krupka as “the most convenient structures for surface resistance measurements” [134]. The use of a dielectric resonator allows for smaller designs at lower frequencies as well as increased sensitivity due to an increased Q-factor contribution from the sample. Also, the resonators are designed to operate in the, often termed,  $TE_{01\delta}$  mode because, in this mode, surface currents have only azimuthal components. This means that the system is insensitive to the electrical contacts between the end plates (sample) and sides. The field distribution of this mode can be seen in Figure 4.2.

One of the early treatments of a dielectric resonator is given by Hakki and Coleman [135] for the purpose of measuring the dielectric properties of a dielectric rod. In this simple design, they consider a dielectric rod placed between two infinite metal plates. By solving Maxwell’s equations they are able to provide exact field solutions for the resonator operating in  $TE_{0np}$  modes and, as a result, equations for the resonant frequency and Q-factor.

In his 1993 paper, Krupka provides a comprehensive overview of the technique and proposes a design measuring  $10\times 10\text{mm}$  operating at 18 GHz achieving an accuracy of  $\pm 30\mu\Omega$  [136]. This illustrates the high measurement accuracy that can be achieved.

A previous study examining surface roughness using a dielectric resonator is presented by Iwai et al. [137]. However, their setup requires two incidental measurement pieces and relies on previously acquired values for dielectric loss tangent.

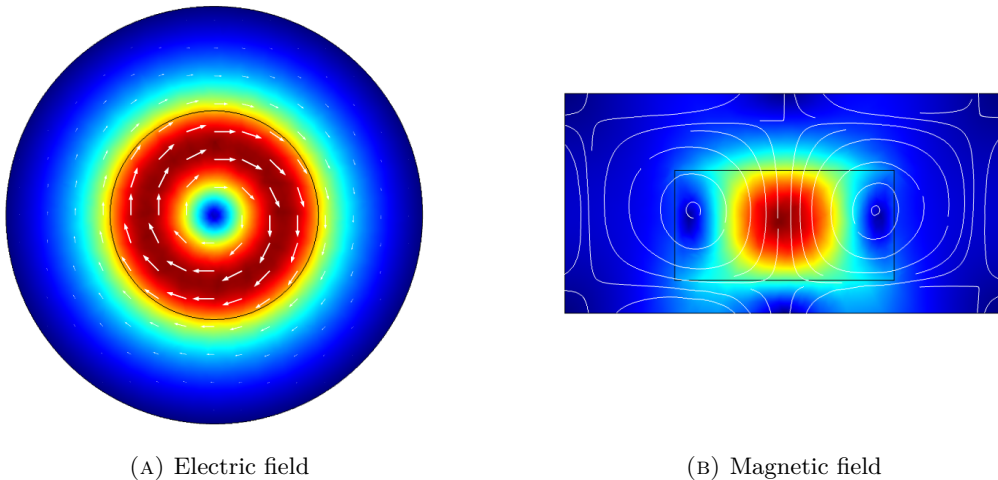


FIGURE 4.2: Simulated dielectric resonator  $TE_{01\delta}$  EM-Fields.

#### 4.2.2 Measurement Procedure

For a dielectric resonator, Equation 4.2 can be modified to give Equation 4.3 which includes the surface resistance of the sample ( $R_{ss}$ ), surface resistance of the cavity ( $R_M$ ),

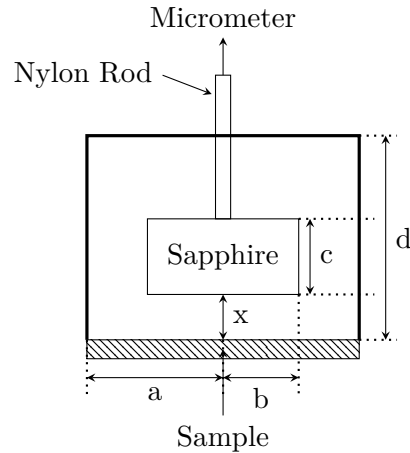


FIGURE 4.3: Dielectric resonator design schematic.

loss tangent of the dielectric ( $\tan\delta$ ), geometric factors ( $G$ ) and geometric electric energy filling factor ( $p_{ed}$ ) [134].

$$\frac{1}{Q} = G_s R_{ss} + G_M R_M + p_{ed} \tan\delta \quad (4.3)$$

where

$$G = \frac{1}{\omega_0 \mu_0} \frac{\int_S |H_S|^2 dS}{\int_V |H|^2 dV} \quad (4.4)$$

$$p_{ed} = \frac{\int_{V_D} |E|^2 dV_D}{\int_V |E|^2 dV} \quad (4.5)$$

where  $S$  is the metal surface of the cavity,  $V$  is the volume of the entire structure and  $V_D$  is the volume of the dielectric. It is assumed that the conductive and magnetic losses in the dielectric are zero.

As has been previously mentioned, in order to calculate  $R_{ss}$ , accurate knowledge of each of the co-efficients in Equation 4.3 must be known. The geometric co-efficients can be found by analytically evaluating the integrals or finding solutions numerically using simulation. Modern full 3D simulations allow for accurate determination of the co-efficients including correction for coupling structures. Methods for accurate determination of the loss factors has had various treatments in the literature. All methods revolve around setting up a series of simultaneous equations based on Equation 4.3. For instance, to simultaneously measure the dielectric loss tangent using another resonant mode [134] or constructing two resonators at the same frequency but with differing dimensions [136] [138] [139].

A new procedure to obtain the co-efficients in Equation 4.3 and subsequently accurately measure surface resistance of a single metallic sample is proposed. The basis of the system is seen in Figure 4.3. The gap between the sample and dielectric,  $x$ , can be varied

by the operation of a micrometer mounted on the top of the structure. This adjustable geometry enables us to isolate the contribution to the  $Q$  from the fixed resonator walls and the attached test piece.

Equation 4.6 below shows the modified version of Equation 4.3 used in our analysis to separately include a frequency term and additional loss term introduced by the supporting dielectric rod.

$$\frac{1}{Q} = \frac{g_w(x)}{f(x)} R_{sw} + \frac{g_b(x)}{f(x)} R_{sb} + h(x) \tan \delta_{DR} + j(x) \tan \delta_{Rod} \quad (4.6)$$

where the subscripts  $w$  and  $b$  represent the cavity walls and base respectively,  $f$  is the resonator frequency dependent on the dielectric position,  $x$ ,  $g$ ,  $h$  and  $j$  are geometrical functions also dependent on the dielectric position,  $R_{sw}$  and  $R_{sb}$  is the surface resistance of the walls and base and  $\tan \delta_{DR}$  and  $\tan \delta_{Rod}$  are the loss tangents of the dielectric puck and supporting rod.

The geometrical functions are obtained from simulation by, in turn, setting the undesired terms to zero.

In order to obtain an accurate value of the dielectric constant for the dielectric puck, required for accurate simulation, simulation and experimental data is compared for resonant frequency at the two extremes of dielectric position. For an anisotropic material such as sapphire, the measured value could differ significantly from the accepted value due to inaccuracies in construction such as a slightly off axis dielectric support. In the ideal case, the electric field is purely azimuthal which means that only the basal plane component of the permittivity tensor ( $\epsilon=9.5$ ) has to be considered.

Next, a test piece is attached composed of the same material as the host cavity, in place of a sample so that  $R_{sw} = R_{sb} = R_s$ .

From its definition, it is observed that  $R_s$  will vary as  $\sqrt{f}$ .  $f_0$  is defined as the frequency when  $x = 0$  and we let

$$R_s(f) = R_{s0} \cdot \sqrt{\frac{f}{f_0}} \quad (4.7)$$

similarly,  $\tan \delta$  will vary as  $f$  so we let

$$\tan \delta(f) = \tan \delta_0 \frac{f}{f_0} \quad (4.8)$$

Now we have

$$\frac{1}{Q_D} = \frac{(g_w(x) + g_b(x)) R_s(f)}{f} + h(x) \tan \delta_{DR}(f) + j(x) \tan \delta_{Rod}(f) \quad (4.9)$$

By fitting Equation 4.9, the derived  $Q$ , to experimental data for various values of  $x$ , the values of  $R_{s0}$  and  $\tan \delta_0$  can be calculated. By fitting across a wide range of  $x$ , more confidence is gained in the fitted result.

To conclude, values have been obtained for all the terms in Equation 4.6 except for the desired parameter,  $R_{sb}$ . Test pieces can be attached to the resonator and using a measurement of the Q-factor the surface resistance of the piece can be calculated.

In contrast to previous approaches, this design makes effort to measure all parasitic elements of the Q-factor and does so with a single resonator structure and operating mode.

It is worth noting that the analysis presented only allows for the calibration procedure to be valid at a fixed temperature. It is possible to extend the equations to include a temperature term but this is not done here.

### 4.2.3 Resonator Design

Since it is desirable to maximise the Q of the resonator and maximise the relative losses in the sample, it is important to use materials with as low loss as possible. Furthermore, the dielectric constant of the dielectric puck will strongly influence the size of the fixture for a desired frequency. The materials chosen for construction were a trade-off between performance, cost and ease of manufacture. The metal cavity was constructed from aluminium and the dielectric puck from sapphire. Since sapphire is well known to be anisotropic, a c-plane crystal was used so that any rotation of the puck would not effect the results. The support rod was constructed in nylon.

It is important to ensure that additional cavity modes present do not interfere with the desired measurement mode. The mathematical fitting calibration procedure described in 4.2.2 should produce the best results when performed over the widest possible range of  $x$  (0 to middle). Therefore, it is important that any additional modes do not interfere with the dielectric in any position.

The interfering modes are a mixture of heavily perturbed cavity modes and a number of so-called 'hybrid' dielectric modes. However, without an analytical model it can be difficult to accurately identify the modes. The process to obtain the ideal dimensions is, primarily, an iterative one where many different dimensions are simulated and the best qualitatively selected by comparing the mode distributions. However, knowledge of how changing the dimensions will effect certain modes can be useful and direct design choices. For instance, scaling the height to move  $TM_{nm0}$  modes will not be effective in changing their frequency.

The mode distribution will be fixed by the ratio of the 4 key dimensions: cavity height and radius and dielectric puck height and radius. Once a suitable ratio is found, the overall size can be scaled to suit frequency requirements and aperture size for the sample. Figure 4.4 shows the mode distribution for the chosen design with dimensions shown in Table 4.1. The  $TE_{01\delta}$  measurement mode is seen to have significant separation across the entire  $x$  range.

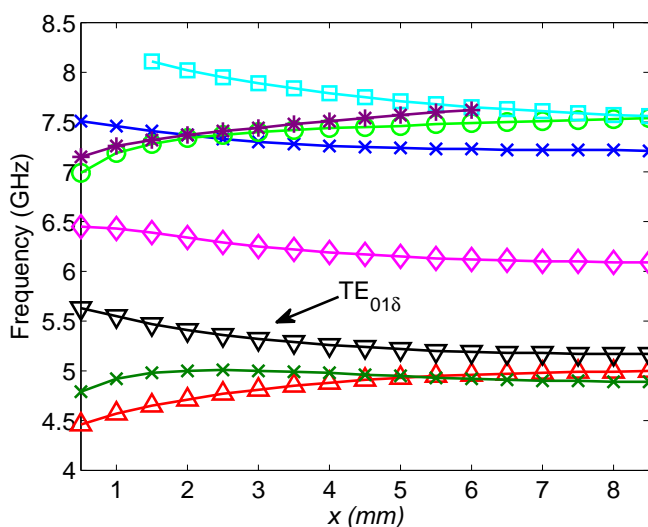


FIGURE 4.4: Changing frequency of the various cavity and dielectric modes as the dielectric position,  $x$ , is changed. The measurement mode,  $TE_{016}$ , is highlighted and is seen to not be intersected by another mode across the full range of  $x$ .

Dimension	a	d	b	c
Size (mm)	18	27	10	10

TABLE 4.1: Dielectric resonator dimensions, labeled in Figure 4.3.

In order to support TE operation, co-axial, inductive, loop coupling is employed half way along the cavity walls. An aluminium A-frame is used to support the micrometer and ensures full travel is possible. The nylon rod is attached to the micrometer shaft by means of a small slot and holding pin.

The completed constructed resonator can be seen in Figure 4.5.

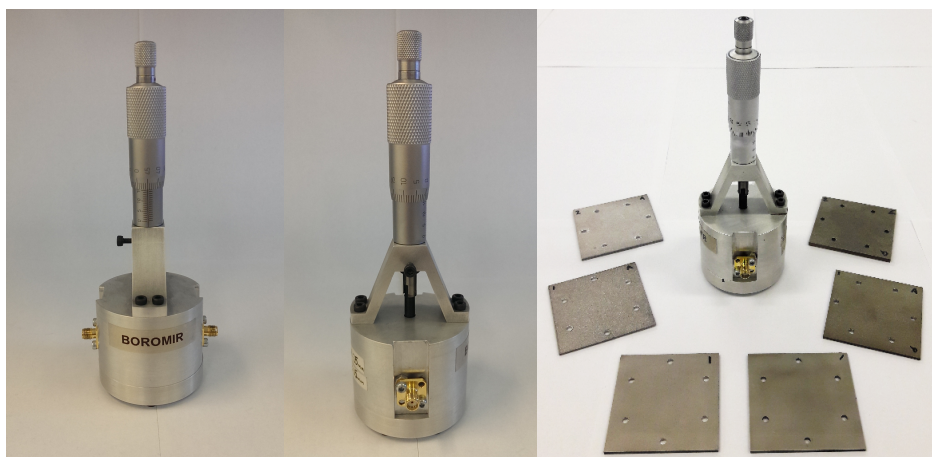


FIGURE 4.5: Completed dielectric resonator alongside sample pieces.

#### 4.2.4 Errors and Accuracy

The random errors associated with the raw  $Q$  and frequency measurement are typically very small ( $<0.1\%$ ) and it is hoped samples can be compared with high precision. As has been previously described, in order to maximise the measurement accuracy, it is important to maximise the contribution the measured sample makes to total system losses. Figure 4.6 shows the contribution from each component to the total system loss. It can be seen that, as designed, the sample losses are greatest when the dielectric is in close proximity to the bottom, sample, plate. Therefore, when taking a sample measurement, the  $Q$  value is taken at the smallest  $x$  value possible. Usually, this is 0.1mm to avoid damaging the dielectric which can occur if it contacts the rough sample surface.

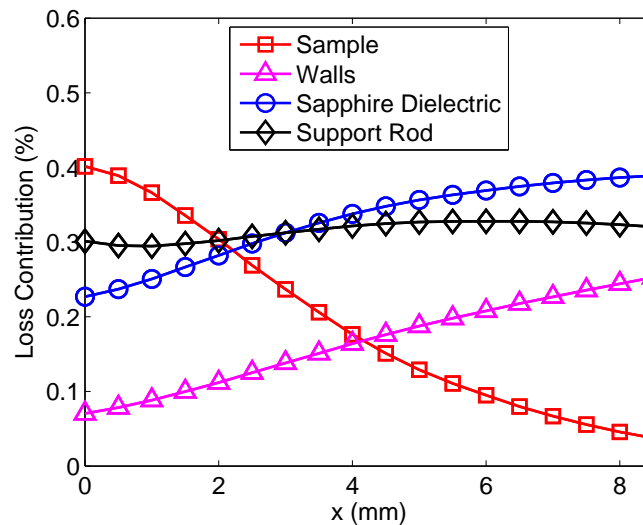


FIGURE 4.6: Loss contributions of the various components in the dielectric resonator . Calculated assuming an aluminium sample base plate using Equation 4.6.

An additional and obvious source of uncertainty is temperature variation between the calibration and various sample measurements. In order to get some indication of the significance of variation, the entire test fixture was placed in an oven and the  $Q$  monitored as the temperature was varied between 20-30°C. The fixture temperature was measured directly with a PT100 thermistor in contact with the metal cavity surface. Figure 4.7 shows the result of this experiment.

Whilst the temperature was varied slowly and uniformly over the course of ~2 hours, in an attempt to ensure there is no temperature gradient across the fixture, a slight hysteresis was observed. The assumption is that this is a result of the dielectric temperature not matching the cavity temperature exactly. Furthermore, the data reveals a relatively significant change, when compared with the measurement error in the  $Q$  itself, in  $Q$  across only a relative small temperature range. For example, the data indicates a ~3% change in  $Q$  with a ~3°C change in temperature. This magnitude of temperature change is routinely encountered within the laboratory day to day. Therefore, it is important to calibrate for each measurement if any temperature variation is expected.

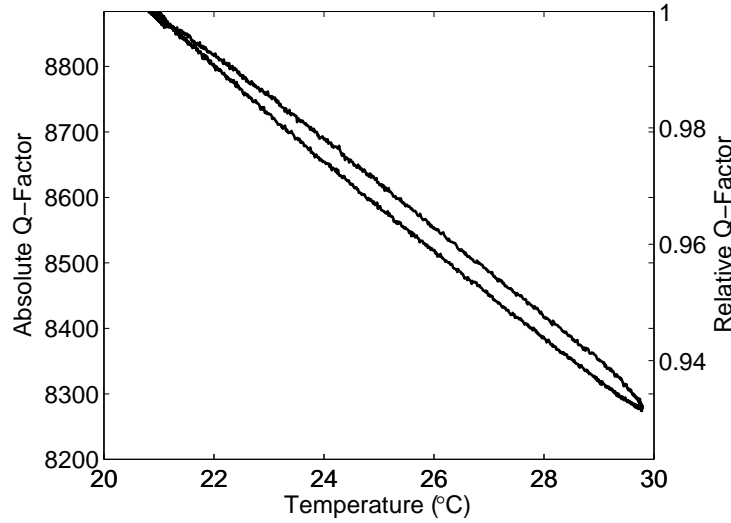


FIGURE 4.7: DR test fixture measured Q-Factor with changing temperature. Measured in-situ in an oven with an aluminium sample piece.

In comparison with random errors, the absolute measurement error is inevitably much larger and is primarily the result of inaccuracies in the geometry factors and calibrated loss factors. It is difficult to quantify the absolute error without a calibrated test piece. It is not straightforward to obtain a standard test piece due to the complex, non-linear, relationship between surface roughness and surface resistance. However, for verification purposes, the copper from a piece of high quality RF substrate was used. (Electro-deposited type produced by Rogers Corporation - RT/duroid 5880, 1.016mm, 18 $\mu$ m copper)

Some indication of the overall robustness of the system can be seen by considering how well the analytical model fits the measured data across a range of  $x$  values. Figure 4.8 compares the measured Q and the Q derived from the fitted model in two conditions: Fitting across the entire range of  $x$  and fitting in the range 0-2mm. Table 4.2 shows the resultant values for  $R_s$ ,  $\tan\delta_{DR}$  and  $\tan\delta_{Rod}$  and the RMS Q Error. The permittivity of the support rod and sapphire dielectric puck for simulation was set at 3.75 and 9.45 respectively using the frequency method described above.

Firstly, the model is seen to be able to accurately reproduce the measured Q. In the worst case, the RMS Q error is seen to be  $\sim 0.4\%$ . When fitting across the whole range, the measured conductivity of the copper test piece is seen to be too high given the generally accepted conductivity value of  $\sim 5.8 \times 10^7$  S/m [140]. However, limiting the fit to the 0-2mm range produces a reasonable result. Note here that the top surface and not the bonded side of the copper is measured. The bonded side will have a lower effective conductivity due to the lamination process [141]. Furthermore, the aluminium conductivity is more realistic for the grade used (6082-T6 -  $2.63 \times 10^7$  S/m). Using this limited range is acceptable since it still covers the range where the base plate losses have largest contribution to the Q factor. The discrepancy of the model is attributed to the

inaccurate modeling of the effect of the coupling structures found midway up the cavity wall.

Fitting Range (mm)	$f_0$ (GHz)	$\sigma$ Al (S/m)	Al $R_s$ ( $\Omega$ )	$\tan\delta_{DR}$	$\tan\delta_{Rod}$	Q Error RMS	$\sigma$ Cu (S/m)
0-2	5.722	$2.52 \times 10^7$	0.0300	$3.056 \times 10^{-5}$	0.0162	35.02	$5.7 \times 10^7$
0-8.5	5.722	$3.00 \times 10^6$	0.0276	$2.684 \times 10^{-5}$	0.02114	17.57	$8.0 \times 10^7$

TABLE 4.2: Measured dielectric resonator loss terms.  $\epsilon_1$  of the sapphire was found to be 9.45.

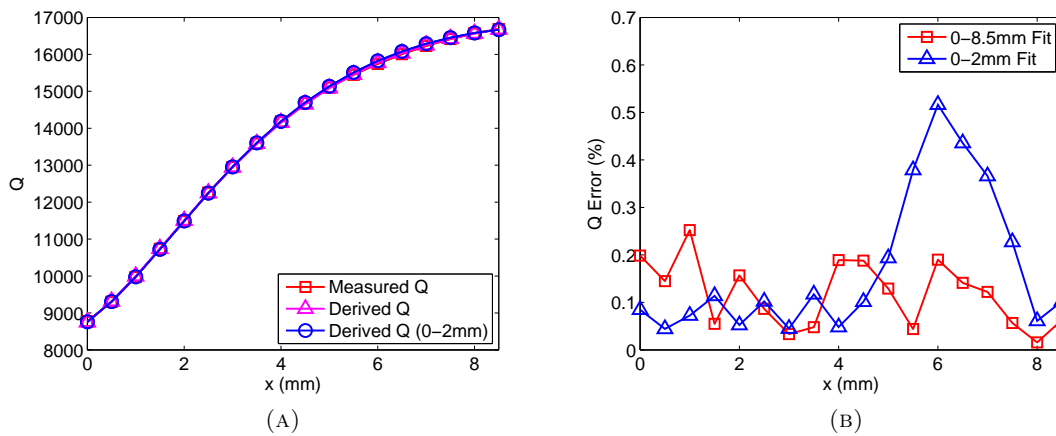


FIGURE 4.8: Dielectric resonator Q as measured and subsequently derived from the resonator model. (A) Q as a function of the dielectric position  $x$ . (B) Error between the measured Q and the Q subsequently derived from the model.

These initial results have highlighted a number of improvements which could be made to improve the design.

Firstly, the proportion of loss which can be attributed to the nylon support rod is much higher than expected. Replacement of the nylon with a low loss dielectric such as PTFE would dramatically reduce its contribution to almost negligible levels. This would have the beneficial effect of increasing overall Q and removing the number of terms which need to be fit to in the characteristic equation.

Secondly, re-location of the coupling ports could improve the accuracy of the simulation and, as a result, increase the confidence in absolute values. Location along the top surface would ensure they are positioned such that the effect of the changing field due to the movement of the dielectric would be negligible.

### 4.3 Loss and Roughness

#### 4.3.1 Simulation

An understanding of the effect of roughness has on surface resistance and subsequently the microwave losses can be obtained through simulation.

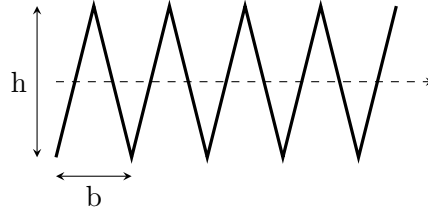


FIGURE 4.9: 2D simulated roughness profile.

Figure 4.9 shows the basic simulation setup where  $h$  is the feature height and  $b$  is the feature size. Adjusting the feature height will lead to changing surface roughness. The simulation was conducted at 2.45 GHz and the conductivity set to  $2.585 \times 10^7 S/m$  such that the skin depth,  $\delta$ , was fixed at  $2\mu m$ . The number of features was fixed at 10.

The RMS surface roughness,  $r_q$ , is defined as

$$r_q = \sqrt{\frac{1}{n} \sum_{i=1}^n z_i^2} \quad (4.10)$$

where  $n$  is the number of measurement points and  $z$  is the distance from the average surface.

The power loss in a metal surface,  $S$ , due to induced currents is proportional to the surface resistance and is given by

$$P = \frac{R_s}{2} \int_s |\bar{H}|^2 dS$$

where  $H$  is the tangential magnetic field component at the surface and in the ideal, smooth, case the surface resistance is given by

$$R_s = \sqrt{\frac{\omega\mu}{2\sigma}}$$

By evaluating the surface integral, Figure 4.10 shows the loss in a surface,  $P$ , normalised relative to the loss in a perfectly flat surface,  $P_0$ . The graph shows increasing loss with increasing roughness and a peak loss when the surface feature length is  $\sim 3\delta$ .

The loss approaches the perfectly flat case at the extremes where the features are much smaller or larger than the skin depth. A comparison between the large and small feature

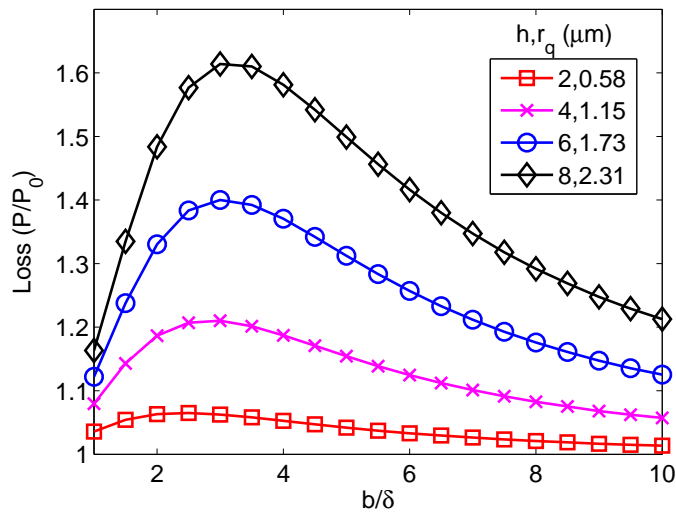


FIGURE 4.10: Simulated normalised microwave surfaces losses relative to the perfectly flat case plotted against feature size for a variety of peak heights,  $h$ , and resultant surface roughness values  $r_q$ .

case can be seen in Figure 4.11. In the large feature limit, the currents behave increasingly like the smooth case simply following the profile extending to a depth governed by the skin effect. Similarly, in the small feature limit, the current flow tends to the flat case but, in contrast to the large feature limit, the surface features with the current simply passing beneath them. The results here concur with previous assumptions that, if the roughness height is much smaller than the distance between roughness peaks, the surface can be considered smooth [142].

Figure 4.12 shows the increasing loss as surface roughness increases and the changing gradient for different feature widths. Alongside the simulated data, the loss given by the Hammerstad model (Equation 4.11) [143] is plotted and is shown to match the simulated loss when the feature size is approximately 3 times larger than the skin depth.

$$\frac{P}{P_0} = 1 + \frac{2}{\pi} \arctan \left[ 1.4 \left( \frac{r_q}{\delta} \right)^2 \right] \quad (4.11)$$

In order to confirm the applicability in 3 dimensions, the simulation was extended to a 3 dimensional surface consisting of an array of pyramids (See Figure 4.13) for a single roughness value ( $r_q \sim 1 \mu\text{m}$ ). Similarly as before, the pyramid base size was adjusted. Figure 4.14 shows the result. A similar trend to the 2 dimensional case was seen with a peak loss at a specific feature size.

### 4.3.2 Roughness Measurement

The surface profile and characteristics have been obtained by two techniques; drag profilometry and white light interferometry (WLI).

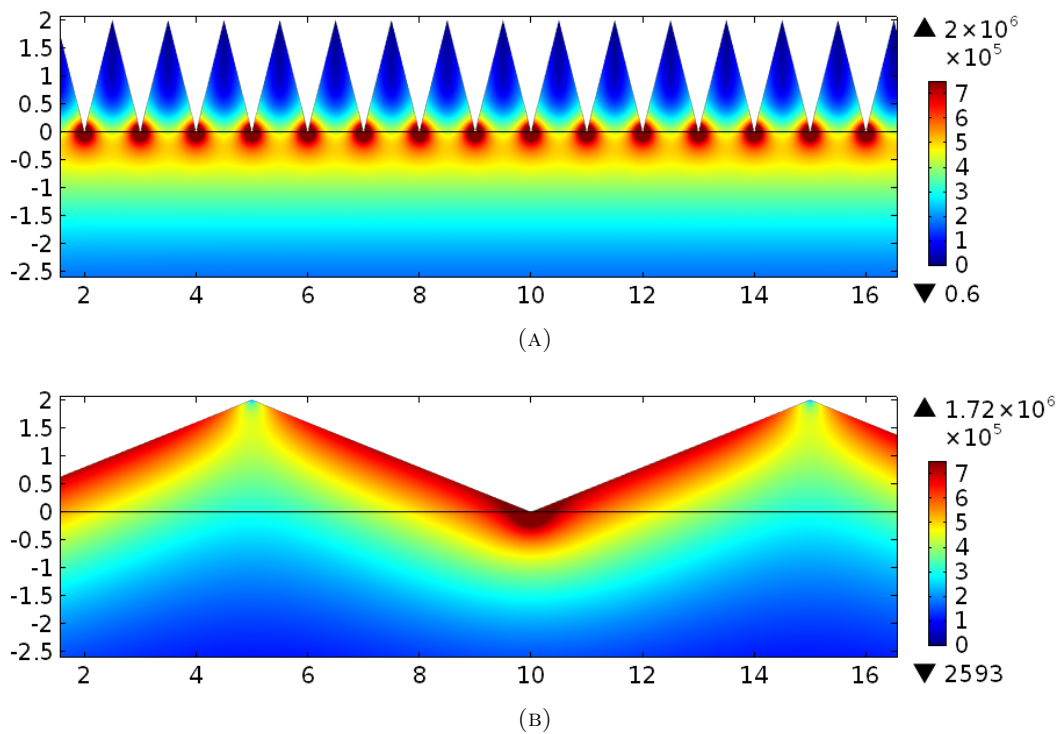


FIGURE 4.11: Simulated current density at the two extremes of feature size. Dimensions in  $\mu\text{m}$ .  $\delta = 2\mu\text{m}$ . (A) Small features. (B) Large features.

Surface profile measurements were taken using a drag profiler: Taylor Hobson, Taly Surf Series 2. A section of a typical profile is shown in Figure 4.15. The total profile length was 35mm; the maximum practical value for the sample size with  $1\mu\text{m}$  point spacing. Vertical resolution is typically better than  $1\mu\text{m}$ . In order to obtain values for surface roughness, a Gaussian low pass filter, with 0.8mm cutoff, is applied to flatten the measurement surface. The tip radius is  $2\mu\text{m}$  which effectively implements a high-pass filter for features smaller than this. The analysis is performed by TalyMap Platinum software.

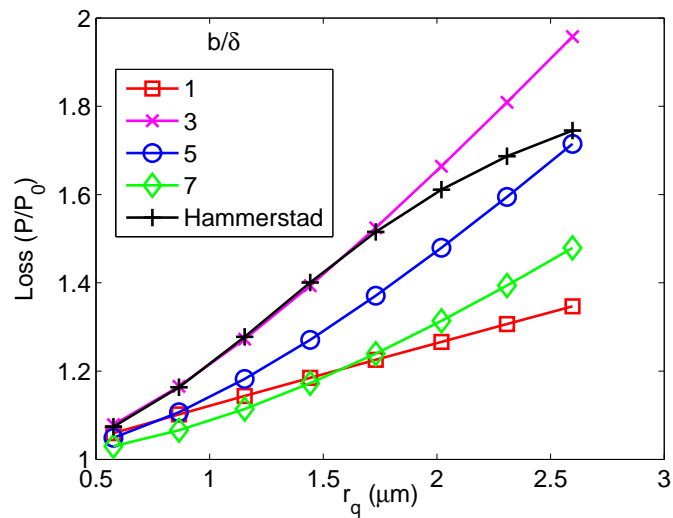


FIGURE 4.12: Simulated losses for different roughness profiles. Normalised surface losses are shown to increase with increasing surface roughness,  $r_q$ . Different feature widths,  $b$ , exhibit a different gradients and the Hammerstad model is shown to match the characteristic when the feature width is 3 times as large as the skin depth..

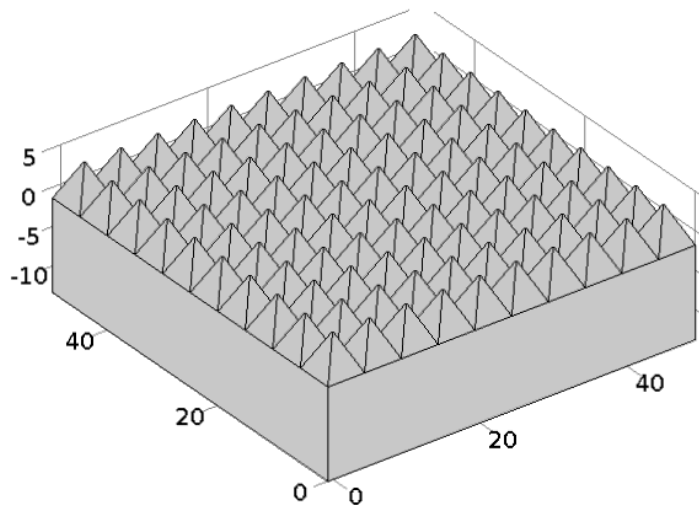


FIGURE 4.13: 3-Dimensional roughness simulation geometry.

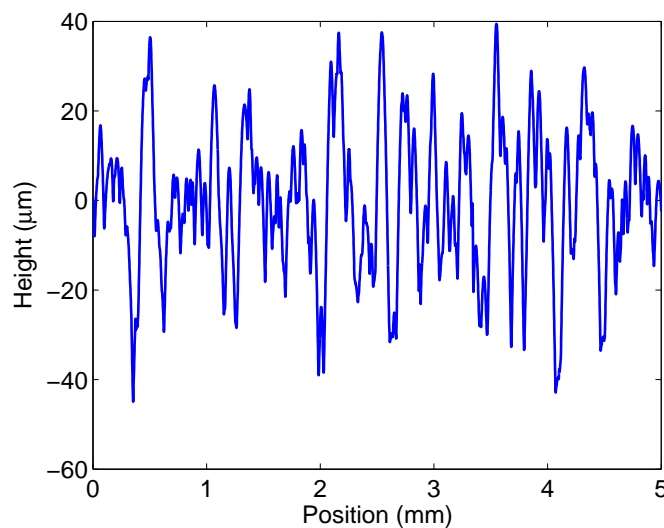


FIGURE 4.15: Section of typical roughness profile from drag profilometer.

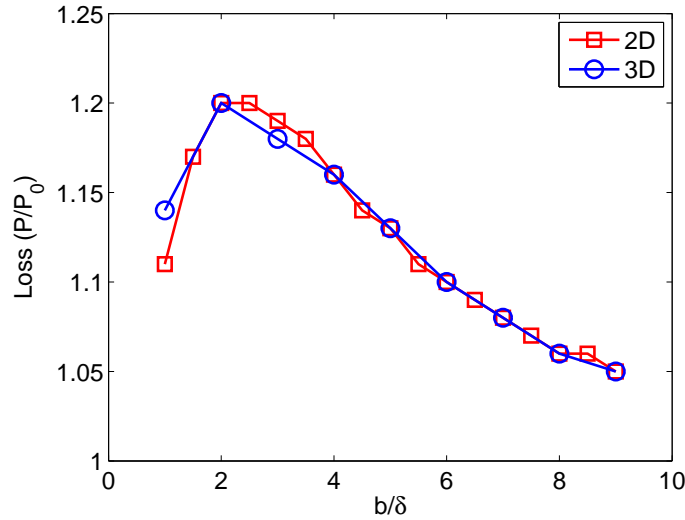


FIGURE 4.14: 2D and 3D roughness simulation loss comparison.

Secondly, in order to add some qualitative analysis of the surfaces, 3 dimensional surface profiles were taken using white light interferometry (WLI). WLI provides only a small measurement area (typically  $<4\text{mm}^2$ ) and is therefore unsuitable in this context to provide accurate values of surface roughness. However, it provides high precision ( $<1\mu\text{m}$ ) and high dynamic range ( $250\mu\text{m}$ ). Specifically the instrument used was a MicroXAM-100-HR White Light Interferometer.

### 4.3.3 Spectral Analysis of Roughness Profile

Whilst the previous simulation analysis can provide convenient insight into why certain surfaces may display certain loss characteristics, the real-world picture is significantly more complex. Real-world surfaces usually appear chaotic in nature composed of both large and small features. These features will, as revealed by the simulation, contribute differently to the loss dependent on both their height and width. Therefore, spectrum analysis by Fourier transform can aid in the understanding of these surfaces and help to correlate real-world surfaces and their measured surface resistance. It is conceded that real-world system is not likely to be a simple addition of the different spectrum components as it is likely that the combinatorial behaviour of features will be non-linear. However, this analysis can still prove useful in exposing general trends and behaviour.

The Fourier transform of two separate surfaces can be seen in Figure 4.23 showing clearly distinct feature spectrums.

The roughness spectrum can then be characterised by the cumulative distribution,  $\phi(\lambda)$

$$\phi(\lambda) = \frac{\int_0^\lambda G(\lambda)d\lambda}{\int_0^\infty G(\lambda)d\lambda} \approx \frac{\sum_{n=0}^\lambda G_n(\lambda)}{\sum_{n=0}^N G_n(\lambda)} \quad (4.12)$$

where  $G(\lambda)$  is the Fourier transform of the surface profile  $Z(x)$ ,  $N$  is the number of elements in the transform and  $\lambda$  is the feature size.

#### 4.4 SLM Plate Samples

Four samples in three different metals were prepared using the Renishaw AM250 machine. The various processing details can be seen in Table 4.3. Samples were built parallel and perpendicular to the build plate (See Figure 4.16), stress relieved and tested either as built or after grit blasting treatment. For the horizontal samples, the wire eroded side, closest to the build plate, was also tested. Vertical samples allowed both sides to be tested. See the Appendix for a full listing of the samples tested.

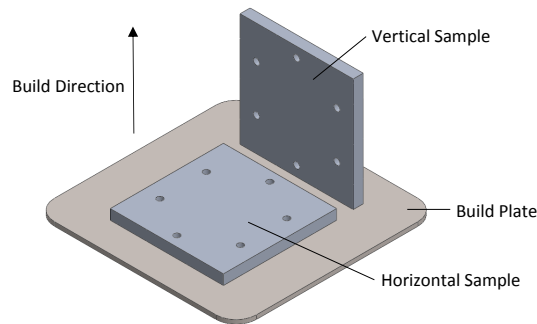


FIGURE 4.16: Build plate and sample orientation.

Metal	Heat Treatment	Grit Blasting	Bulk Conductivity	Bulk Density <sup>3</sup>	$\delta$ (5.7 GHz)
Ti6Al4V	730°C, 1 Hour <sup>1</sup>	50 $\mu\text{m}$ , 6 Bar	$6 \times 10^5 S/m$	4.42 g/cc	8.61 $\mu\text{m}$
Al10SiMg	300°C, 2 Hours <sup>2</sup>	50 $\mu\text{m}$ , 6 Bar	$2.17 \times 10^7 S/m$	2.68 g/cc	1.43 $\mu\text{m}$
CoCr	1050 °C, 2 Hours <sup>2</sup>	50 $\mu\text{m}$ , 2 bar	$1.1 \times 10^6 S/m$	8.3 g/cc	6.35 $\mu\text{m}$

TABLE 4.3: SLM Plate processing details. <sup>1</sup>Vacuum furnace. <sup>2</sup>Argon quench. [1]

The sample dimensions are seen in Figure 4.17. Two directions, X and Y, are defined for surface profile measurements. The samples surface resistance was measured using the dielectric test fixture described previously in this chapter with the sample dielectric separation,  $x$ , set to 0.1mm. The surface resistance was measured on three separate occasions with a calibration performed before each measurement. The average of these three measurements was taken and the error presented the range divided by the number of samples. No temperature control was implemented and the measurements were taken as the lab temperature varied. The temperature of each measurement was taken by a PT100 thermocouple in contact with the sample plate.

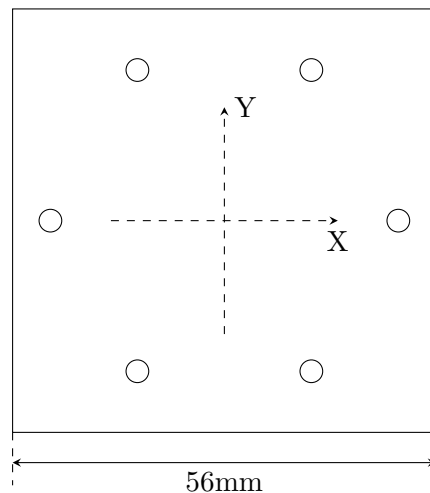


FIGURE 4.17: SLM plate sample dimensions. The directions X and Y are defined for surface profile measurements.

All three metals are known to form a stable surface oxide layer when in contact with air. This surface oxide layer, in all cases, is assumed to be in the order of a few nanometers thick (7nm Titanium[144], 4-10nm Aluminium[145], 4nm Cobalt Chrome [146]). Therefore, due to it being significantly smaller than the skin depth, it can be safely ignored.

## 4.5 Results

Figure 4.18 summarises the measured microwave loss of the various SLM sample plates. Full listings can be found in the Appendix. The loss is normalised by calculating the ratio of measured surface resistance and calculated surface resistance for a perfectly flat surface using the bulk conductivity given in Table 4.3.

Next the surface roughness, given as the RMS value,  $r_q$ , measured in both X and Y directions is seen in Figure 4.19. Again full results are listed in the Appendix.

In addition, the density of the sample is shown plotted against the loss in Figure 4.20. The volume used in the density calculations was calculated using simply micrometer measurements and assumed cuboid structure. Therefore, inaccuracy in this figure is expected to be high and estimated to be  $\sim 5\%$ .

Finally the performance in comparison with the Hammerstand model is seen in Figure 4.21.

## 4.6 Discussion

The first observation is that the ‘As Built’ vertical samples can be highlighted due to their relative distance from the main cluster of measurements (Figure 4.21). The poor

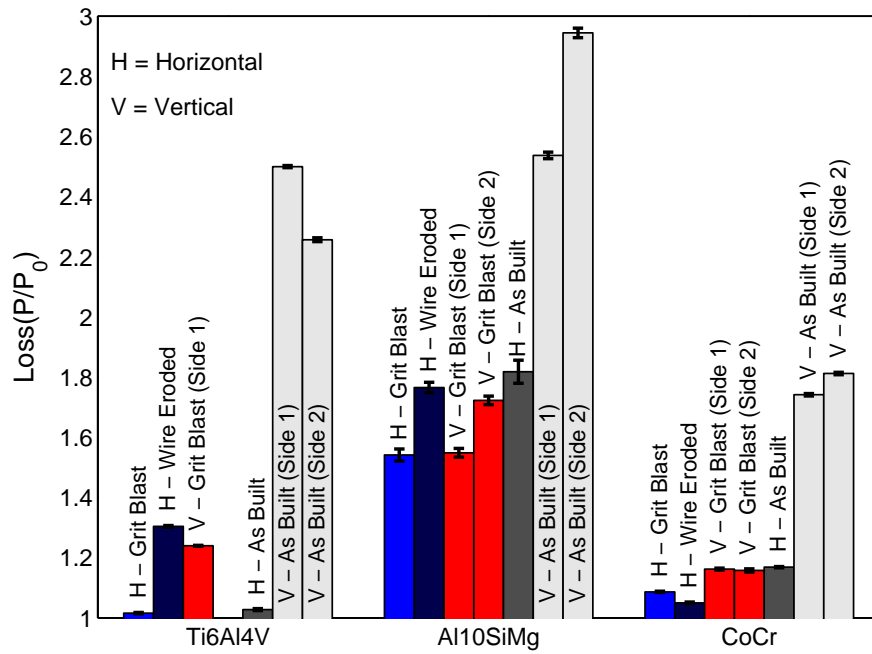


FIGURE 4.18: Normalised loss of SLM plate samples measured at 5.7GHz using dielectric resonator.

performance of these samples can be attributed to loose, unmelted, powder adhering to these samples. This powder can be clearly seen in optical images of the samples. An example is shown in Figure 4.22. This tendency for unmelted powder to remain on steep edges has been previously reported [147]. The presence of spherical features of a surface has also been shown previously to increase loss [148, 149]. The cited study considers a different context, structures created through artificial roughening via electro-deposition on copper substrates, but the result is similar and unsurprising.

Relatively, the aluminium samples perform worse than the other samples. This can be explained by considering their density relative to previously established values. Figure 4.20 shows the aluminium, unlike the other samples, does not reach full density.

Finally, it is noted majority of treated samples perform much better than the widely used Hammerstad model.

Further discussion of the results, along with additional roughness analysis of each sample is done for each metal individually in the following sections.

#### 4.6.1 Ti6Al4V - Titanium

All grit blasted titanium samples show relatively good performance. In the horizontal case, grit blasting has a small positive effect although it is not hugely significant. This result is mirrored by a reduction in roughness.

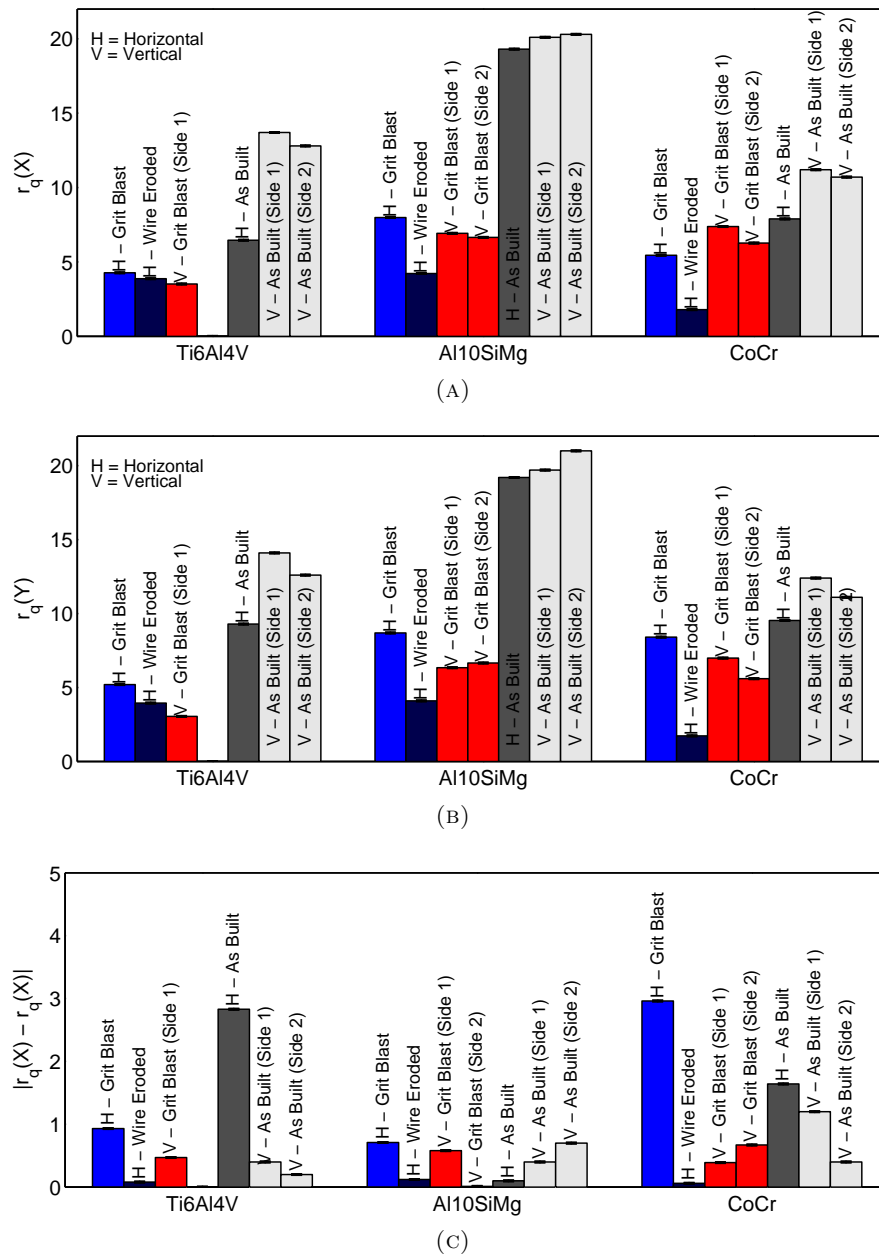


FIGURE 4.19: SLM plate samples RMS surface roughness. (A) Measured in X direction. (B) Measured in Y direction. (C) Difference between directions.

An interesting result is noted when considering the wire cut horizontal sample and vertical samples. These two samples, despite favourable roughness values, show reduced performance in comparison with the horizontal cases. An explanation can be found by considering the spectrum of roughness features shown in Figure 4.23. Earlier simulation revealed that the loss is maximised for features a few times the size of the skin depth. Examination of the cumulative distribution (Figure 4.25) reveals that both the EDM and vertical samples have a higher proportion of smaller roughness features. Qualitatively, this can be seen in the WLI (Figure 4.24) where the horizontal surface shows bigger but wider peaks. It is therefore proposed that these surfaces show greater loss due to these

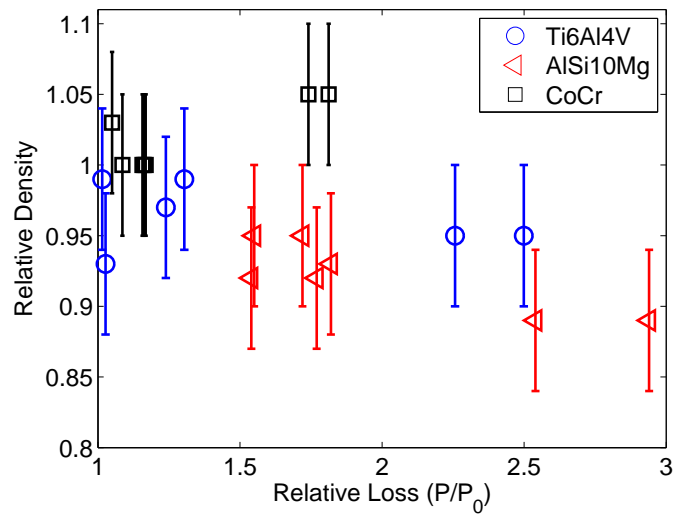


FIGURE 4.20: SLM plate sample density, relative to accepted bulk values, and microwave loss normalised relative to a perfectly flat sample.

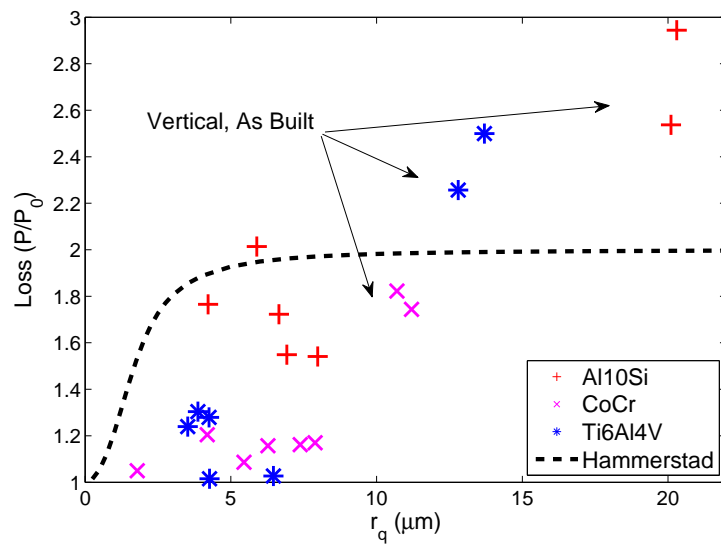


FIGURE 4.21: Surface roughness and microwave loss normalised relative to a perfectly flat sample.

smaller features contributing to a greater extent than the wider yet rougher features of the horizontal surfaces.

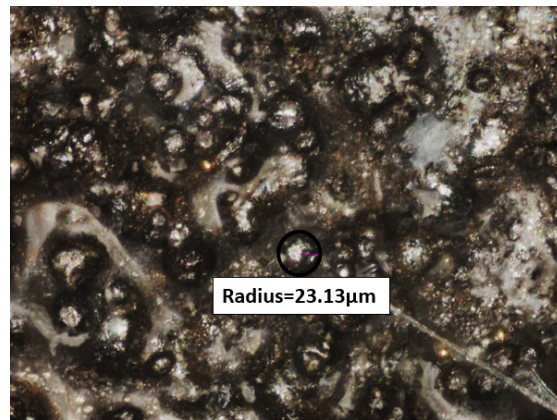


FIGURE 4.22: Microscope image of loose powder on vertical orientation, as-built, aluminium sample.

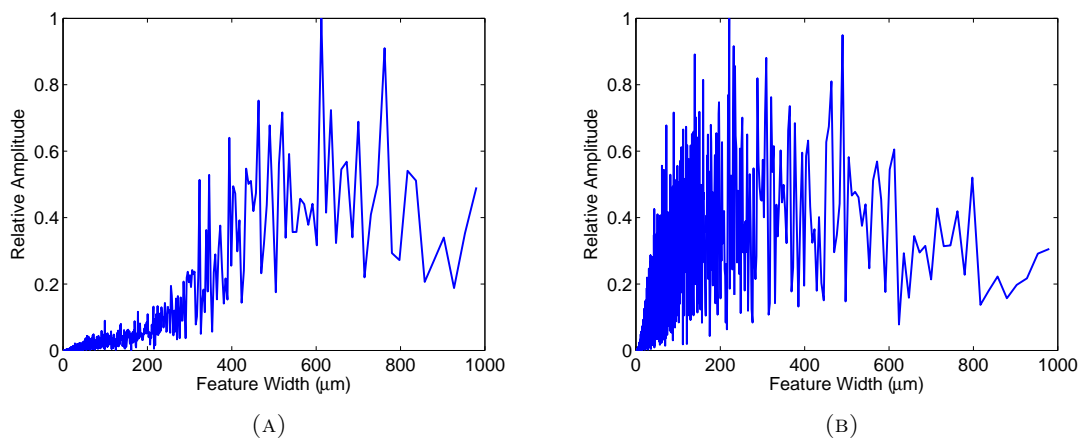


FIGURE 4.23: Feature spectrum of horizontally built Ti6Al4V surfaces. A significantly greater proportion of features smaller than 200  $\mu\text{m}$  are seen in the EDM surface. (A) As-Built surface. (B) Wire eroded EDM surface.

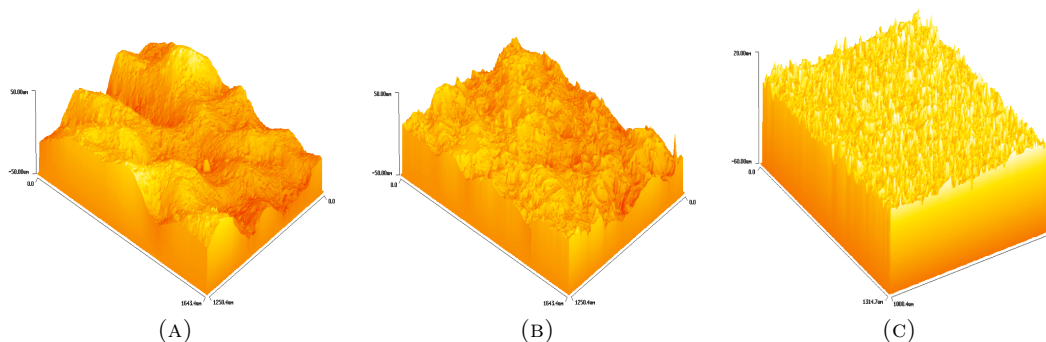


FIGURE 4.24: Changing titanium surfaces as measured by WLI.  $12 \times 16$  mm measurement area. (A) Horizontally produced surface. (B) Vertically produced surface. (C) Wire eroded surface.

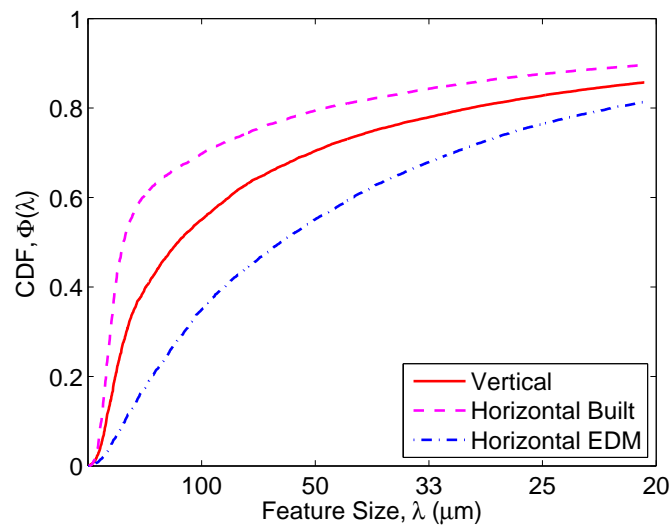


FIGURE 4.25: Additively manufactured titanium surface cumulative feature spectrum.

#### 4.6.2 Al10SiMg - Aluminium

Firstly, in common with the other metals, grit blasting reduces the measured losses. Again, the improvement is significant in the vertical case and less so in the horizontal case.

Across all surfaces, the aluminium surfaces do not reach the relative performance levels of the other metals surfaces with similar values of roughness. Whilst the smaller skin depth of the aluminium is likely to play a role, the drop in performance can be attributed to other micro-structural attributes. Firstly, the density values suggest that the aluminium has not reached full density. Furthermore, Figure 4.26 shows a number of pores in the surface. Comparison of the a raw surface profile with a different sample of similar roughness (Figure 4.27), shows a number of deep fissures. This is indicative of incomplete melting and sub-optimal micro structure. Similar difficulties have been previously reported [150] but it should be noted that the Aluminium process is a significantly less mature when compared to the other metals and it is expected to improve with further development.

In common with the Titanium samples, despite improved surface roughness, the EDM surface and one of the vertical samples show reduced performance. Figure 4.28 shows the cumulative distributions of the 4 sides and highlights the importance of the small features, in this case  $<10 \mu\text{m}$ : the samples whose distributions match at  $10 \mu\text{m}$  show similar performance.

Unlike the other samples, it is seen than a vertical sample has the potential to match the performance of the horizontal sample. Examination of the surface using WLI (Figure 4.29) shows that the morphology of the two surfaces is very similar. As the aluminium

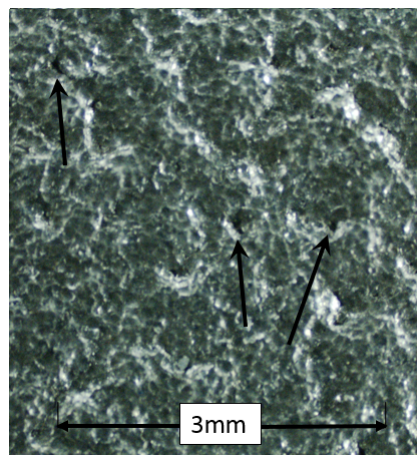


FIGURE 4.26: Horizontal, grit-blasted aluminium surface showing surface pores.

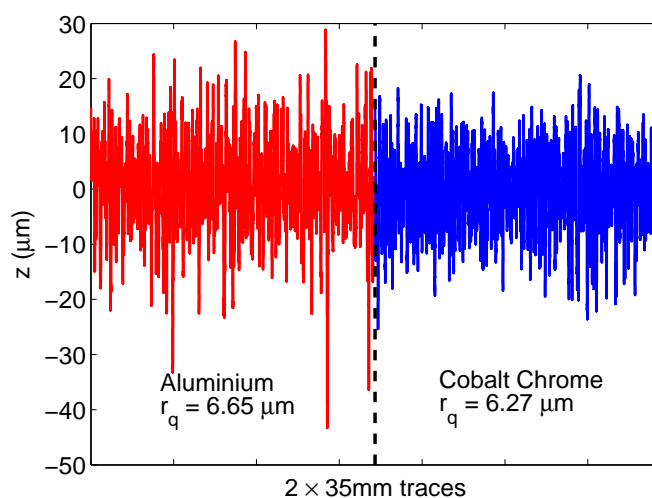


FIGURE 4.27: Vertical, aluminium and cobalt chrome roughness trace comparison.

is relatively soft, the grit blasting physically deforms the surface. The discrepancy in the two surfaces is assumed to be due to inconsistent application of the grit blasting.

### 4.6.3 CoCr - Cobalt-Chrome

Unique to Cobalt Chrome, it is noted that amongst the treated surfaces there are significant differences ( $>1\mu\text{m}$ ) between the X and Y profile directions. Figure 4.31 reveals this discrepancy is the result of a periodic feature. This feature is a result of the linear laser scan pattern and can be seen in the feature spectrum in the Y direction (Figure 4.30). The indicated, stand out, peaks correspond with one and two times the laser spot size ( $70\mu\text{m}$ ).

Whilst the EDM surface exhibits similar spectral behaviour to the other metals, in this case, its absolute roughness is small enough to show improved performance over the grit blasted built sides.

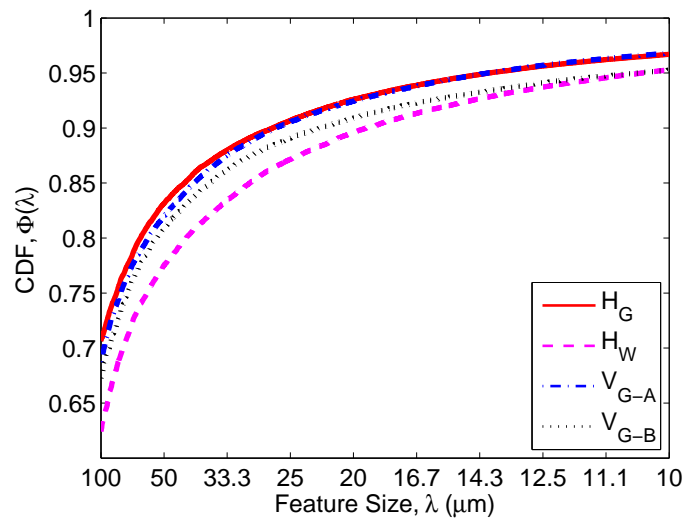


FIGURE 4.28: Aluminium samples cumulative feature distribution. (X) and (Y) refer to drag profile directions. Subscript G refers to a grit blasted surface and W is a wire eroded surface. A and B are the specific sample sides for the vertically built sample.

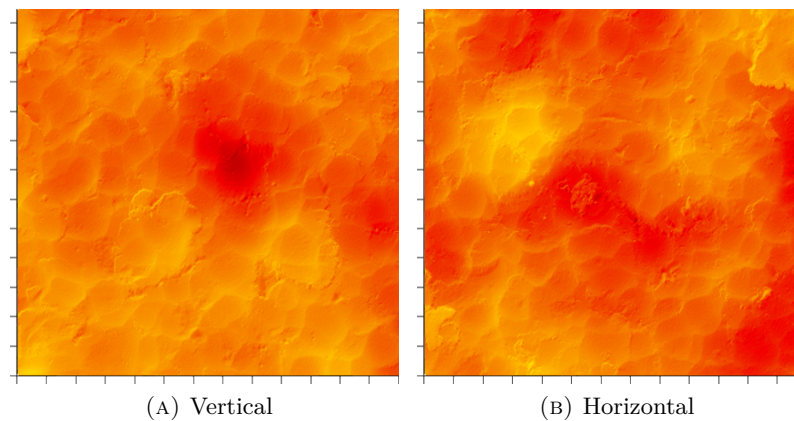


FIGURE 4.29: Changing aluminium surfaces as measured by WLI shown as a relief map.  $1.4 \times 1.4$  mm measurement area. (a) Vertically produced surface. (b) Horizontally produced surface.

Furthermore, the feature spectrums of the horizontal and vertical samples are, in this case, similar and the marginally worse performance of the vertical samples is attributed to a marginally worse roughness figure.

## 4.7 Conclusions

In all cases, the vertical, as built, samples perform poorly. These samples are prone to having loose powder stuck on the surface and this significantly hinders conduction. Grit blasting to remove this loose powder reduced the microwave losses. Grit blasting the horizontally constructed samples also had a positive effect but this was not as significant.

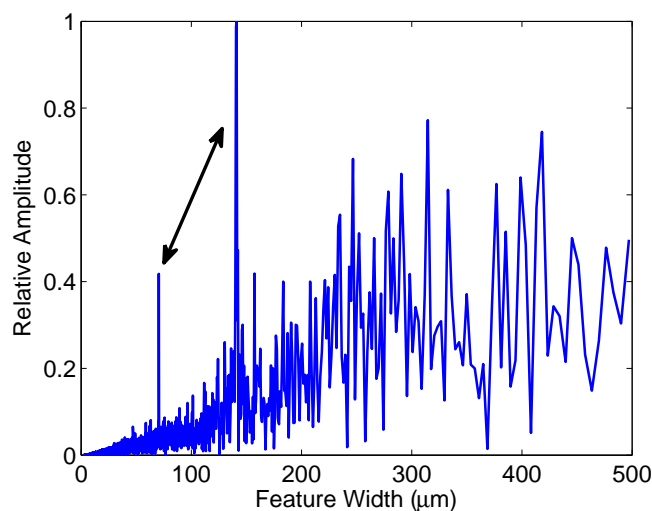


FIGURE 4.30: Horizontally built, grit blasted Cobalt Chrome roughness feature spectrum. Highlighted features as the result of patterning from laser scan.

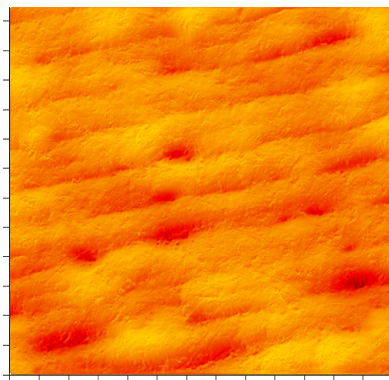


FIGURE 4.31: Horizontally built, grit blasted Cobalt Chrome WLI relief map ( $1.4 \times 1.4\text{mm}$ ).

Secondly, both Aluminium and Titanium show behaviour opposite to the expected trend of decreasing performance with increasing RMS roughness. This has been attributed to certain samples having a greater concentration of roughness features close to the skin depth in size.

It is clear that the majority of treated samples perform much better than the mostly widely used Hammerstad model. This is due to the majority of roughness features falling in the range outside where they significantly affect performance. This is a surprising result as the samples here have demonstrated, in some cases, near perfect metal performance despite having a very rough appearance.

This result is encouraging when considering the application for SLM for building microwave components such as waveguides and cavity filters. Whilst the performance of the Aluminium, in this instance, was disappointing, the other metals indicated potential for SLM produced components to reach similar performance levels as traditionally machined parts despite their apparent roughness.

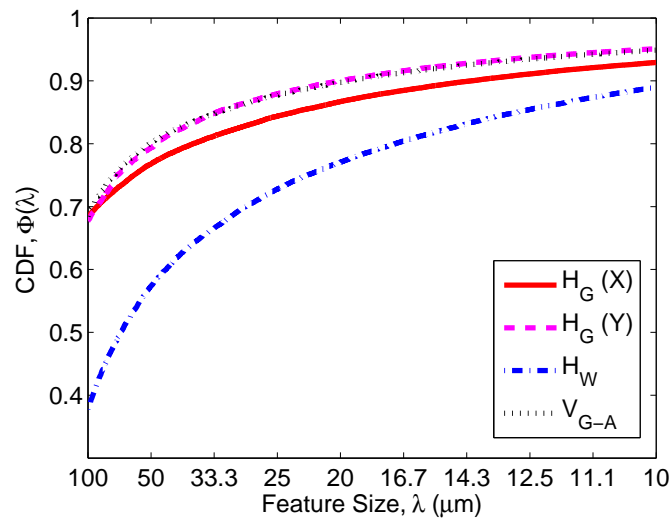


FIGURE 4.32: CoCr cumulative feature distribution. (X) and (Y) refer to drag profile directions. Subscript G refers to a grit blasted surface and W is a wire eroded surface. A is the specific sample side for vertically built sample.

Furthermore, considering the manufacturing of microwave components using SLM, the results demonstrate the importance of having some process to remove loose powder from the surface after building. However, the effect was much less significant in surfaces built in a horizontal orientation. Therefore, this knowledge may impact the design. For instance, orienting the build such that surfaces where current flow is high are built parallel to the build plate. Further work may also consider additional methods of finishing without the requirement of extra machining such as surface re-melting [144].

No clear evidence was discovered of implicit bias towards vertical over horizontally built surfaces. At the study outset, it was expected some difference may be observed due to the different layer structure between horizontal and vertical samples. It is then concluded that the surface roughness and morphology is the dominant factor in determining the surface performance. This is perhaps not a surprising result since the majority of samples exhibited RMS roughness values greater than the skin depth.

Additionally, the results demonstrated the general robustness of the measurement technique. Whilst there is some uncertainty regarding the absolute measurement error, the random errors associated with the measurements were encouragingly very small, typically less than 1%, allowing for high confidence when comparing two measured samples directly. This was achieved despite lack of temperature control and lab temperature variations of up to 4°C. As a result, there is potential for the technique to be applied to probe the SLM parts to, for instance, measure the achieved density. A number of further studies could be undertaken to investigate this potential further. An example may be to measure samples with different laser power or scan strategy.

The results here have, however, shown the very strong influence of surface roughness. It would be imperative to either ensure a very consistent surface finish across the samples

or to perform a correction using surface roughness data. No attempt has been made to do this here but it is clear that a simple roughness value would not provide sufficient information as the roughness spectral distribution would have to be considered.

Furthermore, this microwave technique can potentially offer, for a given measurement area, greater sensitivity to defects than lower frequency methods. This is due to the high accuracy of the measurement and the skin effect giving rise to a relatively small measurement volume for a given measurement surface. This advantage assumes that any defect is present in the surface region.

Finally, the method which has been demonstrated is unique in that it includes calibrated loss factors but is narrow-band and is self contained. In other words, it relies only on a single measurement mode and it does not require a separate physical fixture for calibration.

## Chapter 5

# Effect of Heat Treatment on the Conductivity of Aluminium

### 5.1 Introduction

This chapter presents a study undertaken to investigate the non-linearity observed in the conductivity of Aluminium with heat treatment.

Like any metal, Aluminium is typically modeled as having a linear positive resistivity dependence with increasing temperature. The typical explanation given is that with increased temperature, molecular vibrations increase which acts to decrease the mean free path for the free conduction electrons and therefore conductivity is seen to decrease. However, previous experiments in Section 2.10 revealed an additional effect whereby the resistivity of the metal is permanently improved (i.e. decreased) after heat treatment. A changing conductivity caused by annealing can have a significant impact on a number of microwave spectroscopy techniques. Whilst the effects discussed and measured here can be applied to these different techniques, here the implications for cavity resonators and the perturbation technique in particular are concentrated on. A reduced resistivity will result in an increased resonator Q. During perturbation measurements at elevated temperature, this change may be inadvertently attributed to the sample and not the resonator itself.

One of the key advantages often touted by the cavity perturbation technique is its low cost and simplicity. Cavities can be easily constructed in two relatively simple pieces but, since cost is a key motivator, a trade-off between performance and cost is usually made. This often means the use of a widely available and easily machined metal alloy such as 6082 Aluminium.

The creation of any oxide layer during annealing can be discounted as the driving phenomena as this would act to increase the resistivity of the metal. The oxide layer is only expected to be of nanometer scale thickness and will not grow significantly at the temperatures typically encountered experimentally here ( $<300^{\circ}\text{C}$ ).

However, two distinct effects are suspected as the reason for the observed increase in conductivity.

Firstly, slow heating of alloyed aluminium, as has been done here, will cause diffuse solute impurities to precipitate from the solid solution. Whilst these precipitates can initially act to increase electron scattering and reduce conductivity, generally, as heating progresses it is expected that the nucleation sites will grow in size, becoming less numerous and act to increase conductivity [151, 152, 153]. It is noted that the potential effects are complex and strongly dependent on the alloy constituents and any pre-treatment of the material.

The second effect is the gradual removal of residual stresses initially caused during machining. The machining responsible is usually termed cold working as it occurs below the recrystallization temperature [154]. Residual stresses are known to reduce a metal's conductivity due to the scattering effects of lattice dislocations [155, 156, 157]. Annealing the metal will reduce residual stresses by removal of these lattice distortions and dislocations [158]. This effect will be most pronounced for annealing temperatures above the recrystallization temperature; which is typically under 300°C for most commonly used alloys of aluminium. The use of eddy current techniques, usually at relatively low frequencies, is commonplace to gain a measure of applied and residual stresses [159, 160]. The effect will be compounded at microwave frequencies due to the skin effect since the stresses induced by machining will be present in the cut surface.

In order to examine the validity of this hypothesis, an experimental study was conducted as described below. X-Ray diffraction (XRD) was used to characterise the residual stresses and lattice precipitates. Powder XRD involves placing a multi-grain sample, which can be a powder or polycrystalline solid, under X-Ray radiation and measuring the intensity of the reflected wave across a wide range of angles of incidence. When the path length for waves reflected off different atomic planes differs by an integer of the incident wavelength, constructive interference occurs and a intensity peak is observed - known as a Bragg peak. Each element or compound present will create a number of peaks at different incident angles where each peak is the result of a specific lattice plane (as denoted by the hkl Miller indices). By comparing against known diffraction patterns, elements and compounds can be identified within the material [161].

Furthermore, when a material is strained, elongations and contractions caused by crystalline dislocations and defects are present in the crystal lattice. These deformations will have a direct effect on the elemental d-spacing within the lattice causing shifts in the diffraction peak. The result is a broadening of the peak.

## 5.2 Samples and Procedure

Six samples in total were constructed with 6082-T6 Aluminium. This is a popular alloy, valued for its ease to machine. The main alloying elements are Magnesium, Silicon and

Manganese. The chemical composition taken from the BS EN 573-3:2009 specification is shown in Table 5.1. The T6 designation indicates that the metal has been solution treated to ensure alloying elements are fully dissolved into the aluminium matrix before artificial aging at 100-200°C.

Chemical Element	%
Aluminium	95.2-98.3
Silicon	0.7-1.3
Magnesium	0.6-1.2
Manganese	0.4-1.0
Iron	0-0.5
Chromium	0-0.25
Zinc	0-0.2
Copper	0-0.1
Titanium	0-0.1
Other	0-0.15

TABLE 5.1: 6082 Chemical Composition

The aim of this study is not to completely chemically characterise the Aluminium samples but to simply demonstrate a correlation between residual stress, precipitation and microwave surface resistance. However, the precipitation behaviour for 6XXX series Aluminium alloys has been widely studied. The precipitation sequence is relatively complex but it ends in distinct  $Mg_2Si$  regions [162].

The samples were arranged into three pairs. The first sample was plate like ( $56 \times 56 \times 5$ mm) and prepared for use with the dielectric resonator, details of which can be found in Chapter 4. The second was a small puck, with 5mm radius and 3mm thickness, designed to fit in the sample holders used for X-Ray diffraction.

The three pairs of samples were treated in air as described in Table 5.2 and allowed to cool.

Sample	Treatment
1	None
2	150°C, 6 hours
3	300°C, 12 hours

TABLE 5.2: 6082-T6 Aluminium sample treatment regimes.

The first temperature of 150°C is high enough to cause significant material recovery but without significant precipitation of  $Mg_2Si$  - although a number of studies report the initial clustering of Silicon and Magnesium ions at these lower temperatures [163, 164].

However, this process will be already completed during artificial aging in manufacture. The treatment at 300°C should cause significant and measurable precipitation of Mg<sub>2</sub>Si and complete stress relief through recrystallization as previously reported in [165].

XRD was undertaken using a Panalytical Xpert Pro using Cu-K $\alpha$  radiation with a 10mm incident mask.

Assuming simple exponential decay within the material [166] (valid except for very small incident angles not encountered here [167]), the x-ray intensity,  $I$ , at depth  $z$  is related to the incident intensity,  $I_0$ , by

$$\frac{I}{I_0} = e^{-\mu z} \quad (5.1)$$

where, in aluminium, the absorption coefficient,  $\frac{\mu}{\rho}$ , under Cu-K $\alpha$  radiation is 50.4 cm<sup>2</sup>g<sup>-1</sup> [168] and the density,  $\rho$ , is 2.7 gcm<sup>-3</sup>. This leads to an effective penetration depth of approximately 73  $\mu$ m. This value is appreciably larger than the electrical skin depth at microwave frequencies.

In order to conduct XRD, it is important that the radiation source is monochromatic to ensure distinct diffraction peaks. For this reason, a Nickel filter is used to practically eliminate the Cu-K $\beta$  radiation even though it impacts on the intensity of the desired Cu-K $\alpha$ . However, one notable feature of the Cu-K $\alpha$  radiation encountered in the work here is that it itself contains two distinct spectral lines caused by the orbital fine structure; usually labeled K $\alpha_1$  and K $\alpha_2$ . Separated in wavelength by only 0.0004 nm, effective filtering is impossible so its effect must be accounted for during the analysis. The result of this feature will be that each diffraction peak will appear as a doublet. For polycrystalline materials, with relatively broad diffraction peaks, the secondary peak may not be clearly noticeable but for highly crystalline materials it is significant - especially as the separation increases at high diffraction angles. Since the wavelength and relative intensity (0.5) of the secondary K $\alpha_2$  is known [169], the secondary peaks can be mathematically subtracted from the data. This is done automatically by the acquisition software although it can result in some peak distortion.

As shown by Equation 2.18, the power loss in a metallic surface due to microwave eddy currents is proportional to the surface resistance  $R_s$ . As described in Chapter 4, this is measured using a dielectric resonator technique.

## 5.3 Results and Discussion

### 5.3.1 Surface Resistance

In order to remove the effect of surface roughness, which is assumed to not change during heat treatment, the ratio of surface resistance before and after measurement is presented

as the relative loss of each sample. In this instance, Sample 1 serves as a control. The samples were measured on 3 separate occasions before and after treatment to produce the error bars seen (range of measurements divided by 3). Both sides of each sample was measured to produce two measures for each sample as seen in Figure 5.1.

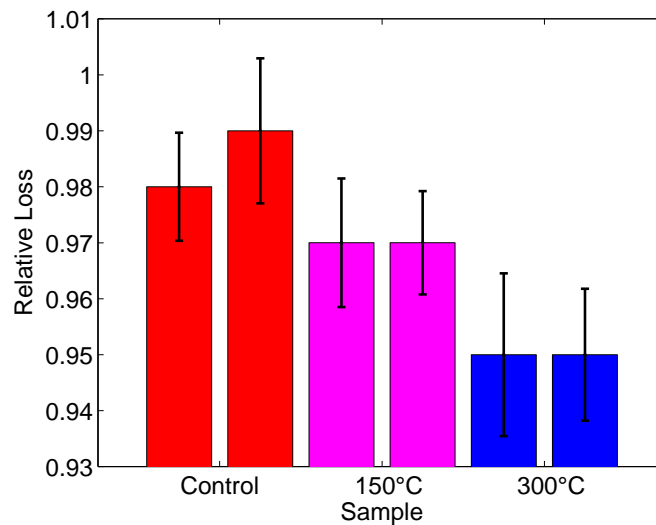


FIGURE 5.1: Relative microwave loss of treated 6082-T6 Aluminium samples. Tested at 5.7 GHz using the dielectric resonator test method described in Chapter 4.

As expected, the results show decreased loss in the treated samples. However, it is clear that Sample 2 has not been treated enough to completely stabilise the material.

### 5.3.2 XRD

Firstly, the complete spectrum is seen in Figure 5.2. The 4 most prominent peaks are identified as belonging to Aluminium. Their relative intensities increases with the heat treatment.

Further examination of the 2 most prominent peaks in Figure 5.3 shows that, in addition to the increase in intensity, the peaks narrow. The narrowing and rising of these primary peaks indicate increasing crystal order and homogeneity. This can be attributed to the removal of crystalline defects and dislocations caused by residual stresses created at manufacture.

The primary expected precipitate,  $Mg_2Si$ , was found at its primary location and, whilst no change was seen for Sample 2, the 300°C treated sample showed a significant change as seen in Figure 5.4. This is in agreement with the previously cited study in [165].

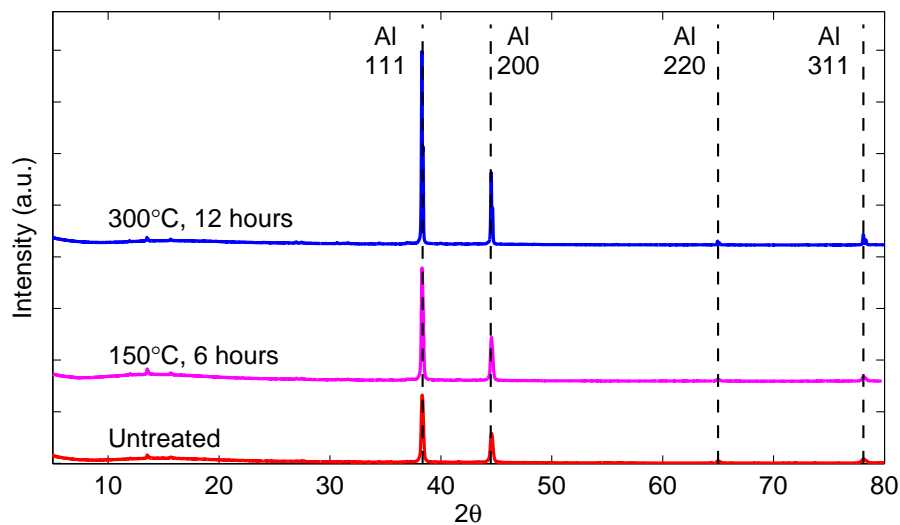


FIGURE 5.2: 6082 XRD Spectrum

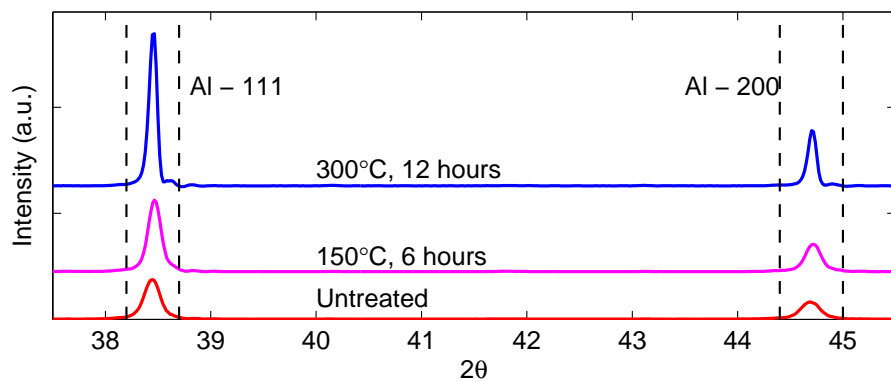


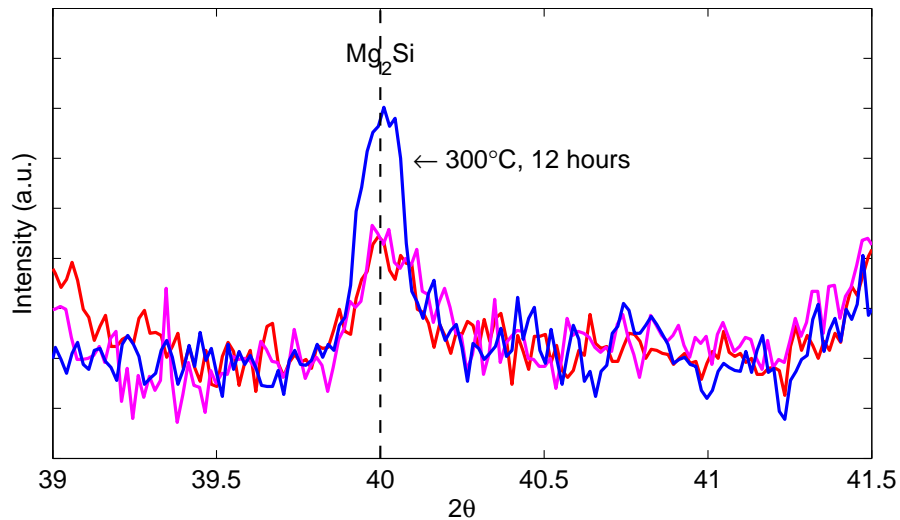
FIGURE 5.3: 6082 XRD - Al

## 5.4 Conclusion

The experimentation has shown the presence of both significant stress relief and precipitation within the sample. In both cases microwave performance was significantly improved; up to 5%.

The sample treated at 150°C showed some improvement without any measurable precipitation occurring. Since the metal was treated at these temperatures at manufacture, this result has demonstrated the clear role residual surface stresses created during machining play in microwave loss.

The treatment at 300°C showed even more significant stress relief as well as the appearance of the  $Mg_2Si$  precipitate. This result indicates that, in this instance, lower recovery temperatures are not enough to completely stress relieve the metal. Whilst the appearance of the precipitate was expected, its role in surface conductive losses cannot be deduced. Although previous studies have shown it to reduce the losses

FIGURE 5.4: 6082 XRD -  $\text{Mg}_2\text{Si}$ 

A curious result can also be seen by examining the result for the control test piece. Whilst significant improvement was seen by treating, an improvement was measured in the control piece. The initial measurements were taken immediately (within 1 day) of manufacture and since the heat treating process was conducted over several days, this piece was able to recover somewhat simply at room temperature in this time.

The implications of this in the context of this work is clear; in order to conduct microwave spectroscopy using the cavity perturbation technique over a range of temperature, the cavity must first be heat treated. Furthermore, even for cavities to be used at room temperature, if measurements over an extended period are to be taken, it must be ensured that the cavity has stabilised since manufacture.

Extensive further work could be undertaken to optimise the annealing process for increased conductivity. Different manufacturing techniques could be investigated to determine their impact with the aim of producing a set of guidelines for manufacture; similar to what exists in the area of superconducting cavity design.

The XRD analysis completed here is relatively qualitative, simply discussing the changes in material properties. Analysis of the XRD peaks can be undertaken to qualitatively measure the material strain or stress and crystallite sizes [170].

Within the wider context of this thesis, the demonstration of the sensitivity of microwave surface resistance measurements to surface stresses is a significant one as it shows the potential for these techniques to be applied to metallic parts produced by SLM.



## Chapter 6

# Basic Scalar Network Analyser

In order to show the feasibility of microwave cavity perturbation within a commercial context, it is important to demonstrate that it is possible to produce electronic hardware capable of the necessary measurements at a low cost. This chapter discusses the various design challenges involved in the creation of such a system and presents measured data from a number of prototype systems.

The modern workhorse of electromagnetic research is the Vector Network Analyser (VNA). Modern VNAs utilise a complex heterodyne architecture to to achieve an extremely broad bandwidth with enhanced filtering and noise performance. In the application of cavity perturbations, the VNA measures the complex transmission and reflection scattering parameters ( $S_{21}$  and  $S_{11}$ ) which are the basis of both resonant and non-resonant material measurement techniques. However, the analysis in Chapter 2 has revealed that for the resonant methods, specifically cavity perturbation, it is only necessary to measure the resonant frequency and Q of the system which can be inferred from the power spectrum measured in reflection or transmission. Therefore, it is possible to ignore phase information and construct a much simpler scalar network analyser for this purpose.

Furthermore, by designing the system to target a specific resonant mode, the bandwidth can be dramatically reduced further reducing cost.

Figure 6.1 shows the a diagram of the complete perturbation measurement system. The system comprised of 4 distinct functional blocks:

1. Digital Controller or PC - Records measurement signals and determines measurement limits and parameters.
2. Data Acquisition Device (DAQ) - Synchronously generates analog frequency control voltages and reads analog power levels from an on-board power meter.
3. Basic Scalar Analyser (BSA) - Main custom circuit which, alongside supporting circuitry, contains a voltage controller oscillator and power meter.

#### 4. Resonator - Cavity type resonator.

Blocks 1 and 2 can be combined into a single physical entity, for instance, in a micro-controller. However, for convenience and for ease of development, in this work, the National Instruments USB-6211 multifunction DAQ is used.

In this context, the BSA does not refer to the entire system but simply the block responsible for generating the microwave signals and read them back. The majority of this chapter is concerned with the design of the BSA.

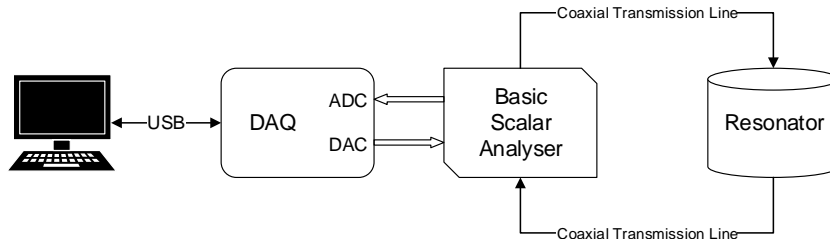


FIGURE 6.1: BSA top-level system schematic.

## 6.1 BSA Prototypes

Various prototype circuits were developed to explore the various design challenges and can be seen in Figure 6.2. The circuit schematics can be found in the Appendix.

The circuits are based around the Hittite HMC385LP4 VCO and Analog Devices ADL5513 power meter.

The VCO provides up to 500MHz bandwidth centered around 2.45 GHz. This is ideal for the measurement of the standard  $TM_{010}$  cylindrical cavity discussed in earlier chapters.

An output power of 4.5dBm ensures a weakly coupled resonator, with an insertion loss of -20-30dB, remains firmly above the noise floor of the measurement.

The power meter specifies up to an 80dB dynamic range with a noise floor at -70 dBm. In practice, with relatively inexpensive supply regulation and bypassing, the noise floor was found to be around -50dBm.

Advantageously, the power meter is only sensitive to up 4GHz meaning a degree of harmonic suppression is built-in. It must be noted that harmonic interference should only be an issue for reflection measurements since the cavity itself acts as a very efficient notch filter in transmission.

The output voltage of the power meter is proportional to the power in dB. The output slope is a function of the supply voltage and a simple network of output resistors. It is desirable to maximise the supply voltage so to exploit the maximum range of the input ADC.



FIGURE 6.2: Photograph of BSA prototype circuits. From the top referred to as A, B and C. Prototype A pictured with connectorised circulator attached.

For convenience, circuits B and C are designed to operate from a 5V supply. This negates the need for an external supply since the 5V can be drawn from the USB bus. Since the tune conditioning op-amps require outputs up to  $\sim 7V$ , a 10V rail is provided by an LM2662 switch capacitor voltage converter which is regulated down to 8V, 5V and 3.3V for the op-amp, power meter and VCO respectively. In order to minimise ripple on the voltage lines, ultra-low ESR switch capacitors are used and care is taken to ensure the linear regulators provide adequate rejection at the boost converter switch frequency.

In addition, to provide some context, the raw material costs for the prototype circuits are presented in the Appendix.

### 6.1.1 Software

A LabVIEW program was developed to acquire the data from the BSA. In addition to curve fitting and data presentation, its primary requirement is to configure the DAQ device for acquisition.

In order to maintain high sample rates, it is imperative that the ADC and DAC are hardware synchronised. This is achieved by configuring for a common start trigger and base sample clock. Additionally, the ADC sample clock may be set as a multiple of the DAC sample clock to enable oversampling and reduce noise.

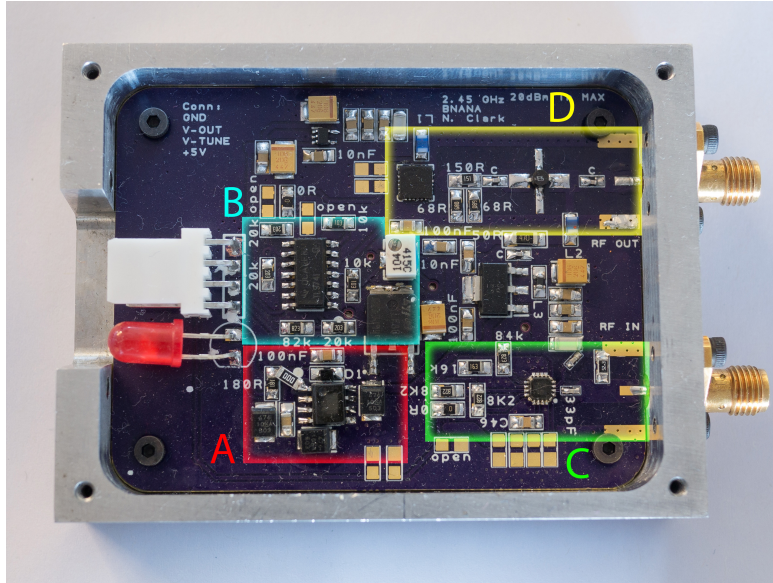


FIGURE 6.3: Prototype C closeup. (A) Voltage doubler circuit. (B) V-tune signal conditioning. (C) Power meter. (D) Oscillator and output amplifier.

### 6.1.2 Basic Specifications

For reference, a list of basic specifications is compiled in Table 6.1.

Specification	Prototype A	Prototype B	Prototype C	Units
Output Power <sup>1</sup>	4.90	3.84	4.10	dBm
Frequency Start	2468.6	2465.8	2367.5	MHz
Frequency Stop	2512.5	2501.5	2500.5	MHz
Dynamic Range <sup>1</sup>	60	51	41	dB
V-Tune Max	5	5	10	V
Supply Voltage	12	5	5	V
Supply Current	160	140	260	mA

<sup>1</sup>Max value across the frequency range.

TABLE 6.1: BSA prototype specifications.

## 6.2 Design Considerations

An outline of the key considerations are presented here.

### 6.2.1 Frequency Resolution

The frequency resolution is ultimately set by the resolution of the ADC and the VCO tune input range. However, some care must be taken to ensure adequate resolution.

For instance, the NI USB 6211 provides a 16 bit analog output resolution corresponding to 65536 unique voltage levels over a  $\pm 10\text{V}$  span. This results in a finite voltage step of 0.31 mV. The Hittite HMC385LP4 provides an average sensitivity of 25 MHz/V over a total span of 0-10V. Therefore, without any signal conditioning the minimum available frequency step is 7.6 kHz.

However, since the entire VCO range is not typically required, this value can be easily improved with the application of some simple signal conditioning.

At the simplest level, this will involve scaling the input voltage and offsetting it to the desired range.

Careful design of the conditioning op-amps ensure this can be achieved. For instance, the schematic in Figure 6.4, implemented in prototype C, scales and offsets the voltage in three stages and utilises a difference amplifier. It is designed to scale a 0 $\rightarrow$ 10V input to a 3 $\rightarrow$ 7V tune voltage and includes a tuning potentiometer which allows for the frequency offset to be finely tuned to the cavity being used. The circuit avoids op-amp common mode input limitations ensuring the entire 0-10V span is unclipped. The use of a rail to rail op-amp additionally allows for a single supply as low as 8V.

Furthermore, since any noise present on the VCO tune voltage will directly affect the output sensitivity, it is important to minimise the noise on this signal. Whilst the Op-amp should reject any noise on its supply, the addition of any reference voltage to the tune voltage will inevitably increase noise. The use of the difference amplifier potentially reduces the reference noise voltage by up to 40%. Direct filtering should be treated with care since it could adversely effect the tune voltage as the frequency sweep speed increases.

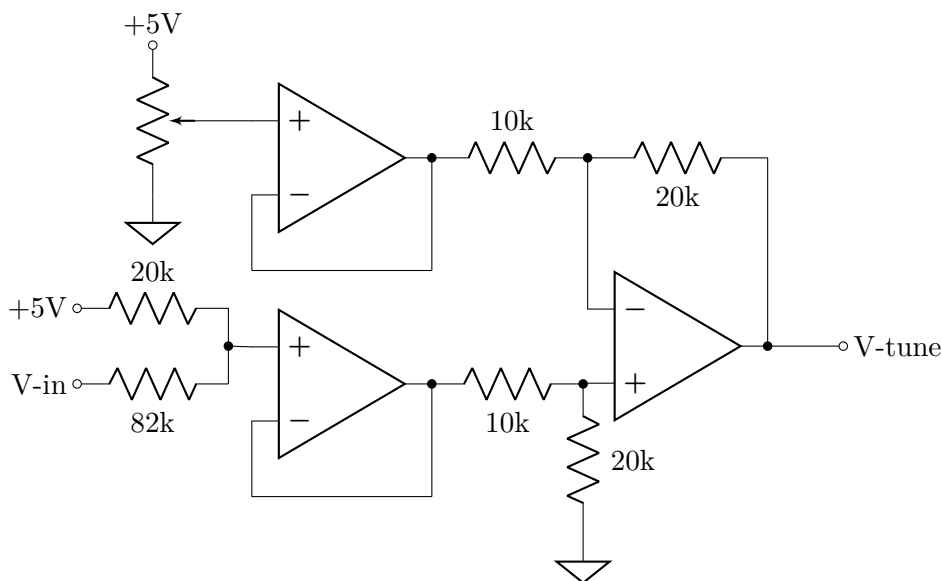


FIGURE 6.4: Tune voltage signal conditioning scaling 0-10V input to 3-7V output with offset voltage noise rejection.

### 6.2.2 Frequency Pulling

Frequency pulling describes the effect changing output impedance has on the oscillator frequency. Since, by its very nature, the resonator system presents a very different impedance environment to a matched load this presents a significant challenge in this context. One solution might be to use a frequency synthesizer which derives its output frequency from a stable reference but this does add not insignificant cost and complexity.

The worst case scenario is seen in Figure 6.5. It can be seen that around the resonant peak, a step change in frequency occurs severely distorting the measurement trace.

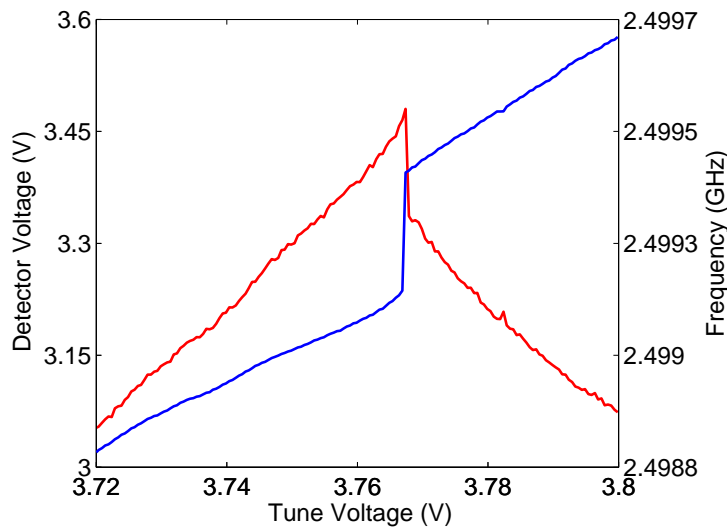


FIGURE 6.5: Measured response, using prototype A, of empty cavity without isolation between oscillator and cavity.

This step change can be attributed to the abrupt phase change seen in  $S_{11}$  at the resonant frequency seen in Figure 6.6. It is also observed that for a weakly coupled resonator, it presents an effective open circuit to the oscillator across the entire frequency band. Loading the resonator will only act to reduce the change in  $S_{11}$  caused by the resonator.

In order to solve this problem, additional isolation between the VCO and cavity must be provided. The simplest solution is to place a circulator between the VCO and cavity system. Typically this can provide  $\sim 20$ dB isolation. Observing the output frequency characteristic, Figure 6.7, shows that the circulator is effective in removing the pulling effect of the cavity.

Whilst the circulator removes the strong non-linearity in the circuit frequency response caused by the cavity resonance, there is still a significant difference in the output frequency when driven into a matched load. A comparison of the two cases can be seen in Figure 6.8. The difference in frequencies is also seen to change across the band. Since the magnitude of  $S_{11}$  is fixed across the band, this demonstrates the strong dependence on the complex value of  $S_{11}$ . As a result, any frequency calibration with a limited amount of isolation will only be valid for a specific cable length.

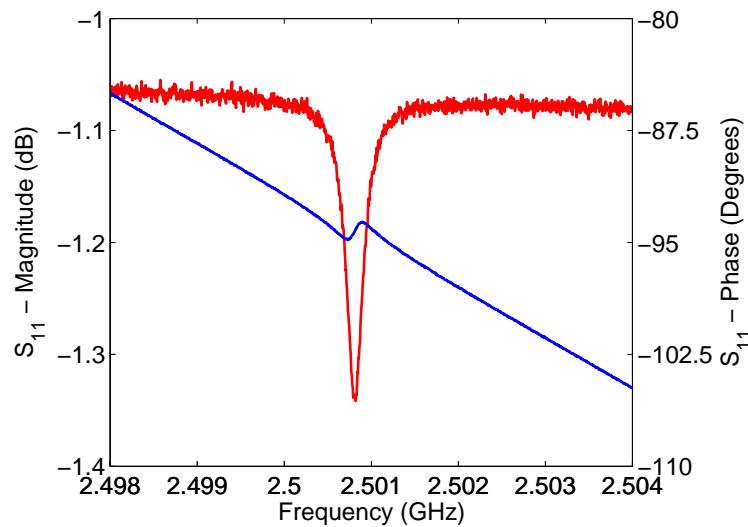


FIGURE 6.6:  $S_{11}$  of empty cavity and cable. Measured using an Agilent ENA.

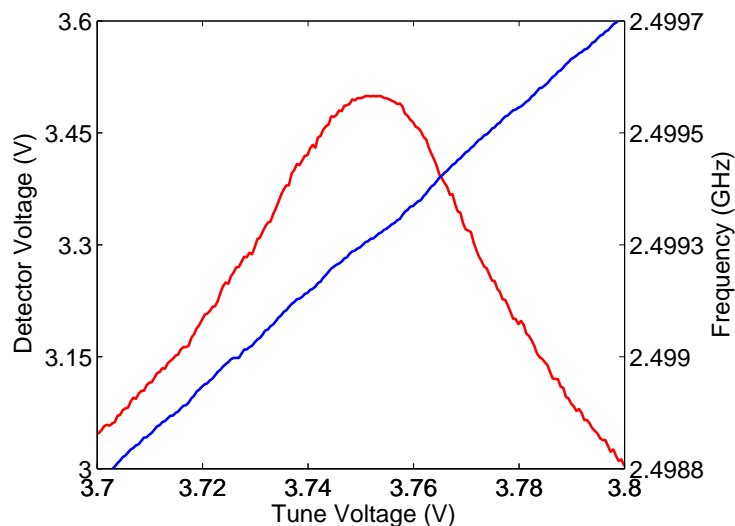


FIGURE 6.7: Measured response, using prototype B, of empty cavity with a circulator providing isolation between the oscillator and cavity. The strong non-linear frequency response has been successfully suppressed.

For this reason, it would be advantageous to include a port for frequency monitoring so that an external directional coupler does not have to be left attached to the system. This could be achieved with a board level coupler, however, a cheaper option would be to monitor the frequency via tune or bias port leakage.

As an alternative to a circulator, a small amplifier can provide significant isolation at much lower cost and with a much smaller physical footprint. In addition, since the amplifier provides some gain, additional isolation can be provided by an inline attenuator without loss of dynamic range.

For instance, the Mini-Circuits ERA-5SM provides  $\sim 22$ dB of isolation and  $\sim 19$ dB of gain which, when coupled with an attenuator, can therefore provide up to 60dB of isolation

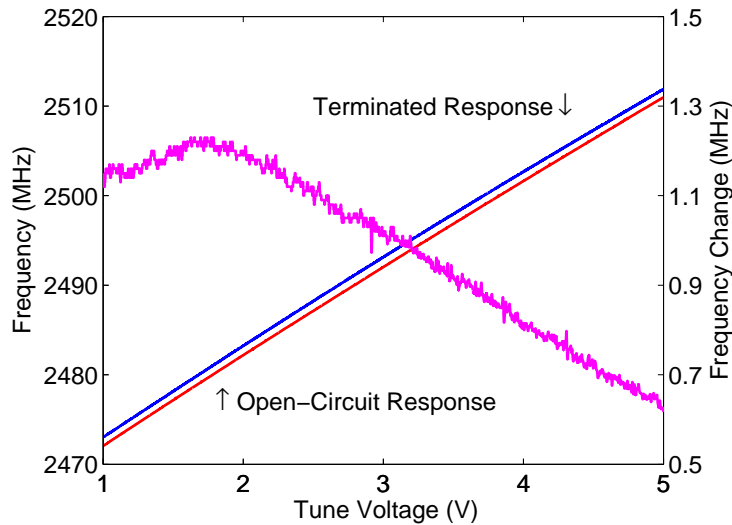


FIGURE 6.8: Comparison of output frequency of prototype B measured either by direct termination into the spectrum analyser or via a 20dB directional coupler with the output left open-circuit.

without any loss of dynamic range.

However, the PA will be a significant source of noise and non-linearity. As a result, noise suppression in the bias line becomes important to avoid gain fluctuations which directly impact the measurement noise. Additionally the gain of an amplifier can be significantly effected by the load impedance and, as discussed, this impedance will fluctuate with the load condition of the resonator.

Generally, as mentioned, harmonic generation can be safely ignored since, given careful design, the cavity should filter unwanted harmonics, however, it is acknowledged that the addition of a PA will significantly increase their presence. Also, mixing products will be amplified and can appear in the output signal. The output spectrum from prototype C is seen in Figure 6.9 clearly showing the mixing products from the on-board switching components.

### 6.2.3 Noise and Dynamic Range

In order to maximise dynamic range, it is important to minimise the power meter noise floor by reducing the noise presented to it. One of the most significant sources will be noise leaking from the VCO out onto its supply and tune lines. Also, since the power meters are wide-band, they are sensitive to noise arising from any switch-mode power supplies. Furthermore, the oscillator frequency itself is sensitive to noise in its supply, a phenomenon known as ‘pushing’. For instance the HMC385LP4 specifies pushing of 2 MHz/V.

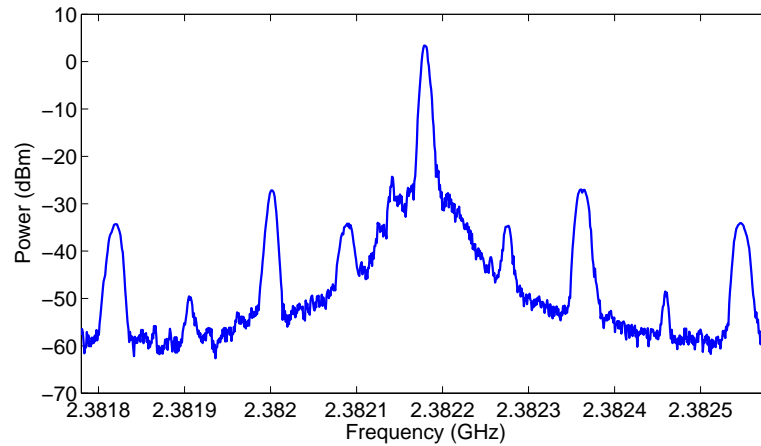


FIGURE 6.9: Mixing products generated by amplifier. Prototype C output measured directly with Agilent N9010A spectrum analyser.

Therefore, with all these factors combining it is important to regulate the supply well and have generous use of noise reduction capacitors. RF chokes on the oscillator supply and tune are also advantageous.

#### 6.2.4 Temperature

The VCO used here specifies a frequency drift rate of  $0.25 \text{ MHz}/^\circ\text{C}$ . This frequency drift can be very problematic and is easily measurable given the system resolution. This has not been extensively investigated here but it is imperative that the circuit is allowed time to come to an equilibrium temperature before operation and is operated across consistent ambient temperatures. It can be expected that a large part of any discrepancy between measurements made with a commercial network analyser and the BSA can be attributed to temperature drift.

#### 6.2.5 Tune Ramp

Inevitably, all VCOs will suffer from a degree of post tuning drift. This is the transient frequency error observed on the application of a step change in voltage. Whilst this can be difficult to measure, since it will only become increasingly problematic as the sweep time is increased, the problem can be generally avoided by adjusting the ramp pattern as seen in Figure 6.10.

#### 6.2.6 Speed

One potential benefit of the BSA system is the speed at which measurements can be taken.

Typical DAQ systems are capable very of fast acquisitions. For instance, the NI USB-6211 has a maximum rate input and output rate of  $250 \text{ kS/s}$ . Assuming a minimum

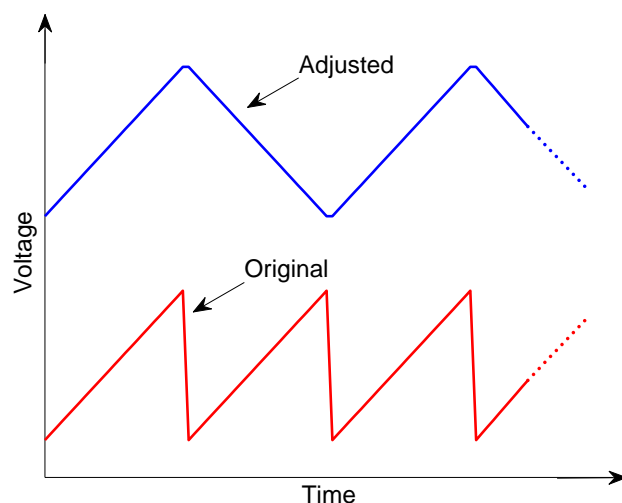


FIGURE 6.10: Modified frequency tune voltage ramp to minimise post tuning drift.

sweep of 50 points, this enables a trace rate of 5 kHz. Whilst many modern VNAs can perform sweeps at comparable rates, they typically lack the interface to be able to receive traces at this rate for processing. The NI USB-6211 contains an on-board waveform buffer so, for a limited time, 5 kHz measurements can be taken allowing material property changes on the order of milli-seconds to be measured.

It is important to ensure any op-amps used in any tune voltage signal conditioning have a bandwidth suitable for this operation.

### 6.2.7 Reflection Measurement

A more flexible system can be conceived which is shown in Figure 6.11. By utilising the isolated port on a circulator and an RF switch, a single system can measure either reflected or transmitted power. Practically, a significant limitation of this system will be the isolation the RF switch can provide. Cheap solid-state switches can practically only provide up to 40dB isolation. This effectively limits the dynamic range of the system to this value which is clearly highly undesirable. In reality, to avoid the complexities of a mechanical relay, it might be simpler to provide an external connection to the isolated port and either terminate it or connect it manually as required to the power meter input.

### 6.2.8 Filtering and Averaging

The primary filtering method is achieved by curve fitting the Lorentzian resonant line-shape as described in Section 2.6. For large numbers of points this is effective at reducing the random error associated with the measurement.

However, additional averaging can be done at the individual frequency points. In effect this can be seen as oversampling the ADC to increase effective resolution. Figure 6.12

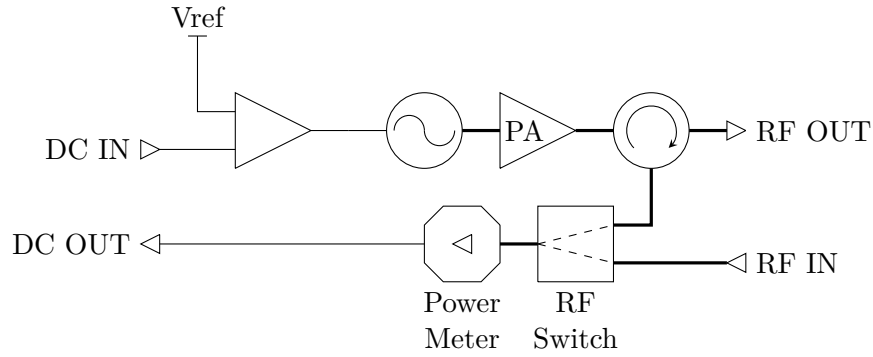


FIGURE 6.11: BSA system diagram extended to include switchable measurement of reflected power through the circulator.

demonstrates the effect this can have. It is particularly effective for lower numbers of samples which is useful to reduce noise whilst retaining a high sweep speed.

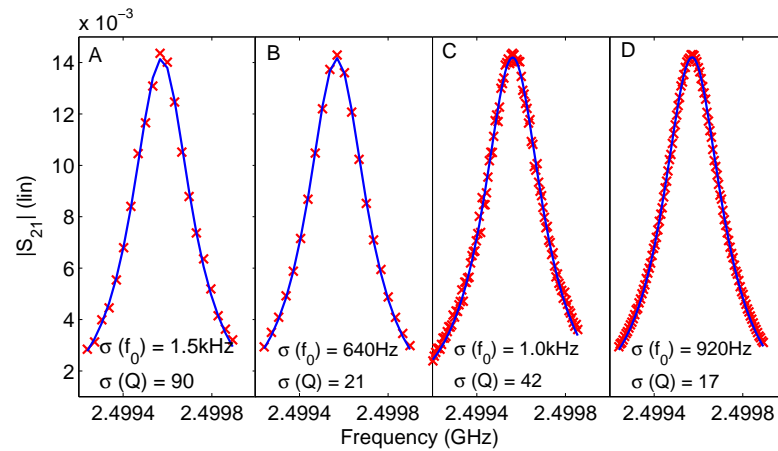


FIGURE 6.12: A comparison between averaging types showing the acquired data and subsequent Lorenzian fit. Obtained from prototype B with a point rate of 2kHz. Plots A and B contain 21 points and C and D contain 101 points. Plots A and C have no point averaging whereas in B and D each point is the average of 10 ADC samples. Additionally, the standard deviation over 100 sweeps for the resonant frequency and Q factor is shown in each case.  $Q = 8590$ .

## 6.3 Calibration

### 6.3.1 Frequency Calibration

Utilising an Agilent EXA N9010A spectrum analyser, the output frequency is measured across the input voltage range. As discussed in Section 6.2.2, due to a potential offset caused by imperfect isolation, the frequency is measured through a circulator or directional coupler placed in the signal path with the output left short-circuit.

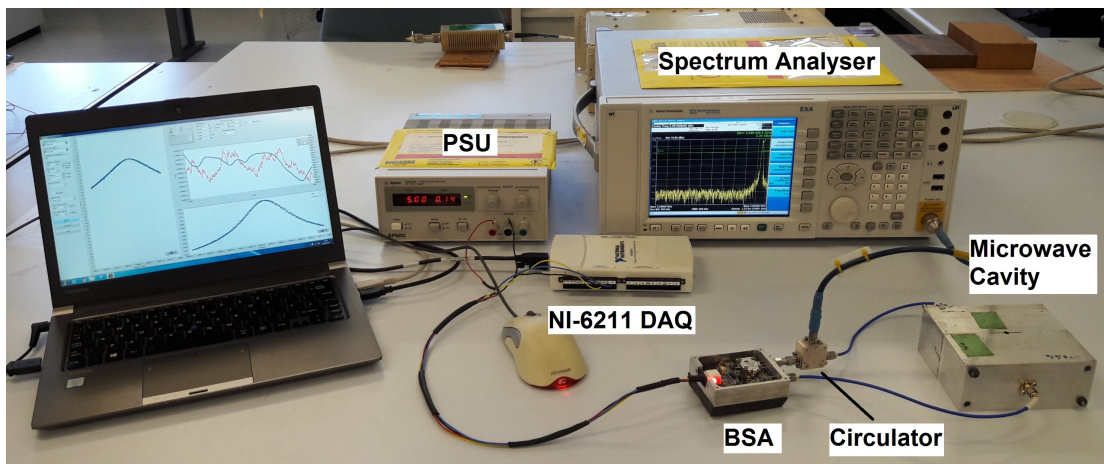


FIGURE 6.13: BSA calibration setup.

A polynomial curve is fitted to the data and subsequently used to specify the voltages for the DAC in order to generate the desired frequency points in the sweep. The raw frequency-voltage characteristic for prototype B and C can be seen below in Figure 6.14.

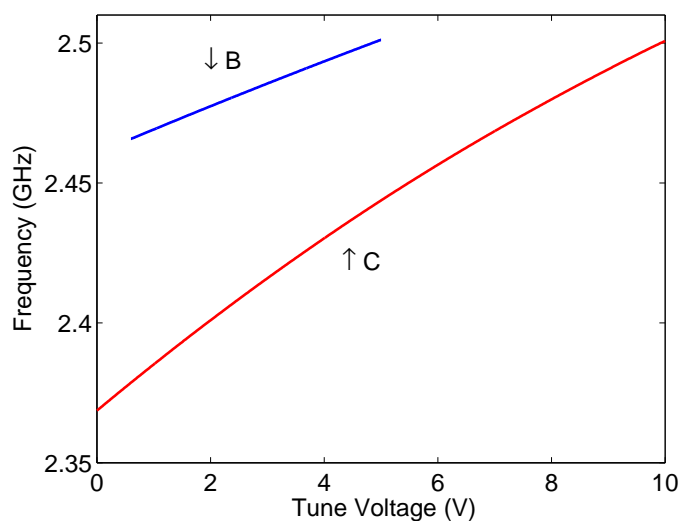


FIGURE 6.14: Output frequency characteristic for prototype BSAs B and C.

### 6.3.2 Power Meter Calibration

The response of the power meter is measured by utilising a variable attenuator connected as seen in Figure 6.15. It assumes that the variable attenuator, cabling and coupler are linear and do not vary across the measured frequency band.

The calibration proceeds as follows:

1. Set the variable attenuator to the minimum possible value.

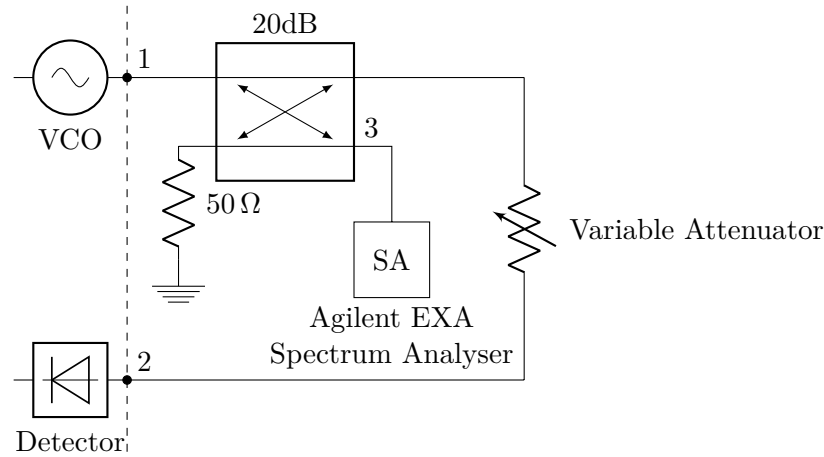


FIGURE 6.15: Calibration setup. Left of dashed line is BSA.

2. Measure, using a calibrated network analyser, the minimum loss in the complete calibration path. This is denoted by  $S_{21-min}$
3. Connect the BSA (Port 1 - RF in, Port 2 - RF out)
4. Measure, across the full range of tune voltages, the power, denoted by  $P_{3-min}$ , and frequency at Port 3.
5. Measure, across the full range of tune voltages, the power meter output voltage. The corresponding loss is then given by:  $Loss(dB) = P_{3-min} + P_3 + S_{21-min}$
6. Repeat Step 5, adjusting the variable attenuator each time until the desired number of points has been acquired.

The result is a set of response curves relating power meter output voltage and the loss between the input and output ports at a variety of excitation frequencies. A polynomial fit of the calibration data is used to calculate the corresponding loss of a measured voltage at the closest calibration frequency. Some variation is seen across the measurement band, particularly at low power levels, as seen in Figure 6.16. Whilst it is apparent that the noise floor of the power meter is lower than measured here ( $\sim 50$ dB), the noise floor of the measurement hardware was reached since it sees a signal attenuated by 20dB due to the directional coupler. Therefore only a measurement of  $|S_{21}| > 50$ dB can only be deemed valid, however, as is seen in Figure 6.17, this is close to the hardware limit.

An alternative method would be to measure the power meter and output frequency response separately using a calibrated signal source and power meter. This would enable absolute power measurements but the ‘closed-loop’ calibration described here has a distinct advantage since variations in the output power across the band and any non-linearity caused by coupling between the input and output circuits are accounted for automatically.

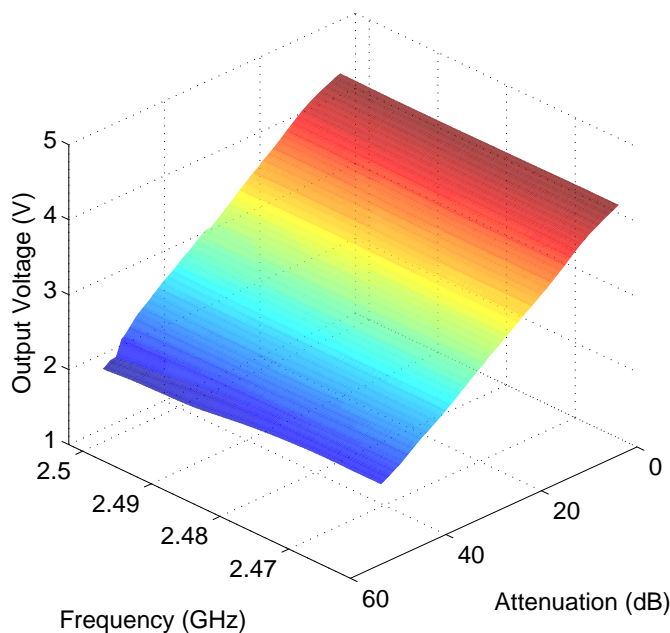


FIGURE 6.16: Measured power meter output voltage characteristic for prototype B.

After calibration, the resulting BSA response to a variable attenuator is seen in Figure 6.17. The apparent continuous nature of the noise floor suggests it is limited by imperfect isolation from the output stage and not the fundamental thermal noise floor. The maximum variation across the band, when measured through a fixed attenuator, in the middle of the range is seen to be  $\sim 0.6$  dB. In a 480 kHz band in the centre of the range, a span similar to a typical measurement bandwidth, this variation is reduced to  $<0.005$  dB. Finally, given a nominal input sensitivity of 0.16 mV, this translates to an input sensitivity of  $\sim 0.003$  dB.

## 6.4 Sample Measurements and Sensitivity

Since the BSA is designed for the specific purpose of cavity perturbation, its ultimate performance metric is its ability to resolve changes in resonator frequency and  $Q$ .

Figure 6.18 shows the perturbation of a 3 mm PTFE rod sample.

The random error was minimised using a span of 101 points narrowed the the 3 dB resonant bandwidth, an oversampling factor of 10 and a sample rate of 10 kHz. This results in a sweep speed of 10 ms.

Using the standard error formed from 20 sweeps, the resonant frequency and  $Q$  error is seen to be 110 Hz and 6.7 respectively. Note that this is the instantaneous measurement error and that measurements taken at different times are likely to be dominated by an error due to temperature drift. In order to maintain this precision, temperature would

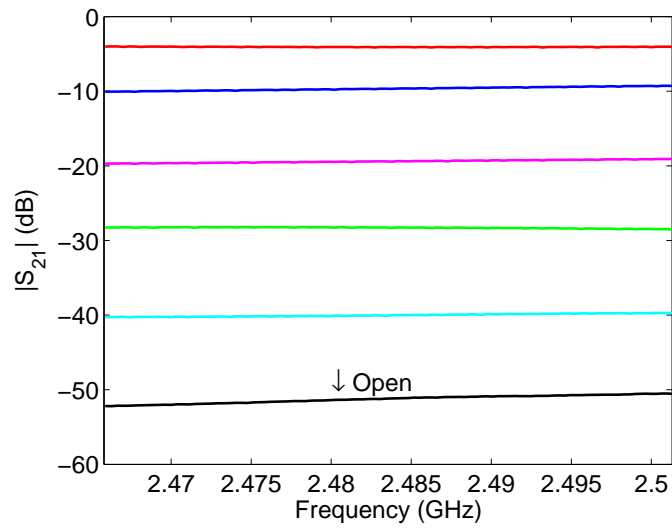


FIGURE 6.17: BSA output response to a variable attenuator showing the effectiveness of the calibration. Open response is also shown were the BSA input is left unconnected. Measured with prototype B with additional external circulator.

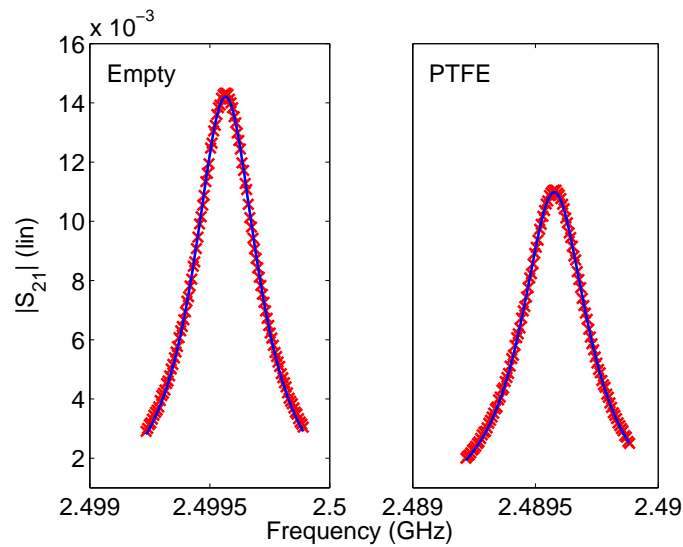


FIGURE 6.18: Raw measurement traces of cavity perturbation of a 3mm PTFE rod. Taken using Prototype B.

need to be held stable to less than  $0.001^{\circ}\text{C}$ . Therefore, without correction, uncertainty 1 or 2 orders of magnitude larger might be more realistic.

A comparison of the perturbation of the PTFE rod between the BSA and Agilent ENA is seen in Table 6.2. The small error in fractional frequency shift is very encouraging. Unsurprisingly, the discrepancy in Q shift is much larger due to its reliance on simultaneously accurate frequency and power readings.

	$\frac{f_s - f_0}{f_0}$	$\frac{1}{Q_0} - \frac{1}{Q_s}$
BSA	$-3.98 \times 10^{-3}$	$-3.74 \times 10^{-6}$
Agilent-ENA	$-4.00 \times 10^{-3}$	$-3.92 \times 10^{-6}$

TABLE 6.2: PTFE rod cavity perturbation comparison between BSA (Prototype B) and Agilent-ENA.

## 6.5 Discussion and Conclusions

This chapter has demonstrated the ability to produce a small and cheap electronic device which, through an optimised design and calibration procedure, is able to successfully undertake perturbation measurements.

Simple calibration was performed and the BSA was observed to accurately measure the Q and resonant frequency of a  $TM_{010}$  cavity in the empty and perturbed case. Further work should involve further characterisation by exercising across the full dynamic of the system with a variety of samples.

The main compromises in order to achieve the low cost has been the sacrifice of flexibility to allow for complex S-parameter measurements and a massively reduced bandwidth designed to target a specific resonant mode.

Whilst the accuracy and sensitivity is significantly less than what can be achieved with a commercial network analyser, the impact on perturbation measurements is not as significant because, as discussed in Section 2.11, the dominant form of error derives from sample preparation.

It should be stressed that the aim of this project has not been to develop a replacement for the commercial network analyser which can undertake highly accurate measurements. The BSA is intended to exploit the main advantage of perturbation measurements; the ability to detect small changes in sample properties. Therefore, as long as the raw sensitivity is available, it should be possible to calibrate for a specific application.

Within the context of this thesis, this chapter demonstrates the electronics required in order to develop a particle size sensor based upon the measurement principle explored in Chapter 3. At this level of cost and complexity, it is easily conceivable for a particle size sensor to be included in every SLM system - perhaps as part of an automated powder recycling procedure.

Before industrial application, it is appreciated that further development is required but it is expected that significant enhancements to the sensitivity and accuracy can be obtained without large investment by, for instance, reduction of supply noise and increasing isolation between the input and output stages. Further isolation between input and output paths could be achieved with mechanical design changes such as metallic separating walls between stages.

Errors due to temperature drift remain a significant concern. However, after thorough characterisation, it would be conceivable to add a temperature correction from an embedded temperature sensor without significantly impacting the unit cost.

Further enhancements could include the addition of a frequency monitoring port separate from the main signal path and active monitoring of the output power. The active monitoring could significantly increase performance by introducing common mode rejection of noise on the amplifier and power meter bias voltages. This would be achieved by taking the output as the difference between the detected output and input power levels. This would require the addition of a board level coupler and second power meter integrated circuit.



## Chapter 7

# Heating in a Single-Mode Cavity Resonator

### 7.1 Introduction

The single-mode approach to microwave heating is a well established technique. Reactors can be purchased commercially with efficiency and control being the main selling features. For instance, CEM Microwave provide one of the most popular single mode ‘microwave synthesizers’ [171, 172]. However, their technology still relies on a magnetron for microwave generation which limits the degree of control available. Techniques are available which can control the power output of the magnetron [173] or control the delivered power to a cavity through a frequency offset or impedance mismatch [174] but due to the relatively broadband nature of a magnetron they are unlikely to match modern, solid-state microwave sources and amplifiers which can be utilised to allow fine control of the applied power.

The various design constraints are discussed in the following chapter but systems which incorporate all the features necessary for precise control and flexibility and which cater to the desired sample geometries cannot be obtained easily or affordably. Therefore, bespoke systems need to be developed to cater to all these requirements.

Simultaneous measurement of dielectric properties through perturbation techniques is another useful feature a system can incorporate. Techniques which use a separate measurement mode have been previously demonstrated [175] with the obvious disadvantage of needing relatively broadband control electronics. It is possible to use a single mode for simultaneous heating and characterisation by sweeping the application frequency. However, care must be taken to ensure power delivery is maintained and controlled as the system match will vary significantly with frequency [176].

Another approach to mode tracking and simultaneous measurement was demonstrated in [177]. Whilst increasing complexity significantly, it enables continuous uninterrupted

power application and narrow-band operation. The approach involves using a mixer to modulate the high power carrier to produce a double side-band spectrum. The transmission of the side-bands are then monitored to calculate the resonator parameters.

In addition to heating, electro-magnetic effects can be observed in samples by exposure to high strength fields. In order to avoid heating, power can be continuously pulsed at high speed. Solid state switched allow very fast switch speeds with rise times to the order of ns and pulse durations less than 100 $\mu$ s. In this way, the power delivery can be finely modulated whilst keeping the field strength high.

## 7.2 Theory of Operation

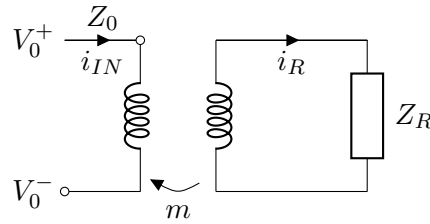


FIGURE 7.1: Single port resonator equivalent circuit.

Analysing the circuit model in Figure 7.1, a detailed understanding of the coupling behaviour of a resonator excited by a single port can be understood. To begin, form the following base relations:

$$v_0^+ - v_0^- = Z_0 \cdot i_{IN} \quad (7.1)$$

$$j\omega_0 i_{IN} m + i_R Z_R = 0 \quad (7.2)$$

$$v_0^+ + v_0^- = j\omega_0 m \cdot i_R \quad (7.3)$$

Substituting the first and second into the third gives,

$$v_0^+ + v_0^- = \frac{\omega_0^2 m^2}{Z_R Z_0} (v_0^+ - v_0^-) \quad (7.4)$$

This is further simplified by replacing the complex resonator impedance  $Z_R$  with (Equation 2.26)

$$Z_R = R \left( 1 + 2jQ \frac{\omega - \omega_0}{\omega_0} \right) \quad (7.5)$$

and finally, knowing that  $S_{11} = \frac{v_0^-}{v_0^+}$  we can form an expression for the reflection coefficient

$$S_{11} = \frac{g - 1 - 2jQ \frac{\Delta\omega}{\omega_0}}{g + 1 + 2jQ \frac{\Delta\omega}{\omega_0}} \quad (7.6)$$

where

$$g = \frac{\omega_0^2 m^2}{Z_0 R} = \frac{\omega_0 m^2 Q}{Z_0 L} \quad (7.7)$$

At resonance ( $\Delta\omega = 0$ ), this simplifies to

$$S_{11} = \frac{g - 1}{g + 1} \quad (7.8)$$

It is observed that when  $g = 1$ , this expression reduces to zero. In this condition, the resonator is said to be critically coupled and all the supplied energy is coupled into the resonator; no energy is reflected back to the source and the cavity system is matched to the feed impedance.

In order to initially setup this critical condition, the mutual inductance,  $m$ , is modified. In the setup demonstrated here, coupling is achieved with a short circuit loop on the cavity side wall (Figure 7.2). The mutual inductance and subsequent coupling co-efficient  $g$  is modified by changing its effective area; achieved by rotating the loop.

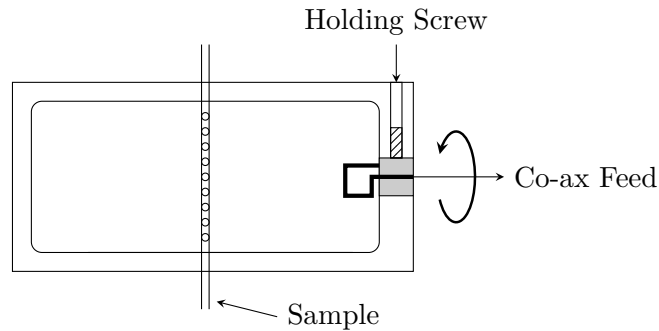


FIGURE 7.2: Single-mode microwave heating cavity cut-away diagram. The sample is positioned in order to maximise exposure to electric or magnetic field as required. In the typical  $TM_{010}$  setup and for electric field heating, the sample is placed axially and coupling is provided by a short circuit loop. The loop is held by a screw but can be rotated in order to modify the coupling co-efficient and achieve critical coupling.

The loop must be made large enough such that critical coupling is possible given the resonator  $Q$ . However, it is desirable to keep the loop small within this limit since increasing the loop size means increasingly small changes in rotation are required to achieve critical coupling. Figure 7.3 shows real data as the loop is rotated and the cavity cycles through the under, over and critically coupled states. Typically,  $|S_{11}|$  reaches a minimum of  $<-40\text{dB}$ . This corresponds to 99.99% power transmission into the resonator system.

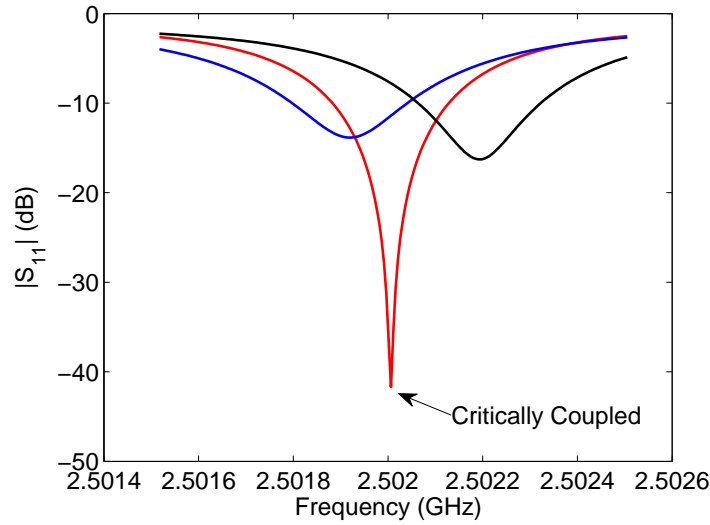


FIGURE 7.3: Effect of rotating coupling loop to the reflected power. At a specific position,  $|S_{11}|$  is minimised and the cavity is critically coupled. Either side of this position the cavity is under or over coupled. The resonant frequency is also modified during rotation due to the perturbation by the coupling loop.

Close inspection of Equation 7.7 reveals that  $g$  is also both a function of the excitation frequency  $\omega_0$  and Q-factor. This presents additional challenges.

As a sample is heated, it is typical for its EM properties to change which will lead to changes in the resonator frequency and Q. Firstly, it is important that the centre frequency is tracked by the driving oscillator to maintain optimum power delivery but, in addition, the coupling may require adjusting to maintain the critical condition.

For most liquid samples, the effect can be very pronounced. For instance, it is well known that the dielectric constant and loss factor of water will significantly decrease with temperature [178]. Figure 7.4 demonstrates the effect as water is heated within a  $TM_{010}$  cavity without frequency or coupling control. However, for the majority of samples, simple frequency tracking without tuning of the coupling is sufficient to main acceptable levels of reflected power.

Next, in order to calculate the precise energy dissipated within the sample, the following is considered.

The power dissipated in the resonator,  $P_{diss}$ , is related to the power delivered by the source,  $P_{in}$ , by

$$P_{diss} = (1 - |S_{11}|^2)P_{in} \quad (7.9)$$

and the total power dissipated has contributions from the cavity walls,  $P_c$ , and the sample,  $P_s$ ,

$$P_{diss} = P_s + P_c \quad (7.10)$$

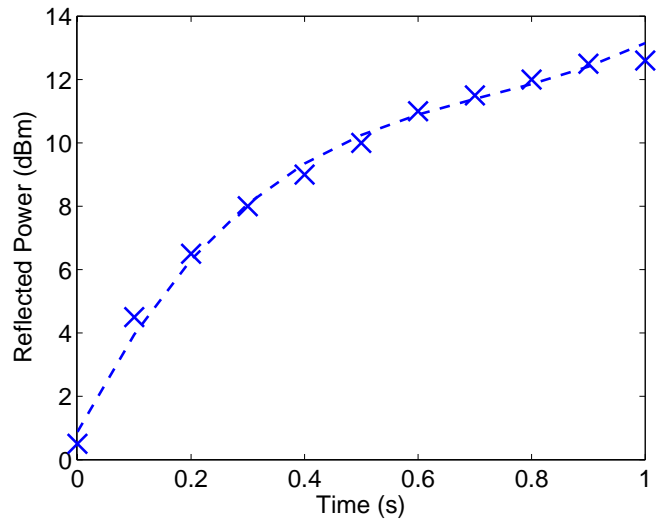


FIGURE 7.4: Reflected power as water is heated via electric field in the  $TM_{010}$  mode. Reflected power is seen to increase as the cavity becomes increasingly de-tuned due to the changing dielectric properties of water.

The  $Q$  of the resonator loaded by the sample is

$$\frac{1}{Q} = \omega \frac{U}{P_{diss}} = \omega \frac{U}{P_s + P_c} \quad (7.11)$$

where  $U$  is the total energy stored in the resonator. The total  $Q$  is then seen to be composed of a contribution from the sample and metal wall

$$\frac{1}{Q} = \frac{1}{Q_c} + \frac{1}{Q_s} \quad (7.12)$$

The ratio of energy lost in the cavity walls compared to the whole system is then

$$\frac{P_c}{P_{diss}} = \frac{Q}{Q_c} \quad (7.13)$$

which leads to the energy lost in the sample;

$$P_s = P_{diss} \left( 1 - \frac{Q}{Q_c} \right) \quad (7.14)$$

Therefore, by measuring the  $Q$  of the empty cavity and the  $Q$  once loaded by the sample the system energy balance is known.

It is desirable to maximise the empty cavity to increase the efficiency of energy delivery to the sample. Cavities can be designed with high  $Q$ -factors, typically  $>10\,000$ , which allow systems to be designed where the majority of energy can be dissipated in the sample. For a non-depolarising geometry, from perturbation theory (Equation 2.14b),  $Q_s$  is

$$\frac{1}{Q_s} = \frac{\varepsilon_2 V_s}{G_{nmp} V_c} \quad (7.15)$$

Using this, it is calculated that for a 0.13cc sample of water with  $\varepsilon_2 = 9$  [179], in the standard 4.6cm radius TM<sub>010</sub> cavity with an unloaded Q of 10 000,  $P_s$  is 99.4% of  $P_{diss}$ .

As has been stated, knowledge of the loaded and unloaded resonator Q can be used to calculate the proportion of energy dissipated within the sample. It is therefore convenient to have a mechanism for measurement of this quantity. Usually this is done using a weakly coupled transmission measurement as detailed in previous chapters, however, this is not always available in a one port heating system. It is possible to extract the Q from the  $S_{11}$  trace using Equation 7.6, however, it is convenient to consider the following:

$$|S_{11}|^2 = \frac{(1 - g)^2 + 4Q^2 \left(\frac{\Delta\omega}{\omega_0}\right)^2}{(1 + g)^2 + 4Q^2 \left(\frac{\Delta\omega}{\omega_0}\right)^2} \quad (7.16)$$

$$\begin{aligned} 1 - |S_{11}|^2 &= \frac{4g}{(1 + g)^2 + 4Q^2 \left(\frac{\Delta\omega}{\omega_0}\right)^2} \\ &= \frac{P_0}{1 + 4Q_L^2 \left(\frac{\Delta\omega}{\omega_0}\right)^2} \end{aligned} \quad (7.17)$$

It is observed that Equation 7.17 above is a similar lorentzian line-shape as measured by  $S_{21}$  and can be used to extract the Q-factor. In this case,  $Q = Q_L(1 + g)$ . The co-efficient  $g$  can be calculated from the value of  $S_{11}$  at the centre frequency when  $\Delta\omega = 0$ .

A typical  $S_{11}$  and transformed lorentzian plot can be seen in Figure 7.5.

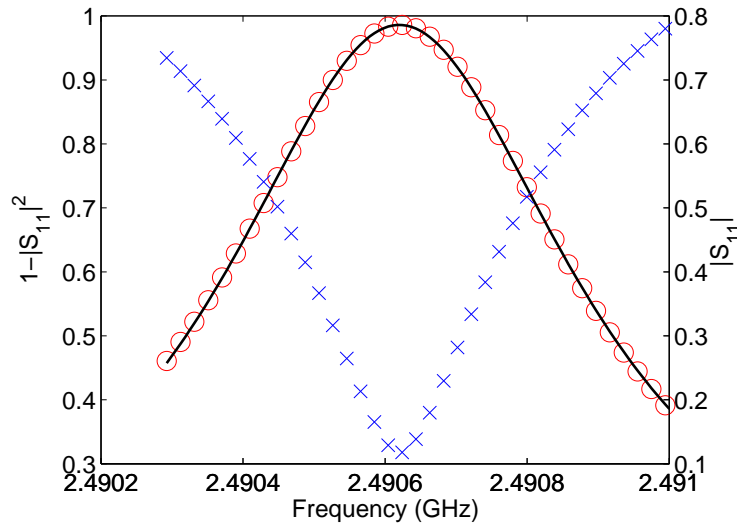


FIGURE 7.5:  $|S_{11}|$  transformed to lorentzian line-shape in order to extract Q using curve fitting procedure.

Since the magnitude of Equation 7.8 is taken,  $g$  can take two reciprocal values;  $g = \frac{1+|S_{11}|}{1-|S_{11}|}$  or  $\frac{1-|S_{11}|}{1+|S_{11}|}$ , representing the over and under-coupled cases. With an insertion loss of -30dB, selecting the incorrect  $g$  would result in a 0.4% inaccuracy in the unloaded  $Q$ ; an error higher than the typical measurement noise. Care must be taken when coupling the resonator to make sure the assumed value of  $g$  is correct. For instance, if using the rotating loop technique to achieve critical coupling, the under-coupled value of  $g$  can safely be assumed by starting the loop in the position of minimal coupling and rotating until the desired value  $|S_{11}|$  is achieved without passing the critical point.

### 7.3 System Description

Figure 7.6 shows the basic system construction. The various components connect via USB to a PC where control software is used to control the heating.

The switch is included to allow for high speed RF pulsing. By rapidly changing the switch position with varying duty cycle, the average power delivered to the cavity can be finely tuned. The switch allows for two RF paths: in the first position the signal is minimally attenuated and in the other the signal is effectively attenuated 20dB by the directional coupler. This ensures a signal is still present in the 'off' state allowing for the coupling condition to be continuously monitored.

Additionally, by sweeping the source frequency and using the attenuated path, the reflection co-efficient,  $|S_{11}|$ , can be obtained without heating the sample. This is useful for adjusting the coupling loop.

The second coupler allows for continuous monitoring of the input power.

The amplifier has 50dB gain with 1dB compression at 44dBm. The purpose of the 15dB pre-amp is to ensure full dynamic range of the PA can be obtained since the variable attenuator has a minimum insertion loss of 10dB.

The software includes a routine whereby, at periodic intervals (typically every 2-5s), the oscillator is swept in a small span around the excitation frequency and the reflected power synchronously measured. The frequency at which least reflection occurs is set as the new excitation frequency. In this way power delivery is kept high.

In addition to the main N-Type coupling, the cavity includes 2 weakly coupled SMA loops. The purpose of these is to perform dielectric characterisation using a standard 2-port network analyser. One port characterisation was not suitable in this case due to the slow sweep speed required to synchronise the oscillator and power meters; in order to sweep with enough points to accurately determine cavity  $Q$ , the system would spend significant time de-tuned allowing the sample to cool. In order to isolate the VNA from the high power system, a switch arrangement was constructed as seen in Figure 7.8. Using a simple diode capacitor arrangement with a schmitt trigger, a short delay (Measured at ~2ms) is introduced to guarantee isolation between the high power

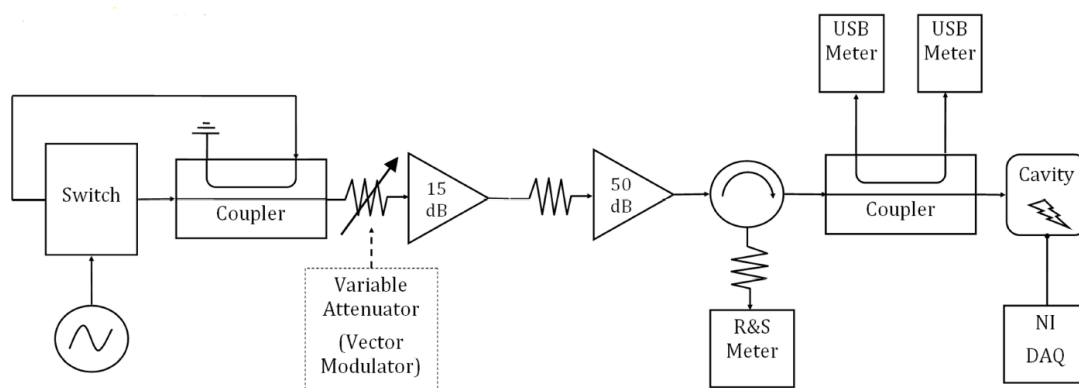


FIGURE 7.6: Heating system schematic.

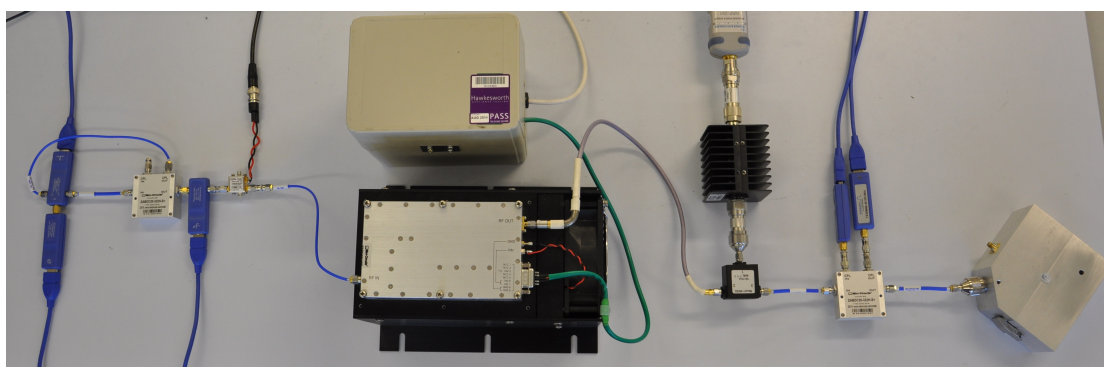


FIGURE 7.7: Heating system with 30W RFPA.

excitation and VNA. It can be driven either from an external +5V signal or by the operation of the toggle switch.

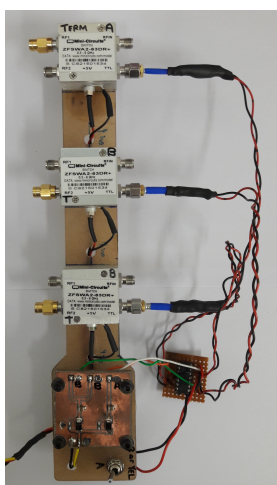


FIGURE 7.8: VNA isolator switch configuration.

By way of demonstration, using this setup, an epoxy resin (Hexel RTM6-2), held in a 3mm wide straw, was heated at 2.5 GHz axially in  $TM_{010}$  and the dielectric response recorded as shown in Figure 7.9. The response is typical of an epoxy during heat

treatment [180]. Initially the loss and dielectric constant increases as the resin becomes a gel before gradual decrease during the cure. Once allowed to cool, the rod has visibly hardened and the permittivity decreased.

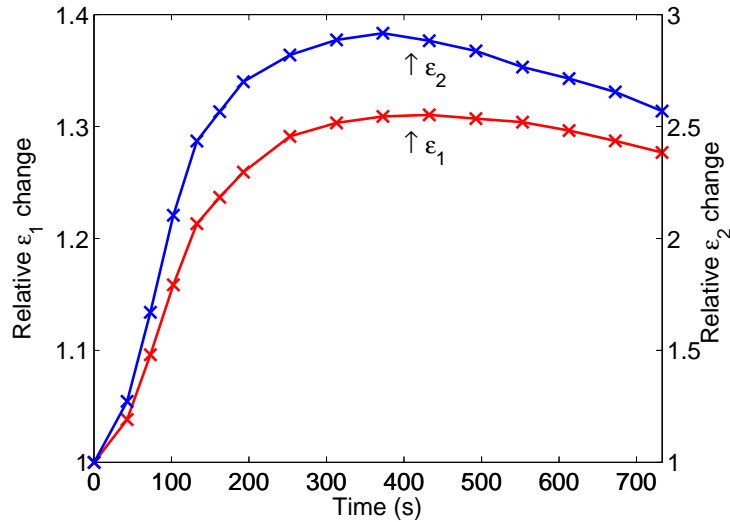


FIGURE 7.9: Dielectric response measured during simultaneous dielectric heating of epoxy resin. Maximum temperature of approximately  $60^\circ\text{C}$  reached.

## 7.4 Conclusion

Through the work undertaken here, a comprehensive understanding of the challenges surrounding microwave heating have been explored and experienced experimentally. However, the initial system has many shortcomings and potential improvements; significant further work is required to refine the system. The main next step is to produce a custom source circuit with embedded control which combines all the elements described in the system. By removing the inherent latency present in USB control, opportunities for fast control and characterisation can be realised.

With this high speed embedded circuit, it is envisaged that various algorithms for mode tracking, coupling control and material characterisation can be experimented with. The main goal being consistent and well-characterised power delivery to a sample. In the case of simultaneous mode tracking and coupling control, a significant challenge will be to uncouple the two effects since, in both cases, the non-optimal setup results in increased power reflection. For instance, experiments could be undertaken where extremely narrow band but continuous sweeps take place and the gradient analysed to determine proximity to the minimum value of  $S_{11}$ .

Additionally, temperature feedback control can be implemented with the use of a non-contact or non-metallic temperature probe such as IR spectroscopy or a fluoropic probe. Within the context of this thesis, single-mode microwave heating could have significant impact in the development of microwave heating technology for use in ALM. The

majority of powder bed fusion technologies, both metallic and non-metallic, require pre-heating of the powder bed before laser application. Microwave power can potentially fulfill this role allowing for cheaper laser technology or simpler mechanical design requiring less insulation. In order for this to succeed, comprehensive understanding of the bulk heating properties of the powders must be obtained. A single-mode approach can contribute to this.

## Chapter 8

# Final Summary and Further Work

### 8.1 Microwave Cavity Perturbation

Whilst the cavity perturbation technique is approaching 75 years old, its still encourages much discussion. The work presented here provides all the information required in order to design a cavity perturbation system and undertake measurements of both electric permittivity and magnetic permeability. The technique offers a number of advantages including relatively simple sample geometry and preparation requirements and the potential for high precision comparisons.

Furthermore, careful selection of the cavity construction allows the technique to be extended over a broad temperature range with measurements here possible up to 300°C. and by using a reference mode, very fine temperatures changes, not typically possible with traditional techniques, can be monitored and corrected for.

Whilst the aluminium cavity construction prevents the extension to temperatures much higher than this, construction in copper and an isolated waveguide feed system could extend this range dramatically opening up the potential for dielectric or magnetic spectroscopy on a a much greater variety of chemistry.

### 8.2 Perturbation and Metal Powders

In the magnetic field, this thesis was able to demonstrate the ability to monitor the average particle size within a spherical metallic powder using the perturbation technique across 3 frequencies using different resonant modes.

The next step in this work would be the real-world demonstration of this technique in the manufacturing context. The ultimate goal being the ability to use the measurements as an input to an automatic powder or machine control system.

From a scientific perspective, further work could also concern the effect of non-spherical particles.

Concerning the electric field, some indirect evidence for the action of the oxide layer was observed by heating the powder. However, measurements in the electric field were found to be very sensitive to electrical contacts between particles which are very difficult to control when the powder is measured in its bulk form. Further work here could investigate different sample preparation methods to potentially suspend the powder negating this problem.

### 8.3 SLM and Surface Resistance

The work here presents the first systematic study of microwave surface resistance of surfaces produced by SLM where two parameters, build orientation and surface finish were controlled.

However, a large number of process parameters remain unexplored. For instance: the laser scan strategy; various mechanical and chemical polishing techniques; post-build heat treatment temperature and atmosphere and sample geometry.

In addition, to further investigate the potential of surface resistance as a measure of mechanical performance it would be interesting to compare parts where build quality has been intentionally compromised by, for instance, reducing laser power or using deteriorated feedstock.

### 8.4 Cavity Q and Annealing

Chapter 5 examined the, as yet unexplored link, between residual stress in machined aluminium and microwave cavity Q. It was observed that the annealing of an aluminium cavity permanently increased its conductivity as shown by an increased resonant Q. XRD was used to confirm the hypothesis that high temperature annealing of the aluminium-alloy was reducing residual stresses formed during machining and causing precipitation of solute impurities. The application and significance of these measurements is that, in order to undertake high temperature perturbation measurements, the cavity must first be heat treated to stabilise its resonant Q.

Whilst a general link was made, significant further work could be undertaken in order to further quantify the effects. This could involve different aluminium grades, machining types and treatment regimes.

### 8.5 Scalar Network Analyser

Whilst in the research lab use of an expensive, broad-band and high precision VNA is appropriate, in order for the perturbation technique to remain relevant in a commercial context, it is vital that low-cost measurement electronics can be obtained. By way of

demonstration, a small, cheap scalar network analyser is produced designed around the excitation of a single cavity mode.

## 8.6 Single-mode Microwave Heating

The details concerning the design of a single-mode microwave heating system were presented and discussed. Using this knowledge a basic heating system was developed able to dynamically track the resonant mode in order to maintain consistent power application. Following this PhD, further work is commencing to significantly progress this system. Using embedded control it is hoped that various mode tracking algorithms can be explored to maximise power delivery. Additionally, dynamic electrical control of coupling is desirable and could be investigated using a veractor or other variable components to modify the cavity impedance.

## 8.7 Closing Remarks

Application of microwave techniques in the area of additive layer manufacturing has proven to be a fruitful endeavour. Modern advances in electronics has made these measurements affordable and they can often provide information only accessible by much more complex techniques. I hope this thesis begins a long and fruitful collaboration between Cardiff University and Renishaw plc as they look to leverage and bring together expertise in two distinct areas.



# Bibliography

- [1] Renishaw, “Metals for Additive Manufacturing - Data Sheets.” [Online]. Available: <http://www.renishaw.com/en/data-sheets-additive-manufacturing--17862> [Accessed: 2017-01-04]
- [2] W. Meiners, K. Wissenbach, and A. Gasser, “Selective Laser Sintering at Melting Temperature,” *US Patent, US6215093 B1*, 1996.
- [3] Renishaw, “AM250 Laser Melting (metal 3D printing) Machine.” [Online]. Available: <http://www.renishaw.com/en/am250-laser-melting-metal-3d-printing-machine--15253> [Accessed: 2015-03-20]
- [4] M. Seifi, A. Salem, J. Beuth, O. Harrysson, and J. J. Lewandowski, “Overview of Materials Qualification Needs for Metal Additive Manufacturing,” *Journal of The Minerals, Metals & Materials Society*, vol. 68, no. 3, pp. 747–764, 2016.
- [5] W. E. Frazier, “Metal additive manufacturing: A review,” *Journal of Materials Engineering and Performance*, vol. 23, no. 6, pp. 1917–1928, 2014.
- [6] M. Mahesh, B. Lane, A. Donmez, S. Feng, S. Moylan, and R. Fesperman, “Measurement Science Needs for Real-time Control of Additive Manufacturing Powder Bed Fusion Processes,” *National Institute of Standards and Technology*, 2015.
- [7] W. J. Sames, F. A. List, S. Pannala, R. R. Dehoff, and S. S. Babu, “The metallurgy and processing science of metal additive manufacturing,” *International Materials Reviews*, vol. 61, no. 5, pp. 315–360, 2016.
- [8] B. Ferrar, L. Mullen, E. Jones, R. Stamp, and C. J. Sutcliffe, “Gas flow effects on selective laser melting (SLM) manufacturing performance,” *Journal of Materials Processing Technology*, vol. 212, no. 2, pp. 355–364, 2012.
- [9] P. O’Regan, P. Prickett, R. Setchi, G. Hankins, and N. Jones, “Metal Based Additive Layer Manufacturing: Variations, Correlations and Process Control,” *Procedia Computer Science*, vol. 96, pp. 216–224, 2016.
- [10] J. A. Slotwinski, E. J. Garboczi, and K. M. Hebenstreit, “Porosity Measurements and Analysis for Metal Additive Manufacturing Process Control,” *Journal of*

- Research of the National Institute of Standards and Technology*, vol. 119, pp. 494–527, 2014.
- [11] H. W. Mindt, M. Megahed, N. P. Lavery, M. A. Holmes, and S. G. R. Brown, “Powder Bed Layer Characteristics: The Overseen First-Order Process Input,” *Metallurgical and Materials Transactions A: Physical Metallurgy and Materials Science*, vol. 47, no. 8, pp. 1–12, 2016.
- [12] R. J. Hebert, “Viewpoint: metallurgical aspects of powder bed metal additive manufacturing,” *Journal of Materials Science*, vol. 51, no. 3, pp. 1165–1175, 2016.
- [13] S. K. Everton, M. Hirsch, P. Stravroulakis, R. K. Leach, and A. T. Clare, “Review of in-situ process monitoring and in-situ metrology for metal additive manufacturing,” *Materials & Design*, vol. 95, pp. 431–445, 2016.
- [14] R. Sorrentino and O. A. Peverini, “Additive manufacturing: A key enabling technology for next-generation microwave and millimeter-wave systems,” *Proceedings of the IEEE*, vol. 104, no. 7, pp. 1362–1366, 2016.
- [15] M. D’Auria, W. J. Otter, J. Hazell, B. T. W. Gillatt, C. Long-Collins, N. M. Ridler, and S. Lucyszyn, “3-D Printed Metal-Pipe Rectangular Waveguides,” *IEEE Transactions on Components, Packaging and Manufacturing Technology*, vol. 5, no. 9, pp. 1339–1349, 2015.
- [16] E. A. Rojas-Nastrucci, J. Nussbaum, T. M. Weller, and N. B. Crane, “Meshed Rectangular Waveguide for High Power, Low Loss and Reduced Weight Applications,” in *2016 IEEE MTT-S International Microwave Symposium*, San Francisco, 2016.
- [17] P. I. Deffenbaugh, T. M. Weller, and K. H. Church, “Fabrication and Microwave Characterization of 3D Printed Transmission Lines,” *IEEE Microwave and Wireless Components Letters*, vol. 25, no. 12, pp. 1–3, 2015.
- [18] N. Arnal, T. Ketterl, Y. Vega, J. Stratton, C. Perkowski, P. Deffenbaugh, K. Church, and T. Weller, “3D multi-layer additive manufacturing of a 2.45 GHz RF front end,” in *2015 IEEE MTT-S International Microwave Symposium*, Phoenix, 2015.
- [19] M. Liang, C. Shemelya, E. MacDonald, and H. Xin, “3D printed multilayer microstrip line structure with vertical transition toward integrated systems,” in *2015 IEEE MTT-S International Microwave Symposium*, Phoenix, 2015.
- [20] H. Kazemi, D. Miller, A. Mohan, Z. Griffith, Y. Jin, J. Kwiatkowski, L. Tran, and M. Crawford, “350mW G-band medium power amplifier fabricated through a new method of 3D-copper additive manufacturing,” in *2015 IEEE MTT-S International Microwave Symposium*, Phoenix, 2015, pp. 1–3.

- [21] D. L. Creedon, M. Goryachev, N. Kostylev, T. B. Sercombe, and M. E. Tobar, "A 3D printed superconducting aluminium microwave cavity," *Applied Physics Letters*, vol. 109, no. 3, pp. 3–6, 2016.
- [22] B. Zhang, Z. Zhan, Y. Cao, H. Gulan, P. Linner, J. Sun, T. Zwick, and H. Zirath, "Metallic 3-D Printed Antennas for Millimeter- and Submillimeter Wave Applications," *IEEE Transactions on Terahertz Science and Technology*, vol. 6, no. 4, pp. 1–9, 2016.
- [23] B. Zhang and H. Zirath, "A Metallic 3-D Printed E-Band Radio Front End," *IEEE Microwave and Wireless Components Letters*, vol. 26, no. 5, pp. 10–12, 2016.
- [24] G. L. Huang, S. G. Zhou, T. H. Chio, and T. S. Yeo, "Fabrication of a High-Efficiency Waveguide Antenna Array via Direct Metal Laser Sintering," *IEEE Antennas and Wireless Propagation Letters*, vol. 15, pp. 622–625, 2016.
- [25] J. A. Lorente, M. M. Mendoza, A. Z. Petersson, L. Pambaguian, A. A. Melcon, and C. Ernst, "Single part microwave filters made from selective laser melting," in *39th European Microwave Conference*, Rome, 2009, pp. 1421–1424.
- [26] J. Karlsson, A. Snis, H. Engqvist, and J. Lausmaa, "Characterization and comparison of materials produced by Electron Beam Melting (EBM) of two different Ti-6Al-4V powder fractions," *Journal of Materials Processing Technology*, vol. 213, no. 12, pp. 2109–2118, 2013.
- [27] R. Engeli, T. Etter, S. Hövel, and K. Wegener, "Processability of different IN738LC powder batches by selective laser melting," *Journal of Materials Processing Technology*, vol. 229, pp. 484–491, 2016.
- [28] J. Whiting and J. Fox, "Characterization of Feedstock in the Powder Bed Fusion Process: Sources of Variation in Particle Size Distribution and the Factors that Influence them," in *International Solid Freeform Fabrication Symposium*, Austin, 2016.
- [29] H. Gu, H. Gong, J. J. S. Dilip, D. Pal, A. Hicks, H. Doak, and B. Stucker, "Effects of Powder Variation on the Microstructure and Tensile Strength of Ti6Al4V Parts Fabricated by Selective Laser Melting," *International Journal of Powder Metallurgy*, vol. 51, no. 1, pp. 470–483, 2015.
- [30] B. Liu, R. Wildman, C. Tuck, I. Ashcroft, and R. Hague, "Investigation the Effect of Particle Size Distribution on Processing Parameters Optimisation in Selective Laser Melting Process," in *International Solid Freeform Fabrication Symposium*, Austin, 2011, pp. 227–238.
- [31] I. M. Robertson and G. B. Schaffer, "Some Effects of Particle Size on the Sintering of Titanium and a Master Sintering Curve Model," *Metallurgical and Materials*

- Transactions A: Physical Metallurgy and Materials Science*, vol. 40, no. 8, pp. 1968–1979, 2009.
- [32] J. A. Slotwinski, E. J. Garboczi, P. E. Stutzman, C. F. Ferraris, S. S. Watson, and M. A. Peltz, “Characterization of Metal Powders Used for Additive Manufacturing,” *Journal of Research of the National Institute of Standards and Technology*, vol. 119, pp. 460–493, 2014.
- [33] B. J. Dawes and R. Bowerman, “Introduction to the Additive Manufacturing Powder Metallurgy Supply Chain,” *Johnson Matthey Technology Review*, vol. 59, no. 3, pp. 243–256, 2015.
- [34] R. O’Leary, R. Setchi, P. Prickett, G. Hankins, and N. Jones, “An Investigation into the Recycling of Ti-6Al-4V Powder Used Within SLM to Improve Sustainability,” *SDM’2015: 2nd International Conference on Sustainable Design and Manufacturing*, (2015), pp. 14–17, 2015.
- [35] H. P. Tang, M. Qian, N. Liu, X. Z. Zhang, G. Y. Yang, and J. Wang, “Effect of Powder Reuse Times on Additive Manufacturing of Ti-6Al-4V by Selective Electron Beam Melting,” *Journal of The Minerals, Metals & Materials Society*, vol. 67, no. 3, pp. 555–563, 2015.
- [36] V. Seyda, N. Kaufmann, and C. Emmelmann, “Investigation of Aging Processes of Ti-6Al-4 V Powder Material in Laser Melting,” *Physics Procedia*, vol. 39, pp. 425–431, jan 2012.
- [37] A. Strondl, O. Lyckfeldt, H. Brodin, and U. Ackelid, “Characterization and Control of Powder Properties for Additive Manufacturing,” *Journal of The Minerals, Metals & Materials Society*, vol. 67, no. 3, pp. 549–554, 2015.
- [38] A. Porph, D. Slocombe, and P. P. Edwards, “Microwave Absorption in Powders of Small Conducting Particles for Heating Applications.” *Physical Chemistry Chemical Physics : PCCP*, vol. 15, no. 8, pp. 2757–63, 2013.
- [39] L. Chen, C. Ong, C. Neo, V. Varadan, and V. Varadan, *Microwave Electronics: Measurement and Materials Characterisation*. Chichester: John Wiley & Sons, 2004.
- [40] A. P. Gregory and R. N. Clarke, “A review of RF and microwave techniques for dielectric measurements on polar liquids,” *IEEE Transactions on Dielectrics and Electrical Insulation*, vol. 13, no. 4, pp. 727–743, 2006.
- [41] D. J. Rowe, A. Porph, D. A. Barrow, and C. J. Allender, “Novel Coupling Structure for the Resonant Coaxial Probe,” *IEEE Transactions on Microwave Theory and Techniques*, vol. 60, no. 6, pp. 1699–1708, 2012.

- [42] A. A. Abduljabar, D. J. Rowe, A. Porch, and D. A. Barrow, "Novel Microwave Micro fluidic Sensor Using a Microstrip Split-Ring Resonator," *IEEE Transactions on Microwave Theory and Techniques*, vol. 62, no. 3, pp. 1–10, 2014.
- [43] J. Krupka, A. P. Gregory, O. C. Rochard, R. N. Clarke, B. Riddle, and J. Baker-Jarvis, "Uncertainty of complex permittivity measurements by split-post dielectric resonator technique," *Journal of the European Ceramic Society*, vol. 21, no. 15, pp. 2673–2676, 2001.
- [44] S. Palanivel, A. K. Dutt, E. J. Faierson, and R. S. Mishra, "Spatially dependent properties in a laser additive manufactured Ti-6Al-4V component," *Materials Science and Engineering A*, vol. 654, pp. 39–52, 2016.
- [45] E. C. Santos, K. Osakada, M. Shiomi, Y. Kitamura, and F. Abe, "Microstructure and mechanical properties of pure titanium models fabricated by selective laser melting," *Proceedings of the Institution of Mechanical Engineers, Part C: Journal of Mechanical Engineering Science*, vol. 218, no. 7, pp. 711–719, 2004.
- [46] H. Gong, K. Rafi, H. Gu, G. D. Janaki Ram, T. Starr, and B. Stucker, "Influence of defects on mechanical properties of Ti-6Al-4V components produced by selective laser melting and electron beam melting," *Materials and Design*, vol. 86, pp. 545–554, 2015.
- [47] H. Gong, K. Rafi, H. Gu, T. Starr, and B. Stucker, "Analysis of defect generation in Ti-6Al-4V parts made using powder bed fusion additive manufacturing processes," *Additive Manufacturing*, vol. 1, pp. 87–98, 2014.
- [48] L. Facchini, E. Magalini, P. Robotti, A. Molinari, S. Höges, and K. Wissenbach, "Ductility of a Ti-6Al-4V alloy produced by selective laser melting of prealloyed powders," *Rapid Prototyping Journal*, vol. 16, no. 6, pp. 450–459, 2010.
- [49] K. Kempen, L. Thijs, J. Van Humbeeck, and J.-P. Kruth, "Mechanical Properties of AlSi10Mg Produced by Selective Laser Melting," *Physics Procedia*, vol. 39, pp. 439–446, 2012.
- [50] A. Uriondo, M. Esperon-Miguez, and S. Perinpanayagam, "The present and future of additive manufacturing in the aerospace sector: A review of important aspects," *Proceedings of the Institution of Mechanical Engineers, Part G: Journal of Aerospace Engineering*, vol. 229, no. 11, pp. 2132–2147, 2015.
- [51] J. Garcia-Martin, J. Gómez-Gil, and E. Vázquez-Sánchez, "Non-Destructive Techniques Based on Eddy Current Testing," *Sensors*, vol. 11, no. 3, pp. 2525–2565, 2011.
- [52] R. Roy, D. Agrawal, J. Cheng, and S. Gedevisanishvili, "Full sintering of powdered-metal bodies in a microwave field," *Nature*, vol. 399, pp. 668–670, 1999.

- [53] E. Jerby, Y. Meir, A. Salzberg, E. Aharoni, A. Levy, J. P. Torralba, and B. Cavallini, "Incremental metal-powder solidification by localized microwave-heating and its potential for additive manufacturing," *Additive Manufacturing*, vol. 6, pp. 53–66, 2015.
- [54] H. Fujiwara, S. Toyota, L. Anggraini, K. Ameyama, and D. Agrawal, "Microwave heating behavior of fine stainless steel powders in H-field at 2.45 GHz," in *International Microwave Power Institute's 44th Annual Symposium*, Denver, 2010, pp. 79–83.
- [55] N. Yoshikawa, E. Ishizuka, and S. Taniguchi, "Heating of Metal Particles in a Single-Mode Microwave Applicator," *Materials Transactions*, vol. 47, no. 3, pp. 898–902, 2006.
- [56] O. O. Klein, S. Donovan, M. Dressel, and G. Grüner, "Microwave cavity perturbation technique: Part I: Principles," *International Journal of Infrared and Millimeter Waves*, vol. 14, no. 12, pp. 2423–2457, 1993.
- [57] S. Donovan, O. Klein, M. Dressel, K. Holczer, and G. Grüner, "Microwave cavity perturbation technique: Part II: Experimental scheme," *International Journal of Infrared and Millimeter Waves*, vol. 14, no. 12, pp. 2459–2487, 1993.
- [58] M. Dressel, O. Klein, S. Donovan, G. Grüner, and G. Grüner, "Microwave cavity perturbation technique: Part III: Applications," *International Journal of Infrared and Millimeter Waves*, vol. 14, no. 12, pp. 2489–2517, 1993.
- [59] M. Eichelbaum, R. Stösser, A. Karpov, C.-K. Dobner, F. Rosowski, A. Trunschke, and R. Schlögl, "The microwave cavity perturbation technique for contact-free and in situ electrical conductivity measurements in catalysis and materials science." *Physical Chemistry Chemical Physics : PCCP*, vol. 14, no. 3, pp. 1302–12, 2012.
- [60] Y. Guan and Y. Nikawa, "Measurement of temperature-dependent complex permittivity for materials using cylindrical resonator under microwave irradiation," *Electronics and Communications in Japan (Part II: Electronics)*, vol. 90, no. 11, pp. 1–8, 2007.
- [61] H. Kobayashi and S. Ogawa, "Dielectric Constant and Conductivity Measurement of Powder Samples by the Cavity Perturbation Method," *Japanese Journal of Applied Physics*, vol. 10, pp. 345–350, 1971.
- [62] J. Sheen, "Measurements of microwave dielectric properties by an amended cavity perturbation technique," *Measurement*, vol. 42, no. 1, pp. 57–61, 2009.
- [63] R. G. Carter, "Accuracy of Microwave Cavity Perturbation Measurements," *IEEE Transactions on Microwave Theory and Techniques*, vol. 49, no. 5, pp. 918–923, 2001.

- [64] H. Kawabata, T. Kobayashi, Y. Kobayashi, and Z. Ma, "Measurement accuracy of a TM<sub>0</sub>m<sub>0</sub> mode cavity method to measure complex permittivity of rod samples," *2006 Asia-Pacific Microwave Conference*, pp. 1465–1470, dec 2006.
- [65] B. Meng, J. Booske, and R. Cooper, "Extended Cavity Perturbation Technique to Determine the Complex Permittivity of Dielectric Materials," *IEEE Transactions on Microwave Theory and Techniques*, vol. 43, no. 11, pp. 2633–2636, 1995.
- [66] A. J. Estlin and E. Bussey, "Errors in Dielectric Measurements Due to a Sample Insertion Hole in a Cavity," *IRE Transactions on Microwave Theory and Techniques*, pp. 650–653, 1960.
- [67] R. A. Waldron, "Perturbation theory of resonant cavities," *Proceedings of the IEE - Part C: Monographs*, vol. 107, no. 12, pp. 272–274, 1960.
- [68] R. Carter, "Accuracy of microwave cavity perturbation measurements," *IEEE Transactions on Microwave Theory and Techniques*, vol. 49, no. 5, pp. 918–923, 2001.
- [69] M. Lin, Y. Wang, and M. N. Afsar, "Precision Measurement Of Complex Permittivity And Permeability By Microwave Cavity Perturbation Technique," *Spectroscopy and Material Properties*, vol. 62, pp. 62–63.
- [70] Y. Ye, T. Liu, X. Zeng, J. He, and C. Akyel, "Accurate Permittivity Measurement Using the Cavity Perturbation Technique at ISM 5.8Ghz Radio Band," in *2007 International Conference on Microwave and Millimeter Wave Technology*. IEEE, 2007.
- [71] K. Mathew and U. Raveendranath, "Cavity Perturbation Techniques for Measuring Dielectric Parameters of Water and Other Allied Liquids," *Sensors Update*, vol. 7, no. 1, pp. 185–210, 2000.
- [72] J. A. Cuenca, E. Thomas, S. Mandal, O. Williams, and A. Porch, "Broadband Microwave Measurements of Nanodiamond," in *Microwave Conference (APMC), 2014 Asia-Pacific*, Sendai, Japan, 2014, pp. 441–443.
- [73] D. M. Pozar, *Microwave Engineering*, 4th ed. Wiley, 1998.
- [74] J. Cuenca, "Characterisation of Powders Using Microwave Cavity Perturbation," PhD Thesis, Cardiff University, 2015.
- [75] J. M. Jin, *The Finite Element Method in Electromagnetics*, 2nd ed. Wiley IEEE Press, 2002.
- [76] T. Itoh, *Finite Element Software for Microwave Engineering*, G. Pelosi and P. P. Silverster, Eds. Wiley Interscience, 1996.

- [77] J. A. Cuenca, S. Klein, R. Rüger, and A. Porch, "Microwave Complex Permeability of Magnetite Using Non-demagnetising and Demagnetising Cavity Modes," in *44th European Microwave Conference*, Rome, 2014, pp. 128–131.
- [78] M. P. Robinson and J. Clegg, "Improved Determination of Q-Factor and Resonant Frequency by a Quadratic Curve-Fitting Method," *IEEE Transactions on Electromagnetic Compatibility*, vol. 47, no. 2, pp. 399–402, 2005.
- [79] P. J. Petersan and S. M. Anlage, "Measurement of Resonant Frequency and Quality Factor of Microwave Resonators: Comparison of Methods," *Journal of Applied Physics*, vol. 84, no. 6, p. 29, 1998.
- [80] M. Sanchez, E. Martin, and J. Zamarro, "New vectorial automatic technique for characterisation of resonators," *IEE Proceedings H - Microwaves, Antennas and Propagation*, vol. 136, no. 2, pp. 147–150, 1989.
- [81] S. Chatterjee, "Microwave cavity resonators. Some perturbation effects and their applications," *Journal of the British Institution of Radio Engineers*, vol. 13, no. 10, pp. 475–484, 1953.
- [82] Z. Pourgholamhossein, F. Talaei, G. Askari, and M. Sadeghi, "Analysis and Implementation of a Dual Mode Cavity Band Pass Filter," in *Progress In Electromagnetics Research Symposium Proceedings*, Prague, 2015, pp. 2099–2106.
- [83] L. Chen, C. Ong, and B. Tan, "Cavity perturbation technique for the measurement of permittivity tensor of uniaxially anisotropic dielectrics," *IEEE Transactions on Instrumentation and Measurement*, vol. 48, no. 6, pp. 1023–1030, 1999.
- [84] J. O. Artman and P. E. Tannenwald, "Measurement of susceptibility tensor in ferrites," *Journal of Applied Physics*, vol. 26, no. 9, pp. 1124–1132, 1955.
- [85] E. Spencer, R. LeCraw, and F. Reggia, "Microwave Dielectric Constants and Permeabilities of Ferrite Spheres," *Proceedings of the IRE*, vol. 44, no. 6, pp. 790–800, 1956.
- [86] D. J. Rowe, A. A. Abduljabar, A. Porch, D. A. Barrow, and C. J. Allender, "Improved Split-Ring Resonator for Micro fluidic Sensing," *IEEE Transactions on Microwave Theory and Techniques*, vol. 62, no. 3, pp. 689–698, 2014.
- [87] A. Sihvola, *Electromagnetic Mixing Formulas and Applications*. London: The Institution of Electrical Engineers, 1999.
- [88] M. Lin and M. N. Afsar, "A new cavity perturbation technique for accurate measurement of dielectric parameters," in *Microwave Symposium Digest*, no. 4. San Francisco: IEEE, 2006, pp. 1630–1633.

- [89] A. Parkash, J. K. Vaid, and A. Mansingh, "Measurement of Dielectric Parameters at Microwave Frequencies by Cavity-Perturbation Technique," *IEEE Transactions on Microwave Theory and Techniques*, vol. 27, no. 9, pp. 791–795, 1979.
- [90] S. B. Jones and S. P. Friedman, "Particle shape effects on the effective permittivity of anisotropic or isotropic media consisting of aligned or randomly oriented ellipsoidal particles," *Water Resources Research*, vol. 36, no. 10, p. 2821, 2000.
- [91] A. Arai, J. Binner, and T. Cross, "Comparison of techniques for measuring high temperature microwave complex permittivity," *Journal of Microwave Power and Electromagnetic Energy*, vol. 31, no. 1, pp. 12–18, 1996.
- [92] M. R. Stuart, "Dielectric constant of quartz as a function of frequency and temperature," *Journal of Applied Physics*, vol. 26, no. 12, pp. 1399–1404, 1955.
- [93] M. Matsubara, "A method for evaluating a complex permittivity of dielectric material by using whispering gallery modes on a spherical resonator," *2006 Asia-Pacific Microwave Conference*, pp. 1575–1578, 2006.
- [94] M. D. Janezic and J. Baker-jarvis, "Full-Wave Analysis of a Split-Cylinder Resonator for Nondestructive Permittivity Measurements," *IEEE Transactions on Microwave Theory and Techniques*, vol. 47, no. 10, pp. 2014–2020, 1999.
- [95] J. Hartnett, M. Tobar, E. Ivanov, and J. Krupka, "Room temperature measurement of the anisotropic loss tangent of sapphire using the whispering gallery mode technique," *IEEE Transactions on Ultrasonics, Ferroelectrics and Frequency Control*, vol. 53, no. 1, pp. 34–38, 2006.
- [96] M. Ignatenko, M. Tanaka, and M. Sato, "Absorption of Microwave Energy by a Spherical Nonmagnetic Metal Particle," *Japanese Journal of Applied Physics*, vol. 48, no. 6, p. 067001, 2009.
- [97] K. I. Rybakov, V. E. Semenov, S. V. Egorov, a. G. Ereemeev, I. V. Plotnikov, and Y. V. Bykov, "Microwave heating of conductive powder materials," *Journal of Applied Physics*, vol. 99, no. 2, pp. 023 506–1,9, 2006.
- [98] J. Cheng, R. Roy, and D. Agrawal, "Experimental Proof of Major Role of Magnetic Field Losses in Microwave Heating of Metal and Metallic Composites," *Journal of Materials Science Letters*, vol. 20, no. 17, pp. 1561–1563, 2001.
- [99] J. Ma, J. F. Diehl, E. J. Johnson, K. R. Martin, N. M. Miskovsky, C. T. Smith, G. J. Weisel, B. L. Weiss, and D. T. Zimmerman, "Systematic Study of Microwave Absorption, Heating, and Microstructure Evolution of Porous Copper Powder Metal Compacts," *Journal of Applied Physics*, vol. 101, no. 7, p. 074906, 2007.

- [100] A. Mondal, A. Shukla, A. Upadhyaya, and D. Agrawal, "Effect of porosity and particle size on microwave heating of copper," *Science of Sintering*, vol. 42, no. 2, pp. 169–182, 2010.
- [101] K. Kashimura, S. Suzuki, M. Hayashi, T. Mitani, N. Shinohara, and K. Nagata, "Surface-plasmon-like modes of graphite powder compact in microwave heating," *Journal of Applied Physics*, vol. 112, no. 3, p. 034905, 2012.
- [102] K. Kashimura, N. Hasegawa, S. Suzuki, M. Hayashi, T. Mitani, N. Shinohara, and K. Nagata, "Effects of relative density on microwave heating of various carbon powder compacts microwave-metallic multi-particle coupling using spatially separated magnetic fields," *Journal of Applied Physics*, vol. 113, no. 2, p. 024902, 2013.
- [103] P. Mishra, A. Upadhyaya, and G. Sethi, "Modeling of microwave heating of particulate metals," *Metallurgical and Materials Transactions B*, vol. 37, no. 5, pp. 839–845, 2006.
- [104] ASTM International, "ASTM B348-13, Standard Specification for Titanium and Titanium Alloy Bars and Billets." [Online]. Available: <http://www.astm.org/> [Accessed: 2017-03-29]
- [105] V. Parshin, E. Serov, K. Van Klooster, and R. Ravanelli, "Resonator techniques for reflectivity and surface resistivity at high temperature: Methodology and measurements," in *18th International Conference on Microwave Radar and Wireless Communications*, Vilnius, 2010, pp. 1–5.
- [106] M. Jamesh, S. Kumar, and T. S. N. Sankara Narayanan, "Effect of Thermal Oxidation on Corrosion Resistance of Commercially Pure Titanium in Acid Medium," *Materials and Corrosion*, vol. 64, no. 10, pp. 902–907, 2013.
- [107] D. Velten, V. Biehl, F. Aubertin, B. Valeske, W. Possart, and J. Breme, "Preparation of TiO<sub>2</sub> layers on cp-Ti and Ti6Al4V by thermal and anodic oxidation and by sol-gel coating techniques and their characterization," *Journal of Biomedical Materials Research*, vol. 59, no. 1, pp. 18–28, 2002.
- [108] E. Gemelli and N. H. A. Camargo, "Oxidation Kinetics of Commercially Pure Titanium," *Revista Materia*, vol. 12, no. 3, pp. 525–531, 2007.
- [109] J. Lausmaa, B. Kasemo, and H. Mattsson, "Surface spectroscopic characterization of titanium implant materials," *Applied Surface Science*, vol. 44, no. 2, pp. 133–146, 1990.
- [110] W. Lee and C. Hyun, "XPS study of porous dental implants fabricated by electro-discharge-sintering of spherical Ti-6Al-4V powders in a vacuum atmosphere," *Applied Surface Science*, vol. 252, no. 12, pp. 4250–4256, 2006.

- [111] R. N. S. Sodhi, "X-ray photoelectron spectroscopic comparison of sputtered Ti, Ti6Al4V, and passivated bulk metals for use in cell culture techniques," *Journal of Vacuum Science & Technology A: Vacuum, Surfaces, and Films*, vol. 9, no. 3, p. 1329, 1991.
- [112] A. Templeton, X. Wang, S. J. Penn, S. J. Webb, L. F. Cohen, and N. M. Alford, "Microwave Dielectric Loss of Titanium Oxide," *Journal of the American Ceramic Society*, vol. 83, no. 1, pp. 95–100, 2000.
- [113] N. M. Alford and S. J. Penn, "Sintered alumina with low dielectric loss," *Journal of Applied Physics*, vol. 80, no. 10, pp. 5895–5898, 1996.
- [114] V. D. Buchelnikov, D. V. Louzguine-Luzgin, A. P. Anzulevich, I. V. Bychkov, N. Yoshikawa, M. Sato, and A. Inoue, "Modeling of microwave heating of metallic powders," *Physica B: Condensed Matter*, vol. 403, no. 21-22, pp. 4053–4058, 2008.
- [115] T. Gupta, M. Akhtar, and B. Animesh, "A Unit Cell Approach to Model and Characterize the Metal Powders and Metal-Dielectric Composites at Microwave Frequencies," *Progress in Electromagnetics Research*, vol. 49, pp. 363–387, 2013.
- [116] M. Ignatenko and M. Tanaka, "Effective Permittivity and Permeability of Coated Metal Powders at Microwave Frequency," *Physica B: Condensed Matter*, vol. 405, no. 1, pp. 352–358, 2010.
- [117] Good Fellow, "Titanium/Aluminium/Vanadium (Ti90/Al 6/V 4)." [Online]. Available: <http://www.goodfellow.com/E/Titanium-Aluminium-Vanadium.html> [Accessed: 2017-03-29]
- [118] T. Galek, K. Porath, E. Burkel, and U. van Rienen, "Extraction of effective permittivity and permeability of metallic powders in the microwave range," *Modelling and Simulation in Materials Science and Engineering*, vol. 18, no. 2, p. 025015, 2010.
- [119] V. D. Buchelnikov, D. V. Louzguine-Luzgin, G. Xie, S. Li, N. Yoshikawa, M. Sato, A. P. Anzulevich, I. V. Bychkov, and A. Inoue, "Heating of metallic powders by microwaves: Experiment and theory," *Journal of Applied Physics*, vol. 104, no. 11, p. 113505, 2008.
- [120] MatWeb, "Titanium Ti-6Al-4V (Grade 5)." [Online]. Available: <http://www.matweb.com/search/DataSheet.aspx?MatGUID=b350a789eda946c6b86a3e4d3c577b39> [Accessed: 2016-04-17]
- [121] S. P. Morgan, "Effect of Surface Roughness on Eddy Current Losses at Microwave Frequencies," *Journal of Applied Physics*, vol. 20, no. 4, p. 352, 1949.
- [122] E. O. Hammerstad and F. Bekkadal, *Microstrip Handbook*. Trondheim, Norway: Univ. Trondheim, 1975.

- [123] A. Sain and K. L. Melde, "Characterizing the impact of conductor surface roughness on CB-CPW behavior via reduced computational complexity," *2012 IEEE 21st Conference on Electrical Performance of Electronic Packaging and Systems, EPEPS 2012*, no. 1, pp. 260–263, 2012.
- [124] S. Hall, S. G. Pytel, P. G. Huray, D. Hua, A. Moonshiram, G. A. Brist, and E. Sijercic, "Multigigahertz Causal Transmission Line Modeling Methodology Using a 3-D Hemispherical Surface Roughness Approach," *Methodology*, vol. 55, no. 12, pp. 2614–2624, 2007.
- [125] G. Gold and K. Helmreich, "Surface impedance concept for modeling conductor roughness," in *2015 IEEE MTT-S International Microwave Symposium*, 2015.
- [126] F. Yu and P. B. Nagy, "Numerical method for calculating the apparent eddy current conductivity loss on randomly rough surfaces," *Journal of Applied Physics*, vol. 95, no. 12, pp. 8340–8351, 2004.
- [127] B. Curran, I. Ndip, S. Guttovski, and H. Reichl, "On the Quantification and Improvement of the Models for Surface Roughness," in *IEEE Workshop on Signal Propagation on Interconnects*, Strasbourg, 2009, pp. 1–4.
- [128] Y. Kobayashi, T. Imai, and H. Kayano, "Microwave measurement of temperature and current dependences of surface impedance for high-T<sub>c</sub> superconductors," *IEEE Transactions on Microwave Theory and Techniques*, vol. 39, no. 9, pp. 1530–1538, 1991.
- [129] C. Edgcombe, "Measurement of Surface Resistance of High-T<sub>c</sub> Superconductor by use of Dielectric Resonator," *Electronics Letters*, vol. 27, no. 10, pp. 815–816, 1991.
- [130] T. Kuhleemann and J. Hinken, "Measurements of the thickness dependence of the surface resistance of laser ablated high - T<sub>c</sub> superconducting thin films," *IEEE Transactions on Magnetics*, vol. 27, no. 2, pp. 872–875, 1991.
- [131] N. Klein, U. Dahne, U. Poppe, N. Tellmann, K. Urban, S. Orbach, S. Hensen, G. Muller, and H. Piel, "Microwave surface resistance of epitaxial YBa<sub>2</sub>Cu<sub>3</sub>O<sub>7</sub> thin films at 18.7 GHz measured by a dielectric resonator technique," *Journal of Superconductivity*, vol. 5, no. 2, pp. 195–201, 1992.
- [132] S. J. Fiedziuszko and P. D. Heidmann, "Dielectric Resonator Used as a Probe for High T<sub>c</sub> Superconductor Measurements," in *IEEE MTT-S International Microwave Symposium Digest*, Long Beach, 1989, pp. 555–558.
- [133] J. Krupka, "Measurement of the complex permittivity of metal nanoislands and the surface resistance of thin conducting films at microwave frequencies," *Measurement Science and Technology*, vol. 19, p. 065701, 2008.

- [134] J. Krupka and J. Mazierska, "Improvement of Accuracy in Measurements of the Surface Resistance of Superconductors Using Dielectric Resonators," *IEEE Transactions on Applied Superconductivity*, vol. 8, no. 4, pp. 164–167, 1998.
- [135] B. Hakki and P. Coleman, "A Dielectric Resonator Method of Measuring Inductive Capacities in the Millimeter Range," *IRE Transactions on Microwave Theory and Techniques*, vol. 8, pp. 402–410, 1960.
- [136] J. Krupka, M. Klinger, M. Kuhn, A. Baranyak, M. Stiller, J. Hinken, and J. Modolski, "Surface resistance measurements of HTS films by means of sapphire dielectric resonators," *IEEE Transactions on Applied Superconductivity*, vol. 3, no. 3, pp. 3043–3048, 1993.
- [137] T. Iwai, D. Mizutani, and M. Tani, "Measurement of High-Frequency Conductivity Affected by Conductor Surface Roughness Using Dielectric Rod Resonator Method," in *2015 IEEE International Symposium on Electromagnetic Compatibility (EMC)*, vol. 1, no. 1, Dresden, 2015, pp. 634–639.
- [138] Y. Kobayashi and M. Katoh, "Microwave Measurement of Dielectric Properties of Low-Loss Materials by the Dielectric Rod Resonator Method," *IEEE Transactions on Microwave Theory and Techniques*, vol. 33, no. 7, pp. 586–592, 1985.
- [139] N. J. Parker, A. P. Kharel, J. R. Powell, P. a. Smith, P. D. Evans, and A. Porch, "Measurements and modeling of hts shielded dielectric resonators," *IEEE Transactions on Applied Superconductivity*, vol. 9, no. 2, pp. 1928–1931, 1999.
- [140] *ASM Ready Reference: Electrical and Magnetic Properties of Metals*. ASM International, 2000.
- [141] J. Krupka, "Measurements of the surface resistance and the effective conductivity of copper clad laminates employing dielectric resonator technique," *IEEE MTT-S International Microwave Symposium Digest*, pp. 515–518, 2007.
- [142] B. Curran, I. Ndip, S. Guttowski, and H. Reichl, "A methodology for combined modeling of skin, proximity, edge, and surface roughness effects," *IEEE Transactions on Microwave Theory and Techniques*, vol. 58, no. 9, pp. 2448–2455, 2010.
- [143] H. Braunisch, "Effects of random rough surface on absorption by conductors at microwave frequencies," *IEEE Microwave and Wireless Components Letters*, vol. 16, no. 4, pp. 221–223, 2006.
- [144] J. Vaithilingam, R. D. Goodridge, R. J. Hague, S. D. Christie, and S. Edmondson, "The effect of laser remelting on the surface chemistry of Ti6Al4V components fabricated by selective laser melting," *Journal of Materials Processing Technology*, vol. 232, pp. 1–8, 2016.

- [145] M. Cabrini, S. Lorenzi, T. Pastore, S. Pellegrini, E. Ambrosio, F. Calignano, D. Manfredi, M. Pavese, and P. Fino, "Effect of heat treatment on corrosion resistance of DMLS AlSi10Mg alloy," *Electrochimica Acta*, vol. 206, pp. 346–355, 2016.
- [146] X. Z. Xin, J. Chen, N. Xiang, Y. Gong, and B. Wei, "Surface characteristics and corrosion properties of selective laser melted Co-Cr dental alloy after porcelain firing," *Dental Materials*, vol. 30, no. 3, pp. 263–270, 2014.
- [147] G. Strano, L. Hao, R. M. Everson, and K. E. Evans, "Surface roughness analysis, modelling and prediction in selective laser melting," *Journal of Materials Processing Technology*, vol. 213, no. 4, pp. 589–597, 2013.
- [148] P. G. Huray, S. Hall, S. Pytel, F. Oluwafemi, R. Mellitz, D. Hua, and P. Ye, "Fundamentals of a 3-D "snowball" model for surface roughness power losses," in *11th IEEE Workshop on Signal Propagation on Interconnects, SPI 2007*, Ruta di Camogli, Genova, 2007, pp. 121–124.
- [149] S. G. Pytel, P. G. Huray, S. H. Hall, R. I. Mellitz, G. Brist, H. M. M. Iii, L. Walker, and M. Garland, "Analysis of Copper Treatments and the Effects on Signal Propagation," in *58th Electronic Components and Technology Conference*, Lake Buena Vista, FL, 2008, pp. 1144–1149.
- [150] N. T. Aboulkhair, N. M. Everitt, I. Ashcroft, and C. Tuck, "Reducing porosity in AlSi10Mg parts processed by selective laser melting," *Additive Manufacturing*, vol. 1, pp. 77–86, 2014.
- [151] M. A. Salazar-Guapuriche, Y. Zhao, A. Pitman, and A. Greene, "Correlation of Strength with Hardness and Electrical Conductivity for Aluminium Alloy 7010," *Materials Science Forum*, vol. 519-521, pp. 853–858, 2006.
- [152] Y. Liu, D. M. Jiang, and W. J. Li, "The effect of multistage ageing on microstructure and mechanical properties of 7050 alloy," *Journal of Alloys and Compounds*, vol. 671, pp. 408–418, 2016.
- [153] G. Lin, Z. Zhang, H. Wang, K. Zhou, and Y. Wei, "Enhanced strength and electrical conductivity of Al-Mg-Si alloy by thermo-mechanical treatment," *Materials Science and Engineering A*, vol. 650, pp. 210–217, 2016.
- [154] S. O. Adeosun, O. I. Sekunowo, S. A. Balogun, and L. O. Osoba, "Effect of Deformation on the Mechanical and Electrical Properties of Aluminum-Magnesium Alloy," *Journal of Minerals & Materials Characterization & Engineering*, vol. 10, no. 6, pp. 553–560, 2011.
- [155] G. R. Metcalfe, "The use of electrical conductivity measurements in detecting heat and fire damage in aircraft structure," in *NDT Technology in Aerospace, IEE Colloquium on*, London, 1990.

- [156] M. Sinvani, A. J. Greenfiel, A. Bergmann, M. Kaveh, and N. Wisser, "Effect of annealing on the temperature dependence of the electrical resistivity of aluminium," *Journal of Physics F: Metal Physics*, vol. 11, no. 1, p. 149, 1981.
- [157] C. S. Çetinarslan, "Effect of cold plastic deformation on electrical conductivity of various materials," *Materials and Design*, vol. 30, no. 3, pp. 671–673, 2009.
- [158] O. P. Agnihotri, "Dislocation densities in heavily cold-worked copper and aluminium," *British Journal of Applied Physics*, vol. 17, no. 5, pp. 603–605, 2002.
- [159] M. Zergoug, G. Kamel, and N. Boucherou, "Mechanical Stress Analysis By Eddy Current Method," *The Journal of American Science*, vol. 4, no. 4, pp. 4–9, 2008.
- [160] F. C. Schoenig, J. A. Soules, H. Chang, and J. J. DiCillo, "Eddy Current Measurements of Residual Stresses Induced by Shot Peening in Titanium Ti6Al4V," *Materials Evaluation*, vol. 55, pp. 22–26, 1995.
- [161] C. Kittel, *Introduction to Solid State Physics*, 8th ed. New York: Wiley, 2005.
- [162] A. Gupta, D. Lloyd, and S. Court, "Precipitation Hardening Processes in an Al-0.4% Mg-1.3% Si-0.25% Fe Aluminum Alloy," *Materials Science and Engineering: A*, vol. 301, no. 2, pp. 140–146, 2001.
- [163] G. Edwards, K. Stiller, G. Dunlop, and M. Couper, "The precipitation sequence in Al-Mg-Si alloys," *Acta Materialia*, vol. 46, no. 11, pp. 3893–3904, 1998.
- [164] M. Murayama and K. Hono, "Pre-precipitate clusters and precipitation processes in Al-Mg-Si alloys," *Acta Materialia*, vol. 47, no. 5, pp. 1537–1548, 1999.
- [165] N. Kumar, P. N. Rao, R. Jayaganthan, and H. G. Brokmeier, "Effect of cryorolling and annealing on recovery, recrystallisation, grain growth and their influence on mechanical and corrosion behaviour of 6082 Al alloy," *Materials Chemistry and Physics*, vol. 165, pp. 177–187, 2015.
- [166] J. Liu, R. E. Saw, and Y. H. Kiang, "Calculation of Effective Penetration Depth in X-Ray Diffraction for Pharmaceutical Solids," *Journal of Pharmaceutical Sciences*, vol. 99, no. 9, pp. 3807–3814, 2010.
- [167] L. G. Parratt, "Surface studies of solids by total reflection of x-rays," *Physical Review*, vol. 95, no. 2, pp. 359–369, 1954.
- [168] M. J. Cooper, "X-ray absorption coefficients for certain metals," *Acta Cryst.*, vol. 18, p. 813, 1965.
- [169] N. Maskil and M. Deutsch, "Structure and wavelength of the Cu Ka<sub>2</sub> x-ray emission line," *Physical Review A*, vol. 37, no. 8, pp. 2947–2952, 1988.
- [170] National Physical Laboratory, "Determination of Residual Stresses by X-ray Diffraction - Issue 2," *Measurement Good Practice Guide No. 52*, 2005.

- [171] J. Robinson, S. Kingman, D. Irvine, P. Licence, A. Smith, G. Dimitrakis, D. Obermayer, and C. O. Kappe, "Understanding microwave heating effects in single mode type cavities-theory and experiment." *Physical chemistry chemical physics : PCCP*, vol. 12, no. 18, pp. 4750–4758, 2010.
- [172] CEM-Microwave, "Discover SP - Microwave Synthesizer." [Online]. Available: <http://cem.com/discover-sp> [Accessed: 2016-12-16]
- [173] Diana Martin, Angela Jianu and D. Ighigeanu, "A Method for the 2.45-GHz Magnetron Output Power Control," *IEEE Transactions on Microwave Theory and Techniques*, vol. 19, no. 2, pp. 347–351, 2003.
- [174] Hua-Feng Huang, "Temperature Control in a Microwave Resonant Cavity System for Rapid Heating of Nylon Monofilament," *Journal of Microwave Power*, vol. 11, no. 4, pp. 305–313, 1976.
- [175] J. M. Catalá-Civera, A. J. Canós, P. Plaza-González, J. D. Gutiérrez, B. García-Baños, and F. L. Peñaranda-Foix, "Dynamic Measurement of Dielectric Properties of Materials at High Temperature during Microwave Heating in a Dual Mode Cylindrical Cavity," *IEEE Transactions on Microwave Theory and Techniques*, vol. 63, no. 9, pp. 2905–2914, 2015.
- [176] J. Jow, M. C. Hawley, M. Finzel, J. Asmussen, H.-H. Lin, and B. Manring, "Microwave Processing and Diagnosis of Chemically Reacting Materials in a Single-Mode Cavity Applicator," *IEEE Transactions on Microwave Theory and Techniques*, vol. 35, no. 12, pp. 1435–1443, 1987.
- [177] J. Naylor, S. Gooding, C. John, A. Morgan, O. Squires, J. Lees, D. A. Barrow, and A. Porch, "Efficient Microwave Heating and Dielectric Characterization of Microfluidic Systems," in *14th International Conference on Miniaturized Systems for Chemistry and Life Sciences*, no. October, Groningen, 2010, pp. 2092–2094.
- [178] W. J. Ellison, "Permittivity of pure water, at standard atmospheric pressure, over the frequency range 0-25 THz and the temperature range 0-100C," *Journal of Physical and Chemical Reference Data*, vol. 36, no. 1, pp. 1–18, 2007.
- [179] U. Kaatze, "Complex permittivity of water as a function of frequency and temperature," *Journal of Chemical and Engineering Data*, vol. 34, no. 4, pp. 371–374, 1989.
- [180] J. Jow, M. Finzel, J. Asmussen, and M. C. Hawley, "Dielectric and Temperature Measurements During Microwave Curing of Epoxy in a Sweeping Resonant Cavity," *1987 IEEE MTT-S International Microwave Symposium Digest*, vol. 87, no. 1, pp. 465–468, 1987.

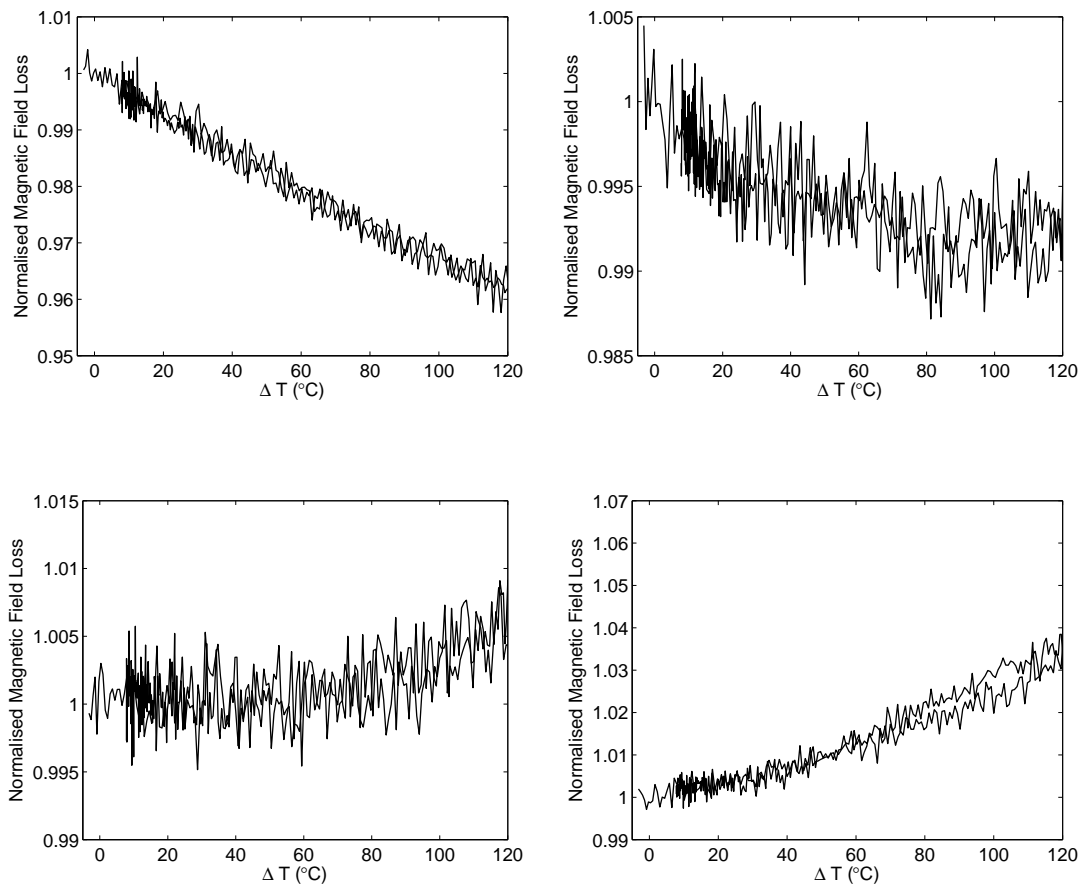
# Appendix

## Appendix A

	Fraction	$\mu_2$ (0.5mm)	$\mu_2$ (1mm)	$\mu_2$ (2mm)
TE <sub>011</sub>	<16 $\mu\text{m}$	-	$0.128 \pm 0.004$	$0.133 \pm 0.004$
	16-32 $\mu\text{m}$	$0.345 \pm 0.02$	$0.324 \pm 0.010$	$0.341 \pm 0.015$
	32-45 $\mu\text{m}$	$0.465 \pm 0.02$	$0.423 \pm 0.014$	$0.431 \pm 0.02$
	> 45 $\mu\text{m}$	$0.399 \pm 0.02$	$0.390 \pm 0.013$	$0.399 \pm 0.02$
TE <sub>012</sub>	<16 $\mu\text{m}$	-	$0.192 \pm 0.006$	$0.206 \pm 0.006$
	16-32 $\mu\text{m}$	$0.420 \pm 0.02$	$0.401 \pm 0.013$	$0.43 \pm 0.02$
	32-45 $\mu\text{m}$	$0.450 \pm 0.02$	$0.415 \pm 0.014$	$0.43 \pm 0.02$
	> 45 $\mu\text{m}$	$0.345 \pm 0.02$	$0.342 \pm 0.011$	$0.356 \pm 0.015$
TE <sub>022</sub>	<16 $\mu\text{m}$	-	$0.227 \pm 0.007$	-
	16-32 $\mu\text{m}$	$0.444 \pm 0.02$	$0.434 \pm 0.014$	-
	32-45 $\mu\text{m}$	$0.447 \pm 0.02$	$0.408 \pm 0.013$	-
	> 45 $\mu\text{m}$	$0.324 \pm 0.02$	$0.324 \pm 0.011$	-

Fractionated powder permeability across different size sample holders.

## Appendix B



Changing loss of fractioned Ti6Al4V samples with increasing temperature. Clockwise from top left:  $< 16 \mu\text{m}$ ,  $16-32 \mu\text{m}$ ,  $32-45 \mu\text{m}$ ,  $> 45 \mu\text{m}$ .

## Appendix C

Sample	Metal	Build Orientation	Finishing
Ti <sub>H_G</sub>	Ti6Al4V	Horizontal	Grit Blasted
Ti <sub>H_W</sub>	Ti6Al4V	Horizontal	Wire Eroded
Ti <sub>V_G</sub>	Ti6Al4V	Vertical	Grit Blasted
Ti <sub>H_N</sub>	Ti6Al4V	Horizontal	As Built
Ti <sub>V_N-A/B</sub>	Ti6Al4V	Vertical	As Built
Al <sub>H_G</sub>	Al10SiMg	Horizontal	Grit Blasted
Al <sub>H_W</sub>	Al10SiMg	Horizontal	Wire Eroded
Al <sub>V_G-A/B</sub>	Al10SiMg	Vertical	Grit Blasted
Al <sub>H_N</sub>	Al10SiMg	Horizontal	As Built
Al <sub>V_N-A/B</sub>	Al10SiMg	Vertical	As Built
CoCr <sub>H_G</sub>	CoCr	Horizontal	Grit Blasted
CoCr <sub>H_W</sub>	CoCr	Horizontal	Wire Eroded
CoCr <sub>V_G-A/B</sub>	CoCr	Vertical	Grit Blasted
CoCr <sub>H_N</sub>	CoCr	Horizontal	As Built
CoCr <sub>V_N-A/B</sub>	CoCr	Vertical	As Built

Samples produced by SLM for surface characterisation. Samples were built parallel (horizontal - *subscript H*) and perpendicular (vertical - *subscript V*) to the build plate, stress relieved and tested either as built (*subscript N*) or after grit blasting (*subscript G*) treatment. For the horizontal samples, the wire eroded side (*subscript W*), closest to the build plate, was also tested. Vertical samples allowed both sides (*subscripts A & B*) to be tested.

## Appendix D

Sample	$r_q$ ( $\mu\text{m}$ ) X Direction	$r_q$ ( $\mu\text{m}$ ) Y Direction	Relative Density $\pm$ 0.05
Ti <sub>H</sub> _G	4.27	5.20	0.99
Ti <sub>H</sub> _W	3.87	3.95	0.99
Ti <sub>V</sub> _G	3.52	3.05	0.97
Ti <sub>H</sub> _N	6.46	9.29	0.93
Ti <sub>V</sub> _N-A	13.7	14.1	0.95
Ti <sub>V</sub> _N-B	12.8	12.6	0.95
Al <sub>H</sub> _G	7.98	8.69	0.92
Al <sub>H</sub> _W	4.22	4.10	0.92
Al <sub>V</sub> _G-A	6.92	6.34	0.95
Al <sub>V</sub> _G-B	6.65	6.66	0.95
Al <sub>H</sub> _N	19.3	19.2	0.93
Al <sub>V</sub> _N-A	20.1	19.7	0.89
Al <sub>V</sub> _N-B	20.3	21.0	0.89
CoCr <sub>H</sub> _G	5.45	8.41	1.00
CoCr <sub>H</sub> _W	1.79	1.73	1.03
CoCr <sub>V</sub> _G-A	7.38	6.99	1.00
CoCr <sub>V</sub> _G-B	6.27	5.6	1.00
CoCr <sub>H</sub> _N	7.89	9.53	1.00
CoCr <sub>V</sub> _N-A	11.2	12.4	1.05
CoCr <sub>V</sub> _N-B	10.7	11.1	1.05

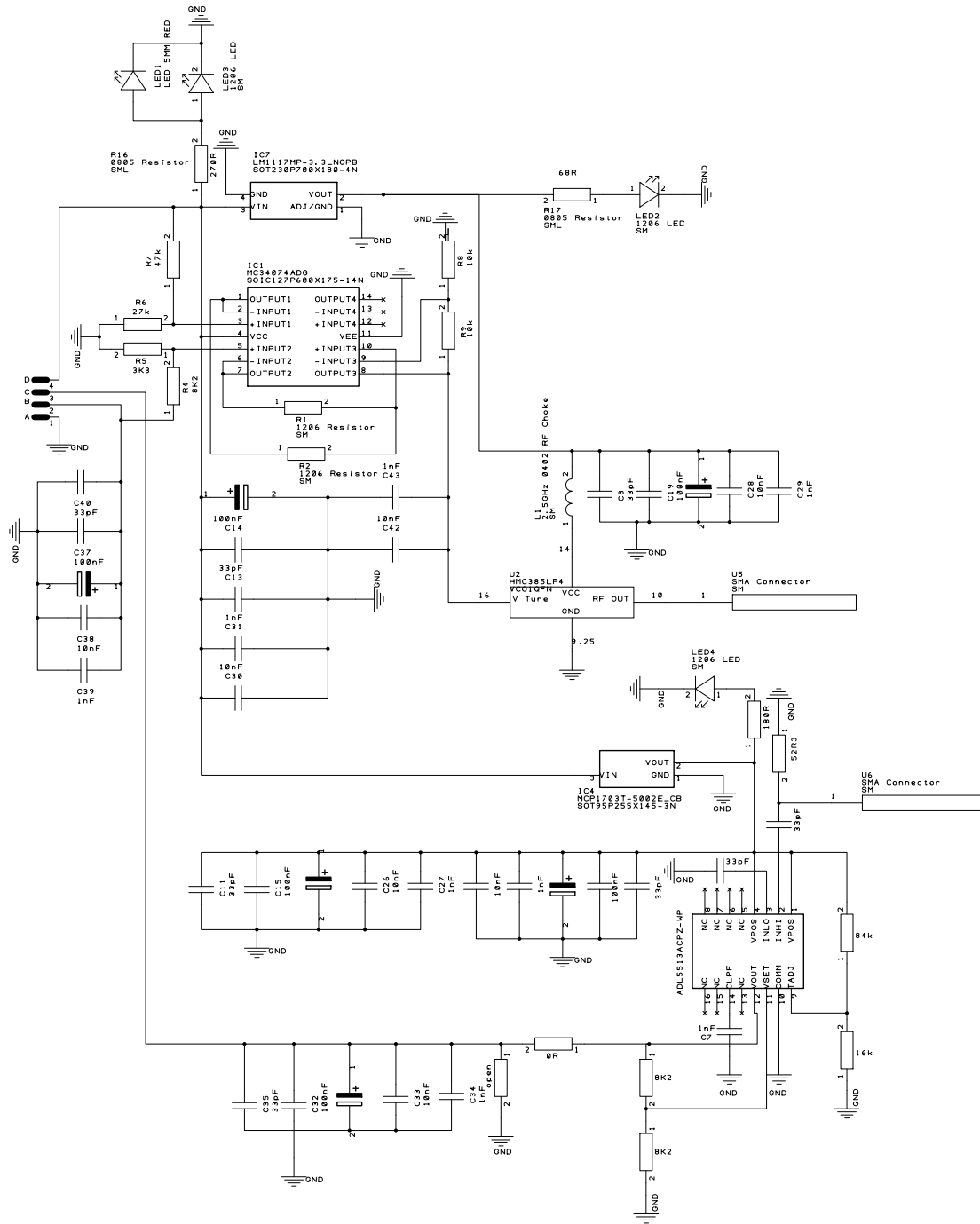
SLM test plate density and roughness in both measurement directions.

## Appendix E

Sample	$R_S$ ( $\Omega$ )	$\frac{P}{P_0}$
Ti <sub>H_G</sub>	$0.1963 \pm 0.0005$	$1.015 \pm 0.002$
Ti <sub>H_W</sub>	$0.2521 \pm 0.0006$	$1.304 \pm 0.003$
Ti <sub>V_G</sub>	$0.2396 \pm 0.0007$	$1.239 \pm 0.003$
Ti <sub>H_N</sub>	$0.1986 \pm 0.0005$	$1.027 \pm 0.002$
Ti <sub>V_N-A</sub>	$0.4835 \pm 0.0010$	$2.499 \pm 0.004$
Ti <sub>V_N-B</sub>	$0.4365 \pm 0.0010$	$2.257 \pm 0.004$
Al <sub>H_G</sub>	$0.0494 \pm 0.0007$	$1.54 \pm 0.02$
Al <sub>H_W</sub>	$0.0566 \pm 0.0007$	$1.77 \pm 0.02$
Al <sub>V_G-A</sub>	$0.0497 \pm 0.0006$	$1.55 \pm 0.014$
Al <sub>V_G-B</sub>	$0.0553 \pm 0.0006$	$1.72 \pm 0.014$
Al <sub>H_N</sub>	$0.0583 \pm 0.0013$	$1.82 \pm 0.04$
Al <sub>V_N-A</sub>	$0.0815 \pm 0.0005$	$2.54 \pm 0.011$
Al <sub>V_N-B</sub>	$0.0946 \pm 0.0006$	$2.94 \pm 0.02$
CoCr <sub>H_G</sub>	$0.1551 \pm 0.0004$	$1.086 \pm 0.002$
CoCr <sub>H_W</sub>	$0.1498 \pm 0.0005$	$1.050 \pm 0.003$
CoCr <sub>V_G-A</sub>	$0.1659 \pm 0.0003$	$1.162 \pm 0.0013$
CoCr <sub>V_G-B</sub>	$0.1652 \pm 0.0006$	$1.157 \pm 0.004$
CoCr <sub>H_N</sub>	$0.1668 \pm 0.0005$	$1.168 \pm 0.002$
CoCr <sub>V_N-A</sub>	$0.2487 \pm 0.0004$	$1.741 \pm 0.003$
CoCr <sub>V_N-B</sub>	$0.2589 \pm 0.0009$	$1.812 \pm 0.006$

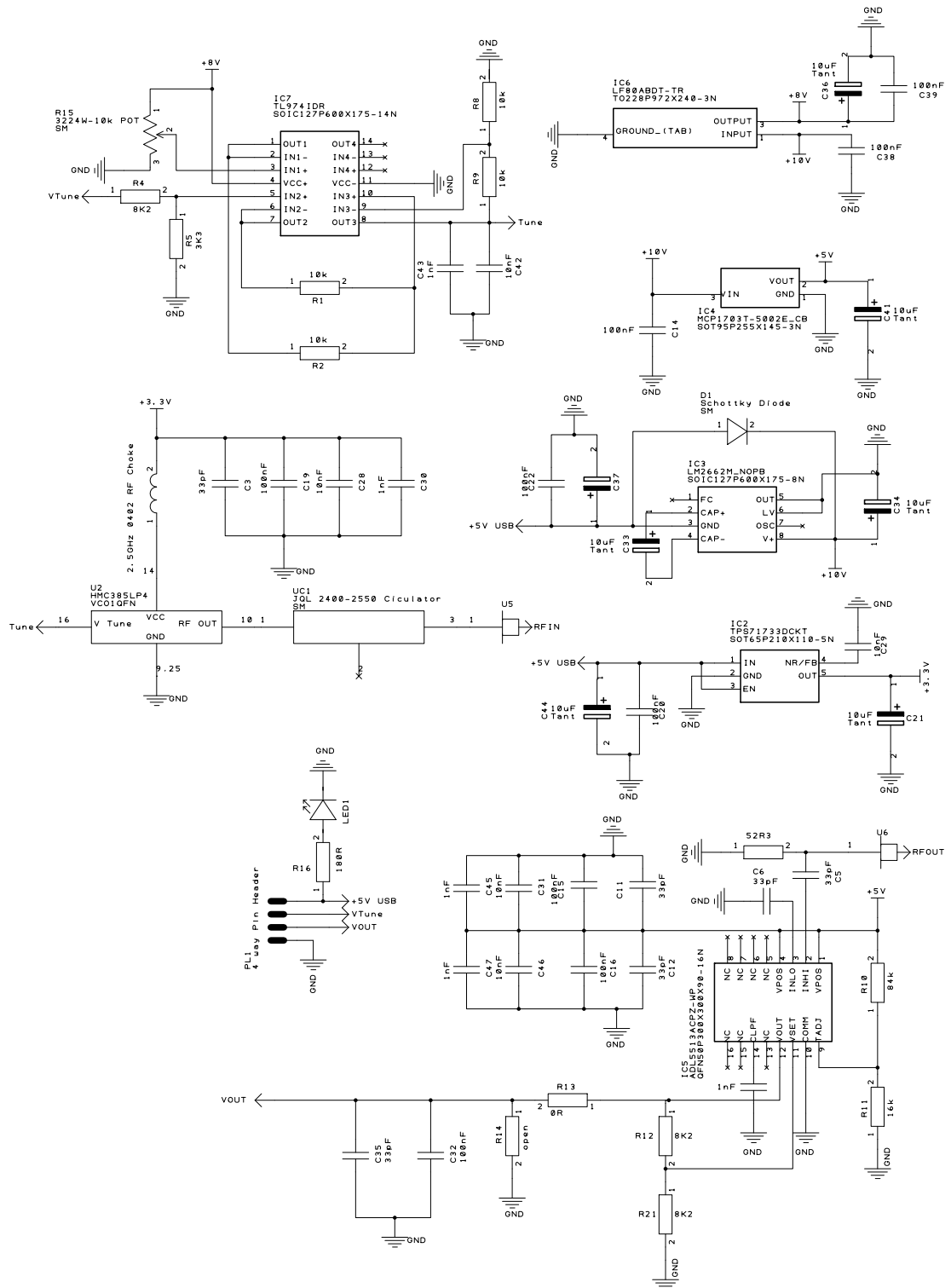
SLM surface resistance measurements.

Appendix F



BSA prototype A schematic

Appendix G



BSA prototype B schematic



## Appendix I

Component	Description	Cost (each)
Hittite HMC385LP4	RF Voltage Controlled Oscillator	£ 15
Analog Devices ADL5513	RF Log Scale Power Meter	£ 6.90
TL974	Quad Op-amp	£ 0.53
LF08AB	8V Regulator	£ 0.35
UA78M05	5V Regulator	£ 0.23
TPS71733	3.3V Regulator	£ 0.73
LM2662	Voltage Doubler	£ 1.60
Kemet T591 Series	47uF Low ESR Caps	£ 0.32
Kemet T491 Series	10uF Decoupling Capacitors	£ 0.30
-	SM Capacitors	£ 0.01
-	5% Tolerance 0.25W Resistors	£ 0.01
3224W	100K SMD Trimming Potentiometer	£ 2.80
65 x 45mm PCB	Dual-layer 1.6mm FR4	£ 4
Wirewound Inductor	4.8nH RF Choke, SRF @ 2.5 GHz	£ 0.20
Mini-Circuits ERA-5SM+	RF Power Amplifier	£ 3
JCD2400T2550SMO	Drop-in circulator	£ 45
JCC2400T2550SO	Connectorised Circulator	£ 180
-	Panel-Mount SMA Connector	£ 5.40
-	Aluminium Enclosure	£ 2
	Prototype A	£ 42
	Prototype B	£ 92
	Prototype C	£ 47

Approximate raw material cost of BSA prototype circuits. Rounded to 2 significant figures. Costs valid Q1 2017, are in GBP exclusive of VAT and, where discounts apply, assume quantities of at least 100.